ENGINEERING THE IONIC POLYMER/GAS INTERFACIAL PROPERTIES OF A FUEL CELL CATALYST LAYER AND PERFORMANCE OPTIMIZATION OF VARIOUS REVERSIBLE FUEL CELLS

By

Regis P. Dowd, Jr.

Submitted to the graduate degree program in Chemical & Petroleum Engineering and the Graduate Faculty of the University of Kansas in partial fulfillment of the requirements for the degree of Doctor of Philosophy.

_____

Chairperson Trung Van Nguyen

_____

Laurence Weatherley

_____

Kevin Charles Leonard

_____

Prajnaparamita Dhar

_____

Xianglin Li

Date Defended: May 11, 2017

The Dissertation Committee for Regis P. Dowd, Jr.

certifies that this is the approved version of the following dissertation:

ENGINEERING THE IONIC POLYMER/GAS INTERFACIAL PROPERTIES OF A FUEL CELL CATALYST LAYER AND PERFORMANCE OPTIMIZATION OF VARIOUS REVERSIBLE FUEL CELLS

_____

Chairperson Trung Van Nguyen

_____

Laurence Weatherley

_____

Kevin Charles Leonard

_____

Prajnaparamita Dhar

_____

Xianglin Li

Date approved: May 11, 2017

ABSTRACT

The primary barrier to full-scale commercialization of proton exchange membrane fuel cells (PEMFCs) is their inability to operate at high power density and energy efficiency. High power density operation is currently limited by high liquid water saturation levels in the cathode catalyst layer. Due to the wettability of the ionomer phase, water produced in the cathode catalyst layer wets the ionomer-gas interface and negatively impacts mass transport of oxygen to the catalyst reaction sites. Therefore, proper water management is vital for operating PEMFCs at high power density. Despite fuel cell water management improvements to membranes, gas diffusion layers, microporous layers, and flow field designs, developing and understanding water transport in the fuel cell catalyst layer continues to be an area of great importance. Previous approaches for improving water management in the catalyst layer resulted in more complicated designs and increased costs. The main objective of this doctoral work is to improve water management in a fuel cell cathode catalyst layer to enable a PEMFC to operate with increased power density and energy efficiency. The work involves (1) validating the hypothesis that specific heat treatment conditions lead to a hydrophobic or hydrophilic ionomer/gas interface, (2) developing a process to incorporate these conditions into the fabrication of the membrane electrode assembly (MEA), and (3) characterizing and testing the MEAs to confirm that the desired ionomer interfacial properties were achieved and that they led to improved fuel cell performance. XPS results confirm specific heat treatment conditions lead to a hydrophobic or hydrophilic ionomer interface. Fuel cell test results show that MEAs with hydrophobic ionomer/gas interfaces generate 133% more power over those with conventional MEAs.

The remainder of this doctoral work focuses on performance optimization of various reversible fuel cells, including the hydrogen-bromine (H_2-Br_2), hydrogen-iodine (H_2-I_2), and

hydrogen-vanadium fuel cells. The H_2-Br_2 and H_2-I_2 reversible fuel cell systems can be operated in the acidic or alkaline modes. The alkaline versions were evaluated because of the advantages over the acidic systems such as higher cell potential, lower corrosivity, and lower catalyst cost for the hydrogen evolution and oxidation reactions. The results confirmed that the alkaline H_2-Br_2 and H_2-I_2 fuel cells have a higher cell voltage than their corresponding acidic systems while maintaining similarly fast electrode reaction kinetics. Hydrogen-vanadium reversible fuel cells were tested to determine the effect of operating and design variables, such as electrolyte flow rate, carbon electrode type, and membrane type and thickness, on the fuel cell performance. Higher performance was observed with higher vanadium flow rate, thinner membranes and carbon nanotube (CNT) vanadium electrode. Peak power density of greater than 540 mW/cm^2 was obtained using a Nafion NR212 membrane and CNT vanadium electrode.

Finally, a new technique was developed to measure VO_2^+ crossover rate in a hydrogen-vanadium reversible fuel cell. Vanadium crossover through the ion exchange membrane in vanadium-based redox flow battery systems results in self discharge and variations in electrolyte concentration. Measuring crossover of electrolyte species directly with a fuel cell, as compared to an idealized dual-chamber system, allows for determining diffusivity under actual fuel cell testing conditions. This new in-situ technique for measuring VO_2^+ crossover with a fuel cell is shown to be reliable and easy to use. The crossover measurement method shows consistent results with VO_2^+ diffusivities of ~10^{-7} cm^2/s reported in the literature.

ACKNOWLEDGMENTS

First and foremost, I offer my sincerest appreciation and gratitude to my advisor, Dr. Trung Van Nguyen. He introduced me to the fascinating field of electrochemical engineering. From my very first visit to the University of Kansas (KU), Dr. Nguyen generously devoted his time and energy into my well-being. Dr. Nguyen's commitment to his students is remarkable and I am thankful to have met him.

I would not be where I am today without the mentorship and leadership of the many teachers, coaches, Naval leaders, and friends who inspired me throughout my life. There are too many to list here, but a few noteworthy people include Ms. Jackson, Coach Harry Clark, Mr. Greene, Charles Lippe, Frank Garza, RADM Bob Greene, CAPT Erik Burian, CAPT Steven Harrison, CAPT McCormick, Dr. Allen Garner, CDR Bob Dirga, LCDR Joe Rysavy, Kenny Comeaux, Senior Chief Stephenson, Chief Timothy Valeika, Chief Errol Barbee, and Chief Kenneth Green.

The Madison & Lila Self Fellowship deserves a tremendous thank you. The Self Fellowship staff does an amazing job in supporting each and every Self Fellow, including Cathy Dwigans, Patty Dannenberg, Sharon Graham, Stefani Buchwitz, Amy Benoit-Warlick, Tammie Zordel, and Dr. Michael Roberts. The financial support provided by the Self Fellowship enabled me to conduct research in any area of my choosing. The biweekly luncheons, communication coaching sessions, public policy leadership opportunities, management training sessions, and public policy trip to Washington, D.C., were extremely valuable experiences.

I would also like to thank my committee members: Dr. Laurence Weatherley, Dr. Kevin Leonard, Dr. Prajnaparamita Dhar, and Dr. Xianglin Li for their valuable feedback and assistance throughout my PhD studies. The KU Chemical & Petroleum Engineering Department

staff is also deserving of acknowledgement for their helpfulness in navigating the path to graduation.

I would like to thank my colleagues at the DOE National Energy Technology Laboratory (NETL), including Dr. Kirk Gerdes, Dr. Shiwoo Lee, Dr. Harry Abernathy, Dr. Yueying (Lynn) Fan, Dr. Gregory Hackett, and Richard Pineault. Dr. Gerdes' dedication and commitment to his research team at NETL was motivating and I am thankful for the opportunity to complete an 8-month graduate research internship under his guidance. NETL researchers and staff made my transition to West Virginia and research experience interesting, challenging, and successful.

I would also like to thank my fellow lab mates: Dr. Venkata Yarlagadda, Dr. Jahangir Masud, Dhruv Konwar, Ankit Verma and Yuanchao Li for their frequent assistance and valuable insight. Venkata deserves a special thank you for teaching me the ropes in the lab during my first year. I will always be grateful for the long days and nights Venkata spent in the lab showing me how to fabricate and test fuel cells.

Last but not least, I would like to express my sincerest appreciation to my friends and family. Even though they never fully understood why getting a Ph.D. takes so long, they always found words of encouragement to keep me motivated. Finally, I would like to thank my wife and mother for their unconditional love and support.

ADDITIONAL ACKNOWLEDGMENTS

Significant portions of this dissertation have been previously published in the Journal of the Electrochemical Society (ECS) as open access articles under the terms of the Create Commons Attribution 4.0 License, which permits unrestricted reuse of the work in any medium, provided the work is properly cited.

Reprinted from:

1. R.P. Dowd Jr., C.S. Day and T.V. Nguyen, "Engineering the Ionic Polymer Phase Surface Properties of a PEM Fuel Cell Catalyst Layer," *Journal of The Electrochemical Society*, **164**, F138 (2017).
2. (Patent pending, expected submission June 2017) R.P. Dowd Jr., T.V. Nguyen, "Controlling the Ionic Polymer/Gas Interfacial Properties of a PEM Fuel Cell Catalyst Layer during Membrane Electrode Assembly Fabrication," *Journal of The Electrochemical Society*, (2017).
3. R.P. Dowd Jr., V. Yarlagadda, D. Konwar, G. Lin, G. Weng, C. Li, K. Chan and T.V. Nguyen, "A Study of Alkaline-Based H_2-Br_2 and H_2-I_2 Reversible Fuel Cells," *Journal of The Electrochemical Society*, **163**, F1471 (2016).
4. R.P. Dowd Jr., V.S. Lakhanpal and T.V. Nguyen, "Performance Evaluation of a Hydrogen-Vanadium Reversible Fuel Cell," *Journal of The Electrochemical Society*, **164**, F564 (2017).
5. (Submitted) R.P. Dowd Jr., D. Powers, R. Wycisk, P.N. Pintauro and T.V. Nguyen, "Hydrogen-Vanadium Reversible Fuel Cell Crossover Study," *Journal of The Electrochemical Society*, (2017).

Additionally, permission has been obtained to reuse the work previously published in ECS Transactions. Reprinted with permission from:

1. R.P. Dowd Jr., C.S. Day and T.V. Nguyen, "Engineering the Ionic Polymer Phase Surface Properties of a PEM Fuel Cell Catalyst Layer," *ECS Transactions*, **72**, 1 (2016).
2. R.P. Dowd Jr., T.V. Nguyen, D.S. Moore, P.N. Pintauro and J.W. Park, "Conductive AFM Study to Differentiate Between the Surface Ionic Conductivity of Nafion and Electrospun Membranes," *ECS Transactions*, **58**, 607 (2013).
3. R.P. Dowd Jr., A. Ying and T.V. Nguyen, "Preliminary Study of a Reversible Hydrogen-Vanadium Flow Battery," *ECS Transactions*, **72**, 11 (2016).

TABLE OF CONTENTS

LIST OF TABLES

LIST OF FIGURES

NOMENCLATURE

AC	Alternating current
AFC	Alkaline fuel cell
AFM	Atomic force microscopy
CL	Catalyst layer
BEV	Battery electric vehicle
CHP	Combined heat and power
CNT	Carbon nanotube
DC	Direct current
DMA	Dynamic mechanical analysis
DMFC	Direct methanol fuel cell
DSC	Differential scanning calorimetry
EES	Electrochemical energy storage
EIS	Electrochemical Impedance Spectroscopy
EV	Electric vehicle
FC	Fuel cell
FCEV	Fuel cell electric vehicle
GDL	Gas diffusion layer
GIXRD	Grazing incidence x-ray diffraction
HER	Hydrogen evolution reaction
HEV	Hybrid electric vehicle
HOPG	Highly oriented pyrolytic graphite
HOR	Hydrogen oxidation reaction

ICE	Internal combustion engine
KU	University of Kansas
LCO	Lithium cobalt oxide
LFP	Lithium iron phosphate
LMO	Lithium manganese oxide
LTO	Lithium titanate oxide
MCFC	Molten carbonate fuel cell
MEA	Membrane electrode assembly
MPL	Microporous layer
NASA	National Aeronautics and Space Administration
NiCad	Nickel cadmium
NMH	Nickle metal hydride
OCV	Open circuit voltage
ORR	Oxygen reduction reaction
PAFC	Phosphoric acid fuel cell
PC	Polarization curve
PD	Power density
PEM	Proton exchange membrane
PEMFC	Proton exchange membrane fuel cell
PFSA	Perfluorosulfonic acid
PGM	Platinum group metal
PHEV	Plug-in hybrid electric vehicle
PHI	Physical Electronics

PPSU	Polyphenylsulfone
PTFE	Polytetrafluoroethylene
RFB	Redox flow batteries (also called reversible or regenerative fuel cells)
RH	Relative humidity
RT	Room temperature
SOC	State of charge
SOFC	Solid oxide fuel cell
T_g (GTT)	Glass transition temperature
TMA	Thermal mechanical analysis
XPS	X-ray photoelectron spectroscopy
XRD	X-ray diffraction

CHAPTER 1: Introduction

1.1 Background

In the U.S., transportation is second only to electricity generation in terms of volume and rate of increase of annual greenhouse gas emissions.[1] Additionally, worldwide energy demand is projected to grow by an astonishing 56% between 2010 and 2040.[2] PEMFC technology is expected to have significant societal impact by enabling the U.S. to meet future energy demands as well as curb greenhouse gas emissions. PEMFCs convert chemical energy from a fuel into electrical energy with very high conversion efficiency. A few application areas for fuel cell technology includes electric grid optimization, load leveling, portable electronics and electric vehicle use. The major barriers for full-scale commercialization of PEMFC technology includes the high PEMFC costs and inadequate worldwide fuel (hydrogen gas) supply network.

1.1.1 Grid Optimization and Load Leveling

The electric grid is designed to meet the highest expected demand, which occurs at most 5% of the time. During off-peak hours, namely 11 pm to 7 am, the electric grid is underutilized.[3] Furthermore, the integration of solar and wind energy technology into the electric grid continues to expand. In 2015, the total capacity added worldwide from renewable energy sources reached an all-time high of 153 GW.[4] Solar energy sources accounted for about one third of total added capacity at ~49 GW.[4] Figure 1.1 shows the annual growth rates of world renewable supply from 1990 to 2014.[5] Solar PV accounted for the largest growth rate at more than 46%, while wind energy was second at ~24%. The intermittent nature of solar and wind energy causes conventional power plants (coal, natural gas, and nuclear) to ramp up and down electricity production throughout the day to compensate for changing wind and solar conditions. Cycling

electricity production at power plants leads to increased operating costs and reduced equipment reliability.[6]

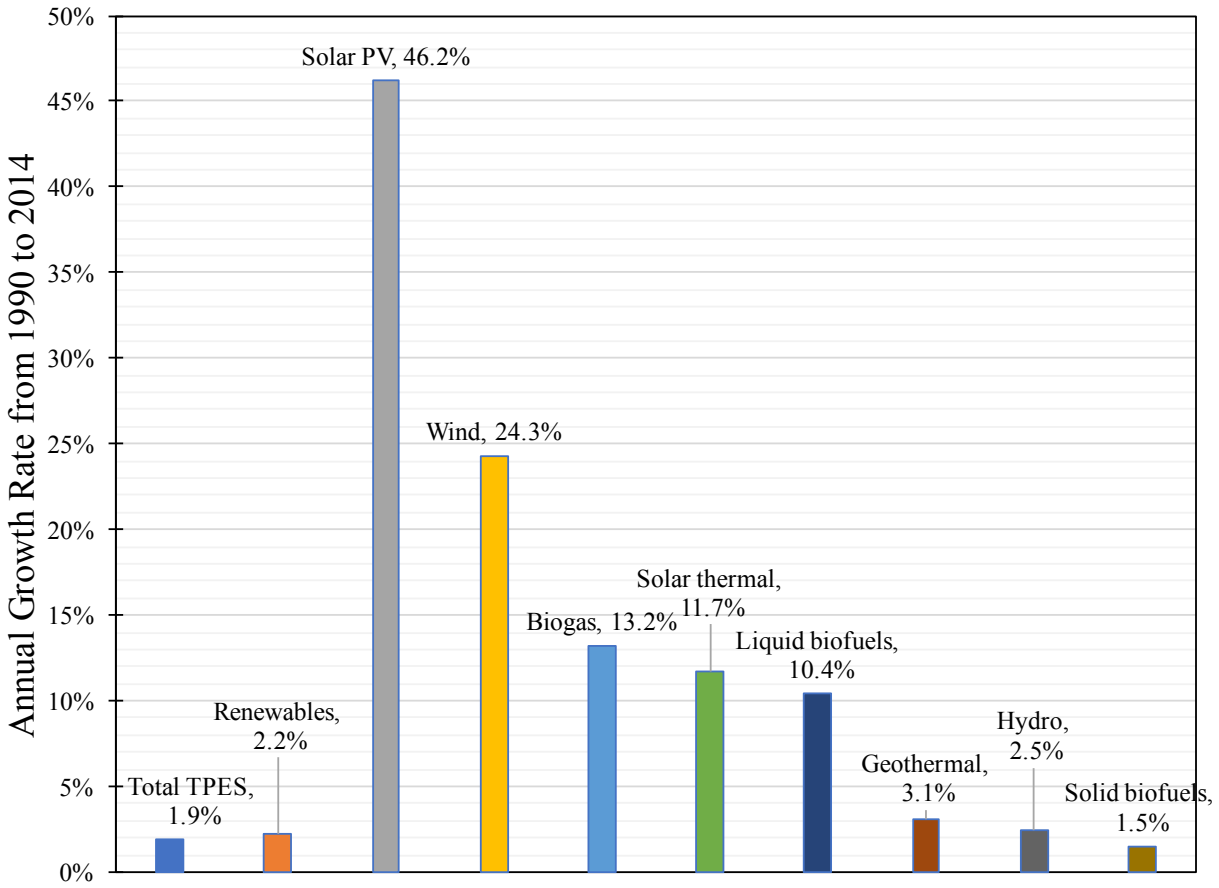

Figure 1.1. Annual growth rates of world renewables supply (1990 to 2014).[5]

One way to reduce power plant operating costs and increase equipment reliability is to develop efficient, cost-effective and on-demand energy storage technologies. This would enable power plants to operate at constant power by storing excess energy into energy storage devices during off-peak hours and discharging the stored energy from the energy storage devices during peak hours. The overall concept of using energy storage devices to enable power plants to run at constant power is called load leveling. Figure 1.2 demonstrates the concept of load leveling on

the electric grid in order to enable constant power generation at conventional power plants. Power plants operate more efficiently and safer when running at steady state output.[6]

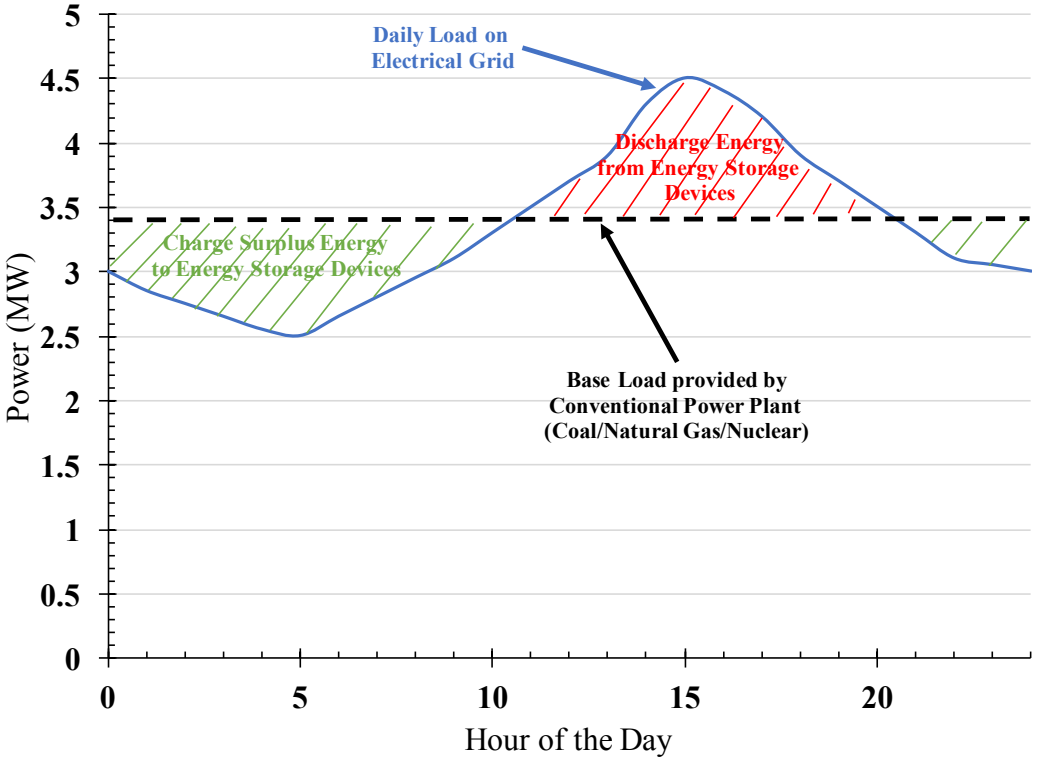

Figure 1.2. Electric grid load leveling.

Grid optimization (i.e. smart grid) involves the integration of energy technologies, advanced utility control, and energy storage that results in the perfect balance of electric grid reliability, availability, efficiency, and cost. A smart grid would likely contain distributed energy generation sources, energy storage devices, electric vehicles, fast and reliable communications to monitor and control the flow of energy, and "intelligent" appliances. The use of electric grid load leveling and grid optimization will free up a significant amount of capacity and enable us to meet the growing worldwide energy demand.

1.1.2 Future of the Electric Vehicle (EV)

According to the International Energy Agency, EV worldwide market share only totaled 180,000 vehicles at the end of 2011.[7] From 2011 to 2012, global EV sales volume more than doubled. EV annual sales volume continues to grow at an exceptional rate. As shown in Figure 1.3, the U.S. and Japan dominate the world EV sales market. As EV range increases and total vehicle cost of ownership continues to decrease, EV sales are expected to continue to rise globally.

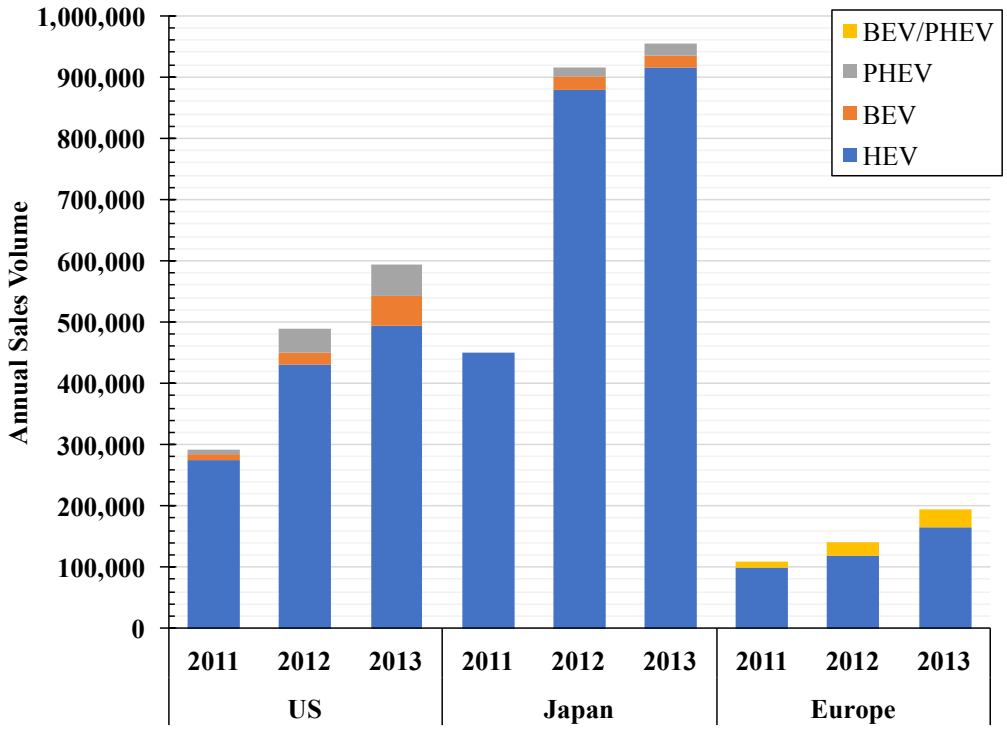

Figure 1.3. Global annual EV sales volume.[7]

EVs are classified according to the vehicle's power source. A battery electric vehicle (BEV) is powered solely by a battery. A hybrid electric vehicle (HEV) contains two or more energy sources, such as both an internal combustion engine (ICE) and a battery coupled to an electric motor. Other forms of energy that can be used in HEVs are fuel cells (FCEV) or

compressed air energy storage. A plug-in HEV (PHEV) is simply a HEV that can be recharged by plugging the vehicle directly into an external source of electric power. Currently, the most commonly produced HEV contains an ICE and battery/electric motor. One of the advantages of an electric motor over an ICE is that an electric motor provides instant torque and maximum horsepower to the wheel at zero revolutions per minute. HEVs are classified as either parallel or series. In a parallel hybrid, the ICE and electric motor can both provide power to the wheels at the same time. In a series hybrid, the ICE only charges the battery while the electric motor provides power to the wheels. Both types of hybrids have advantages and disadvantages. Typically, the series hybrid is more efficient but less powerful than the parallel hybrid.

Instead of simply viewing electric vehicles solely as an energy sink on the electric grid, electric vehicles can also serve as an energy source during peak hours. Smart programming could utilize the extra energy stored in electric vehicles which are connected to the grid during high energy demand periods. Conversely, electric vehicles could be used to store excess energy from the electric grid during low energy demand periods. Figure 1.4 shows a simplified graphic of how electric vehicles connected to the electric grid could play a major role in load leveling and smart grid implementation.

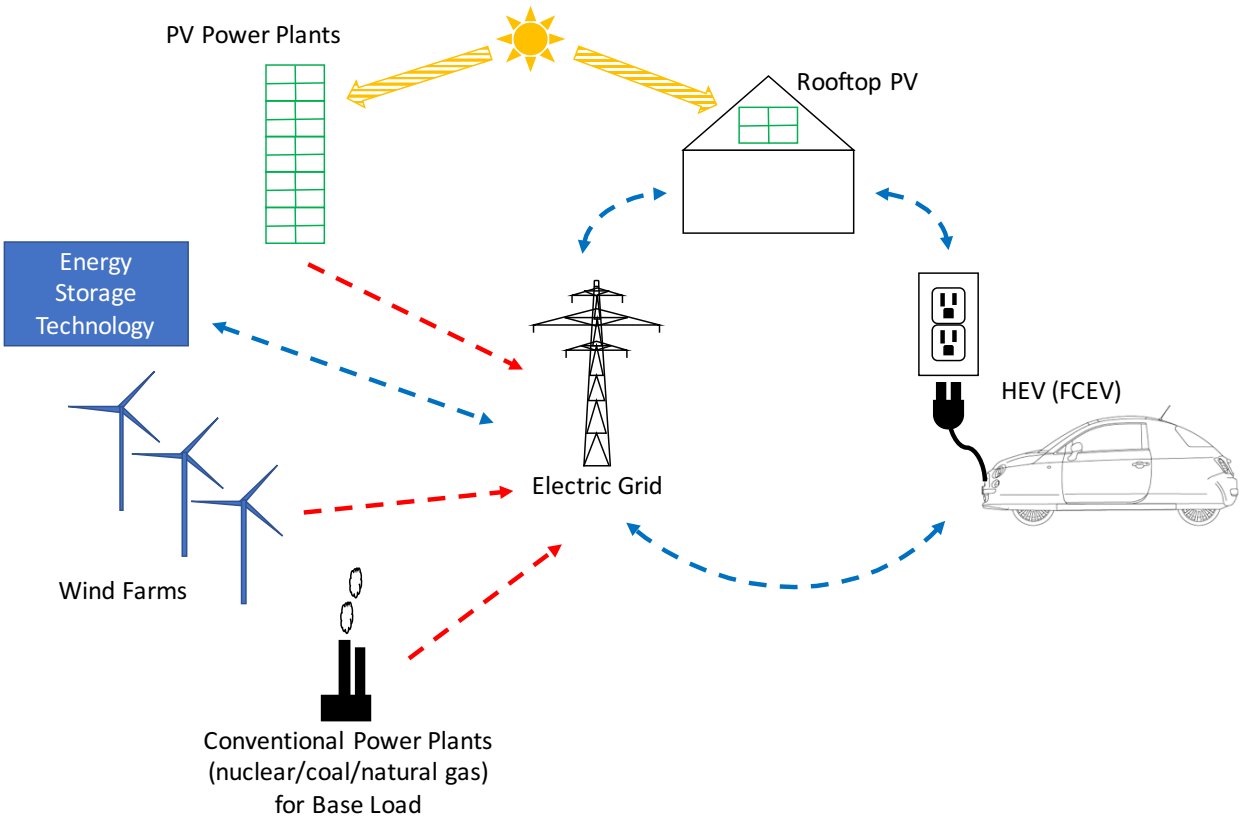

Figure 1.4. Incorporation of HEV and energy storage technology into smart electric grid for load leveling.

1.2 Electrochemical Energy Storage (EES) Systems

EES systems include secondary batteries (i.e. rechargeable batteries), electrochemical capacitors, fuel cells, and flow batteries. EES system characteristics make them advantageous over other power generation technologies for a wide range of applications. EES systems offer almost instantaneous response and very high energy conversion efficiency (60-90%) compared to ICE energy conversion efficiency (<15-35%).[8] High energy conversion efficiency is due to EES systems converting chemical energy directly into electrical energy, whereas for an ICE the chemical energy is first converted to thermal energy. Due to the large amount of unrecoverable heat produced by an ICE, its conversion efficiency is very low. As shown in Figure 1.5, the high

energy density achievable with fuel cells and flow batteries make them suitable for large-scale energy storage applications.[9] Capacitors have high power density but low energy density, therefore making them great for pulsed power applications but poor candidates for large-scale energy storage.

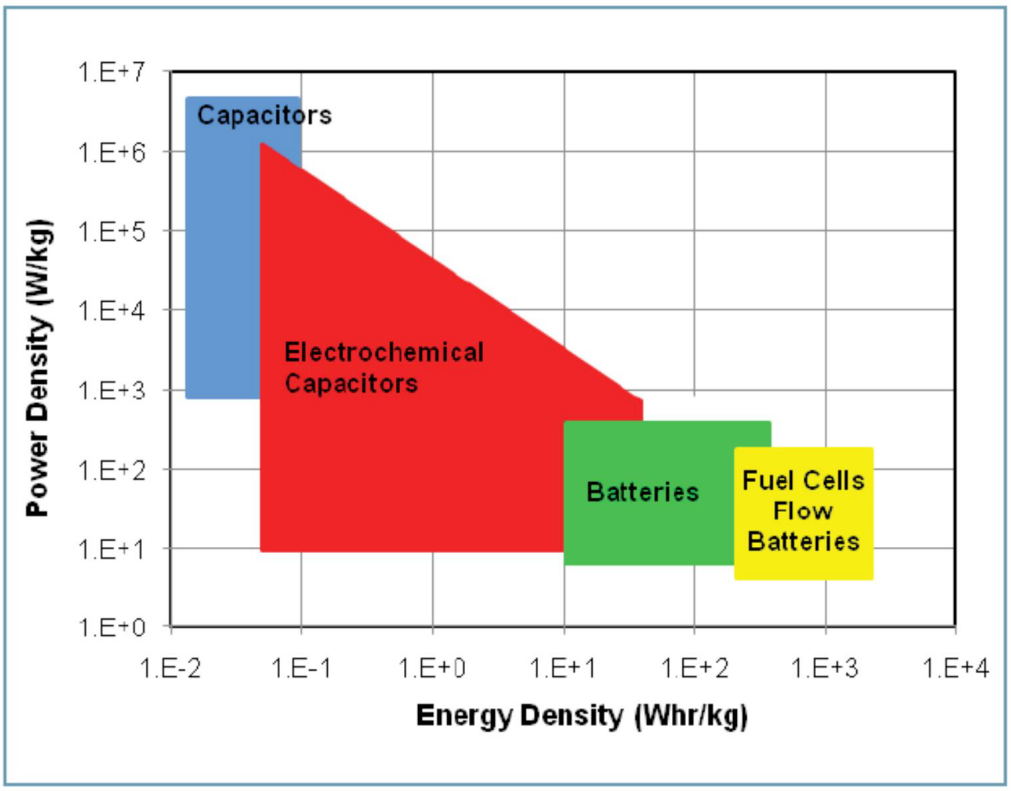

Figure 1.5. Power and energy density ranges for various EES devices.[9]

[Nguyen et al. (2010)]

1.2.1 Secondary Batteries (Rechargeable Batteries)

Conventional batteries are classified as either a primary or secondary battery. A primary battery (e.g. alkaline battery, etc.) is unable to be recharged, whereas a secondary battery (e.g. nickel cadmium, lithium ion, lead acid, etc.) can be recharged for repeated uses. Conventional batteries (primary and secondary batteries) and fuel cells (including flow batteries) have two main

differences. In a fuel cell, the electro-active materials are stored external to the electrodes; whereas for a conventional battery the electrodes are themselves part of the electrochemical fuel. Therefore, conventional battery electrodes are consumed and undergo significant chemical and physical changes as their chemical energy is converted into electrical energy. Secondly, conventional batteries offer little to no scale-up advantages, thus only able to be scaled-out.[9] Fuel cells can be easily scaled-up by increasing the size of the electroactive material storage containers without making any changes to the energy conversion device. In order to scale-up a conventional battery, identical components must be added to the system, such as separators, current collectors, and enclosure materials. Therefore, when increasing conventional battery capacity, internal resistances go up resulting in lower power density and efficiency. These differences are unique to fuel cell technology and make them a great candidate for large-scale EES.

There are many types of secondary battery chemistries. Each battery chemistry has its own unique benefits and challenges. Battery technology is limited by the tradeoff of five major attributes including power, energy, durability, cost and safety.[10] Table 1.1 provides a brief summary of secondary battery advantages and disadvantages. The most common secondary battery technologies include the lead acid, nickel cadmium, nickel metal hydride, and lithium ion batteries. Examples of lithium ion batteries are lithium cobalt oxide (LCO), lithium iron phosphate (LFP), lithium manganese oxides (LMO), lithium nickel manganese cobalt oxide, lithium nickel cobalt aluminum oxide, and lithium titanate oxide (LTO).

Table 1.1. Secondary battery technology advantages and disadvantages.[11]

Secondary Battery Chemistry	Advantages	Disadvantages
Lead acid	• Lowest cost secondary battery • Mature, reliable and well-understood technology • Highly recyclable • Lead is abundantly available • Able to deep discharge • No memory effect • Reasonable self-discharge rate	• Low cycle lifetime • Low specific energy density
Nickel Cadmium (NiCad)	• Similar depth of discharge (DOD) as lead acid • More robust than lead acid • Longest cycle life • Better energy density than lead acid • Can be stored fully charged • Faster charge/discharge rates then lead acid • Memory issues can be reversed/reconditioned	• Difficult to determine state of charge (SOC) based on cell voltage
Nickel Metal Hydride (NMH)	• Higher energy density than NiCad • Improved high rate capability • High tolerance to over-discharge • Easy construction • No dendrite formation • No toxic materials	• Faster self-discharge than NiCad • Recycling process not mature
Lithium Ion	• Highest energy density of all secondary batteries • Intercalation compounds react reversibly • Design flexibility	• High cost

Currently, lead acid is the most affordable battery technology. Demonstrated in 1859, lead acid batteries are the most successful electrochemical system ever developed.[12] Almost every country in the world manufactures lead acid batteries. Over 200 million automotive lead acid batteries were produced in 1991.[12] Moreover, the lead acid battery is the nation's most highly recycled consumer product, partly due to the fact that the U.S. has been recycling lead for

over 75 years.[13] Due to its high recyclability and worldwide production, lead acid batteries are an attractive and viable technology for a mass-produced EV.

Nickel cadmium and nickel metal hydride batteries are slightly more expensive than lead acid.[12] Due to the toxicity of cadmium, European Parliament has voted to ban nickel cadmium batteries at the start of 2017.[14] Nickel metal hydride batteries offer significantly higher energy density over nickel cadmium batteries.[11] Many applications have utilized nickel metal hydride battery technology, including power tools and hybrid electric vehicles. Other types of technology sectors utilizing nickel metal hydride include communications, peak shaving systems, and solar power energy storage systems.

Lithium ion batteries are currently the most expensive EV battery technology. Significant cost reduction breakthroughs have yet to occur with lithium-ion technologies for EV use. Therefore, the expected cost for Li-ion batteries is expected to be in the range of $150-$440/kWh in 2020.[15] Due to the many different types of lithium ion battery technologies in the marketplace, recycling can also be challenging and costly.[16]

1.3 Fuel Cells

1.3.1 Brief History of Fuel Cells

The fuel cell was first demonstrated by Sir William Grove in 1839. Francis Bacon's research team in England later developed the "Bacon Cell", a 6 kW alkaline fuel cell that stood as a benchmark for future fuel cell technology.[17] Following Bacon's pioneering fuel cell work in the early and mid 20th century, the U.S. space program developed the fuel cell for space exploration.[18] One of the first major applications of fuel cell technology was by the U.S. National Aeronautics and Space Administration (NASA) to power the Apollo space vehicle during missions to the moon. The Apollo's command module was primarily powered by a set of three

fuel cells, which also provided clean drinking water for the astronauts. NASA later adopted the fuel cell design for the Space Shuttle. During the 1970s and 1980s, the commercialization of space technology led to significant technological progress with fuel cells. More recently, increased environmental concerns have led to the adoption of fuel cell technology by the automobile industry in order to meet efficiency and emission standards. Besides the obvious applications in the transportation sector, fuel cells are currently designed for remote and backup power, large-scale energy storage, and portable electronic applications.

1.3.2 Fuel Cell Benefits

Fuel cells have many advantages over other technologies (i.e. combustion engine). Fuel cells directly convert chemical energy into electrical energy, therefore making them ideal for powering electric motors or being connected directly to the electrical grid. Energy conversion technologies that rely on converting thermal energy to mechanical energy (i.e. Otto or Diesel cycle for heat engines) have a maximum attainable efficiency as predicted by Carnot's theory, whereas Carnot's theory does not apply to fuel cells. This major difference means fuels cells are able to attain higher energy conversion efficiency. The commonly cited advantages for fuel cells are high efficiency, simplicity in design, low carbon emissions and low noise (i.e. stealth).[18] Other benefits include high energy density (Wh/L), high specific energy (Wh/kg), low thermal signature, quick startup time, rapid response to varying loads and rapid refueling.[19]

1.3.3 Fuel Cell Types

Various types of fuel cells have been successfully developed and commercialized in the past few decades. Typically, fuel cells are distinguished from each other by the type of electrolyte they use. For example, PEMFCs use a proton exchange membrane to transport hydronium ions from the cathode to the anode, whereas a solid oxide fuel cell (SOFC) uses a dense layer of solid state

electrolyte to move oxide ions. Table 1.2 below lists the most common types of fuel cells in use today. Each type of fuel cell has a unique set of operating parameters, preferred applications, and mobile ion type moving through the electrolyte. Fuel cells are also further classified as either low, medium or high temperature. Each fuel cell type has a unique set of advantages and challenges. For example, the low operating temperature of the PEMFC makes them suitable for low power and mobile applications, while the high operating temperature and fuel variability for SOFCs make them suitable for high power combined heat and power (CHP) applications. The specific advantages and challenges of each technology determines their suitability for various applications (i.e. space, land vehicle, portable electronics, CHP applications).

Table 1.2. Fuel Cell Types[18]

Fuel Cell Type	Operating Temperature	Mobile Ion	Applications & Notes
PEMFC	RT-90°C	H^+	Vehicles, Mobile Devices, low power CHP
Alkaline (AFC)	RT-90°C	OH^-	Space vehicles
Direct Methanol (DMFC)	RT-90°C	H^+	Portable electronics (low power, long lifetime)
Phosphoric Acid (PAFC)	~220C	H^+	Medium-scale CHP
Molten Carbonate (MCFC)	~650°C	$CO_3^=$	Medium/high-scale CHP (up to MW capacity)
Solid Oxide (SOFC)	500-1000°C	$O^=$	Medium/high-scale CHP (multi-MW)
Biological	20-40°C	Various	Low power applications, Biosensors, Wastewater treatment
Redox flow cells (i.e. regenerative/reversible fuel cell)	Various	Various	More details provided in Section 1.6

A picture of a SOFC button cell (broken in half for demonstration purposes) alongside a quarter is shown in Figure 1.6. SOFC button cells are typically used for laboratory-scale experiments due to their small size and low cost. Researchers at the US DOE NETL (National Energy

Technology Laboratory) are incorporating the SOFC into a SOFC/GT (gas turbine) combined cycle due to its increased efficiency over the conventional gas turbine cycle.[18, 20] The SOFC/GT combined cycle is expected to lead to reduced fuel consumption and reduced carbon emissions for the same amount of generated electricity. As shown in Figure 1.7, the combined cycle first converts a fraction of the fuel's chemical energy directly into electricity as it flows through the SOFC. Then, the SOFC outlet gases are directed into an after-burner in order to produce a high-temperature, high-pressure gas. Finally, the gases are directed through a gas turbine to produce additional electricity via an alternator.

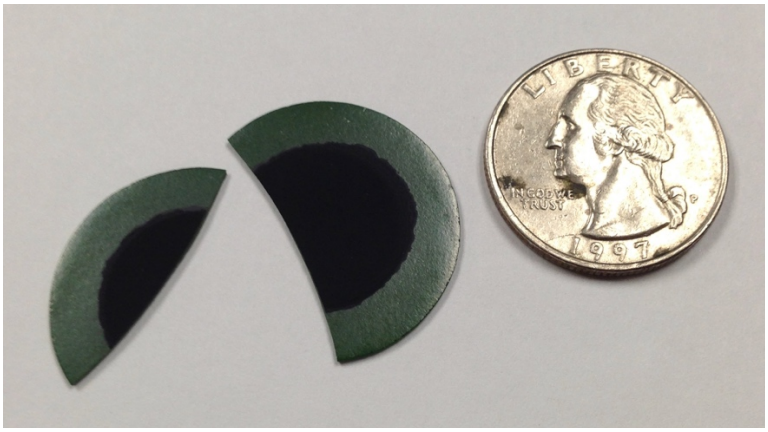

Figure 1.6. SOFC button cell from MSRI Inc., shown next to a quarter for size comparison.

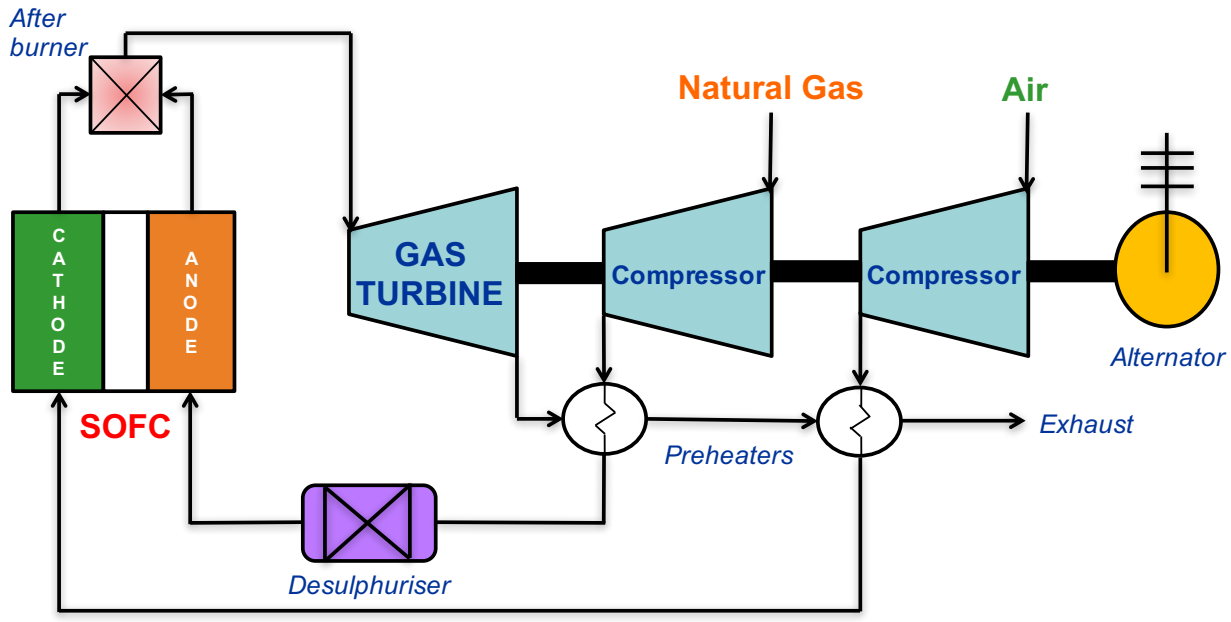

Figure 1.7. Combined SOFC/GT Cycle.[18]

In Figure 1.8 and Figure 1.9, two different types of PEMFCs are shown. Figure 1.8 includes photographs of a 5-cell air-breathing PEMFC, which is ideal for remote and/or portable applications. A larger PEMFC, shown in Figure 1.9, is an 18-cell stack constructed for higher voltage and power applications.

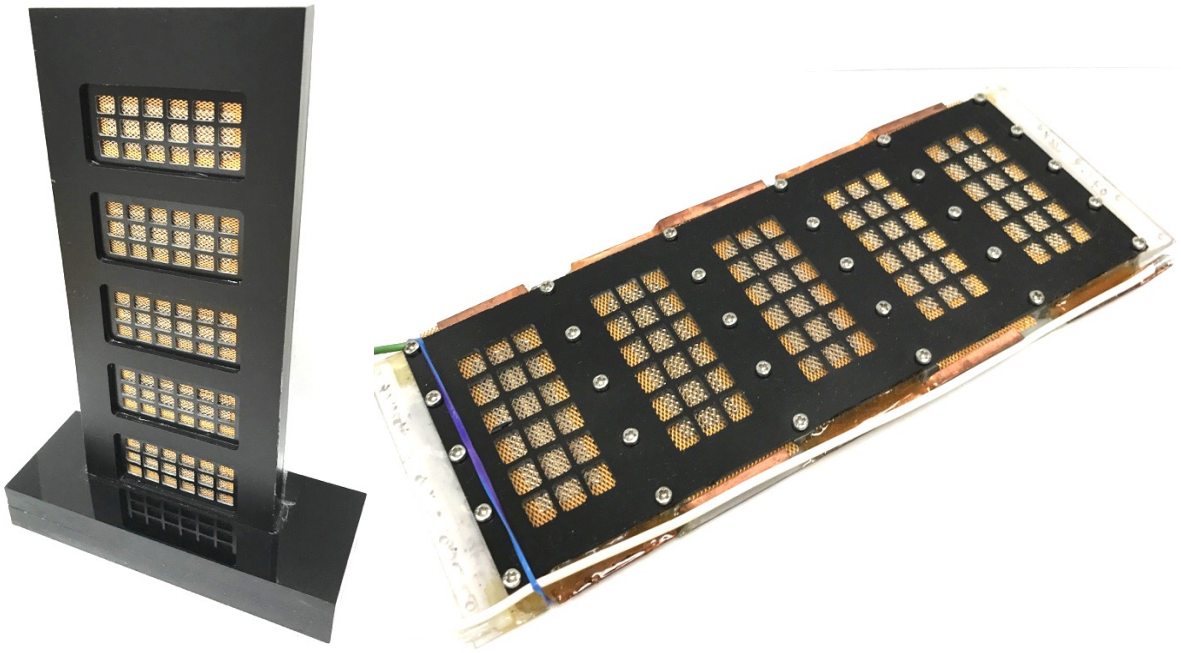

Figure 1.8. Photographs of a 5-cell portable air-breathing PEMFC made by NK Technologies, LLC.

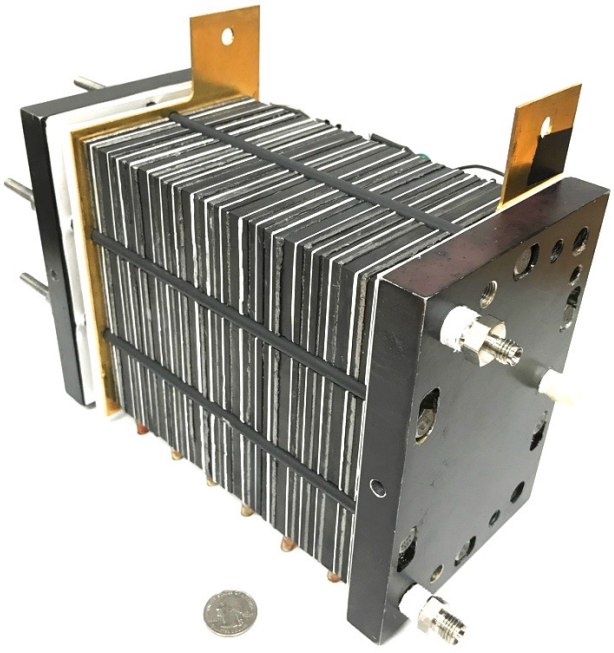

Figure 1.9. Photograph of an 18-cell PEMFC made by TVN Systems, shown next to a quarter for size comparison.

1.4 PEM Fuel Cell (PEMFC)

Fuel cell material development, modeling and system optimization has centered on the PEMFC over the past few decades due to its potential application for automotive purposes. The high power density, quick start-up time, low environmental impact, rapid response to varying loads, and low operating temperature of PEMFCs makes them an ideal technology for automobile applications.[19] A PEMFC converts chemical energy into electrical energy with very high efficiency (>80%). The three main components of a PEMFC are the proton exchange membrane (PEM), anode, and cathode. During operation, hydrogen flowing through the anode oxidizes at the surface of a catalyst to produce electrons and protons. Since the membrane is electrically insulating, electrons are forced out through an external circuit and then return to the cathode side of the fuel cell. The flow of electrons through the external circuit can be used to produce useful work. The protons produced at the anode migrate across the proton conducting membrane and react at the surface of a catalyst with oxygen and electrons to produce water. A generalized schematic and chemical reactions of a PEMFC are shown in Figure 1.10.

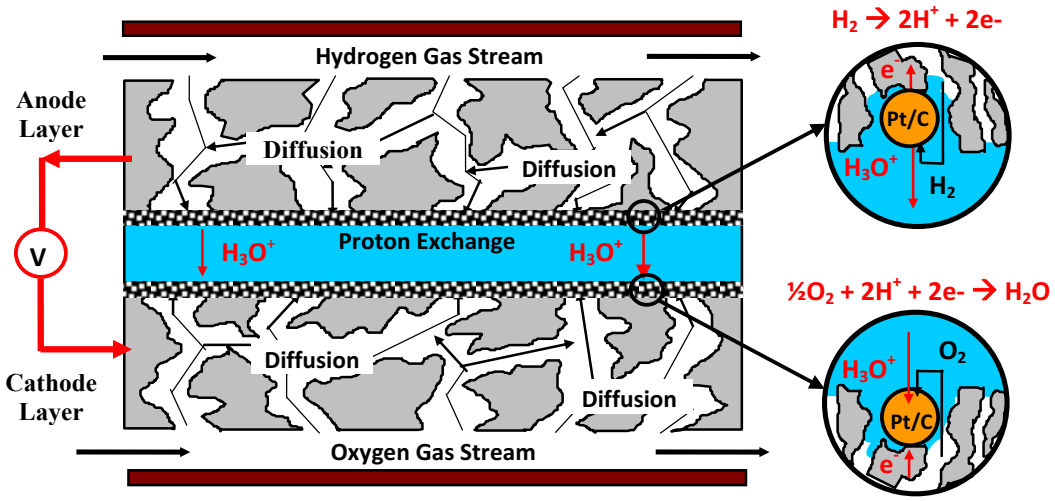

Figure 1.10. Visualized transport processes in a PEMFC.[21]

Various materials have been used to construct PEMFCs. At a minimum, the PEMFC is comprised of a polymer electrolyte membrane, electrodes (cathode and anode), reactant flow fields, and current collectors. Commonly, a flow field and current collector are combined into a single component called a bipolar plate. A fully constructed PEMFC, made from carbon flow fields, PTFE gaskets, and stainless steel end plates, is shown in Figure 1.11. In the following sections, each PEMFC component is discussed in greater detail.

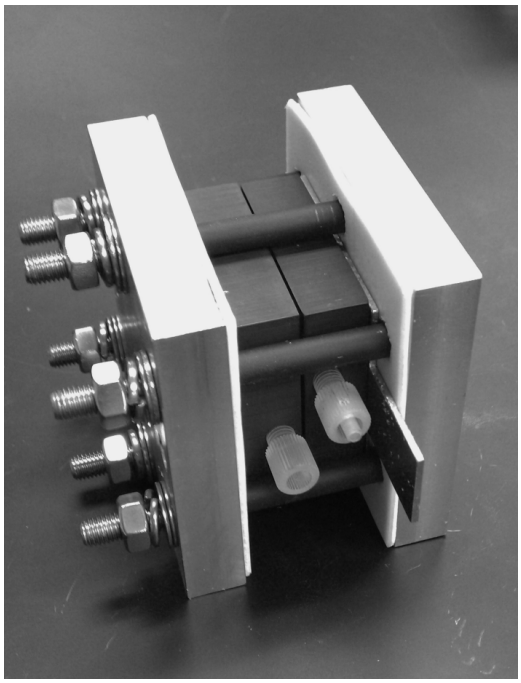

Figure 1.11. Photograph of PEMFC (single cell) in Nguyen's Research Laboratory at KU.

1.4.1 Components of a PEM Fuel Cell (PEMFC)

1.4.1.1 Polymer Electrolyte Membrane (PEM)

PEMs are categorized by the ion charge that they able to transport (i.e. cation, anion, or both). A cation exchange membrane has negatively charged functional groups to be able to conduct positively charged ions (cations), whereas an anion exchange membrane has positively charged functional groups in order to conduct negatively charged ions (anions). Bipolar membranes have both negatively and positively charged functional groups, such that cations can conduct through one half the membrane's thickness and anions can conduct through the other half.

Perfluorosulfonic acid (PFSA) polymers (e.g. Nafion®, Aquivion®) are the most common class of polymers used in PEMFCs.[22] PFSA polymers are used in fuel cells as both the proton conducting membrane and CL ionomer. Dupont's™ Nafion® PFSA membranes, shown in Figure 1.12, have a polytetrafluoroethylene (PTFE) backbone structure with perfluoroethylene ether

pendant side chains that terminate in sulfonate groups ($-SO_3H$). The PTFE backbone provides Nafion® with good chemical and physical stability, whereas the sulfonate end groups give Nafion® its ionic conductivity (i.e. proton transport). The two distinct phases segregate into hydrophobic (PTFE backbone) and hydrophilic (ionic clusters) domains.[23, 24] The morphology of Nafion® relies on the content, distribution and state of water.[23] Additionally, the conductivity of Nafion® is directly correlated to the hydration state of the ionic groups.[25, 26] Each sulfonate ionic group can be associated with up to 14 molecules of water when fully hydrated with water vapor and 22 molecules of water when saturated with liquid water.[24, 27-29] The absorption of water can result in immense swelling of the polymer to over 150% of the polymer's dry volume.[27, 28, 30] The dependence of the polymer's conductivity on the hydration state makes water management a vital component during fuel cell operation.[25, 29, 30]

Figure 1.12. Chemical structure of Nafion.

Equivalent weight is defined as the mass of the chemical (expressed in grams) per mole of negative or positive charge. A polymer with a higher equivalent weight will have fewer functional groups than one with a lower equivalent weight. Additionally, a polymer with a lower equivalent weight (i.e. higher number of functional groups) will be able to absorb more water molecules and, therefore, swell more. Typically, a higher equivalent weight polymer has increased durability than a lower equivalent weight polymer. Since fuel cell operation relies on proton conduction across the PEM, a lower equivalent weight polymer will likely achieve higher performance but may also exhibit lower durability.

Two others types of polymer electrolyte membranes commonly used in PEMFCs include Aquivion and 3M PFSA membranes. The structure and equivalent weight of all three commonly-used polymer electrolyte membranes are shown in Table 1.3. Aquivion has a shorter functional side group which results in a lower equivalent weight. The second ether group located in the pendant side chain of Nafion is absent in both the Aquivion and 3M PFSA membranes.

Table 1.3. Polymer electrolyte membrane examples.

Polymer Type	Chemical Structure	Equivalent Weight
Nafion	$-(CF_2CF_2)_n-(CFCF_2)-$ $\quad\quad\quad

components is continued in section 1.4.1.2.

1.4.1.1.1 Electrospun Nanofiber Composite (ENC) Membranes

Multiple research groups have developed electrospun nanofiber composite (ENC) membranes in order to overcome the negative hydration effects outlined above.[33-36] The purpose of making ENC membranes is to increase the number of ionic pathways available for protons to move through the membrane, but also physically prevent the membrane from swelling at high relative humidity. The increased number of ionic pathways will raise the overall efficiency of the PEM fuel cell, while prevention of membrane swelling will enable increased chemical selectivity through the membrane.

In the section that follows, ENC membranes are characterized with atomic force microscopy (AFM) in order to take a closer look at its surface structure. The ENC membranes were manufactured by Dr. Peter Pintauro's research group at Vanderbilt University. His group electrospun a dual fiber mat, one fiber being PFSA and the second fiber being polyphenylsulfone (PPSU), an uncharged/inert polymer. After processing to allow PPSU to fill the void space between PFSA fibers, a functional membrane is obtained. Figure 1.13 shows a schematic of the final membrane morphology.

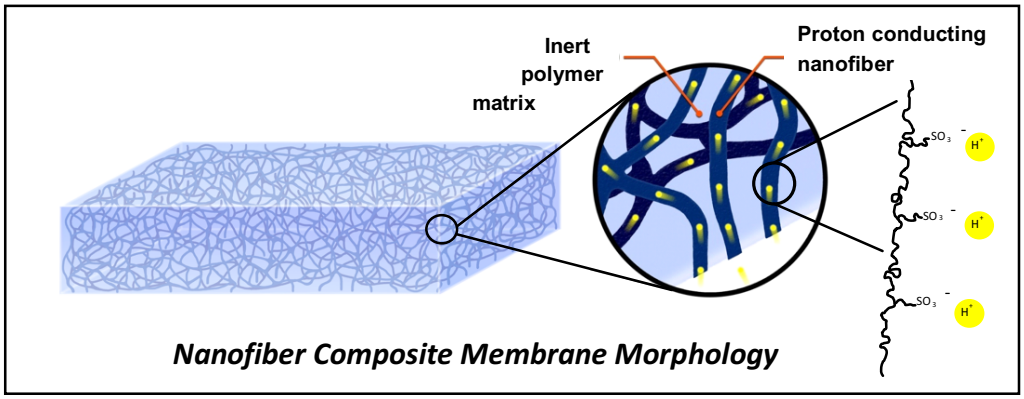

Figure 1.13. Electrospun nanofiber membrane morphology.[37]

The potential and limitations of AFM have been extensively studied by Aleksandrova.[32] McLean and Ionescu-Zanetti explored the local charge transfer properties of polymer blends using multimodal AFM.[38, 39] They found that highly conductive regions of certain polymer blends coincided with regions of high phase contrast and increased roughness. Saha investigated the current-voltage characteristics of polypyrrole nanotubes using AFM.[40] Saha showed how the current-voltage characteristic is dependent on whether the sample contains thin-walled tubes versus solid rod-like nanotubes.

AFM has the ability to operate in multiple modes; including static force, dynamic force, phase contrast (i.e. hardness), force modulation, spreading resistance (i.e. conductivity), and lateral force. While in static force mode, an AFM measures the surface topography by measuring the deflection of a cantilever as it moves across the sample. When the cantilever is deflected due to a change in surface topography, a laser detection system detects a change in the reflected laser beam, as shown in Figure 1.14. These measurements are used to produce an image of the sample's surface topography.

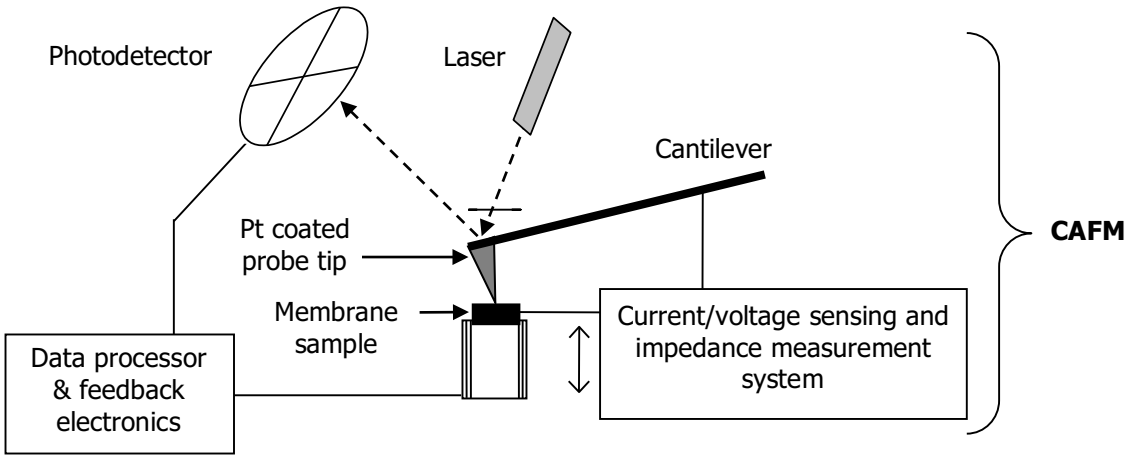

Figure 1.14. AFM setup for static force mode.[41]

During phase contrast mode, the cantilever is excited with a sinusoidal frequency close to the cantilever's free resonance frequency while the vibration amplitude and phase shift are measured. The phase shift between the cantilever vibration and a reference signal are due to sample-tip interactions. The phase shift is a measure of the energy dissipation between the sample-tip interactions and is a measure of the elasticity, viscoelasticity, adhesion, and contact area. The phase shift measurements are used to produce material contrast images to give us insight into the type of sample-tip interactions. While operating an AFM in spreading resistance mode, a voltage bias is applied to the surface of the sample through the use of a catalytic cantilever tip. A membrane electrode assembly (MEA), made by hot-pressing a PEM onto a catalyst-coated electrode, was used as the sample in this experiment. The AFM setup for spreading resistance mode is shown in Figure 1.15. Two types of membranes, Nafion® 212, a perfluorosulfonic acid (PFSA) material, and an electrospun composite nanofiber membrane, were used when fabricating the MEA.

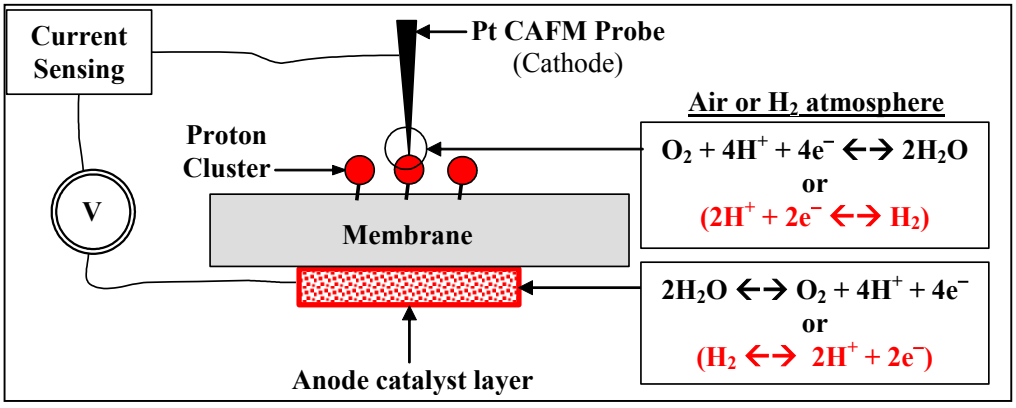

Figure 1.15. AFM setup for spreading resistance mode.[41]

The ability to characterize the surface of the electrospun membranes was important in order to validate whether these membranes have a sufficient number of ionic cluster sites for proton transport but also prevent the PEM from being over saturated with water which would allow non-proton species to cross the membrane. We hypothesized that there will be a high correlation between the phase contrast and spreading resistance modes. We also expected that the ionic phase of the membranes surface to be more viscoelastic and adhesive than the inert phase.

A Veeco AFM Bioscope with Nanoscope Controller and a Nanosurf® FlexAFM were used in contact and tapping modes in order to measure the topography, phase contrast, and conductivity for electrospun and Nafion® 212 membranes. Both AFMs were used to verify measurement readings and reproducibility. All of the electrospun membranes characterized in this experiment were made by allowing the inert polymer (PPSU) to soften, flow, and fill the void space between Nafion® PFSA nanofibers.[36] It is expected that this approach will be more effective in minimizing membrane swelling. Prior to and after each AFM measurement, highly oriented pyrolytic graphite (HOPG) and a calibration grid were used to ensure proper AFM calibration and to verify tip durability throughout the experiment.

In order to accurately measure the conductivity (resistance) of the membrane, a platinum

coated cantilever was used to apply a voltage bias to the surface of a PEM hot pressed onto a platinum coated SGL35BC gas diffusion electrode made by TVN Systems, Inc. The PEMs were made by hot pressing a membrane onto the gas diffusion layer (GDL) at 80 PSI and 285°F for 5 minutes. The AFMs were operated inside electrically shielded Faraday cages and on vibration isolation tables to minimize background noise while conducting the measurements.

Figure 1.16 through Figure 1.21 show side-by-side comparisons of the AFM results. Both two and three-dimensional AFM images for topography, phase contrast, and conductivity are given. The electrospun nanofiber membrane's topography was consistently smoother than Nafion® 212. As expected, the phase contrast measurement of Nafion® 212 was more uniform than the electrospun membranes. The nanofibers within the electrospun membranes can be easily recognized using either phase contrast or spreading resistance modes. The non-uniformity of the phase contrast and spreading resistance images for the electrospun membrane was due to the use of two different types of polymers, one ionic and the other inert. The ionic polymer used in the electrospun membrane is expected to exhibit a larger phase contrast measurement than the inert polymer due to greater adhesive properties. As expected, the phase contrast measurement of Nafion® 212 shows a surface with varying amounts of ionic clusters due to the migration of the ionic groups ($-SO_3^-H^+$) within the polymer to the membrane's surface. The movement of the ionic groups to the surface is due to the attraction of the ionic groups to the humidity in the air at the membrane's surface.

(a) **(b)**

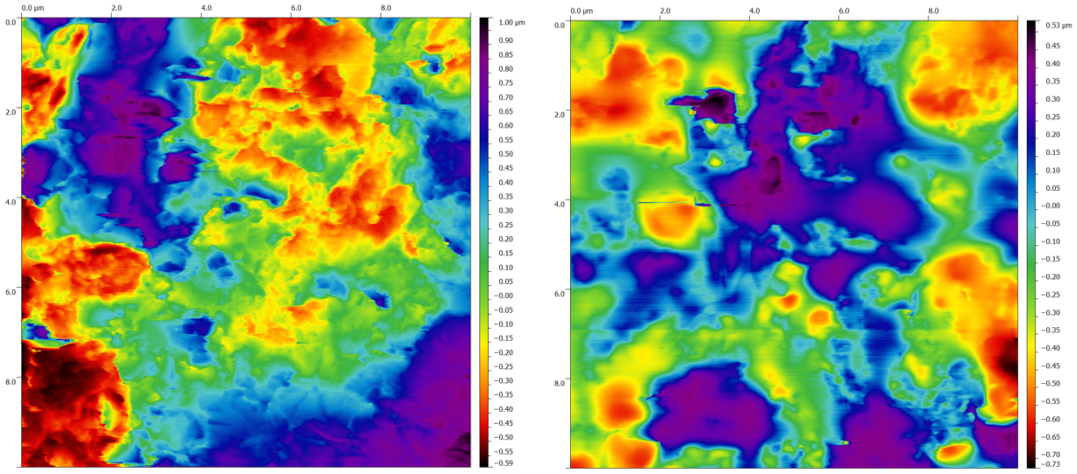

Figure 1.16. 2D topography of **(a)** Nafion® and **(b)** electrospun nanofiber Nafion/polyphenylsulfone membrane.

(a) **(b)**

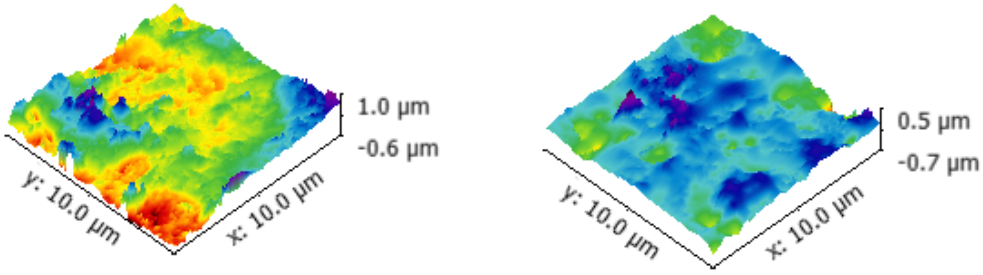

Figure 1.17. 3D topography of **(a)** Nafion® and **(b)** electrospun nanofiber Nafion/polyphenylsulfone membrane.

The phase contrast images show both positive and negative values. For the Nafion® 212 membrane, this is due to varying amount of ionic groups ($-SO_3^-H^+$) on the membrane's surface. The darker domains in Figure 1.18a and Figure 1.19a correspond to areas with a larger number of ionic groups ($-SO_3^-H^+$) and the lighter domains correspond to areas rich in the fluorinated carbon backbone structure of Nafion® 212. The softer ionic groups are expected to have a larger

phase contrast value due to the increased amount of surface/tip interactions (i.e. elasticity, viscoelasticity, adhesion, etc.). For the electrospun membrane, this is due to the difference in properties between the ionic fibers and the inert polymer matrix. The darker domains in Figure 1.18b and Figure 1.19b correspond to the ionic fibers and the lighter domains correspond to the inert matrix. The ionic fibers are expected to have a larger phase contrast value due to the increased amount of surface/tip interactions (i.e. elasticity, viscoelasticity, adhesion, etc.).

(a) **(b)**

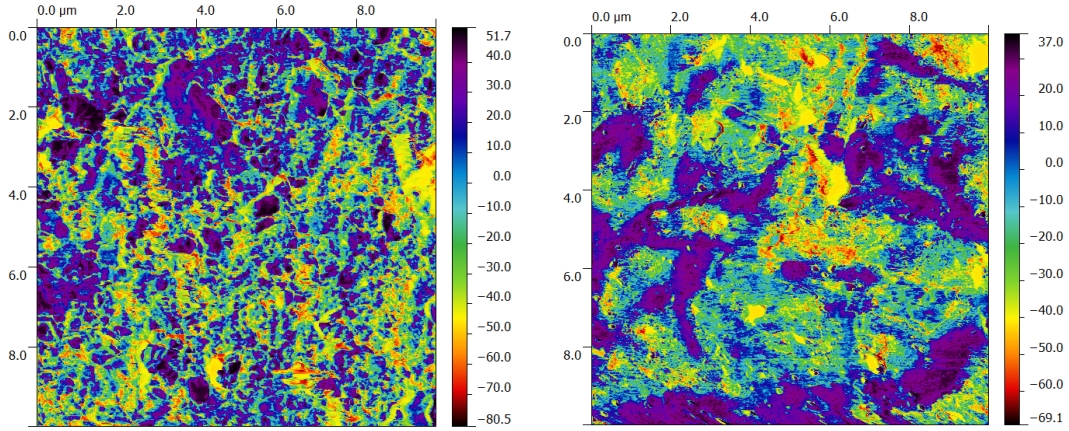

Figure 1.18. 2D phase contrast of **(a)** Nafion® and **(b)** electrospun nanofiber Nafion/polyphenylsulfone membrane.

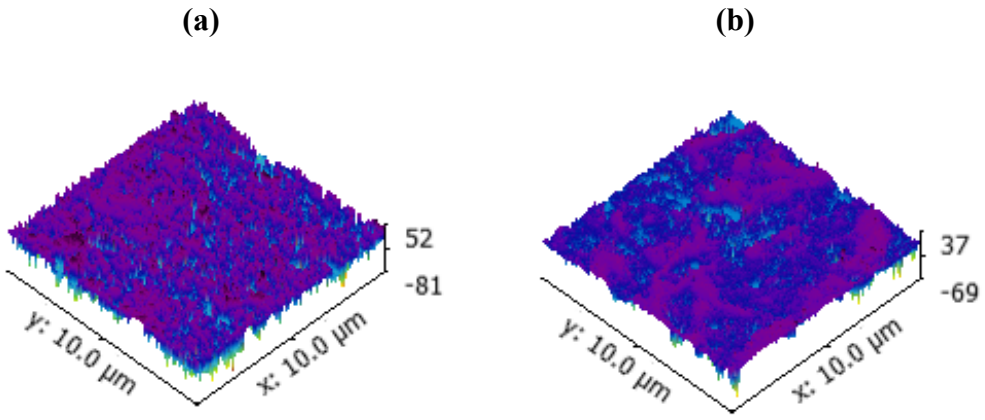

Figure 1.19. 3D phase contrast of **(a)** Nafion® and **(b)** electrospun nanofiber Nafion/polyphenylsulfone membrane.

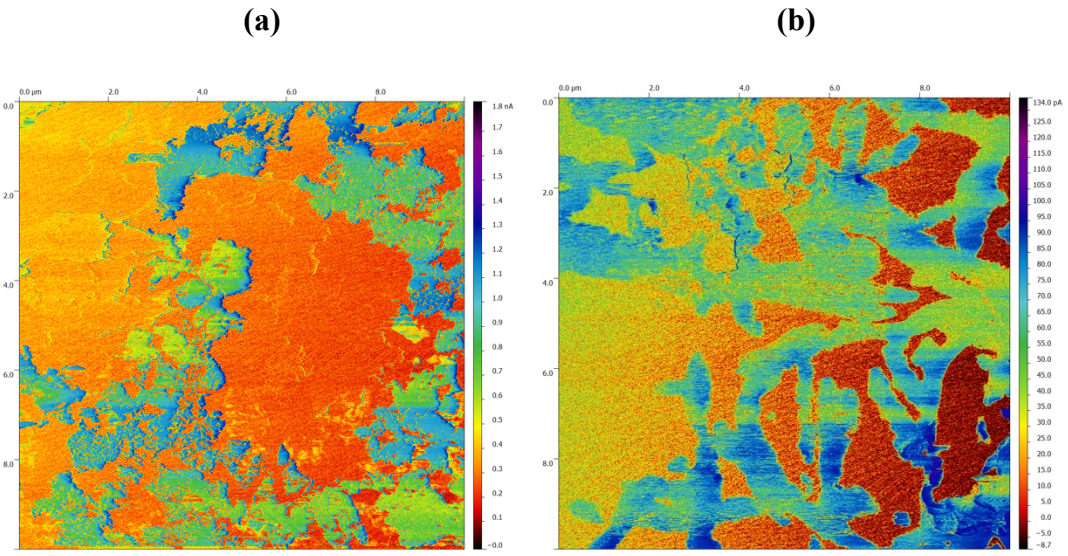

Figure 1.20. 2D conductivity of **(a)** Nafion® and **(b)** electrospun nanofiber Nafion/polyphenylsulfone membrane.

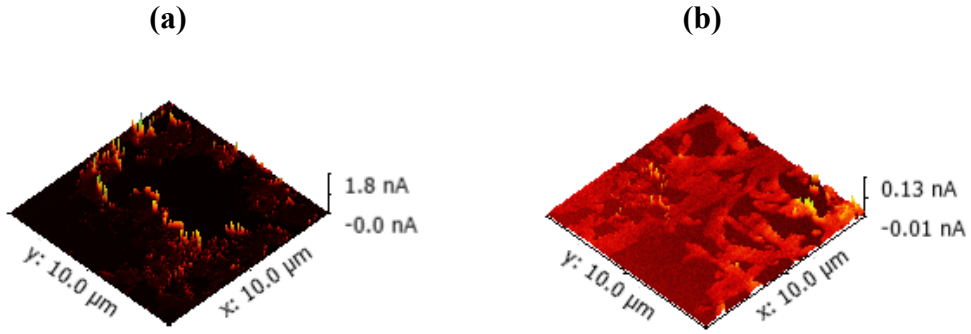

Figure 1.21. 3D conductivity of **(a)** Nafion® and **(b)** electrospun nanofiber Nafion/polyphenylsulfone membrane.

In this section, multimodal AFM was used to measure the topography, phase contrast, and conductivity of electrospun composite nanofiber membranes. We were able to correlate the phase contrast and conductivity modes to distinguish between the ionic nanofibers and inert regions within the electrospun membranes. In the next section, we continue our introduction to the various components of a PEMFC.

1.4.1.2 Electrodes (GDL/MPL/CL) and Membrane Electrode Assembly (MEA)

The anode and cathode are comprised of three distinct layers: a gas diffusion layer (GDL), a microporous layer (MPL), and a catalyst layer (CL). The membrane electrode assembly (MEA), considered the heart of a PEMFC, is a seven-layer assembly comprised of a proton exchange membrane sandwiched between two electrodes.[42] The highly porous GDL provides a transport pathway for gas to be directed from the gas flow field towards the catalyst reaction site. A MPL is placed between the GDL and CL in order to lower the contact resistance between the two layers.[43] By using a MPL, catalyst utilization is increased.[43] Additionally, the low porosity of the MPL increases the back transport of water from the cathode to the anode.[43] The CL is comprised of 3 distinct phases: an ionically-conductive ionomer, a void space for gas/liquid transport, and an electrically-conductive solid support coated with catalyst. As shown in Figure 1.22, the

ionomer phase (dark blue color) provides ionic access (i.e. proton transport) to the catalyst reaction sites, whereas the electrically-conductive phase (grey color) provides electronic access to the catalyst reaction sites. The void space allows gaseous reactants to diffuse to the catalyst reaction sites while also providing a pathway for liquid water to be removed.

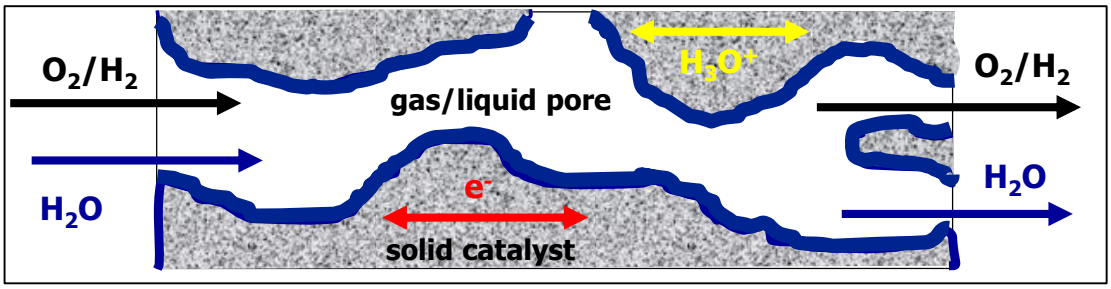

Figure 1.22. CL structure and transport.[21]

1.4.1.3 Flow Fields

Flow fields are used to deliver reactants to and remove products from the electrodes. For example, during operation the cathode of a PEMFC consumes oxygen gas and produces liquid water. Various flow field channel designs have been developed, including serpentine, interdigitated, parallel and parallel serpentine. Figure 1.23 illustrates the flow path for each flow field design. The interdigitated flow field (shown in Figure 1.23A) forces the reactants to flow into the electrode (out of the page) in order to clear the channel shoulders and reach the outlet flow channels. Therefore, the interdigitated design improves mass transport of reactants into the electrode.[44] In the other three flow field designs shown in Figure 1.23, reactants flow parallel to the electrode face. In the parallel flow-through setups, reactants must be transported into the electrode solely by diffusion, vice diffusion and convection. One advantage of flow-through designs is that less pressure drop is required between the inlet and outlet in order to achieve high flow rates. Typically, more pressure drop is encountered with the interdigitated flow field design.

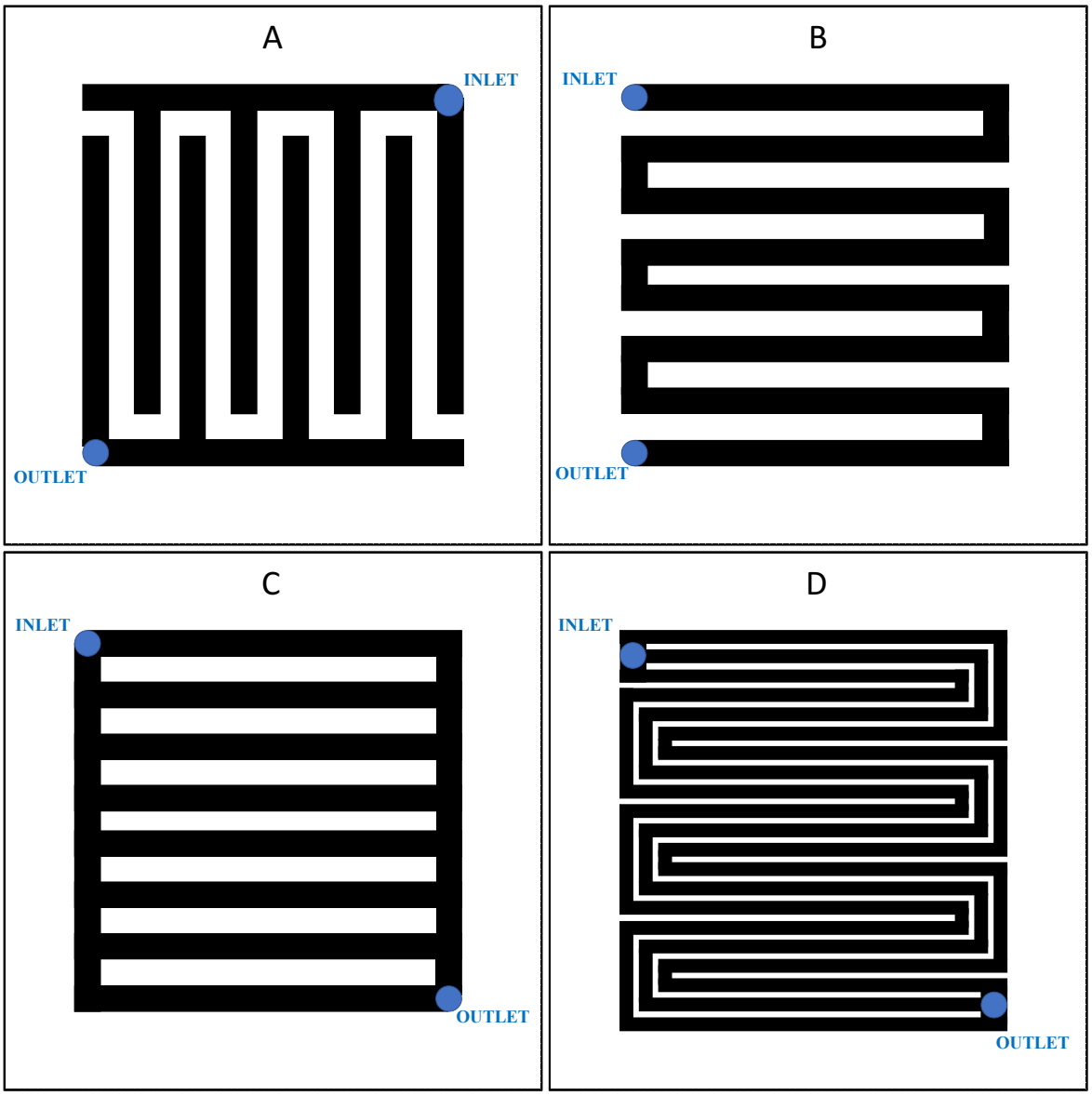

Figure 1.23. Various flow field designs including (A) Interdigitated, (B) Serpentine, (C) Parallel, and (D) Parallel Serpentine.[18, 44-47]

1.4.1.4 Current Collectors (Bipolar plates)

Current collectors allow electrons to flow into and out of the fuel cell and are made from highly conductive materials (i.e. metals). In some laboratory-based fuel cell systems, current collectors are placed in contact with the back side of the flow field and provide a connection point to

connect testing equipment (i.e. galvanostat or potentiostat) in order to control current flowing out of the fuel cell or the potential gradient across the fuel cell terminals. In other cases, especially for industrial-grade fuel cells, the current collectors and flow fields are manufactured from a single piece of conductive material. This single piece is called a bipolar plate. A bipolar plate can serve as the current collector, flow fields, and provide temperature control. Most importantly, as shown in Figure 1.24, the bipolar plate allows for two fuel cells to be connected in series. Therefore, when a bipolar plate is used to connect two fuel cells in series, the electrons flowing out of the anode from fuel cell #1 are then consumed by the cathode of fuel cell #2. Multiple fuel cells can then be connected in series by placing a bipolar plate between each fuel cell. Since the typical operating voltage of a single PEMFC is ~0.5V, multiple PEMFCs can be connected in series to achieve the desired voltage for each application. The total combined voltage for voltage sources connected in series is simply the sum of the individual cell voltages. For example, if the overpotential of each fuel cell is 0.5V, then the total combined voltage when the two fuel cells are connected in series is 1V (i.e. sum of 0.5V and 0.5V).

The bipolar plate also has separate feed channels for air/oxygen to flow to the cathode of fuel cell #1 and hydrogen to flow to the anode of fuel cell #2. Pictures of the front side and back side of a bipolar plate (made from carbon) are shown in Figure 1.25. Notice, the machined serpentine flow channels on each side of the bipolar plate. The flow channels on the front side allow air/oxygen to flow to the cathode, while the flow channels on the back side allow hydrogen to flow to the anode. The anode/cathode gases are unable to mix due to the unique bipolar plate design. Notice in Figure 1.25 that point 1 on the front side of the bipolar plate coincides with point 1 on the back side. Therefore, gas flow through point 1 will allow gas to enter/exit the flow

field channels on the back side of the bipolar plate, but will not allow the same gas to be introduced into the flow channels on the front side of the bipolar plate.

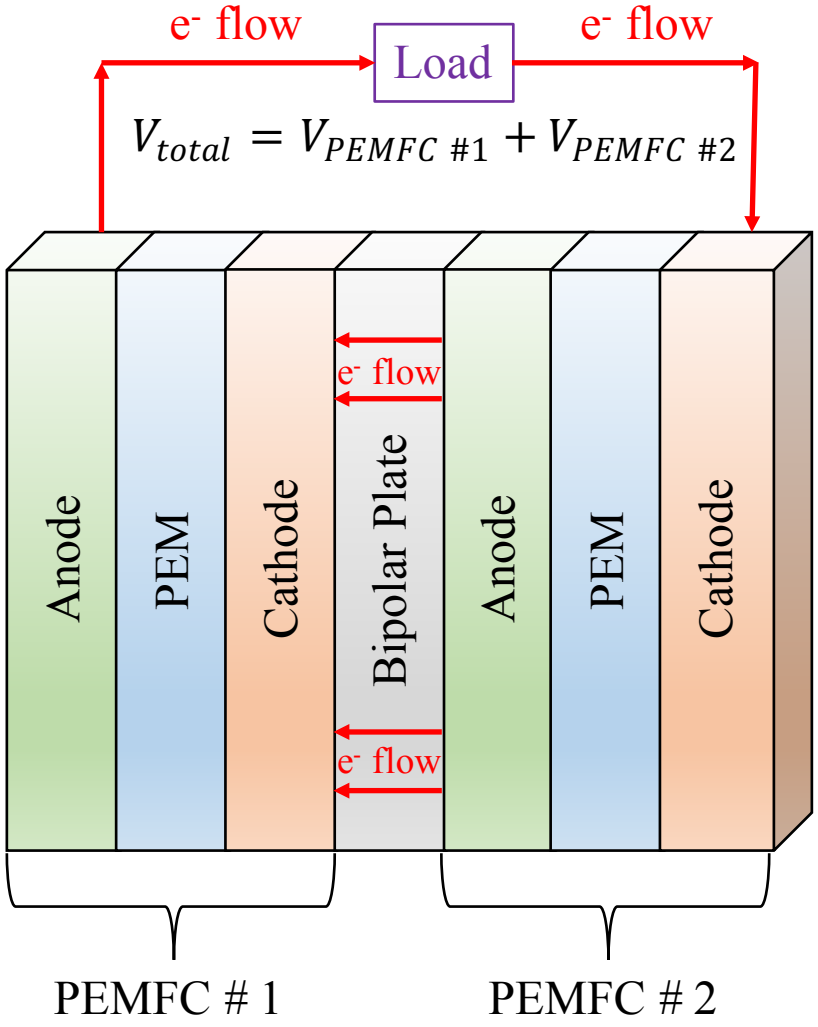

Figure 1.24. Bipolar plate connecting two PEMFCs in series.

(A) Front side

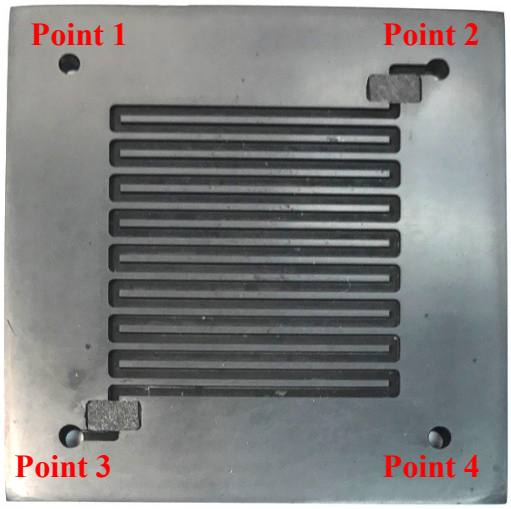

(B) Back side

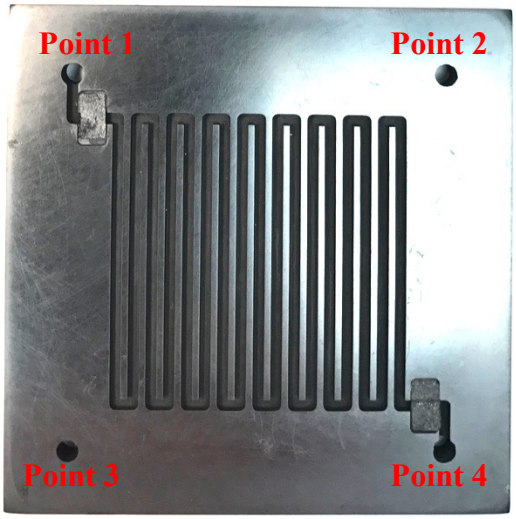

Figure 1.25. Pictures of the (A) front side and (B) back side of a bipolar plate in Nguyen's Research Laboratory at KU.

1.4.2 Operating Principles - Cell Voltage and Efficiency

The measured open circuit voltage for a hydrogen-oxygen PEMFC is approximately 1V. Figure 1.26 shows the baseline polarization curve for a hydrogen-oxygen PEMFC. The open circuit voltage (OCV) is the data point at zero current density. The difference between the theoretical voltage and OCV at zero current density is due to hydrogen crossover to the oxygen side (and vice versa) which creates a mixture potential (i.e. self-discharge). The ideal fuel cell polarization

curve (horizontal line) would have little voltage loss when delivering high currents. The ideal (no loss) polarization curve is shown in Figure 1.26 as a red dotted horizontal line. There is a voltage loss between the ideal and the baseline PEMFC polarization curves. There are at least six interchangeable names that engineers and scientists use for this voltage difference.[18] The voltage difference is often called overpotential, overvoltage, polarization, irreversibility, voltage losses or voltage drop. The baseline polarization curve in Figure 1.26 can be divided into three distinct regions, called the activation loss, ohmic loss, and mass transport regions. Each of these regions are dominated by specific mechanisms that result in the voltage loss from the ideal polarization curve. The activation loss region is dominated by kinetic losses due to the slowness of the reactions occurring at the surface of the electrodes. In the case of the hydrogen-oxygen PEMFC, the slowest reaction is the oxygen reduction reaction (ORR) taking place at the cathode. The ohmic loss region is dominated by ohmic losses comprised of the electrical resistance of the electrodes, electrical resistance of the electrical connections and the ionic resistance of the membrane. The mass transport region is dominated by concentration loss near the surface of the electrode as the fuel (i.e. hydrogen and oxygen) is consumed. It is worth noting that even though the activation loss, ohmic loss and mass transport regions are dominated by kinetic, ohmic and mass transport losses, respectively, the total voltage loss in each region is composed of all the different types of voltage loss phenomena. Other types of voltage loss include fuel crossover and internal currents. Fuel crossover refers to the ability of fuel or oxidant to cross through the membrane. Internal currents refer to the ability (low total contribution) of electrons to conduct through the membrane. Contributions from each of these irreversible voltage loss phenomena results in the baseline polarization curve diverging from the ideal (no loss) polarization curve in Figure 1.26.

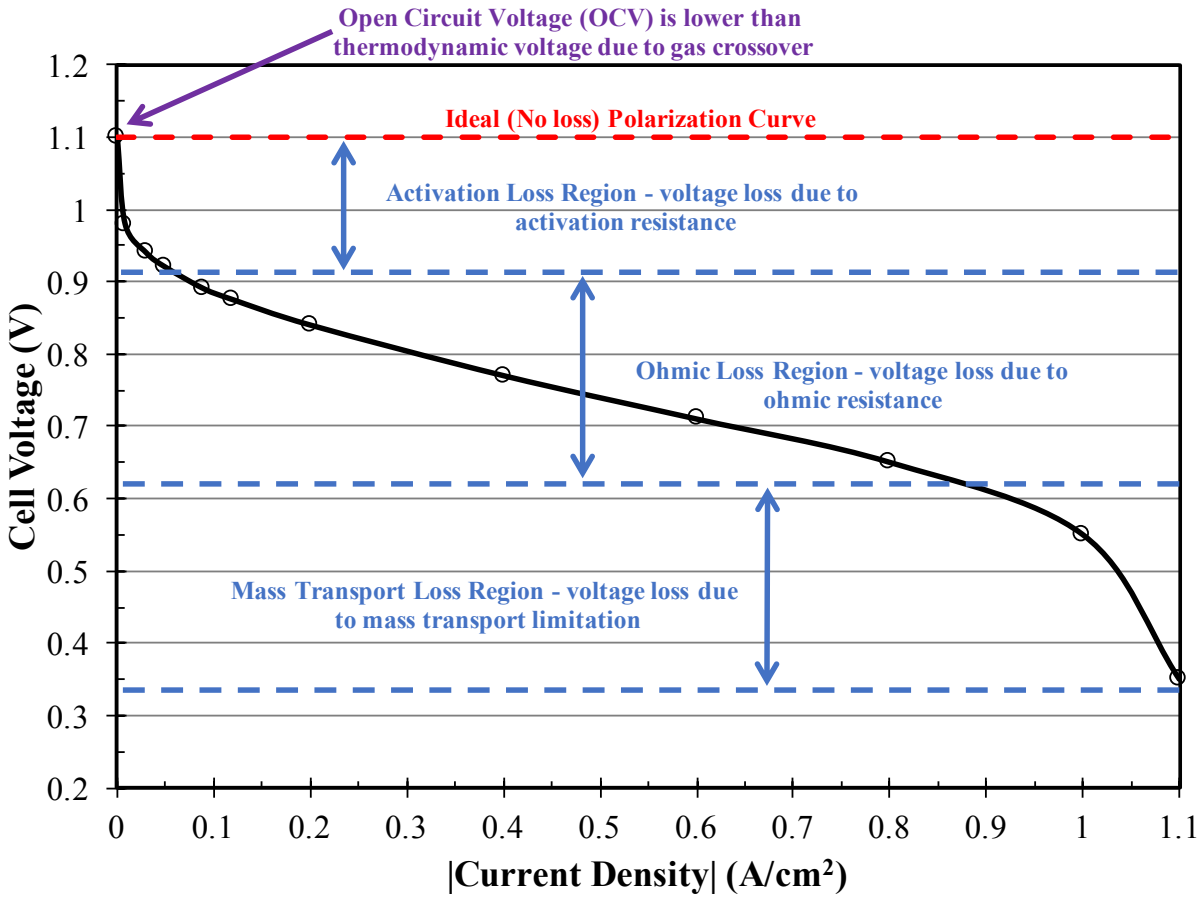

Figure 1.26. Baseline hydrogen-oxygen PEMFC polarization curve.[47]

Figure 1.27 shows the baseline hydrogen-oxygen PEMFC polarization curve from Figure 1.26 graphed against both a fuel cell with a flooded electrode and second with an improved ohmic and mass transport design. The improved cell could be due to using interdigitated flow fields vice serpentine and improved connections to the current collectors. The flooded cell is common at high current density operation when using a poor engineering design that allows water produced at the cathode to slow down oxygen transport to the catalyst reaction site in the cathode.

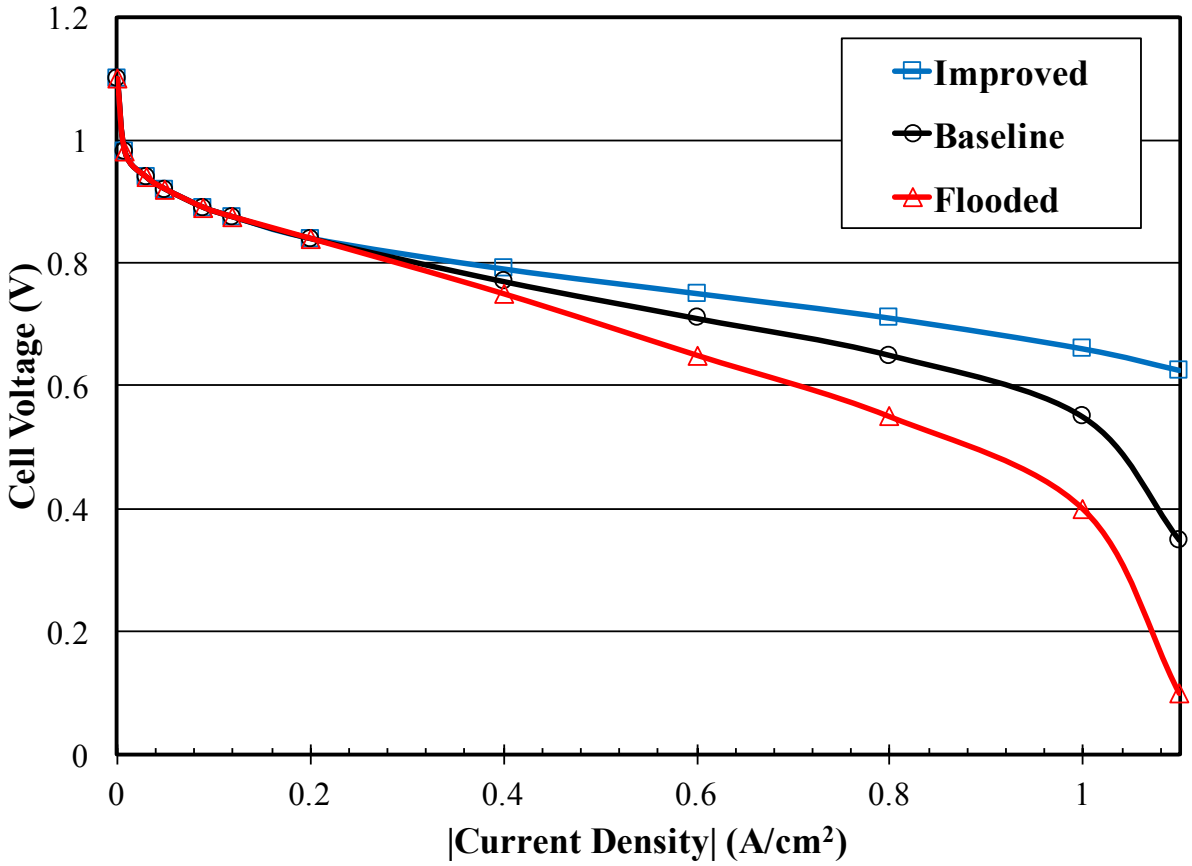

Figure 1.27. PEMFC polarization curves

As previously mentioned, in order for a PEMFC to power a high voltage application, multiple cells are arranged in series to obtain the required voltage. The size of the PEMFC electrode active area is designed for the required application. In other words, for high power applications, the PEMFC electrode area is larger in order to produce more current. Larger electrode area results in increased current and, therefore, greater power (i.e. power = current * voltage). Smaller electrode areas are sufficient for small power applications.

The Nernst and Butler-Volmer equations are the most widely used electrochemical equations. The Nernst equation, shown in Eq. [1] below, relates the reduction potential of an

electrochemical reaction to the standard reduction potential, temperature and the activities of the species involved in the reaction.

$$E_{red} = E^0_{red} + \frac{RT}{nF} ln \frac{\prod(a_k)^{s_k}}{\prod(a_l)^{s_l}} \quad \textbf{[1]}$$

E_{red} is the reduction potential at the temperature of interest, E^0_{red} is the standard reduction potential at the temperature of interest, R is the universal gas constant, T is temperature in Kelvin, n is the moles of electrons, F is Faraday's constant, $a_k$is the activity of oxidized species k, a_l is the activity of reduced species l, s_k is the stoichiometric coefficient of species k, and s_l is the stoichiometric coefficient of species l. The Nernst equation is derived from standard thermodynamic relationships. The Butler-Volmer equation, shown in Eq. [2], describes the complete current-potential characteristics of an electrode reaction (i.e. electrokinetics).

$$i = i_0 \left\{ C_R^{\beta} exp\left[\frac{\alpha_a F}{RT}(E - E^0)\right] - C_0^{\alpha} exp\left[\frac{-\alpha_c F}{RT}(E - E^0)\right]\right\} \quad \textbf{[2]}$$

i is the overall current density, i_0 is the exchange current density, C_R^{β} is the concentration of the reduced species, β is the stoichiometric coefficient of the reduced species, C_0^{α} is the concentration of the oxidized species, α is the stoichiometric coefficient of the oxidized species, $(E - E^0)$ is the overpotential, R is the universal gas constant, T is temperature in Kelvin, F is Faraday's constant, α_a is the anodic transfer coefficient, and α_c is the cathodic transfer coefficient. More simply, the Butler-Volmer equation explains how the electrical current depends on the electrode potential and concentration of reactants/products involved in the electrochemical reaction.

When discussing fuel cell efficiency, it is helpful to start the conversation about how to calculate the maximum efficiency of a heat engine (i.e. Carnot efficiency limit). Carnot's theory applies to engines that convert thermal energy into work. The Carnot efficiency limit for a heat

engine is shown in Eq. [3], where T_H is the temperature of the hot reservoir and T_C is the temperature of the cold reservoir.

$$\eta_{Max}^{Heat\ Engine} = \eta_{Carnot} = \left(1 - \frac{T_C}{T_H}\right) * 100 \quad \textbf{[3]}$$

Now, suppose T_H and T_C were 600ºC and 400ºC, respectively. The Carnot efficiency limit would be ~33%. In a heat engine, a portion of the generated heat is lost to the surroundings without producing any useful work, which results in low efficiency. Since a fuel cell or battery can produce useful power while all components are at the same temperature, the Carnot efficiency limit does not apply.[18] Since a fuel cell converts chemical energy into electrical energy, the fuel cell efficiency is defined using enthalpy of formation and Gibbs free energy values as follows:

$$\eta_{Max}^{Fuel\ Cell} = \frac{\Delta\overline{g_f}}{\Delta\overline{h_f}} * 100 \quad \textbf{[4]}$$

If we use the enthalpy of formation at the higher heating value (HHV) for water (-285.85 kJ/mol) and the Gibbs free energy of liquid water at 80ºC (-228.2 kJ/mol), the maximum fuel cell efficiency is calculated with Eq. [4] to be 80%.[18] Using the Gibbs free energy of liquid water at 25ºC, the maximum fuel cell efficiency is 83%. In practice, fuel cells are typically operated at higher temperatures since the voltage losses (previously discussed at the start of section 1.4.2) are lower at higher temperatures. The maximum fuel cell efficiency in Eq. [4] does not tell the entire story and, therefore, voltage efficiency must be discussed. The voltage efficiency is derived by first calculating the maximum attainable voltage, assuming all the energy (enthalpy of formation) in a molecule of hydrogen fuel is converted into electricity. Substituting the HHV of hydrogen and Faraday's constant into Eq. [5] below, a maximum voltage of 1.48V is calculated.

$$V_{Max} = \frac{-\Delta\overline{h_f}}{2F} \quad \textbf{[5]}$$

The two in the denominator of Eq. [5] is included since two moles of electrons are produced for every mole of hydrogen gas that reacts in the fuel cell. Now, the cell voltage efficiency can be written as Eq. [6].[18]

$$\eta_{Max}^{Voltage} = \frac{V_{Fuel\,Cell}}{1.48} * 100 \quad \textbf{[6]}$$

Another modification is required to Eq. [6] since traditionally not all the hydrogen flowing through the fuel cell reacts. The unreacted hydrogen is typically either recirculated back to the fuel cell inlet or discarded. The unused hydrogen gas can be accounted for by including a fuel utilization coefficient (C_f), which is a ratio between the mass of hydrogen reacted to the total mass of hydrogen fed to the fuel cell. Therefore, the final equation for maximum voltage efficiency is provided in Eq. [7].[18]

$$\eta_{Max}^{Voltage} = C_{fuel}\frac{V_{Fuel\,Cell}}{1.48} * 100 \quad \textbf{[7]}$$

By measuring the fuel cell's open circuit voltage and substitution into Eq. [7], the maximum fuel cell efficiency can be easily determined. Assuming a fuel cell voltage of 1V and fuel utilization coefficient of 0.95, the maximum fuel cell efficiency is 64%.

1.4.3 Balance of Plant (humidifiers, blowers, computer control)

Various types of auxiliary equipment are necessary to control and operate a fuel cell. The auxiliary equipment needed depends on the specific type of application (i.e. portable electronics, large-scale power generation, vehicle). The auxiliary equipment is referred to as the 'balance of plant'. Some of the key functions for the auxiliary equipment include delivering reactants at the proper temperature and humidity, separating products from the outlet streams, electrical controllers to convert alternating current (AC) to/from direct current (DC), and computer logic boards to direct information flow and adjust control parameters. A few types of auxiliary

equipment include pumps, blowers, circuit boards, gas/liquid storage containers, computers, and various types of valves, piping, tubing, and electrical wiring.

1.4.4 PEMFC Water Management

Water management in a PEMFC is important for peak performance and long lifetime.[30, 48-50] Insufficient hydration will cause the proton exchange membrane and CL ionomer to dry out, thus reducing the ionic conductivity and negatively impacting performance. Too much water can lead to flooding, therefore lowering mass transport of reactant gases to the catalyst reaction sites and resulting in reduced performance. During operation, multiple water transport mechanisms occur across a fuel cell. First, protons produced at the anode will drag water molecules from the anode to the cathode. A proton drags two to three water molecules depending on membrane temperature and hydration state.[51] Secondly, since the oxygen reduction reaction produces water at the cathode, a water concentration gradient is established with peak water concentration inside the cathode CL. The water concentration gradient created by the production of water in the cathode CL results in back diffusion of water from the cathode to the anode as well as movement of water from the cathode CL out into the cathode oxygen flow channels.[49] Typically, the overall effect of these water transport mechanisms during high current density operations will lead to drying out of the anode side of the proton exchange membrane.[48, 49] Therefore, the hydrogen gas supply inlet is typically humidified to maintain proper membrane hydration levels at the anode side. Figure 1.28 shows a simplified sketch of the various water transport mechanisms occurring across a PEMFC.

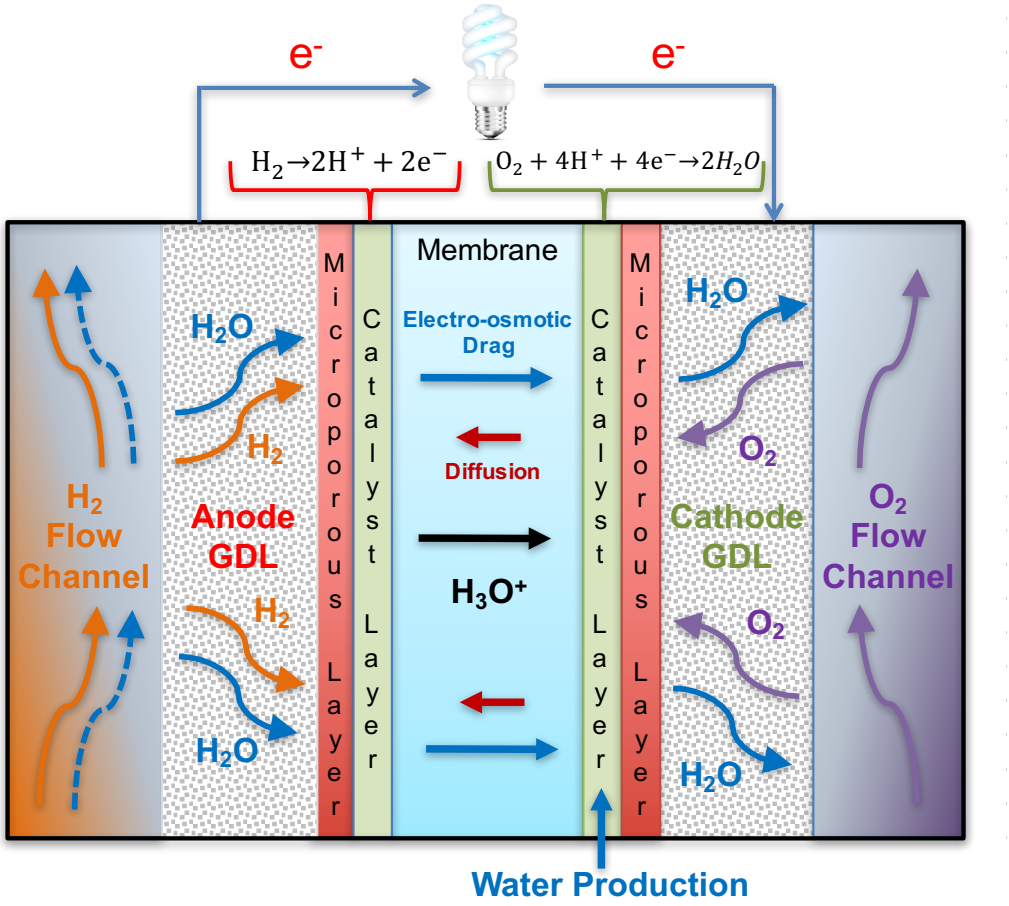

Figure 1.28. Visualized PEMFC water management processes.[52]

A large amount of research has been generated to minimize the impact of water production in the PEMFC cathode catalyst layer. Membrane development has been a major research area. Critical membrane parameters include ionic conductivity (i.e. sheet resistance), water and gas permeability, and mechanical strength. Di Vona and Iwai et al. demonstrated how cross-linking polymers greatly stabilizes the polymer in terms of thermal, mechanical, and hydrolytic degradation.[53, 54] Pintauro et al. demonstrated reduced swelling and increased strength by electrospinning nanofiber composite membranes together.[34] By melting an inert polymer around ionic nanofibers, the membrane swells less which reduces the rate of water crossover during operation by electroosmosis.[34] Another membrane improvement was the discovery of

making membranes via the solution cast process. Thermally-extruded membranes, such as Nafion® 112, are known to develop a PTFE-rich skin during the fabrication process.[39, 55] Whereas Nafion® 212, is generally void of this PTFE-rich skin due to using the solution cast method.[39] Since PTFE-rich regions are ionically nonconductive, the thermally extruded membranes have lower ionic conductivity at the membrane's surface in contact with the fuel cell CL.[39] The PTFE-rich skin leads to more resistance for hydronium ion transport and lower peak performance.[39]

A second area of exploration to improve water management issues includes the development of the MPL. The MPL was initially added to the electrode between the GDL and CL in order to lower the contact resistance between these two electrode layers.[56-59] Kalidindi et al. found that a MPL was also able to improve catalyst utilization and reduce flooding on the cathode GDL.[56-59] The high PTFE content in the MPL prevented water from reaching and collecting in the cathode GDL, as well as increased back transport of water across the membrane towards the anode.[56-59] The back transport of water reduced the need to humidify the hydrogen feed to maintain proper hydration of the anode side of the membrane.[56-59] The critical parameters for MPL and GDL design include layer thickness, PTFE content, and morphology.[56-60] The results of the MPL and GDL research have improved PEMFC performance and enabled reduced catalyst loading.[56-59]

The PEMFC cathode CL must be able to bring all reactants (oxygen gas, electrons, and protons) to the catalyst reaction site, including efficient two-phase flow of oxygen into the CL and water out of the CL. Inadequate two-phase flow can lead to fuel starvation and cell reversal.[42] Cell reversal can cause an increase in local anode potential resulting in irreversible carbon oxidation, as well as water electrolysis.[42] Two different methods are currently employed

in fabricating CLs. In the first method, a carbon-supported catalyst is either sprayed or electrodeposited onto a material that is both conductive and porous, such as carbon paper or carbon cloth.[26, 42] In the second method, the CL is applied directly to the proton exchange membrane.[26, 42, 61] Various techniques have been developed to apply the CL directly to the membrane; including rolling, spraying, or a process similar to screen-printing.[26, 42] Each technique imparts various mechanical and chemical properties to the layers and interfaces between layers.[26, 42, 61] The processing steps for each CL fabrication method play a crucial role in delivering optimal fuel cell performance.[26, 42, 61] Our group primarily creates CLs by spraying a catalyst ink directly onto carbon paper.

Improvement to the polymer electrolyte membrane, MPL, and GDL did little to address water flooding issues in the CL during high current density operations. In an attempt to lower fuel cell costs, research has focused on reducing catalyst loading in CLs.[62-64] One method to reduce catalyst loading has been to keep the percentage of catalyst per carbon support unchanged, while reducing the catalyst loading per geometric area. This technique has resulted in thinner CLs and, therefore, less void volume in the CL for gas and liquid transport.[62-64] On the other hand, if reduced catalyst loading is achieved by lowering the percentage of catalyst on carbon support, then the CL will be thicker. The reduced void volume inherent with thinner CLs makes water management in the cathode CL more challenging, especially during high current density operations. However, the transport distant for thinner CLs is shorter, therefore allowing faster water removal and oxygen delivery to the cathode. As shown in Figure 1.29a, water produced in the cathode CL will collect on the gas/ionomer interface, therefore reducing the mass transport of oxygen to the catalyst. Due to the formation of water on the gas/ionomer interface, oxygen must diffuse into and through a layer of water in order to reach the ionomer

surface. As shown in Figure 1.29b, at high current density operations the entire pore channel will become flooded with water, therefore drastically lowering the transport of oxygen and negatively impacting performance.

Previous studies in our research group addressed the electrode flooding problem by incorporating a hydrophobic phase (e.g. Teflon®) into the cathode CL in order to enable oxygen to be more easily transported to the catalyst reaction site (**NSF-CBET #0651758**: *Water Management in a PEM Fuel Cell by Materials Design and Engineering*).[65] As shown in Figure 1.29c, by incorporating Teflon® particles into the CL gas channels, reactant gases can move down the length of the pores to access catalyst sites throughout the CL. With this approach, fuel cell testing demonstrated improved performance and showed that optimal amounts of Teflon® was highly dependent on the Nafion® content.[65, 66] As shown in Figure 1.29d, one of the drawbacks to this method is that disconnected Teflon regions could disrupt gas transport. Furthermore, the PTFE to ionomer content and the CL fabrication process must be optimized when using other types of ionomers and catalysts. Closer reflection on the CL channel structure shown in Figure 1.29c reveals that even though gases can move down the length of a CL pore more easily due to the incorporation of a PTFE hydrophobic phase, gases will still need to diffuse into and through a layer of water that is coating the pore wall prior to reaching the ionomer. A thin layer of water coating the pore wall will lower gas transport to the catalyst reaction site and limit the maximum achievable current density. The realization that this technique creates a non-ideal transport structure for two-phase flow, as well as new discoveries with biphasic polymers, led our group to reexamine new methods for CL fabrication.

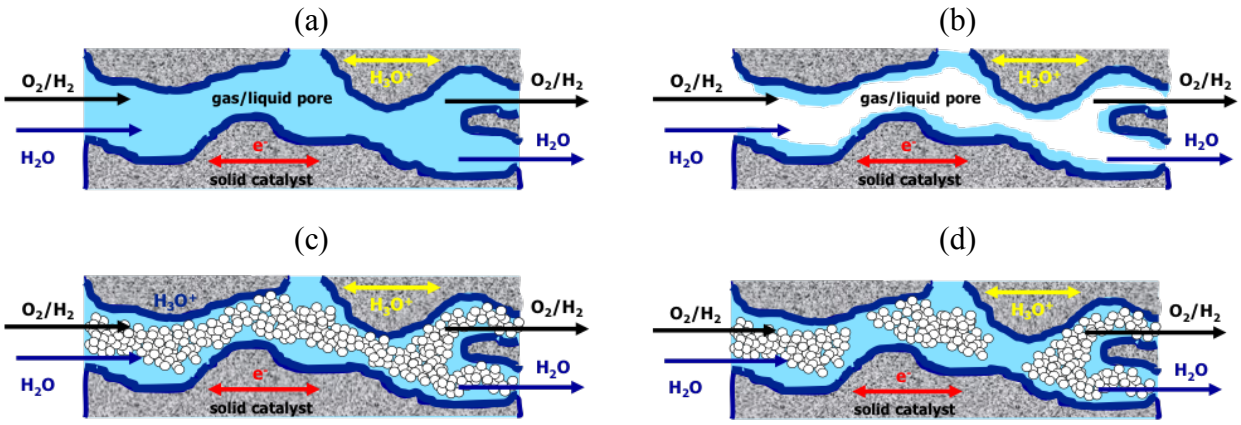

Figure 1.29. Creation of simultaneous gas and liquid pathways in the CL pores.[52]

1.5 Recent Discoveries with PFSA-based Polymers

Recently, it was discovered that PFSA-based polymers exposed to high relative humidity at the air-polymer interface cause the ionic sulfonate groups within Nafion® to rearrange so that the surface is made up of a larger proportion of hydrophilic ionic sulfonate groups.[41] Furthermore, when the PFSA-based polymer is exposed to low relative humidity at the air-polymer interface, the ionic sulfonate groups move inward causing the surface to have a higher proportion of hydrophobic Teflon®-rich regions.[41] Our group verified that the surface structure of Nafion® and electrospun nanofiber composite membranes depend on the relative humidity (RH) of the gas in contact with the membrane.[34, 37, 39] By operating an atomic force microscope (AFM) in both contact and tapping modes, we were able to show the dependence of the membrane's surface on the gas RH.[37, 39, 41, 67] Topography, phase contrast, and conductivity images were captured using the AFM to explore the surface structure of Nafion® and electrospun nanofiber composite membranes.[37, 39, 41] Figure 1.30 shows the variation in surface ionic activity for Nafion® at 20% and 80% RH.

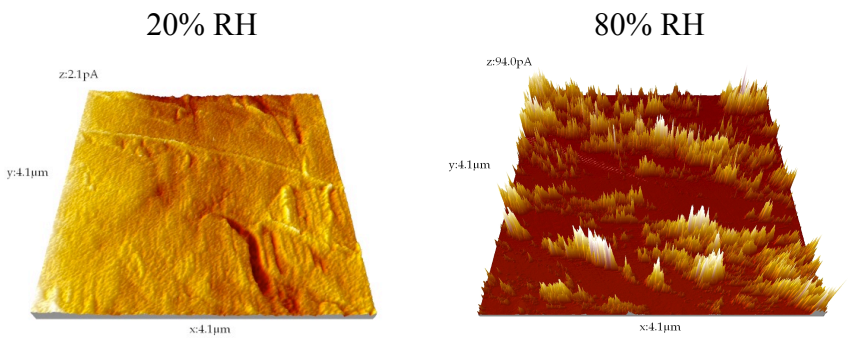

Figure 1.30. Effect of gas phase relative humidity on membrane surface ionic activity.[41]

The recent evidence showing the dependence of the polymer's surface structure on the gas humidity at the air-polymer interface, led me to explore the possibility of creating a permanent membrane surface structure. The notion was if the surface structure of PFSA membranes could be made to be permanently hydrophobic or hydrophilic, then it would be feasible to incorporate this concept into various applications. For example, a permanent hydrophobic ionomer-gas interface inside the gas pores of the CL would be expected to result in improved two-phase transport. Therefore, to determine the feasibility of engineering the CL ionomer-gas interface to be hydrophobic, the concept needed to be first demonstrated using a conventional biphasic membrane (e.g. Nafion®). In chapters 2 and 3, this concept is demonstrated and then incorporated into the ionomer phase surface properties of a PEMFC catalyst layer during the MEA fabrication process. In section 1.6 below, we transition away from our discussion about PEMFC water management in order to introduce flow batteries. Following the flow battery overview, chapters 4, 5 and 6 provide detailed studies into optimizing the performance of various flow batteries.

1.6 Flow Batteries/Reversible Fuel Cells

Flow batteries and reversible fuel cells are continuous and reversible electrochemical conversion systems that operate on reversible reduction and oxidation reactions, hence the name redox

systems. The main difference between a redox flow battery (RFB) and a reversible fuel cell is that while the electrochemical reactions in a RFB do not require a catalyst to achieve an acceptable conversion rate, the reactions in a fuel cell do. Some fuel cells are not considered to be “reversible” (i.e. used as reversible systems) due to their low conversion rates during either discharge or charge.

A RFB stores all of its electro-active materials external to the power conversion device. A hybrid flow battery stores one of the electro-active materials internally and the second electro-active material external to the power conversion device. The zinc-bromine battery is an example of a hybrid flow system because the active zinc material is stored internally as the negative electrode while the active bromine material is stored externally to the battery. RFBs can be classified by the type of active species and solvent used (aqueous vs. non-aqueous). RFBs are constructed by sandwiching an ion exchange membrane or separator between two porous electrodes. During discharge, the anolyte reacts on the surface of the negative electrode to produce electrons, which move through an external electrical circuit to yield useful work before reaching the positive electrode. The charge-carrying ionic species moves through the ion exchange membrane or separator from the negative electrode to the positive electrode in order to maintain electroneutrality. Eqs. [8] and [9] shown below are the general redox reactions for charging and discharging.

Negative electrode:

$$A^{(n-x)+} \underset{charge}{\overset{discharge}{\rightleftarrows}} A^{n+} + xe^- \qquad (n \geq x) \qquad \textbf{[8]}$$

Positive electrode:

$$B^{(m+y)+} + ye^- \underset{charge}{\overset{discharge}{\rightleftarrows}} B^{m+} \qquad \textbf{[9]}$$

A generalized RFB schematic is shown in Figure 1.31. The dominant losses in the system include charge-transfer reaction kinetics, charge and mass transport in the electrolyte and separator, parasitic losses (i.e. pumping, etc.) and crossover of undesired species through the separator. The majority of RFBs utilize completely reversible liquid-phase electrochemical redox couples. As shown in Figure 1.31, the reactants are dissolved in electrolyte and can be stored outside the electrodes inside storage tanks. Therefore, the energy and power density of redox flow batteries are decoupled, enabling increased flexibility in system sizing and design. A review of current flow battery technology is summarized in Section 1.6.1. As shown in Section 1.6.1, flow batteries typically have low energy density as compared to lithium ion battery technology. Therefore, the transportation sector has not seriously considered flow batteries for vehicle use. Flow batteries are expected to be best suited for stationary applications where the mass and volume of the system are not an issue. Some examples include energy storage, load leveling and balancing, and large UPS. Technology demonstrations have been completed for redox flow batteries ranging from 100 kW to 10 MW systems.

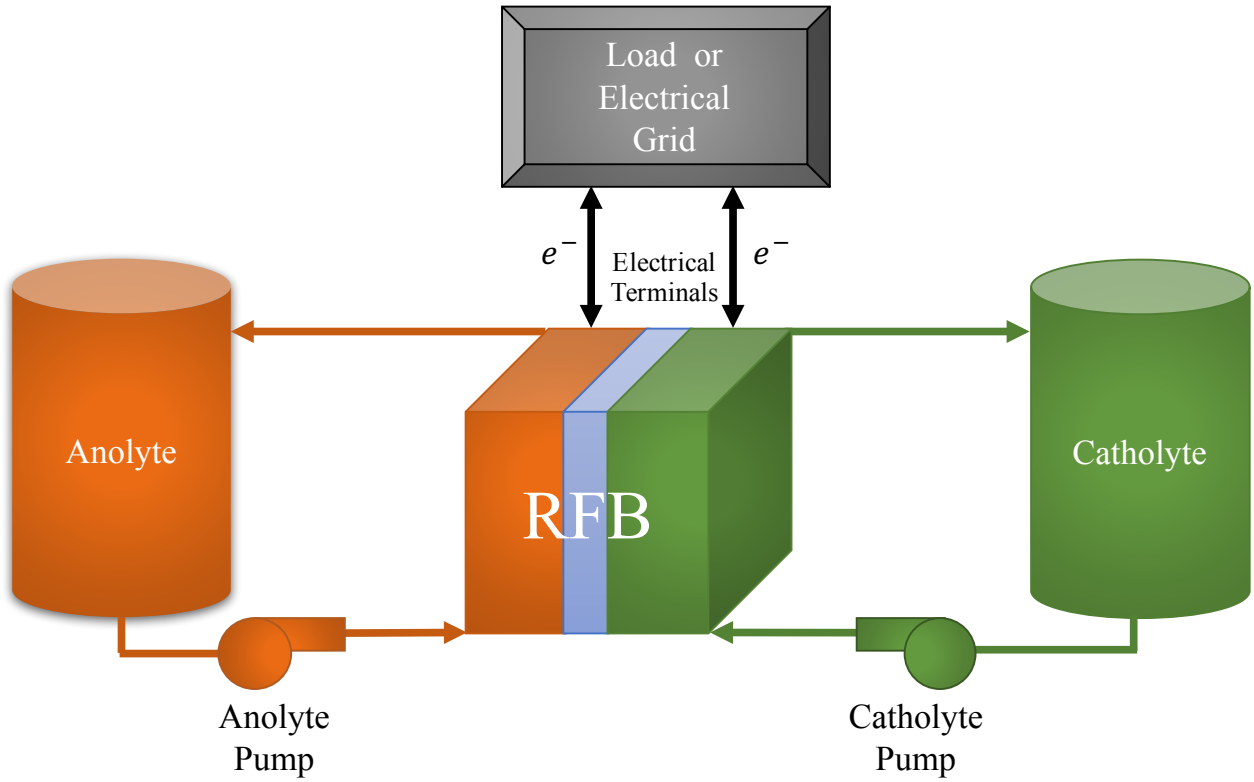

Figure 1.31. Generalized RFB System.

1.6.1 Flow Battery Chemistries[9, 68-71]

1. **<u>Aqueous RFBs</u>**

   a. **Iron-Chromium**

      i. REDOX reactions:

      $Fe^{2+} \leftrightarrow Fe^{3+} + e^-$ (Oxidation in the forward direction)

      $Cr^{3+} + e^- \leftrightarrow Cr^{2+}$ (Reduction in the forward direction)

      ii. OCV: 0.77-1.03 V

      iii. Energy Density: 40 Wh/L

      iv. Electrolyte: HCl/HCl

      v. Highlights:

         a) Uses a PEM and low cost carbon-felt electrodes.

b) Fe kinetics are highly reversible.

c) Cr kinetics are much slower and requires an electrocatalyst.

vi. Development Agencies/Companies: NASA (1970s-80s), EnerVault

vii. Safety Considerations: Hydrochloric acid is corrosive and hazardous at high concentrations. Proper handling and transportation precautions would need to be exercised.

b. Bromine-Polysulphide

i. REDOX reactions:

$$2S_2^{2-} \leftrightarrow S_4^{2-} + 2e^-$$

$$Br_2^- + 2e^- \leftrightarrow 2Br^-$$

ii. OCV: 1.54 V

iii. Energy Density: 80 Wh/L

iv. Electrolyte: NaS_2/NaBr

v. Highlights:

a) 5, 20, and 100 kW systems developed.

b) 15 MW system successfully demonstrated.

c) Both electrolytes are abundant and low cost.

d) Bromine reaction kinetics are fast, reversible and do not require the use of a precious metal catalyst.

vi. Safety Considerations: Bromine (Br_2) is toxic, corrosive, and has a high vapor pressure. Proper handling and transportation precautions would need to be exercised.

c. All-vanadium

i. REDOX reactions:

$V^{2+} \leftrightarrow V^{3+} + e^-$

$VO_2^+ + e^- \leftrightarrow VO^{2+}$

ii. OCV: 1.26 V

iii. Energy Density: 25-35 Wh/L

iv. Electrolyte: H_2SO_4/H_2SO_4

v. Highlights:

a) Due to using vanadium species on both sides of RFB, system is more stable if crossover occurs. In other words, crossover does not result in capacity loss or system degradation.

b) Vanadium is costly.

c) High response time, high roundtrip efficiency (>75%), and long cycle life (>10,000 cycles).

d) Demonstrations successfully performed up to MW in power and MWh in energy storage capability.

vi. Safety Considerations: Sulfuric acid is corrosive and hazardous at high concentrations. Proper handling and transportation precautions would need to be exercised.

d. Vanadium-bromine

i. REDOX reactions:

$V^{2+} \leftrightarrow V^{3+} + e^-$

$\frac{1}{2}Br_2 + e^- \leftrightarrow Br^-$

ii. OCV: 1.1 V

iii. Energy Density: 35-70 Wh/L

iv. Electrolyte: VCl_3-HCl/NaBr-HCl

v. Highlights:

a) The higher solubility of vanadium bromide solutions compared to vanadium sulfate (as in the all-vanadium system) results in higher energy densities.

b) Bromine reaction kinetics are fast, reversible and do not require the use of a precious metal catalyst.

vi. Safety Considerations: Bromine (Br_2) is toxic, corrosive, and has a high vapor pressure. Proper handling and transportation precautions would need to be exercised.

e. Quinone-bromine

i. REDOX reactions:

$$AQDSH_2 \leftrightarrow AQDS + 2e^- + 2H^+$$

$$Br_2 + 2e^- \leftrightarrow 2Br^-$$

ii. OCV: 1.5 V

iii. Energy Density: ~50 Wh/L

iv. Electrolyte: H_2SO_4

v. Highlights:

a) Quinones can be synthesized from low-cost chemicals.

b) Bromine reaction kinetics are fast, reversible and do not require the use of a precious metal catalyst.

vi. Safety Considerations: Bromine (Br_2) is toxic, corrosive, and has a high vapor pressure. Sulfuric acid is corrosive and hazardous at high concentrations. Proper handling and transportation precautions would need to be exercised.

2. **<u>Hydrogen-based systems (These systems which consist of a gaseous fuel cell negative electrode and aqueous battery positive electrode are also called hybrid reversible fuel cells)</u>**

   a. **Hydrogen-vanadium**

      i. REDOX reactions:

      $H_2 \leftrightarrow 2H^+ + 2e^-$

      $VO_2^+ + e^- \leftrightarrow VO^{2+}$

      ii. OCV: 1.0 V

      iii. Energy Density: ~75 Wh/L (assuming 10,000 psi compressed H_2 & 3M $VOSO_4$)

      iv. Electrolyte: PEM/H_2SO_4

      v. Highlights:

         a) As compared to the all-vanadium RFB, the electrolyte cost for the hydrogen-vanadium system is significantly lower due to using half of the vanadium as the all-vanadium system.

         b) A catalyst is required at the hydrogen electrode.

      vi. Safety Considerations: Hydrogen transportation and storage requirements apply. Sulfuric acid is corrosive and hazardous at high concentrations.

Proper handling and transportation precautions would need to be exercised.

b. Hydrogen-iodine (alkaline version)

i. REDOX reactions:

$H_2 + 2OH^- \leftrightarrow 2H_2O + 2e^-$

$I_2 + 2e^- \leftrightarrow 2I^-$

ii. OCV: 1.37 V

iii. Energy Density: ~191 Wh/L (assuming 10,000 psi compressed H_2 & 3M I_2)

iv. Electrolyte: KOH/PEM/KI

v. Highlights:

a) I_2 is safer to use and transport than Br_2.

b) Two phase flow at the hydrogen electrode.

vi. Safety Considerations: Hydrogen transportation and storage requirements apply.

c. Hydrogen-bromine (acidic version)

i. REDOX reactions:

$H_2 \leftrightarrow 2H^+ + 2e^-$

$Br_2 + 2e^- \leftrightarrow 2Br^-$

ii. OCV: 1.1 V

iii. Energy Density: ~150 Wh/L (assuming 10,000 psi compressed H_2 & 3M Br_2)

iv. Electrolyte: PEM/HBr

v. Highlights: Bromine reaction kinetics are fast, reversible and do not require the use of a precious metal catalyst.

vi. Safety Considerations: Bromine (Br_2) is toxic, corrosive, and has a high vapor pressure. Hydrogen transportation and storage requirements apply. Hydrobromic acid is corrosive and hazardous at high concentrations. Proper handling and transportation precautions would need to be exercised.

3. <u>Hybrid RFBs (Systems consisting of solid and aqueous active materials)</u>

a. Zinc-bromine

i. REDOX reactions:

$Zn(s) \leftrightarrow Zn^{2+} + 2e^-$

$Br_2(aq) + 2e^- \leftrightarrow 2Br^-$

ii. OCV: 1.85 V

iii. Energy Density: 60-90 Wh/L

iv. Electrolyte: $ZnBr_2/ZnBr_2$

v. Highlights: Bromine reaction kinetics are fast, reversible and do not require the use of a precious metal catalyst.

vi. Safety Considerations: Bromine (Br_2) is toxic, corrosive, and has a high vapor pressure. Proper handling and transportation precautions would need to be exercised.

b. Zinc-polyiodide

i. REDOX reactions:

$Z \leftrightarrow Zn^{2+} + 2e^-$

$I_3^- + 2e^- \leftrightarrow 3I^-$

ii. OCV: 1.3 V

iii. Energy Density: 167 Wh/L

iv. Electrolyte: ZnI_2/ZnI_2

v. Highlights: Can be operated -20°C to 50°C.

vi. Safety Considerations: N/A

c. Zinc-cerium

i. REDOX reactions:

$Zn \leftrightarrow Zn^{2+} + 2e^-$

$2Ce^{4+} + 2e^- \leftrightarrow 2Ce^{3+}$

ii. OCV: 2.2 V

iii. Energy Density: 35 Wh/L

iv. Electrolyte: CH_3SO_3H

v. Safety Considerations: N/A

d. Soluble lead acid

i. REDOX reactions:

$Pb \leftrightarrow Pb^{2+} + 2e^-$

$PbO_2 + 4H^+ + 2e^- \leftrightarrow Pb^{2+} + 2H_2O$

ii. OCV: 1.76 V

iii. Energy Density: 95 Wh/L

iv. Electrolyte: H_2SO_4

v. Highlights: As with any solid phase system, changes in electrode morphology can play a significant role in degradation and failure issues, such as short circuiting.

vi. Safety Considerations: Sulfuric acid is corrosive and hazardous at high concentrations. Proper handling and transportation precautions would need to be exercised.

e. All-iron

i. REDOX reactions:

$2Fe^{2+} \leftrightarrow 2Fe^{3+} + 2e^{-}$

$Fe^{2+} + 2e^{-} \leftrightarrow Fe$

ii. OCV: 1.2 V

iii. Energy Density: ~12 Wh/L

iv. Electrolyte: $FeCl_2$/$FeCl_2$ & $FeCl_3$

v. Highlights: Due to using a single species, crossover is not much of a concern except for leading to current inefficiency. Similar issues to other solid phase systems, due to Fe electrode undergoing morphological changes. Materials are nonhazardous and low cost.

vi. Safety Considerations: Materials are nonhazardous.

4. <u>Non-aqueous RFBs</u>

a. $[Ru(bpy)_3]^{+}$/$[Ru(bpy)_3]^{2+}$ in acetonitrile (CH_3CN), Tetraethylammonium tetrafluoroborate ($TEABF_4$) as the supporting electrolyte, (bpy is bipyridine)

i. REDOX reactions:

$[Ru(bpy)_3]^{2+} \leftrightarrow [Ru(bpy)_3]^{3+} + e^{-}$

$[Ru(bpy)_3]^{2+} + e^- \leftrightarrow [Ru(bpy)_3]^{1+}$

ii. OCV: 2.6 V

iii. Energy Density: 10 Wh/L

iv. Electrolyte: $TEABF_4$

v. Highlights: Wide working temperature range, high cell voltage, and potentially high energy densities.

vi. Safety Considerations: Organic solvent toxicity, cost, and compatibility must be considered.

b. $M(acac)_3$ (where M=V,Cr, or Mn; acac=acetylacetonate)

i. REDOX reactions:

$M(acac)_3 \leftrightarrow [M(acac)_3]^+ + e^-$

$M(acac)_3 \leftrightarrow [M(acac)_3]^- + e^-$

ii. OCV: 2.2 V (for M=V), 3.4 V (for M=Cr), 1.26 V (for M=Mn)

iii. Energy Density: 18 Wh/L

iv. Electrolyte: Acetylacetonate

v. Highlights: Wide working temperature range, high cell voltage, and potentially high energy densities.

vi. Safety Considerations: Organic solvent toxicity, cost, and compatibility must be considered.

5. <u>Other configurations</u>

a. Lithium-air

i. REDOX reactions: (acidic electrolyte)

$Li \leftrightarrow Li^+ + e^-$

$$Li^+ + e^- + O_2 \leftrightarrow LiO_2 + Li^+ + e^- \leftrightarrow Li_2O_2$$

ii. OCV: 2.91 V

iii. Energy Density: Theoretically, 5-15 times that of conventional Li ion batteries (250-650 Wh/L).

iv. Electrolyte: Either an aqueous or organic solvent capable of dissolving lithium salts (such as $LiPF_6$, $LiAsF_6$, $LiN(SO_2CF_3)_2$, or $LiSO_3CF_3$).

v. Highlights: Multiple challenges with technology currently being investigated.

vi. Safety Considerations: Many aqueous electrolytes are volatile. Short-circuiting battery can lead to overheating, fire and/or explosion.

b. Lithium slurry

i. REDOX reactions: Various chemistries are being explored using either aqueous or organic solvents.

ii. OCV: ~1.5 V (aqueous solvents), ~3 V (organic solvents)

iii. Energy Density: Theoretically, 5-20 times higher than typical aqueous RFBs (~40 Wh/L)

iv. Electrolyte: Various organic and aqueous solvents.

v. Highlights: Limited peer reviewed articles, Dr. Chiang (MIT) is in the process of developing this new technology.

vi. Safety Considerations: Unknown

Chapter 1 introduced various electrochemical energy storage devices, including batteries, fuel cells and flow batteries along with details on PEMFC components, operating principles and balance of plant. In chapters 2 and 3, the experimental design and results for improving water

management in the fuel cell catalyst layer will be discussed. Chapters 4, 5 and 6 present the work on performance optimization of various reversible fuel cell technologies. Chapter 4 examines the alkaline-based H_2-Br_2 and H_2-I_2 reversible fuel cells, while chapters 5 and 6 study the H_2-vanadium reversible fuel cell. Chapter 6 also introduces a new technique for measuring vanadium crossover in a H_2-vanadium reversible fuel cell. Finally, chapter 7 discusses future work and recommendations.

1.7 References for Chapter 1

1. D. R. Dunn, *DOE U.S. Energy Information Administration Monthly Energy Review*, **35**, 1 (2016).

2. L. E. Doman, *DOE U.S. International Energy Outlook 2016*, **484**, 1 (2016).

3. A. H. Hajimiragha, C. A. Cañizares, M. W. Fowler, S. Moazeni, A. Elkamel and S. Wong, *International Journal of Hydrogen Energy*, **36**, 6357 (2011).

4. G. Smith, Solar Power Capacity Tops Coal for the First Time Ever, in *Fortune Energy*, http://fortune.com/2016/10/25/solar-power-capacity-coal-electricity-generation/ (2016).

5. Key Renewables Trends, in *International Energy Agency*, http://www.iea.org/ (2016).

6. K. V. D. Bergh and E. Delarue, *Energy Conversion and Management*, **97**, 70 (2015).

7. Y. Zhou, M. Wang, H. Hao, L. Johnson, H. Wang and H. Hao, *Mitigation and Adaptation Strategies for Global Change*, **20**, 777 (2014).

8. J. I. Liinares, L. E. Herranz and B. Y. Moratilla, *International Journal of Hydrogen Energy*, **36**, 10027 (2011).

9. T. V. Nguyen and R. F. Savinell, Flow Batteries, in *The Electrochemical Society Interface*, p. 54 (2010).

10. O. Egbue and S. Long, *Energy Policy*, **48**, 717 (2012).

11. C. Depcik, Batteries and Battery Packs, in *Hybrid and Electric Vehicles Lecture*, University of Kansas, Mechanical Engineering (2015).

12. K. R. Bullock, *Journal of Power Sources*, **51**, 1 (1994).

13. B. C. International, Lead-Acid Batteries Top the Nations's Recycling List, in *PR Newswire*, http://www.prnewswire.com/news-releases/lead-acid-batteries-top-the-nations-recycling-list-continuous-closed-loop-recycles-battery-lead-indefinitely-70822372.html (2003).

14. B. Chatain, MEPs ban cadmium from power tool batteries and mercury from button cells, in *European Parliament News*, http://www.europarl.europa.eu/news/en/news-room/20131004IPR21519/meps-ban-cadmium-from-power-tool-batteries-and-mercury-from-button-cells (2013).

15. V. V. Viswanathan and M. C. Kintner-Meyer, *Repurposing of batteries from electric vehicles*, Woodhead Publishing, Sawston, Cambridge (2015).

16. M. O. Ramoni and H. Zhang, *Clean Technologies and Environmental Policy*, **15**, 881 (2013).

17. F. T. Bacon, *Nature*, **186**, 589 (1960).

18. J. Larminie, *Fuel Cell Systems Explained*, John Wiley & Sons Ltd, Chichester, England (2003).

19. V. Mehta and J. S. Cooper, *Journal of Power Sources*, **114**, 32 (2003).

20. R. P. Dowd, S. Lee, Y. Fan and K. Gerdes, *International Journal of Hydrogen Energy*, **41**, 14971 (2016).

21. T. V. Nguyen, Engineering of Surface Property of Ionic Polymer Phase in a Fuel Cell Catalyst Layer, in *Proposal to the National Science Foundation* (2012).

22. G. A. Eisman, *Journal of Power Sources*, **29**, 389 (1990).

23. K. Malek, M. Eikerling, Q. Wang, Z. Liu, S. Otsuka, K. Akizuki and M. Abe, *Journal of Chemical Physics*, **129**, 204702 (2008).

24. S. de Almeida and Y. Kawano, *An International Forum for Thermal Studies*, **58**, 569 (1999).

25. A. V. Anantaraman and C. L. Gardner, *Journal of Electroanalytical Chemistry*, **414**, 115 (1996).

26. N. Zamel, *Journal of Power Sources*, **309**, 141 (2016).

27. T. A. Zawodzinski, Jr., T. E. Springer, J. Davey, R. Jestel, C. Lopez, J. Valerio and S. Gottesfeld, *Journal of the Electrochemical Society*, **140**, 1981 (1993).

28. T. V. Nguyen and N. Vanderborgh, *Journal of Membrane Science*, **143**, 14 (1998).

29. K. Glavatskiy, J. G. Pharoah and S. Kjelstrup, *Journal of Membrane Science*, **431**, 96 (2013).

30. J. T. Hinatsu, M. Mizuhata and H. Takenaka, *Journal of The Electrochemical Society*, **141**, 1493 (1994).

31. P. J. James, J. A. Elliott, T. J. McMaster, J. M. Newton, A. M. S. Elliott, S. Hanna and M. J. Miles, *Journal of Materials Science*, **35**, 5111 (2000).

32. E. Aleksandrova, S. Hink, R. Hiesgen and E. Roduner, *Journal of Physics Condensed Matter*, **23**, 234109 (2011).

33. R. Takemori and H. Kawakami, *Journal of Power Sources*, **195**, 5957 (2010).

34. J. B. Ballengee and P. N. Pintauro, *Macromolecules*, **44**, 7307 (2011).

35. A. M. Park and P. N. Pintauro, *Electrochemical and Solid-State Letters*, **15**, B27 (2012).

36. J. B. Ballengee and P. N. Pintauro, *Journal of Membrane Science*, **442**, 187 (2013).

37. R. P. Dowd, T. V. Nguyen, D. S. Moore, P. N. Pintauro and J. W. Park, *ECS Transactions*, **58**, 607 (2013).

38. C. Ionescu-Zanetti, A. Mechler, S. A. Carter and R. Lal, *Advanced Materials*, **16**, 385 (2004).

39. R. S. McLean, M. Doyle and B. B. Sauer, *Macromolecules*, **33**, 6541 (2000).

40. S. K. Saha, Y. K. Su, C. L. Lin and D. W. Jaw, *Nanotechnology*, **15**, 66 (2004).

41. T. V. Nguyen, M. V. Nguyen, G. Lin, N. Rao, X. Xie and D. M. Zhu, *Electrochemical and Solid-State Letters*, **9**, A88 (2006).

42. J. W. Weidner, V. A. Sethuraman and J. W. Van Zee, *The Electrochemical Society Interface*, **2**, 40 (2003).

43. A. Z. Weber and J. Newman, *Journal of The Electrochemical Society*, **152**, A677 (2005).

44. T. V. Nguyen, *Journal of The Electrochemical Society*, **143**, L103 (1996).

45. N. J. Cooper, T. Smith, A. D. Santamaria and J. W. Park, *International Journal of Hydrogen Energy*, **41**, 1213 (2016).

46. J. Houser, J. Clement, A. Pezeshki and M. M. Mench, *Journal of Power Sources*, **302**, 369 (2016).

47. D. Wood, J. Yi and T. V. Nguyen, *Electrochimica Acta*, **43**, 3795 (1998).

48. T. V. Nguyen and R. E. White, *Journal of The Electrochemical Society*, **140**, 2178 (1993).

49. A. Iranzo and P. Boillat, *International Journal of Hydrogen Energy*, **39**, 17240 (2014).

50. A. Debenjak, M. Gašperin, B. Pregelj, M. Atanasijević-Kunc, J. Petrovčič and V. Jovan, *Strojniški vestnik – Journal of Mechanical Engineering*, **59**, 56 (2013).

51. G. Karimi and X. Li, *Journal of Power Sources*, **140**, 1 (2005).

52. R. P. Dowd, Ph.D. Comprehensive Exam, in *Engineering the Ionomer-Gas Interface in a Fuel Cell Catalyst Layer*, University of Kansas (2016).

53. M. L. Di Vona, E. Sgreccia, M. Tamilvanan, M. Khadhraoui, C. Chassigneux and P. Knauth, *Journal of Membrane Science*, **354**, 134 (2010).

54. Y. Iwai, A. Hiroki and M. Tamada, *Journal of Membrane Science*, **369**, 397 (2011).

55. T. V. Nguyen, M. V. Nguyen, K. J. Nordheden and W. He, *Journal of The Electrochemical Society*, **154**, A1073 (2007).

56. A. R. Kalidindi, R. Taspinar, S. Litster and E. C. Kumbur, *International Journal of Hydrogen Energy*, **38**, 9297 (2013).

57. R. Schweiss, M. Steeb and P. M. Wilde, *Fuel Cells*, **10**, 1176 (2010).

58. Z. Qi and A. Kaufman, *Journal of Power Sources*, **109**, 38 (2002).

59. L. R. Jordan, A. K. Shukla, T. Behrsing, N. R. Avery, B. C. Muddle and M. Forsyth, *Journal of Power Sources*, **86**, 250 (2000).

60. J. Benziger, J. Nehlsen, D. Blackwell, T. Brennan and J. Itescu, *Journal of Membrane Science*, **261**, 98 (2005).

61. T. Suzuki, S. Tsushima and S. Hirai, *International Journal of Hydrogen Energy*, **36**, 12361 (2011).

62. M. Moore, P. Wardlaw, P. Dobson, J. J. Boisvert, A. Putz, R. J. Spiteri and M. Secanell, *Journal of the Electrochemical Society*, **161**, E3125 (2014).

63. M. Uchida, Y. C. Park, K. Kakinuma, H. Yano, D. A. Tryk, T. Kamino, H. Uchida and M. Watanabe, *Physical Chemistry Chemical Physics*, **15**, 11236 (2013).

64. A. N. Khorasani, Nanoscale Phenomena in Ultrathin Catalyst Layers of PEM Fuel Cells: Insights from Molecular Dynamics (Master's Thesis), in *Department of Chemistry*, Simon Fraser University (2013).

65. R. Friedmann and T. V. Nguyen, *Journal of The Electrochemical Society*, **157**, B260 (2010).

66. G. S. Avcioglu, B. Ficicilar, A. Bayrakceken and I. Eroglu, *International Journal of Hydrogen Energy*, **40**, 7720 (2015).

67. Y. Wang, R. Song, Y. Li and J. Shen, *Surface Science*, **530**, 136 (2003).

68. P. Alotto, M. Guarnieri and F. Moro, *Renewable and Sustainable Energy Reviews*, **29**, 325 (2014).

69. C. Ponce de León, A. Frías-Ferrer, J. González-García, D. A. Szánto and F. C. Walsh, *Journal of Power Sources*, **160**, 716 (2006).

70. M. Skyllas-Kazacos, M. H. Chakrabarti, S. A. Hajimolana, F. S. Mjalli and M. Saleem, *Journal of The Electrochemical Society*, **158**, R55 (2011).

71. A. Z. Weber, M. M. Mench, J. P. Meyers, P. N. Ross, J. T. Gostick and Q. Liu, *Journal of Applied Electrochemistry*, **41**, 1137 (2011).

CHAPTER 2: Engineering the Ionic Polymer Phase Surface Properties of a PEM Fuel Cell Catalyst Layer

2.1 Abstract

During high power density operations, the performance of polymer electrolyte membrane fuel cells (PEMFCs) may be limited by high water saturation levels in the cathode catalyst layer due to high wettability of the ionic polymer phase. A new heat treatment method was used to create and lock-in the surface structure of Nafion 212. Several surface characterization techniques were used to verify the membrane's surface after heat treatment, including contact angle, atomic force microscopy, X-ray diffraction and X-ray photoelectron spectroscopy. We found that specific heat treatment conditions led to the formation of either a hydrophobic or hydrophilic surface. The modified membrane's surface remained intact even after the membranes were boiled in water for 1 h. Next, a 4-point conductivity technique was used to verify that the heat treatment conditions which led to a hydrophobic surface did not negatively impact the membrane's internal conductivity. Finally, this novel heat treatment method was applied to the cathode catalyst layer of a H_2-Air PEMFC to create a hydrophobic polymer-gas interface inside the gas pores of the cathode catalyst layer. Preliminary results showed 33% increase in peak power. The results of this research will guide the design of a new class of PEMFC catalyst layers.

2.2 Introduction

PEMFCs offer the advantages of high power density and energy conversion efficiency, simplicity in design and operation, the added environmental benefits such as zero carbon emissions, and the production of benign by-products such as water when using the H_2-O_2/(Air)

fuel cell.[1, 2] Additionally, reversible fuel cells (flow batteries) offer a viable solution to the highly desired need for economical grid energy storage in order to take full advantage of load leveling.[3-5] As the use of intermittent energy sources such as wind and solar power continue to rise throughout the world, the need for reliable, efficient and economical energy storage solutions will grow. Excessive liquid water build-up in the fuel cell catalyst layer (CL) at high current densities can lead to electrode flooding, thus restricting transport of gaseous reactants to the catalyst reaction sites. In order to realize the economic viability of fuel cells, the fuel cell CL needs to be redesigned to overcome the negative hydration effects common with PEMFCs.

Water management in a PEMFC is important for peak performance and long lifetime.[6] A large amount of research has been generated to minimize the impact of water production in the PEMFC catalyst layer. One of the first areas of exploration to improve water management pertains to membranes. Critical membrane parameters include ionic conductivity, water and gas permeability, and mechanical strength. Di Vona and Iwai et al. demonstrated how cross-linking polymers greatly stabilizes the polymer in terms of thermal, mechanical, and hydrolytic degradation.[7, 8] Pintauro et al. demonstrated reduced swelling and increased strength by electrospinning nanofiber composite membranes together.[9] By melting an inert polymer around ionic nanofibers, the membrane swells less which reduces the rate of water crossover during operation by electroosmosis. A second membrane improvement was the discovery of making membranes via the solution-cast process. Thermally-extruded membranes, such as Nafion 112, are known to develop a Teflon-like skin during the fabrication process.[2, 10] Nafion 212 is generally void of this Teflon-like skin due to using the solution-cast method. Since Teflon-like regions are ionically nonconductive, the thermally extruded membranes have lower ionic

conductivity at the membrane's surface in contact with the fuel cell CL. The Teflon-like skin leads to more resistance for hydronium ion transport and lower peak performance.

A second area of exploration to improve water management issues includes the development of the microporous layer (MPL). Kalidindi et al. found that a MPL was also able to improve catalyst utilization and reduce flooding on the cathode GDL.[11-14] The high PTFE content in the MPL prevented water from reaching and collecting in the cathode GDL, as well as increased back transport of water across the membrane towards the anode. The back transport of water reduced the need to humidify the hydrogen feed to maintain proper hydration of the anode side of the membrane. The critical parameters for designing the MPL and GDL include layer thickness, PTFE content, and morphology. The results of the MPL and GDL research have improved PEMFC performance and enabled reduced catalyst loading.

Previous studies in our research group addressed the electrode flooding problem by incorporating a hydrophobic phase, such as Teflon, into the cathode CL in order to enable oxygen to be more easily transported to the catalyst reaction site.[15] With this approach, fuel cell testing demonstrated improved performance when incorporating Teflon into the CL and showed that optimal amounts of Teflon were highly dependent on the Nafion content. The CL structure with Teflon integration is presented in Figure 2.1A. For this research, our hypothesis is based on past discoveries about the interfacial properties of perfluorosulfonic acid-based polymers. Previously in our research group, it was discovered that perfluorosulfonic acid-based polymers exposed to high relative humidity at the air-polymer interface cause the ionic sulfonate groups within Nafion to rearrange so that the surface is made up of a larger proportion of ionic sulfonate groups.[16] Furthermore, when the perfluorosulfonic acid-based polymer is exposed to low relative humidity at the air-polymer interface, the ionic sulfonate groups move inward causing the

surface to have a higher proportion of hydrophobic Teflon-rich regions. Our group verified that the surface structure of Nafion and electrospun nanofiber composite membranes depend on the relative humidity (RH) of the gas in contact with the membrane.[9, 10, 17, 18] By operating an atomic force microscope (AFM) in both contact and tapping modes, we were able to show the dependence of the membrane's surface by changing the RH, scanning the surface with an AFM and comparing the AFM images. Topography, phase contrast, and conductivity images were captured using the AFM to explore the surface structure of Nafion and electrospun nanofiber composite membranes. Based on these observations, it is hypothesized that by heat treatment of the ionomer within the fuel cell CL we can engineer the ionomer-gas interface inside the gas pores of the CL to be hydrophobic so that oxygen would be able to access the catalyst reaction sites without having to diffuse through a layer of water. The proposed CL structure for this work is shown in Figure 2.1B.

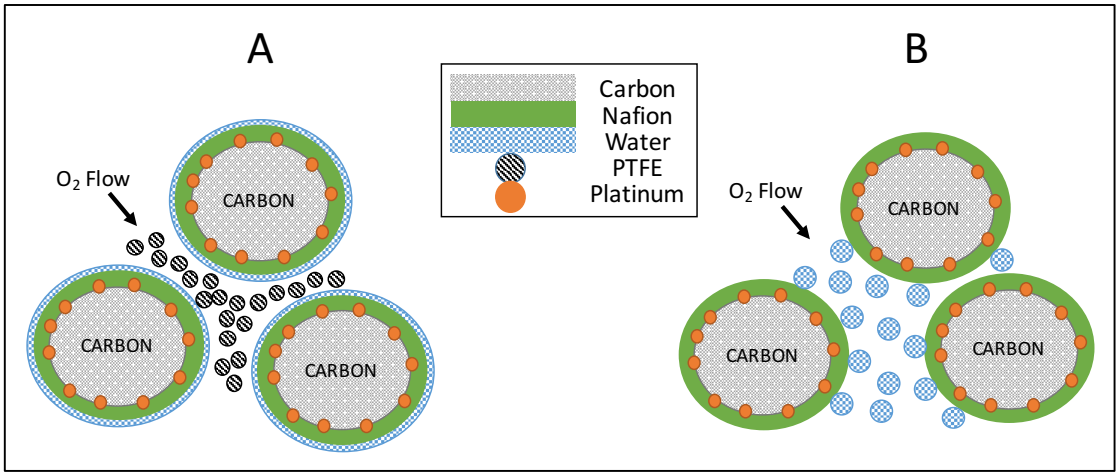

Figure 2.1. Comparison of (A) Teflon-incorporated and (B) Engineered Polymer Surface Catalyst Layer Methods.

The ability to tailor a biphasic polymer's surface relies on an important material property called the glass transition temperature (T_g). The primary ∝-relaxation process is the temperature at which larger segments of the polymer become mobile, whereas the subglass transition

temperature (also called the secondary β-relaxation process) involves localized motion of the polymer backbone and is a precursor to the primary $\propto$-relaxation process.[19] Glass transition is a reversible process that takes place in amorphous materials or in amorphous regions of semi-crystalline materials. At T_g, the amorphous regions of the polymer start to change from a glassy hard state to a rubber-like state. The polymer will start to relax when heated above T_g and the polymer becomes more flexible. The T_g is always lower than the melting temperature for the crystalline phase of the polymer. Additionally, the T_g is not defined as a phase transition even though the polymer undergoes an enormous change in physical properties. There are three general techniques for measuring T_g, including differential scanning calorimetry (DSC), thermal mechanical analysis (TMA), and dynamic mechanical analysis (DMA). DSC is probably the most common way to measure T_g and is a thermoanalytical technique which measures the difference in the amount of heat required to raise the temperature of a sample relative to a reference. For a given sample, DSC generates a curve of heat flux versus temperature. T_g will result in a step in the baseline or the recorded DSC signal due to undergoing a change in heat capacity, although no formal phase change occurs. The biphasic polymer used in these experiments, Nafion 212, has a T_g in the range of 110-130ºC, depending on the degree of hydration and sample aging.[20-22]

Multiple research groups have investigated the surface properties and morphological characteristics of ultrathin Nafion films. Goswami et al. showed the effect of water droplets on the surface structure of Nafion thin films, which is similar to the surface structure dependence of commercially available Nafion membranes.[23] Paul et al. showed how annealing ultrathin Nafion films (~10 nm) leads to surface and bulk reorganization, which directly affects the thin film's surface wettability and proton conductivity.[24] Paul et al. also found that the thickness of solution-

cast Nafion thin films plays an integral role in determining the surface hydrophobicity/hydrophilicity after initial casting.[25] Sub-55 nm Nafion films resulted in hydrophilic surfaces, whereas thicker films led to hydrophobic surfaces.[25] These studies [23-25] did not attempt to create permanent ultrathin film surface structures. Weber et al. suggests that the unexplained transport resistances common with low Pt loading CLs may be due to a variety of interactions that occur in thin-film ionomers.[26] Thin films have been shown to exhibit varying phase separation properties, confinement effects, and wetting characteristics not traditionally seen with conventional micron-thick membranes. Weber et al. concludes that possible solutions to reduce thin-film resistances include using different ionomer structures, different casting solvents, heat treatment modifications, etc. Typical CL ionomer film thicknesses have been measured to be in the range of ~5-10 nm.[24-27] Allen et al. showed the hydrophilic domain size of Nafion films to be around 3.5 nm (dry) – 5 nm (hydrated).[28] Phase separation could prove to be difficult when the thickness of the thin film approaches the hydrophilic domain size. Exploratory research on thin film properties and phenomena is a growing area and the outcome will be of great importance to future CL designs. The work done by Paul et al. and others shows promising extension of membrane skin phenomenon to the CL ionomer thin film.[23-25, 29]

To determine the feasibility of engineering the CL ionomer-gas interface to be either hydrophobic or hydrophilic by creating a skin rich in Teflon-like groups or in ionic sulfonate groups, respectively, we first demonstrated the heat treatment method using a conventional biphasic membrane (Nafion 212). Once the concept of being able to tailor the membrane's surface was proven, we then attempted to incorporate the findings into engineering a new CL structure. A hydrophilic ionomer-gas interface inside the pores of the CL is preferred for electrodes with liquid reactants, such as the all-vanadium redox flow battery.[4] A hydrophobic

ionomer-gas interface inside the pores of the CL is preferred for electrodes with gaseous reactants, such as the H_2-air PEMFC. The novelty of this new approach involves the creation of a surface skin (hydrophilic or hydrophobic) on conventional membranes that survives extreme conditions (1 h water boil) and the application of similar heat treatment conditions to the membrane electrode assembly (MEA) fabrication process in order to create a desired ionomer-gas interface (hydrophobic in this case) inside the pores of the CL. The improved MEA fabrication process leads to better performance during high current density operations.

2.3 Experimental

A stainless steel cylindrical vessel (internal dimensions: 0.152-m diameter and 0.152-m height) was constructed for heat treating membranes in order to control the membrane's exposure to humidity, temperature, and pressure. The heat treatment vessel layout is provided in Figure 2.2. The typical operating temperatures and pressures inside the vessel were 20-160ºC and 0-0.618 MPa, respectively. Maximum design operating temperature and pressure were 190ºC and 1.27 MPa. Therefore, a pressure relief safety valve was installed on the vessel to vent at 1.48 MPa. Dry argon was preheated using high temperature heating tape and insulation prior to introduction into the vessel chamber.

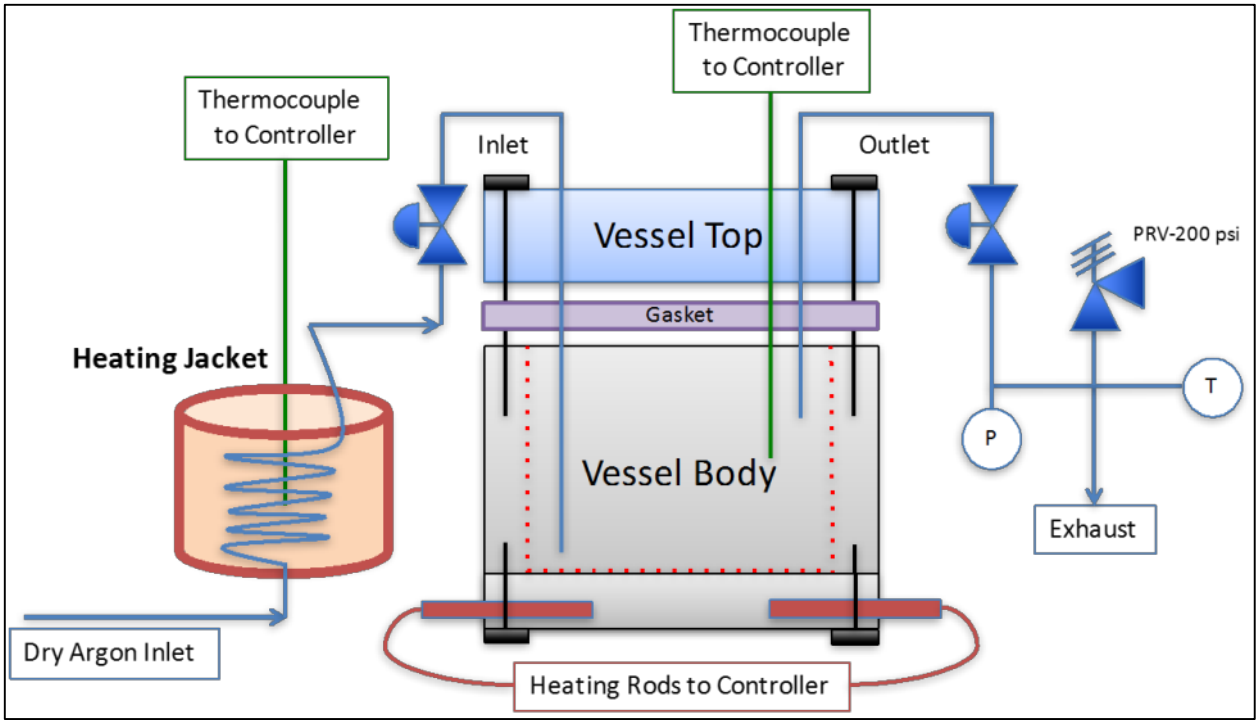

Figure 2.2. Membrane treatment experimental setup.

Membranes (25 cm^2) were mounted inside the vessel with an adequate amount of water and heated above the T_g. By controlling the initial amount of liquid water added to the vessel, one can control the final RH for a given temperature. The amount of water added to the vessel was calculated from the ideal gas law using the vapor pressure of saturated steam, maximum operating temperature, and the internal volume of the vessel. An excess of water (1.1x) was added to the vessel to ensure saturated steam conditions (100% RH) at maximum operating temperature. As the vessel was heated using heating rods inside the vessel's base, the water inside the vessel flashed to create a saturated steam environment. In this first step, heating the membrane above T_g using saturated steam ensured the membrane was relaxed and hydrated to ensure adequate ionic group mobility. Next, steam in the vessel was either vented or maintained in order to create the conditions necessary for creating a hydrophobic or hydrophilic surface, respectively. For the hydrophobic case, saturated steam was vented while maintaining the

membrane's temperature above T_g. Subsequently, dry argon heated to above T_g was directed through the vessel to remove any remaining steam. After the heated argon had been flowing for 1 h, the vessel was allowed to slowly cool to ambient temperature. The vessel was slowly cooled in order to crystallize the membrane and lock the membrane's surface structure in place. For the hydrophilic case, the saturated steam environment was maintained throughout the heat treatment process. Membrane exposure conditions for both the hydrophobic and hydrophilic cases are summarized in Table 2.1.

Table 2.1. Experimental design conditions.

Step Number	Hydrophobic Case	Hydrophilic Case
1	Heat membrane above T_g using saturated steam for 1 h	Heat membrane above T_g using saturated steam for 1 h
2	Vent steam while maintaining temperature above T_g	Allow vessel to cool to ambient temperature with saturated steam locked-in
3	Flush vessel with heated dry argon for 1 h	
4	Allow vessel to cool to ambient temperature while flowing dry argon	

The ability to characterize the surface of the heat-treated membranes was important in order to validate that the exposure conditions create a durable hydrophobic or hydrophilic surface. In this work, we used several surface characterization techniques, including contact angle, multi-mode atomic force microscopy (AFM), X-ray diffraction (XRD), and X-ray photoelectron spectroscopy (XPS). The contact angle formed by placing a water droplet onto the surface of the membrane will be larger for a hydrophobic material than a hydrophilic one. The repulsive forces a hydrophobic material imparts onto a water droplet will tend to make water form a spherical bead on the surface. However, a hydrophilic material will allow the water

droplet to spread out and wet the surface. All contact angle measurements were completed using 2 μL of water delivered to the membrane's surface with a micro-syringe. A high-resolution camera mounted on a tripod was used to capture the contact angle formed between the water droplet and membrane surface. We expect the hydrophobic treated membrane not to be completely void of ionic groups at the membrane's surface. Therefore, the ionic groups will form nanometer-sized ionic pathways from the surface into the internal ionic matrix of the membrane. After a water droplet has been placed onto the membrane's surface, the water will be absorbed into the internal ionic matrix. The speed to which the water droplet will move into the internal ionic matrix will be directly proportional to the relative amount of ionic domains on and near the membrane's surface. Therefore, a more hydrophobic surface will absorb a water droplet placed on the membrane's surface more slowly than a hydrophilic surface. In order to capture the speed at which a water droplet is absorbed into the membrane, high resolution images were captured every 5 min for a total of 20 min.

For the next surface characterization technique, multi-mode AFM (Nanosurf FlexAFM) was employed. The AFM has the ability to be operated in either contact or tapping mode and is able to collect various surface properties, including topography, phase contrast, and conductivity. Phase contrast is able to detect differences in material composition in order to determine the location of ionic and Teflon-like domains on the membrane's surface. Past research has shown that conductive mode is only able to detect the membrane's surface ionic groups that are connected to the internal ionic matrix through the membrane. If a surface ionic group is not connected to the internal ionic matrix, then no current will flow when the AFM tip comes into contact with an ionic domain. Therefore, phase contrast mode was employed for this work in order to measure the relative amounts of ionic and Teflon-like domains on the membrane's

surface.

Grazing incidence XRD (GIXRD) was used to measure the relative amounts of amorphous, crystalline, and ionic domains near the membrane's surface. GIXRD data was collected on a Bruker D8 Discover DaVinci system with a Göbel Mirror and thin film stage, equipped with parallel beam optics, using CuKα radiation (λ=1.5418 Å) at a scanning speed of 4 sec/step with a step size of 0.04°. The angle of x-ray incidence was varied incrementally over a range of 0.1º to 4.0º. Additionally, PXRD patterns were collected using a Bruker D2Phaser equipped with a CuKα radiation source (λ=1.5418 Å) and 1D Lynxeye detector at a scanning speed of 1.0 sec/step with a step size of 0.03° (Bragg-Brentano geometry). Deconvolution was completed using the Bragg-Brentano measurements on the broad amorphous peak centered about 8-22º and the sharp crystalline peak centered at about 17.5º. Blanton et al. demonstrated that deconvolution of these two peaks can be used to calculate relative percent crystallinity of Nafion membranes.[30]

Additionally, the Physical Electronics (PHI) VersaProbe III XPS was used to capture high resolution scans in order to measure the sulfur and carbon atomic percentages near the surface of the membrane. Angle resolved XPS allowed us to rotate the sample stage in order to vary the take-off angle of the photoelectrons reaching the energy analyzer detector. The take-off angle was adjusted in 5º increments over a range of 20-70º. At shallow take-off angles, photoelectrons reaching the detector originate at shallower membrane depths. At higher take-off angles, photoelectrons reaching the detector originate from increased membrane surface depths. Therefore, when analyzing a membrane with a surface layer, we expect atomic concentrations when using higher take-off angles to more closely resemble bulk membrane atomic concentrations than lower take-off angles.

In order to confirm the heat treatment method did not adversely affect the internal conductivity of the polymer, 4-point conductivity measurements were conducted on untreated solution-cast Nafion films, as well as hydrophobic heat-treated ones. As shown in Figure 2.3, 4-point conductivity measurements were collected using 4 parallel gold strips (4 mm wide and 50 nm thick) sputter coated onto a PTFE fixture. A Nafion film was casted over the gold strips so that a smooth 90 um thick membrane covered all 4 gold strips. The solution-cast Nafion films were prepared by pouring a 3% Nafion / 48.5% H_2O / 48.5% isopropyl alcohol solution into the PTFE fixture and allowing it to evaporate at room temperature (21° C) for 48 hours. The resistivity measurements were collected on solution-cast films instead of conventional membranes in order to create an environment which more closely resembles CL morphology. During MEA preparation, the ionomer phase in the CL is heat treated in order to create ionically conductive pathways from the membrane to the catalyst reaction sites. The testing methodology outlined above enabled us to verify that the heat treatment process did not negatively affect the metal-ionomer interface.

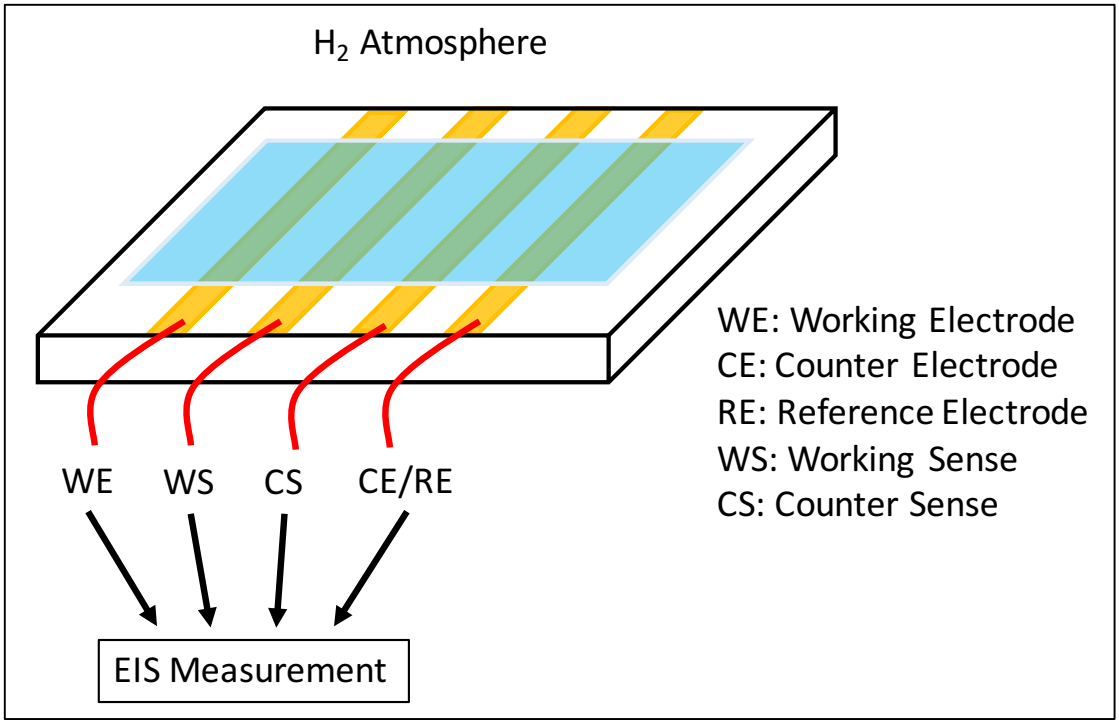

Figure 2.3. Four-point conductivity measurement apparatus.

Next, the membrane's surface was exposed to a saturated H_2 environment for 0.5 h. Then, electrochemical impedance spectroscopy (Gamry EIS 300) was conducted at 5 mV amplitude over a frequency range of 1 Hz to 100 kHz to measure the internal resistance. The solution-cast Nafion film was then heated to 140° C at a ramp rate of 1° C/min, held at 140° C for 1 h, and slowly cooled to room temperature. When heating the film to 140° C, the RH was maintained at 0%. Subsequently, the heat-treated film was rehydrated by covering the film with a thin layer of deionized water for 1 h. Finally, the membrane's surface was exposed to a saturated H_2 environment for 0.5 h and EIS was measured for the heat-treated film. From EIS, the resistance (R) of the membrane was determined by noting the value of the real impedance when the imaginary impedance is zero. Then, the resistivity (ρ) of the membranes were calculated as follows:

$$\rho = R\left(\frac{Cross\text{-}sectional\ Area\ of\ Current\ Flow}{Length\ of\ Current\ Flow}\right) \quad \textbf{[1]}$$

Finally, the heat treatment method was applied to the cathode catalyst layer of an actual H_2-Air PEMFC. During high current density operation, the cathode catalyst layer becomes flooded with water. By creating a hydrophobic polymer-gas interface in the cathode catalyst layer, we expect for water to more easily flow out of the catalyst layer and aid in delivery of reactant (O_2) to the Pt reaction site. Therefore, the MEA preparation method is crucial for creating a durable hydrophobic polymer-gas interface in the catalyst layer. The following steps outline a common MEA preparation technique. First, a catalyst ink (composed of a mixture of Pt-coated carbon powder, Nafion, water, and IPA) is applied to one side of a gas diffusion layer (GDL) and the ink is allowed sufficient time to dry. Then, two catalyst ink coated GDLs are hot pressed onto a polymer electrolyte membrane such that they form an 'electrode-membrane-electrode sandwich with the catalyst layer side of the GDL facing the membrane. Hot pressing is completed at a temperature above Nafion's glass transition temperature (T_g) (~110° C) to ensure that Nafion inside the catalyst layer will form an ionic pathway from the catalyst to the polymer electrolyte membrane. During hot pressing, water absorbed into the membrane will flash to steam and form a saturated steam environment in the gas channels of the catalyst layer. The steam is unable to escape because a PTFE gasket (used to prevent crushing the GDL) forms a barrier between hot press plate and membrane surface (the GDL is located inside the PTFE gasket). Upon cooling the MEA below T_g, steam in the gas channels of the catalyst layer is expected to result in a hydrophilic polymer-air interface. During operation, a hydrophilic interface would allow water to wet the surface of Nafion phase in the catalyst layer, creating an additional layer of water that oxygen would need to diffuse through in order to reach the catalyst reaction site, and, therefore, negatively impact mass transport of oxygen into the cathode active

catalyst layer. On the other hand, if the steam created during MEA hot pressing was allowed to escape, so that a dry environment was present at the polymer-air interface, then the Nafion phase in the catalyst layer could be made to have a durable hydrophobic polymer-air interface. A hydrophobic polymer-air interface in the catalyst layer is expected to lead to higher peak power and higher current densities. In order to provide a pathway for steam to escape during the MEA hot pressing procedure, a stainless steel 50.8-mm diameter, 1.575-mm thick, 100-micron average pore size porous disk was placed between the cathode GDL and heat press plate during MEA fabrication. Therefore, heat was thermally conducted through the porous metal disk to the cathode GDL during hot pressing, instead of heat being thermally conducted directly to the GDL. Subsequently, steam created during hot pressing was able to flow out radially through the porous stainless steel disk instead of being trapped inside the catalyst layer. Flowing a heated dry inert gas through the cathode would be expected to remove generated steam more efficiently by forced convection rather than allowing the steam to escape solely by natural convection, but the heated inert gas method would lead to a more complicated MEA setup. In this study, the porous disk hot pressing technique was explored to determine if sufficient steam could be removed from the CL solely by natural convection. A simpler hot pressing design is more likely to be adopted by industry for incorporation into a large-scale manufacturing process. The MEA hot pressing layouts for both the conventional and porous disk methods are shown in Figure 2.4.

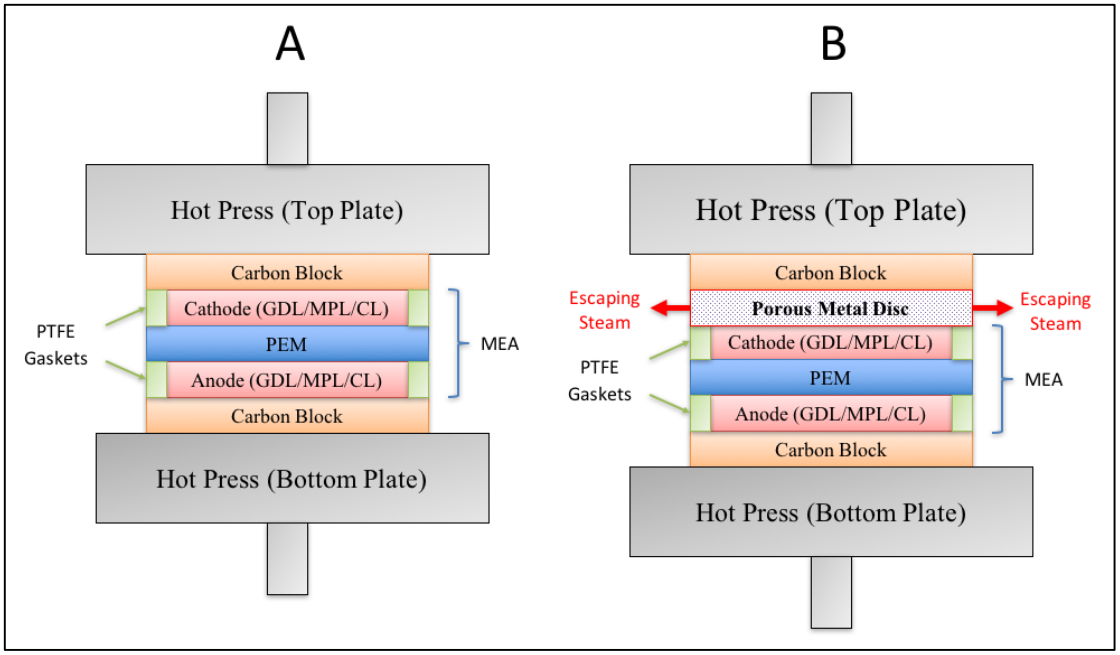

Figure 2.4. MEA hot pressing layouts for the (A) conventional and (B) porous disk methods.

For the PEMFC study, discharge performances at room temperature (~22°C) were collected for both a conventionally-prepared MEA and a MEA prepared using the porous disk heat treatment method outlined above. Fuel cells were tested at room temperature in order to operate the cells in a worst-case condition to ensure flooding occurs at the cathode during high current density operations. For operation at elevated fuel cell temperatures (>50°C), a hydrophobic ionomer-gas interface in the CL is expected to result in better performance over the baseline case anytime the cathode is subjected to flooding conditions. Sigracet GDL-25BC carbon GDLs were used for both the H_2 and air electrodes. A Pt/C/Nafion ink was prepared by mixing (sonicating) appropriate amounts of carbon-supported Pt catalyst, Nafion ionomer, isopropyl alcohol, and water. Then, the microporous layer side of the GDLs were coated with a Pt/C/Nafion layer (0.5 mg/cm^2 Pt geometric area, 0.14 mg/cm^2 Nafion ionomer) using an automatic ultrasonic sprayer. Carbon serpentine flow fields about 2.25 cm^2 (1.5 cm x 1.5 cm) delivered humidified H_2 at 5 psig and humidified air at atmospheric pressure to each electrode.

Both gases were humidified by bubbling the incoming gas through a bottle of room temperature deionized water. Hydrogen gas was delivered to the anode at a rate of approximately 660 mL/min using a recirculation pump, while air was delivered to the cathode at a rate of approximately 350 mL/min using a flow-through setup. Nafion 212 (~51 μm thick) served as the polymer electrolyte membrane for all MEAs and electrical current was collected from the edges of the electrodes. A start-up procedure was used to ensure proper membrane hydration prior to collecting discharge performances. The start-up procedure included operating the PEMFCs at 0.2V until 0.4 A/cm^2 was achieved, then holding the discharge current steady at 0.4 A/cm^2 for 1 h.[31] Discharge polarization curves were collected in constant voltage staircase mode from open circuit voltage (OCV) to 0.2 V in increments of 50 mV. Multiple polarization curves were collected to ensure adequate membrane hydration and repeatable results. The start-up procedure proved to be adequate in fully hydrating the membrane in order to provide consistent results. EIS was completed on each fuel cell at 5 mV amplitude over a frequency range of 1 Hz to 100 kHz in order to measure the internal cell resistance.

2.4 Results and Discussion

After exposing several membranes to various heat treatment conditions, multiple surface characterization techniques were used to validate that the exposure conditions created a durable hydrophobic or hydrophilic surface. To begin, contact angle measurements were collected by placing a water droplet on top of a flat membrane. Contact angle measurements for Nafion 115 as-received, Nafion 212 as-received, hydrophobic-treated Nafion 212, hydrophobic-treated Nafion 212 boiled for 1 h, and hydrophilic-treated Nafion 212 are shown in Figure 2.5. The contact angle measurements for the as-received membranes are shown for comparison purposes.

Comparison of the hydrophobic-treated and hydrophilic-treated membranes enables us to determine whether or not the membrane's surface can be engineered to be rich in Teflon or ionic groups, respectively. Comparison of the hydrophobic-treated and hydrophobic-treated boiled for 1 h determines whether the hydrophobic surface structure is durable. Boiling for 1 h is a harsher condition than a membrane is expected to encounter during operation in a PEMFC.

The initial contact angles at 0 min indicate a high contact angle for the as-received Nafion 115, as-received Nafion 212, the hydrophobic-treated Nafion 212, and hydrophobic-treated Nafion 212 boiled for 1 h membranes. The contact angles at 0 min for these membranes were measured to be ~97 degrees. As expected, the hydrophilic-treated Nafion 212 membrane had a lower contact angle at 0 min of ~67 degrees. Further analysis of the contact angle measurements made every 5 min over the course of 20 min, we observe that the hydrophobic-treated Nafion 212 membrane absorbs greater than 90% of the water droplet by 20 min. The hydrophilic-treated membrane absorbs greater than 90% of the water droplet more quickly, in approximately 15 min. Additionally, after the water droplet had been fully absorbed by each membrane, similar contact angles were achieved when placing a second droplet at the same location as the first droplet. These contact angle results indicate that the hydrophilic-treated membrane contains more surface ionic groups than the hydrophobic-treated membrane. The increased amount of surface ionic groups enables the hydrophilic-treated membrane to absorb the water droplet more quickly into the bulk of the membrane.

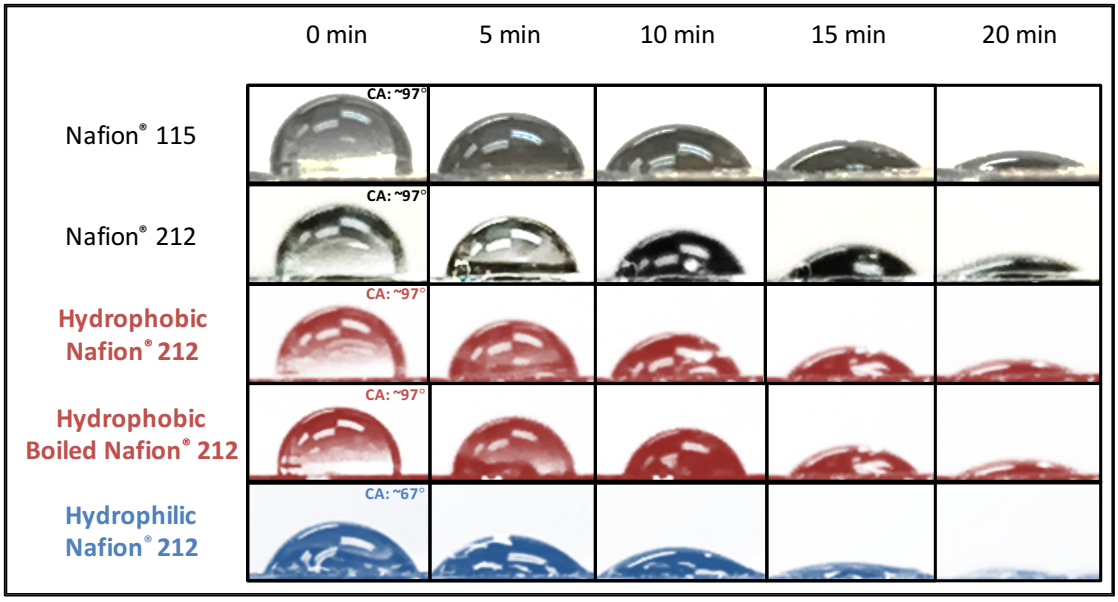

Figure 2.5. Contact angle time lapse measurements.

Next, the AFM was operated in tapping mode to obtain phase contrast images of the treated and untreated membranes. Phase contrast will be able to differentiate between harder Teflon domains and softer ionic domains. Figure 2.6 shows the phase contrast measurements obtained for the Nafion 212 as-received, hydrophilic-treated, hydrophobic-treated, and boiled hydrophobic-treated membranes. The Nafion 212 as-received membranes shows a wide distribution of phase contrast values. The intensity versus phase contrast value graph for Nafion 212 as-received shows two peaks. The lower phase contrast peak (red color / darker greyscale) correlates to Teflon domains. The higher phase contrast peak correlates to ionic domains (blue and green color / lighter greyscale). The hydrophilic-treated, hydrophobic-treated, and hydrophobic boiled membranes all show a single peak in the intensity versus phase contrast value graph. The hydrophilic-treated membrane contains mostly high phase contrast value, colored in blue and green (lighter greyscale). The hydrophobic-treated membrane contains lower phase contrast values, colored in red (darker greyscale). We observe that the boiled hydrophobic-treated membrane is very similar in phase to the hydrophobic-treated membrane. We also

observe the intensity versus phase contrast value graph for the boiled hydrophobic-treated membrane shows a sharper and slightly lower phase contrast value. We do not think the boiling step will permanently change the membrane's surface structure since 100ºC is not above T_g. The quantitative resolution of phase contrast may be causing this perceived difference between hydrophobic and boiled hydrophobic, but further analysis is needed to verify.

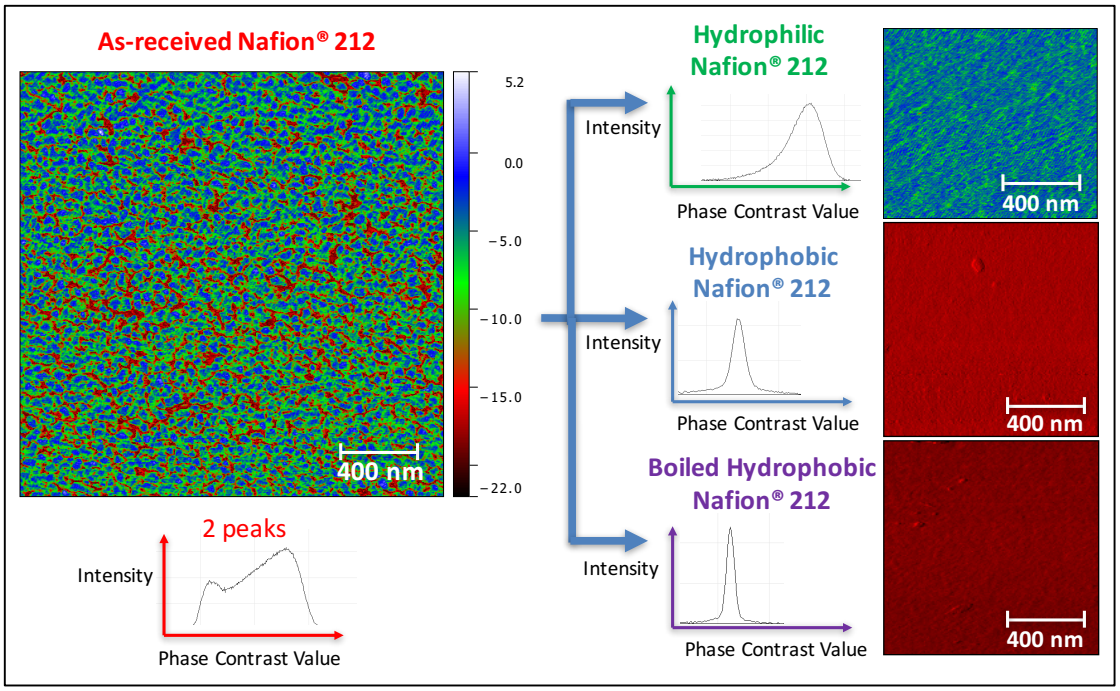

Figure 2.6. AFM 2D phase contrast of Nafion 212 as received, hydrophilic-treated, hydrophobic-treated, and boiled hydrophobic-treated membranes. The lower phase contrast peak (red color / darker greyscale) correlates to Teflon domains. The higher phase contrast peak correlates to ionic domains (blue and green color / lighter greyscale).

Next, XRD was used to probe the surface of the as-received and heat treated membranes. Figure 2.7 shows the wide angle XRD results using an incident beam angle of 3º. The wide angle XRD spectrum for each membrane type contains both a low angle ~1.5-3.0º and wide angle ~17.5º peak. In order to qualitatively compare each membrane, a peak intensity ratio was calculated by dividing the maximum counts per second (CPS) for the low angle peak by the maximum CPS of the wide angle peak. In Figure 2.7A, we observe a low angle to broad

amorphous peak intensity ratio of ~2 for the as-received Nafion 212. A low angle to broad amorphous peak intensity ratio of ~2.75 is observed in Figure 2.7B for as-received Nafion 115. Nafion 115 has a hydrophobic Teflon skin due to the thermal extrusion process. We will use this fact to analyze the next set of XRD scans for the hydrophilic and hydrophobic-treated membranes. As shown in Figure 2.7C and Figure 2.7D, the peak intensity ratio of the hydrophilic-treated membrane resembles the as-received Nafion 212 membrane. The hydrophobic-treated membrane resembles the as-received Nafion 115 membrane. These XRD results confirm our hypothesis that specific heat treatment conditions can create a hydrophobic or hydrophilic skin on a biphasic membrane.

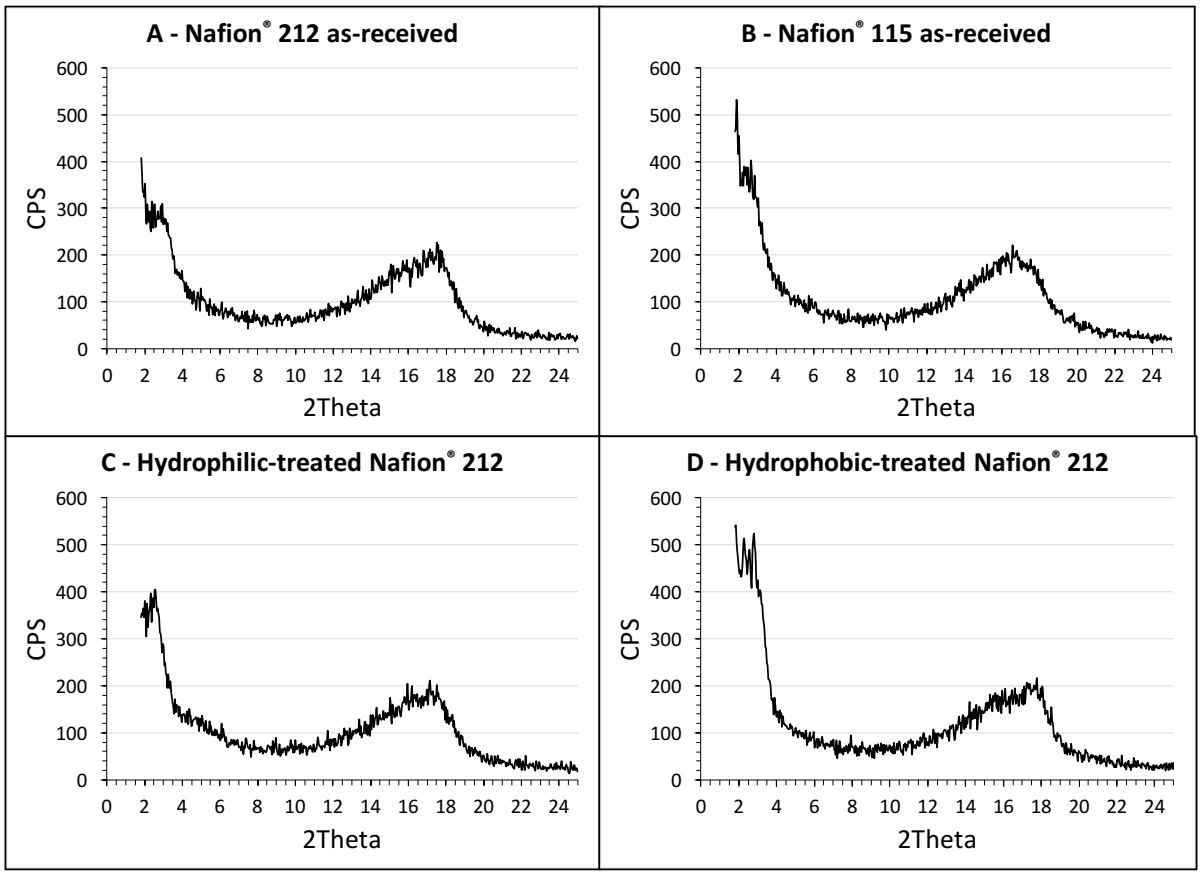

Figure 2.7. Grazing incidence XRD with incident beam set at 3.0 degrees for (A) Nafion 212 as-received, (B) Nafion 115 as-received, (C) Hydrophilic-treated Nafion 212, and (D) Hydrophobic-treated Nafion 212 membranes.

Next, XRD scans were collected in the Bragg-Brentano theta-2theta configuration in order to conduct deconvolution of the broad amorphous peak centered at about 8-22º and the sharp crystalline peak centered at about 17.5º. Since the Bragg-Brentano theta-2theta configuration is representative of the entire sample, it only allows us to estimate percent crystallinity of the membrane's bulk. Even though it is not a surface characterization technique, percent crystallinity calculations using the Bragg-Brentano theta-2theta configuration reveals major differences between the as-received and heat-treated membranes. Figure 2.8 shows an example of how deconvolution is completed on the original XRD scan. Table 2.2 provides the results of the crystallinity calculation using the deconvolution method for the as-received and

heat-treated membranes. As expected, the hydrophobic-treatment resulted in a higher percent crystallinity than the hydrophilic-treatment due to the larger fraction of crystalline Teflon domains near the membrane's surface. The higher fraction of amorphous ionic domains near the hydrophilic-treated membrane's surface results in a lower measured percent crystallinity.

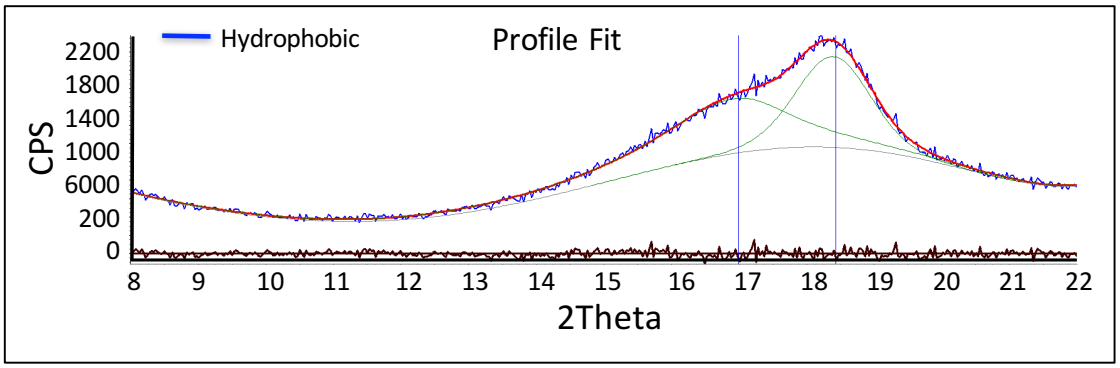

Figure 2.8. Deconvolution of XRD profile for hydrophobic-treated Nafion 212.

Table 2.2. XRD deconvolution to calculate percent crystallinity.

Membrane Type	Percent Crystallinity Range
Nafion 115 as-received	26.8%
Nafion 212 as-received	24.2%
Hydrophobic-treated Nafion 212	36.7%
Hydrophilic-treated Nafion 212	19.1%

Next, angle-resolved XPS was used to measure the atomic concentration of sulfur and carbon at the membrane's surface. The take-off angle was varied from 20º to 70º in 5º increments. Figure 2.9 shows the sulfur to carbon atomic concentration ratio for Nafion 212 as-received, Nafion 115 as-received, hydrophobic-treated Nafion 212, boiled hydrophobic-treated Nafion 212, and hydrophilic-treated Nafion 212. The theoretical sulfur to carbon atomic concentration ratio of 5% for Nafion 212 is included on the graph as a dotted grey line. As expected, the thermally-extruded Nafion 115 as-received membrane has a lower sulfur to carbon atomic concentration ratio (~3.5%) at low take-off angles. As we penetrated deeper into the

membrane at higher take-off angles, the Nafion 115 as-received membrane's sulfur to carbon atomic concentration ratio increases up towards the 5% theoretical bulk sulfur to carbon atomic concentration ratio. The hydrophilic-treated Nafion 212 membrane's sulfur to carbon atomic concentration ratio is about 8% at low take-off angles and trends down to the 5% theoretical bulk at higher take-off angles. The hydrophobic-treated Nafion 212 membrane's sulfur to carbon atomic concentration ratio is about 2% at low take-off angles and trends upwards to the 5% theoretical bulk at higher take-off angles. Finally, the boiled hydrophobic-treated Nafion 212 membrane's sulfur to carbon atomic concentration ratio mirrors the hydrophobic-treated membrane. These XPS measurements support the claim that a membrane's surface can be heat treated to create a durable hydrophobic surface.

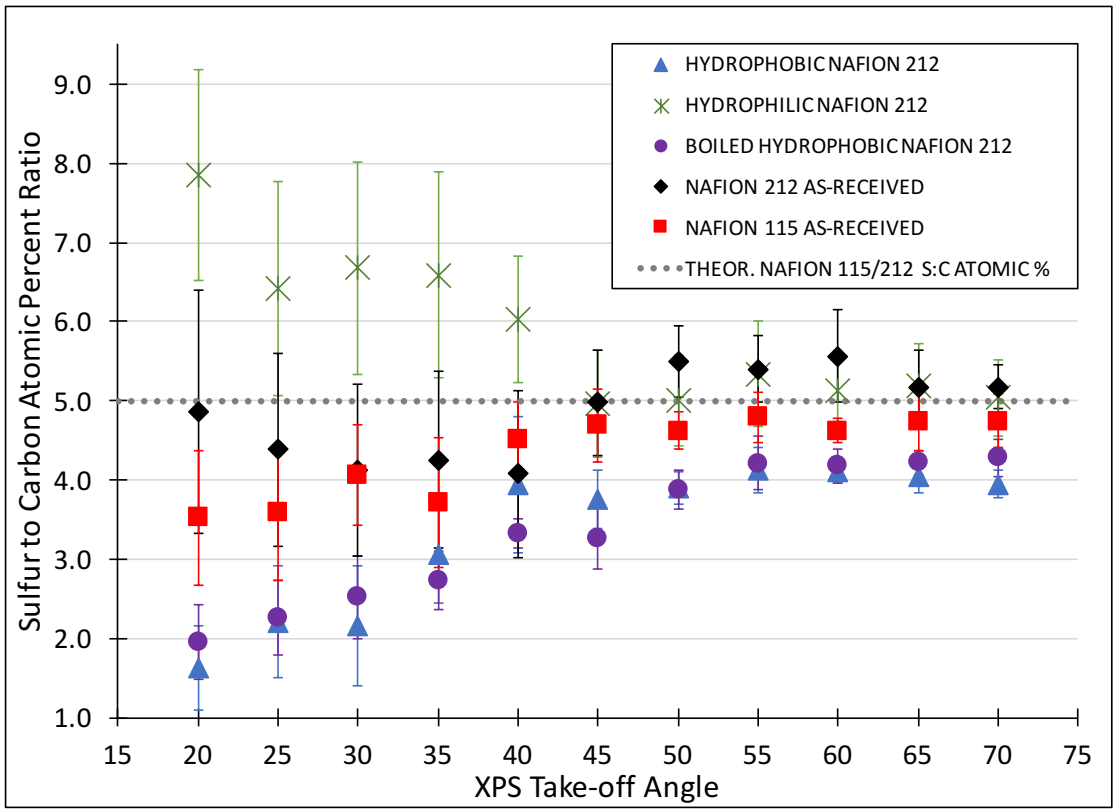

Figure 2.9. Angle-resolved XPS for as-received and heat-treated membranes.

In order to verify that the heat treatment conditions did not negatively affect the membrane's internal conductivity, 4-point conductivity measurements were collected. The resistivity of a solution-cast membrane (95.7 $\pm$ 7.5 ohm-cm) mirrored the resistivity of a heat-treated film (92.4 $\pm$ 4.0 ohm-cm). Therefore, we don't expect the hydrophobic heat treatment process to have an effect on the polymer's internal conductivity and the internal surface area of the membrane. These results indicated that the heat treatment process would not affect the bulk and internal interfacial conductivity of the polymer phase in the fuel cell catalyst layer.

Finally, discharge polarization curves were collected for both a conventionally-prepared MEA and a MEA prepared under hydrophobic heat treatment conditions using the porous metal disk. As shown in Figure 2.10, the discharge polarization curve using the porous metal disk

MEA method shows improved performance at high current densities when compared to the conventional MEA. Figure 2.10 overlays the power density curves for both cases, showing more than a 33% increase in peak power density for the porous metal disk MEA method. The internal cell resistance for each fuel cell was measured using EIS to calculate the iR-corrected polarization and power density curves (included in Figure 2.10). Due to testing the fuel cells at room temperature, the polarization curves are substandard relative to state-of-the-art fuel cell performance. As previously stated, testing was completed at room temperature in order to ensure the cathodes are subjected to flooding conditions during high current density operations. Performance at higher temperatures will be included in future studies. The increase in performance at high current density for the porous disk method is suspected to be due to improved mass transport effect, an increase in the effective proton conductivity in the cathode, or a combination of both phenomena.[32, 33]

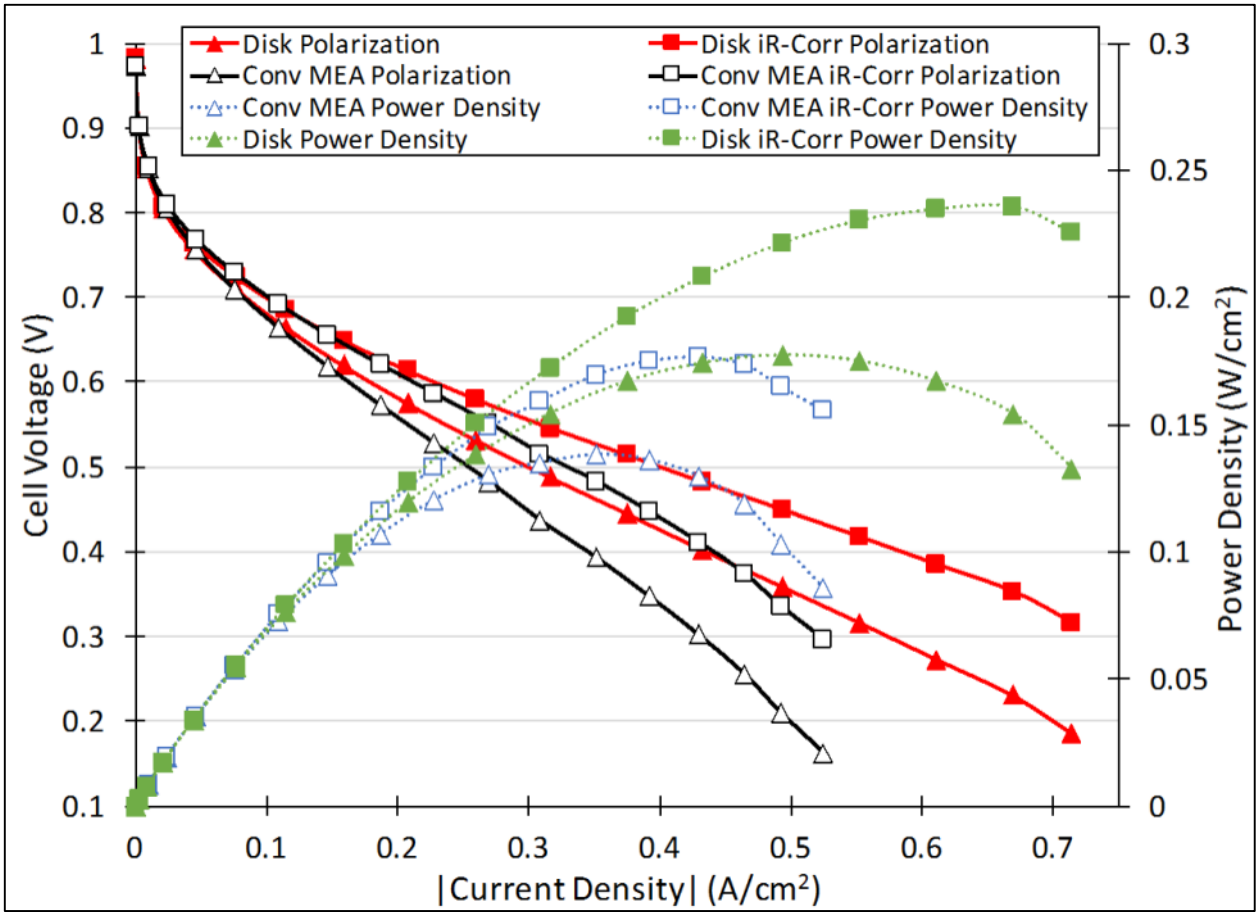

Figure 2.10. H_2-Air PEMFC discharge polarization and power density curves for conventionally-prepared MEA and newly-designed MEA using porous disk.

2.5 Summary

In summary, we used a new heat treatment process to create a durable hydrophobic surface for a biphasic perfluorosulfonic acid membrane. Multiple surface characterization techniques were used to verify the membrane's surface structure prior to and after heat treatment. Contact angle, AFM, XRD, and XPS measurements of the membrane's surface confirm our hypothesis that specific heat treatment conditions can create a durable hydrophobic or hydrophilic surface. Four-point conductivity measurements verified the membrane's bulk and internal interfacial conductivity was not negatively impacted by the hydrophobic heat treatment process.

Finally, the new heat treatment method was incorporated into the cathode catalyst layer by adding a porous metal disk to the MEA fabrication process to allow steam to escape during heat pressing. Discharge performance curves for a H_2-Air PEMFC using the newly designed catalyst layer showed remarkable performance compared to the conventionally-prepared MEA. This increase in fuel cell performance is credited to improved mass transport effect, an increase in the effective proton conductivity in the cathode, or a combination of both manifestations. The improved performance for the new MEA process is evident by the extension of the ohmic region into high overpotentials (i.e. more linear polarization curve). The superior performance at high current densities enabled the newly-designed PEMFC to achieve more than 33% higher peak power density.

We expect that the hydrophobic polymer-gas interface will enable oxygen to more easily diffuse to the catalyst reaction site and aid in proper water removal from the CL. Since the CL oxygen flow channel is approximately 20-100 nm in diameter, we don't expect the polymer-gas interface to be completely void of water. However, we do expect higher channel wall surface area for oxygen transport directly into the hydrophobic membrane-gas interface. Our proposed hydrophobic channel wall structure and contact with water is shown in Figure 2.11B. This is compared to a water-flooded channel in Figure 2.11A and a hydrophilic membrane-gas interface in Figure 2.11B.

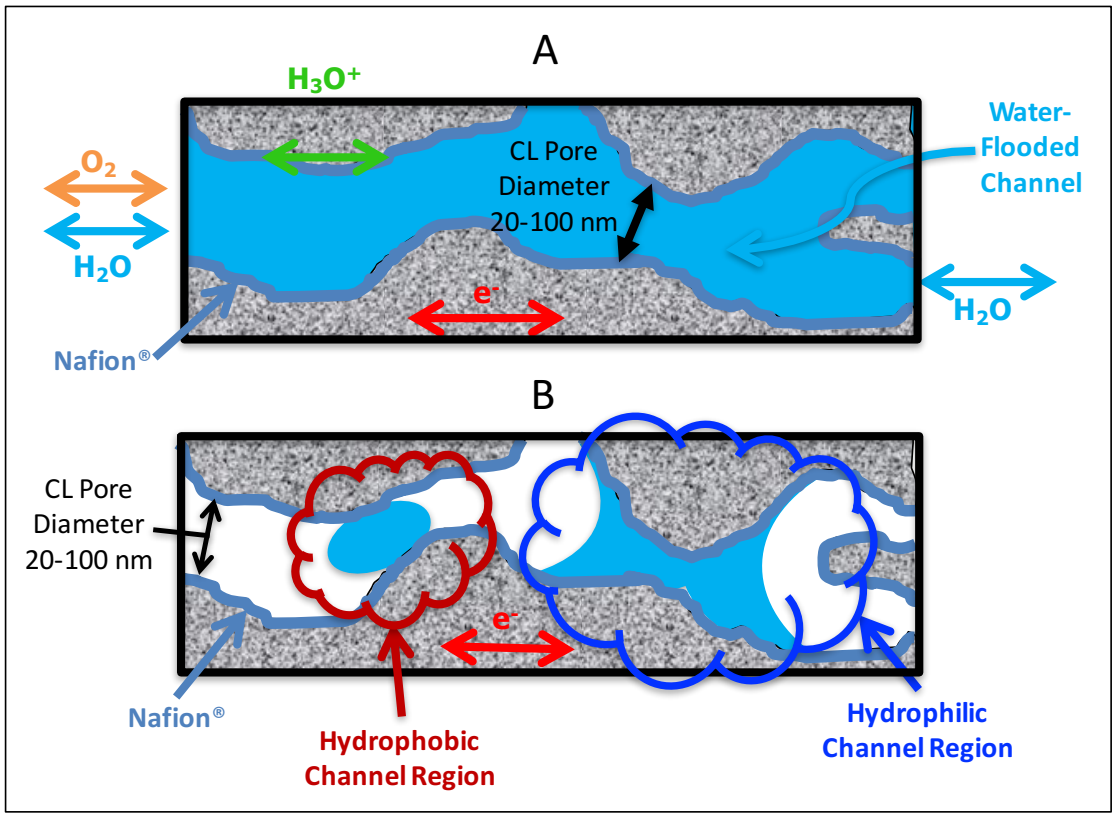

Figure 2.11. Cross-sectional side view of (A) water-flooded CL channel and (B) engineered CL polymer surface.

2.6 Acknowledgments

The authors wish to acknowledge the financial support from the University of Kansas (KU) Madison and Lila Self Fellowship. Supplies and imaging charges for this work were supported by the National Science Foundation through grant numbers EFRI-1038234 and CBET-1518755. The authors would like to thank Dr. Prem Thapa at the University of Kansas for his support and expertise in using the XPS. The authors would also like to thank Applied Porous Technologies, Inc. for providing the porous stainless steel disk used for MEA fabrication.

2.7 References for Chapter 2

1. K. Hongsirikarn, X. Mo, J. G. Goodwin and S. Creager, *Journal of Power Sources*, **196**, 3060 (2011).

2. T. V. Nguyen, M. V. Nguyen, K. J. Nordheden and W. He, *Journal of The Electrochemical Society*, **154**, A1073 (2007).

3. A. Z. Weber, M. M. Mench, J. P. Meyers, P. N. Ross, J. T. Gostick and Q. Liu, *Journal of Applied Electrochemistry*, **41**, 1137 (2011).

4. C. Ponce de León, A. Frías-Ferrer, J. González-García, D. A. Szánto and F. C. Walsh, *Journal of Power Sources*, **160**, 716 (2006).

5. M. Skyllas-Kazacos, M. H. Chakrabarti, S. A. Hajimolana, F. S. Mjalli and M. Saleem, *Journal of The Electrochemical Society*, **158**, R55 (2011).

6. T. V. Nguyen and R. E. White, *Journal of The Electrochemical Society*, **140**, 2178 (1993).

7. M. L. Di Vona, E. Sgreccia, M. Tamilvanan, M. Khadhraoui, C. Chassigneux and P. Knauth, *Journal of Membrane Science*, **354**, 134 (2010).

8. Y. Iwai, A. Hiroki and M. Tamada, *Journal of Membrane Science*, **369**, 397 (2011).

9. J. B. Ballengee and P. N. Pintauro, *Macromolecules*, **44**, 7307 (2011).

10. R. S. McLean, M. Doyle and B. B. Sauer, *Macromolecules*, **33**, 6541 (2000).

11. A. R. Kalidindi, R. Taspinar, S. Litster and E. C. Kumbur, *International Journal of Hydrogen Energy*, **38**, 9297 (2013).

12. R. Schweiss, M. Steeb and P. M. Wilde, *Fuel Cells*, **10**, 1176 (2010).

13. Z. Qi and A. Kaufman, *Journal of Power Sources*, **109**, 38 (2002).

14. L. R. Jordan, A. K. Shukla, T. Behrsing, N. R. Avery, B. C. Muddle and M. Forsyth, *Journal of Power Sources*, **86**, 250 (2000).

15. R. Friedmann and T. V. Nguyen, *Journal of The Electrochemical Society*, **157**, B260 (2010).

16. T. V. Nguyen, M. V. Nguyen, G. Lin, N. Rao, X. Xie and D. M. Zhu, *Electrochemical and Solid-State Letters*, **9**, A88 (2006).

17. R. P. Dowd, T. V. Nguyen, D. S. Moore, P. N. Pintauro and J. W. Park, *ECS Transactions*, **58**, 607 (2013).

18. Y. Wang, R. Song, Y. Li and J. Shen, *Surface Science*, **530**, 136 (2003).

19. G. D. Smith and D. Bedrov, *Journal of Polymer Science Part B: Polymer Physics*, **45**, 627 (2007).

20. O. Colak, A. Acar and E. Ergenekon, *Journal of Testing and Evaluation*, **42**, 1 (2014).

21. S. J. Osborn, M. K. Hassan, G. M. Divoux, D. W. Rhoades, K. A. Mauritz and R. B. Moore, *Macromolecules*, **40**, 3886 (2007).

22. S. de Almeida and Y. Kawano, *An International Forum for Thermal Studies*, **58**, 569 (1999).

23. S. Goswami, S. Klaus and J. Benziger, *Langmuir : the ACS journal of surfaces and colloids*, **24**, 8627 (2008).

24. D. K. Paul and K. Karan, *The Journal of Physical Chemistry C*, **118**, 1828 (2014).

25. D. K. Paul, K. Karan, A. Docoslis, J. B. Giorgi and J. Pearce, *Macromolecules*, **46**, 3461 (2013).

26. A. Z. Weber and A. Kusoglu, *Journal of Materials Chemistry A*, **2**, 17207 (2014).

27. M. Eguchi, K. Baba, T. Onuma, K. Yoshida, K. Iwasawa, Y. Kobayashi, K. Uno, K. Komatsu, M. Kobori, M. Nishitani-Gamo and T. Ando, *Polymers*, **4**, 1645 (2012).

28. F. I. Allen, L. R. Comolli, A. Kusoglu, M. A. Modestino, A. M. Minor and A. Z. Weber, *ACS Macro Letters*, **4**, 1 (2015).

29. P. Dudenas, A. Kusoglu, A. Hexemer and A. Weber, *ECS Transactions*, **75**, 643 (2016).

30. T. N. Blanton and R. Koestner, *JCPDS-International Centre for Diffraction Data*, 128 (2015).

31. G. Lin and T. V. Nguyen, *Journal of The Electrochemical Society*, **152**, A1942 (2005).

32. K. C. Neyerlin, W. Gu, J. Jorne and H. A. Gasteiger, *Journal of The Electrochemical Society*, **154**, B631 (2007).

33. J. P. Owejan, J. E. Owejan and W. Gu, *Journal of The Electrochemical Society*, **160**, F824 (2013).

CHAPTER 3: Controlling the Ionic Polymer/Gas Interfacial Properties of a PEM Fuel Cell Catalyst Layer during Membrane Electrode Assembly Fabrication

3.1 Abstract

During high current density operation, water production in the cathode catalyst layer of a PEM fuel cell can negatively impact performance by lowering mass transport of oxygen into the cathode. In this chapter, a novel heat treatment process for controlling the ionic polymer/gas interfacial properties of the fuel cell catalyst layer is incorporated into the fabrication process of the membrane electrode assembly (MEA). First, XPS was used to characterize the catalyst layer ionomer-gas interface to verify specific heat treatment conditions lead to a hydrophobic or hydrophilic ionomer interface. XPS characterization inside the gas pores of the catalyst layer was completed after scraping off successive portions of the catalyst layer. Next, the MEA fabrication procedure was modified to ensure the catalyst layer was subjected to suitable heat treatment exposure conditions in order to create an optimal hydrophobic ionomer-gas interface inside the cathode catalyst layer. Finally, extensive fuel cell tests were completed on the new MEAs under different operating temperatures, flow field types, and air humidification conditions. The novel MEAs led to more than a 47% increase in peak power when operating at 70°C with interdigitated flow fields and dry air. When the MEAs were tested at 25°C and with humidified air, peak power increased by more than 133% over the conventional MEA process.

3.2 Introduction

The cathode catalyst layer of a polymer electrolyte membrane fuel cell (PEMFC) exhibits high water saturation levels (i.e. flooding conditions) during high current density operations. Water

flooding of the cathode results in reduced fuel cell performance due to lower mass transport rate of oxygen to the catalyst reaction site. Various advances have been developed to overcome water management issues related to PEMFCs. A few of these discoveries include the development of the interdigitated flow field,[1] integration of hydrophobic PTFE nanoparticles into the catalyst layer,[2, 3] and gas diffusion layer fabrication from various types of non-wetting materials.[4, 5] Each of these advances led to improved mass transport performance during high current density operations. More recently, new analytical techniques such as the x-ray photoelectron spectroscopy (XPS) and atomic force microscopy (AFM) have enabled researchers to gain a better understanding of the structure and properties of the PEMFC catalyst layer.[6-12] These high-resolution characterization techniques provide scientists additional insight for designing novel catalyst layers to efficiently deliver reactants to and remove products from the electrodes.

The PEMFC catalyst layer is comprised of three phases: an electrically conductive phase (electron transport), an ionically conductive phase (ionic transport), and void spaces to allow for gas/liquid flow. Typically, a catalyst ink is prepared by mixing carbon powder decorated with catalyst nanoparticles (i.e. Pt), Nafion ionomer, isopropyl alcohol, and water. [3, 13-15] After thorough mixing of the catalyst ink to ensure a homogenous mixture, the catalyst ink is sprayed onto the microporous layer side of a gas diffusion layer (i.e. SGL25BC). The gas diffusion electrode is then dried to allow the water and isopropyl alcohol to evaporate, thus leaving behind the catalyst layer. Next, the membrane electrode assembly (MEA) is prepared by hot pressing a proton exchange membrane between two gas diffusion electrodes such that both catalyst layers face the membrane. The MEA is then assembled between two flow fields for delivering the reactants to the cathode and anode.

During the traditional MEA fabrication process, electrodes are hot pressed onto each side

of the PEM such that the catalyst layer side of the electrodes face the membrane. Prior to hot pressing, gaskets are placed around each electrode to ensure the electrodes are not crushed. Hot pressing is completed at 135°C and 500 kPa for 5 min.[16] During this process, absorbed water inside the PEM will flash to steam. The steam will diffuse into and saturate the gas pores of the catalyst layer, microporous layer, and gas diffusion layer. The gaskets surrounding each electrode prevents the steam from escaping. Since hot pressing is completed above Nafion's glass transition temperature, the catalyst layer ionomer will bond to the membrane and create a MEA. During the hot-pressing technique, ionic pathways are established between the catalyst reaction site and the membrane which allows ionic conduction from the anode to the cathode during fuel cell operation.

At the onset of MEA hot pressing, a saturated steam environment inside the gas pores of the catalyst layer will enable the sulfonate ionic groups of the ionomer phase to relax and, therefore, allow reorientation. This reorientation allows the membrane to bond to the catalyst layer ionomer phase. However, a saturated steam environment during cooling of the MEA below glass transition temperature will lead to an increased amount of sulfonate ionic groups oriented towards the ionomer/gas interface (inside the gas pores of the catalyst layer) due to their affinity for water. Whereas, a dry gas phase environment during cooling will result in a lower number of sulfonate ionic groups oriented towards the ionomer-gas interface. The relative amount of sulfonate ionic groups oriented towards the ionomer/gas interface determines the ionomer's relative hydrophilicity/hydrophobicity. Although the conventional MEA fabrication technique enables the ionomer inside the catalyst layer to form ionic pathways between the catalyst and the membrane, the saturated steam environment inside the gas pores of the catalyst layer during cooling results in a nonhomogeneous ionomer-gas interface (i.e. a mix of hydrophobic and

hydrophilic ionomer/gas interfaces). Our group envisioned a more ideal and ordered cathode catalyst layer structure that would enable improved two phase flow (i.e. the gas phase occupies the annular region adjacent to the ionomer/gas interface and water occupies the region along the center of the gas pores). In this inverted annular or liquid-ring flow configuration,[17] oxygen gas transported into the catalyst layer has direct access to the ionomer layer without having to first dissolve in the liquid water phase and diffuse through this barrier in order to reach the ionomer phase. We expected a hydrophobic ionomer/gas interface inside the gas pores of the catalyst layer would lead to higher fuel cell performance during high current density operations due to improved mass transport of oxygen into and water removal from the cathode catalyst layer.

Previously, our research group demonstrated this interfacial phenomenon with PFSA membranes.[16] Specific heat treatment conditions led to the formation of either a hydrophobic or hydrophilic membrane surface. This heat treatment technique was then incorporated into the MEA fabrication procedure which resulted in more than a 33% improvement in fuel cell performance.[16] The new MEA fabrication procedure in the previous manuscript relied on natural convection to remove the steam from the ionomer-gas interface inside the catalyst layer prior to cooling. In this study, a more thorough analysis is completed when applying the heat treatment method to the fuel cell catalyst layer. The catalyst layer's surface is characterized with XPS before and after heat treatment. XPS is also used to characterize the ionomer-gas interface inside the gas pores of the catalyst layer before and after heat treatment. Additionally, a new MEA fabrication technique is explored by using forced convection to remove steam from the catalyst layer during hot pressing. Various forced convection duration times are investigated in order to construct a cathode catalyst layer for optimal two-phase flow. We hypothesize the saturated steam condition at the onset of the MEA fabrication process is required in order to allow the

ionomer phase adequate time to relax. Forced convection (i.e. purging with dry heated inert gas) during the final minutes of the MEA fabrication process is expected to remove the saturated steam environment and create a more homogenous hydrophobic ionomer-gas interface. Furthermore, in-depth fuel cell testing is completed to compare the two new MEA fabrication techniques (natural convection and forced convection) with the conventional MEA using various types of flow fields, humidification conditions, and operating temperatures.

3.3 Experimental

In order to determine if the ionomer/gas interface inside the gas pores of the catalyst layer could be modified to be hydrophobic or hydrophilic, electrodes were exposed to various heat treatment conditions. Sigracet® GDL-25BC carbon electrodes were selected for this purpose. The microporous layer side (MPL) of the gas diffusion electrodes (GDEs) were coated with a Pt/C/Nafion® layer (0.5 mg/cm^2 Pt geometric area, 0.14 mg/cm^2 Nafion® ionomer) by TVN Systems Inc. For the hydrophobic case, the GDL was first exposed to a saturated steam environment at a temperature above Nafion's glass transition temperature (GTT). Then, the saturated steam environment was replaced with heated dry argon gas while maintaining the temperature above Nafion's GTT. Finally, the GDL was allowed to slowly cool to room temperature while maintaining the dry argon environment. For the hydrophilic case, the GDL was first exposed to a saturated steam environment similar to the hydrophobic treated case. After a sufficient holding time, the saturated steam environment was maintained as the GDL was slowly cooled to room temperature. More specific details on vessel construction and heat treatment conditions can be found in our group's previously published manuscript.[16]

A Physical Electronics (PHI) VersaProbe II XPS (Washington University in St. Louis)

and VersaProbe III XPS (University of Kansas) were used to capture high resolution scans in order to measure the sulfur and fluorine atomic percentages near the catalyst layer's outermost surface. Previously, when analyzing the heat treatment effect on membranes, the sulfur and carbon atomic percentages near the membrane's surface were measured in order to calculate the sulfur to carbon ratio. The sulfur to carbon atomic percent ratio was used to determine the relative hydrophobicity/hydrophilicity of the membrane's surface since a higher amount of sulfonate ionic groups leads to a more hydrophilic skin. If we tried to collect the carbon high resolution scan for the surface of the catalyst layer ionomer (CL coated on the microporous layer side of a carbon GDL), then photoelectrons would be inadvertently collected from the carbon GDL backbone. Therefore, for this XPS study, high resolution XPS scans are collected for sulfur and fluorine. Subsequently, the sulfur to fluorine atomic ratio is calculated and used to determine the relative amount of hydrophobicity/hydrophilicity of the Nafion ionomer thin film at the catalyst layer's surface.

Next, the catalyst layer side of the heat treated GDEs were lightly scraped with a razor blade to reveal the Nafion ionomer inside the gas pores of the catalyst layer. If XPS depth profiling (i.e. sputtering using argon ion beam etching) was completed on the surface of the catalyst layer for the heat treated GDE samples, ion beam etching would preferentially remove the ionomer thin film present in the catalyst layer vice having a uniform removal process.[18] It is well-known that even short sputtering times (<2 min) can cause rapid degradation to polymers.[19] Therefore, the scraping process was implemented instead of ion beam etching since etching would lead to a skewed catalyst layer composition. High resolution scans were collected with the XPS to measure the sulfur and fluorine atomic percentages after each successive removal of a fraction of the catalyst layer. A total of three successive scrapes were used to remove a portion of

the catalyst layer in order to be able to characterize the ionomer-gas interface inside the gas pores of the catalyst layer. Figure 3.1 provides a simplified sketch of how scraping the uppermost surface of the catalyst layer leads to exposure of the ionomer thin film located inside the gas pores of the catalyst layer. Various depth measurement techniques (i.e. profilometer, AFM) could be used to measure the amount of catalyst layer removed during each scrape. After scraping the catalyst layer, XPS was used to characterize the ionomer-gas interface. The ability to characterize the surface and internal ionomer structure for the heat-treated electrodes was important in order to validate that the exposure conditions create a hydrophobic or hydrophilic ionomer-gas interface inside the catalyst layer.

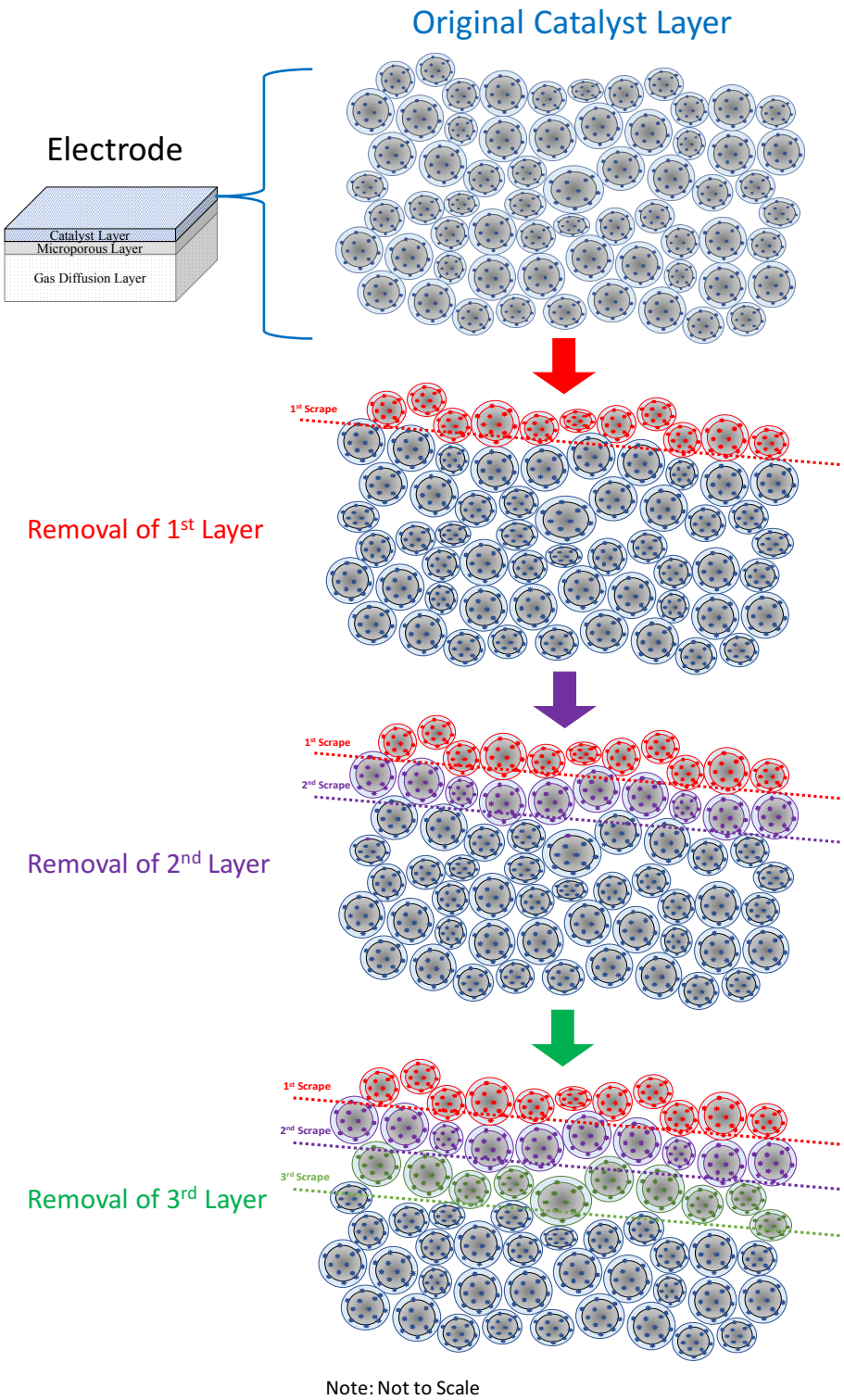

Figure 3.1. Layer by layer removal process of catalyst layer for XPS analysis.

A major purpose of this manuscript was to incorporate the catalyst layer heat treatment exposure conditions into the membrane electrode assembly (MEA) process. In our previous manuscript, we showed how incorporating a porous metal disk into the MEA fabrication technique leads to improved mass transport performance during high current density operations.[16] Fuel cells were tested at room temperature and with humidified air flowing to the cathode in order to measure the performance improvement using the new MEA when flooding conditions were present in the cathode. In this chapter, we explored more realistic operating conditions in order to maximize fuel cell performance. Therefore, higher temperatures, additional flow field types, and air humidification levels were investigated.

Traditionally, the MEA is made by hot pressing two electrodes onto each side of a polymer electrolyte membrane (PEM) such that the catalyst layer side of the electrodes face the membrane. The traditional MEA hot-pressing setup is shown in Figure 3.2A. For this MEA technique, gaskets are placed around each electrode to ensure the electrodes are not crushed during the hot-pressing procedure. The MEA is hot-pressed at 135°C and 500 kPa for 5 min.[20] In this chapter, we explored two new hot pressing techniques to apply the heat treatment method to the cathode catalyst layer during MEA fabrication. Both new methods intended to recreate the conditions necessary to create a hydrophobic ionomer-gas interface inside the gas pores of the catalyst layer. A hydrophobic ionomer-gas interface in the cathode catalyst layer of a H_2-air PEMFC is expected to result in improved gas and liquid transport into and out of the catalyst layer, respectively.

First, natural convection was explored by inserting a porous metal disk (stainless steel 2" diameter, 0.062" thick, 100-micron average pore size) above the cathode. For the natural convection setup, shown in Figure 3.2B, a porous metal disk was placed above the cathode to

allow a pathway for steam to escape. During hot pressing, moisture in the PEM flashes to steam and creates a saturated steam environment inside the gas pores of the catalyst layer. By inserting a porous metal disk above the cathode, the steam concentration gradient created between the pores of the catalyst layer and pores of the metal disk enables natural convection of steam out of the catalyst layer to occur. For the traditional MEA technique, the PTFE gasket surrounding the electrode prevents steam from escaping. Locked-in steam is ideal for creating a hydrophilic ionomer-gas interface inside the gas pores of the catalyst layer. The natural convection setup allows steam to escape radially out through the porous metal disk. Next, forced convection was investigated by inserting an interdigitated carbon flow field face down above the porous metal disk and flowing dry heated argon gas during the MEA fabrication process. The forced convection setup is shown in Figure 3.2C. For the forced convection setup, channels were cut into the gasket surrounding the cathode in order to provide a pathway for heated dry argon to flow through the electrode during hot pressing.

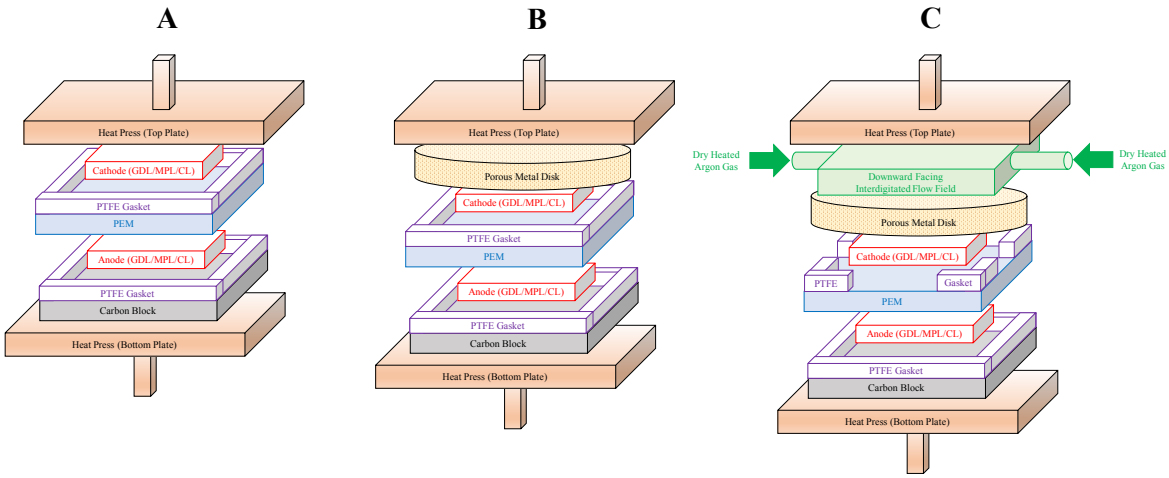

Figure 3.2. MEA hot-press setup for (A) normal MEA, (B) natural convection MEA and (C) forced convection MEA.

For the forced convection setup, flow duration was investigated to determine the effect on fuel cell performance. The following forced convection MEAs were tested: 5 min of forced

convection during the entire hot pressing procedure, 3 min no flow followed by 2 min of forced convection, and 4 min no flow followed by 1 min of forced convection. We hypothesized that there would be an optimal flow duration which would result in peak fuel cell performance. Our hypothesis required an initially saturated steam environment for sufficient duration in order to provide adequate time for the ionomer to relax. A steam environment inside the gas pores of the catalyst layer would enable the ionomer phase to relax and allow the sulfonate ionic groups within the Nafion ionomer to reorient themselves. Next, as dry heated argon flowed through the gas pores of the catalyst layer and steam was removed, the sulfonate ionic groups were expected to reorient themselves and migrate inward towards any remaining moisture inside the bulk of the ionomer. This leads to a hydrophobic ionomer-gas interface due to an ionomer-gas surface rich in fluorinated-carbon backbone structure and void of sulfonate ionic groups.

For PEMFC testing, discharge polarization curves were collected at various fuel cell temperatures, air humidification conditions, and flow fields (cathode side only) using MEAs prepared with the procedure outlined in the paragraph above. In the first study, the effect of fuel cell temperature on fuel cell performance was explored. The following three temperature schemes were used.

a) Fuel cell: 25°C, H_2 humidification bottle: 25°C, Air humidification bottle: 25°C
b) Fuel cell: 25°C, H_2 humidification bottle: 50°C, Air humidification bottle: 25°C
c) Fuel cell: 70°C, H_2 humidification bottle: 95°C, Air humidification bottle: 70°C

In the second study, the effect of flow field type (cathode side only) on fuel cell performance was investigated for the various MEA fabrication techniques. Either a serpentine (1 mm channel width, 1 mm channel depth) or interdigitated (1 mm channel width, 1 mm channel depth, 1 mm shoulder width) carbon flow fields with 2.25 cm^2 flow area were used to deliver air to the

cathode, while an interdigitated flow field delivered hydrogen to the anode. In the third study, the effect of air humidification on fuel cell performance was examined. Air was either humidified by bubbling incoming air through a heated bottle of deionized water, or dry air was delivered directly to the cathode. Table 3.1 lists the key parameters used for each fuel cell study.

Table 3.1. Experimental design conditions.

Study #	**1**	**2**	**3**
Experimental Control	Temperature	Flow field type	Air humidification
MEA Type	• Normal MEA • Natural Convection MEA	• Normal MEA • Natural Convection MEA	• Normal MEA • Natural Convection MEA • Forced Convection MEA
Cathode	SGL 25BC GDL coated with Pt/C/Nafion layer (0.50 mg Pt/cm^2, 0.14 mg/cm^2 Nafion ionomer)	SGL 25BC GDL coated with Pt/C/Nafion layer (0.50 mg Pt/cm^2, 0.14 mg/cm^2 Nafion ionomer)	SGL 25BC GDL coated with Pt/C/Nafion layer (0.50 mg Pt/cm^2, 0.14 mg/cm^2 Nafion ionomer)
Anode	SGL 25BC GDL coated with Pt/C/Nafion layer (0.50 mg Pt/cm^2, 0.14 mg/cm^2 Nafion ionomer)	SGL 25BC GDL coated with Pt/C/Nafion layer (0.50 mg Pt/cm^2, 0.14 mg/cm^2 Nafion ionomer)	SGL 25BC GDL coated with Pt/C/Nafion layer (0.50 mg Pt/cm^2, 0.14 mg/cm^2 Nafion ionomer)
Membrane	NR212	NR212	NR212
Flow Fields for Cathode	Serpentine carbon flow field	Serpentine and interdigitated carbon flow fields	Interdigitated carbon flow fields
Air Flow Rate	350 mL/min	350 mL/min	350 mL/min
Electrolyte Flow Rate	5 mL/min, 6 mL/min, or 12 mL/min	12 mL/min	12 mL/min
H_2 Flow Rate and Pressure	660 mL/min & 0.136 MPa	660 mL/min & 0.136 MPa	660 mL/min & 0.136 MPa
Temperature	• 25°C fuel cell, hydrogen, & air. • 25°C fuel cell & air, 50°C hydrogen • 70°C fuel cell & air, 95°C hydrogen	• 25°C fuel cell, hydrogen, & air. • 70°C fuel cell & air, 95°C hydrogen	• 70°C fuel cell & air, 95°C hydrogen
Humidification	Humidified hydrogen and air	Humidified hydrogen and air	Humidified hydrogen, humidified & dry air

All fuel cell testing was completed using a hydrogen pressure of 0.136 MPa (5 psig) and flow rate of approximately 660 mL/min (Equivalence of 51.7 A/cm^2 at 25°C, 47.7 A/cm^2 at

50°C, and 44.9 A/cm^2 at 70°C) by using a recirculation pump. Air was delivered to the cathode at a rate of approximately 350 mL/min (Equivalence of 8.6 A/cm^2 at 25°C and 7.5 A/cm^2 at 70°C) in a flow-through setup. Nafion 212 (~51 μm thick) was used for the polymer electrolyte membrane for all MEAs and electrical current was collected from the edges of the current collectors. Sigracet GDL-25BC carbon electrodes were used as the substrates for both the hydrogen and air electrodes. A catalyst layer (0.5 mg/cm2 Pt geometric area, 0.14 mg/cm2 Nafion ionomer) was spray coated onto the microporous layer side of the GDLs. A start-up procedure consisted of operating each PEMFC at 0.2V until 0.4 A/cm^2 was achieved, then holding the discharge current steady at 0.4 A/cm^2 for 1 h.[20] Discharge polarization curves were collected by using constant voltage staircases in 50 mV increments from OCV to 0.2 V. Multiple discharge polarization curves were collected for each MEA to ensure repeatable results. EIS was completed at 5 mV amplitude over a frequency range of 1 Hz to 100 kHz on each fuel cell to measure the internal cell resistance. EIS was also completed on the fuel cell fixture without a MEA to measure the electrical resistance of the fuel cell components.

3.4 Results and Discussion

After exposing several catalyst-coated GDEs to various heat treatment conditions, XPS was used to validate that the exposure conditions created a hydrophobic or hydrophilic ionomer-gas interface on the surface and inside the gas pores of the catalyst layer. Figure 3.3 graphs the sulfur to fluorine ratio for the hydrophilic-treated, hydrophobic-treated, and as-received GDEs. The sulfur to fluorine ratio at point 0 (far-left points in Figure 3.3) corresponds to the outermost surface of the catalyst layer prior to applying the scraping procedure. As expected, the hydrophilic-treated GDE had a high sulfur to fluorine ratio than compared to the as-received and

hydrophobic-treated GDEs. After scraping each GDE (to expose the ionomer-gas interface inside the gas pores of the catalyst layer), XPS was used to measure the sulfur to fluorine ratio. The magnitude and trend of the sulfur to fluorine ratio after each successive scrape (to remove a portion of the catalyst layer) continued throughout the catalyst layer for both heat treatment conditions and the as-received GDE. These results support our hypothesis that specific heat treatment conditions can create a hydrophilic or hydrophobic ionomer-gas interface for the thin ionomer film on the surface and inside the catalyst layer.

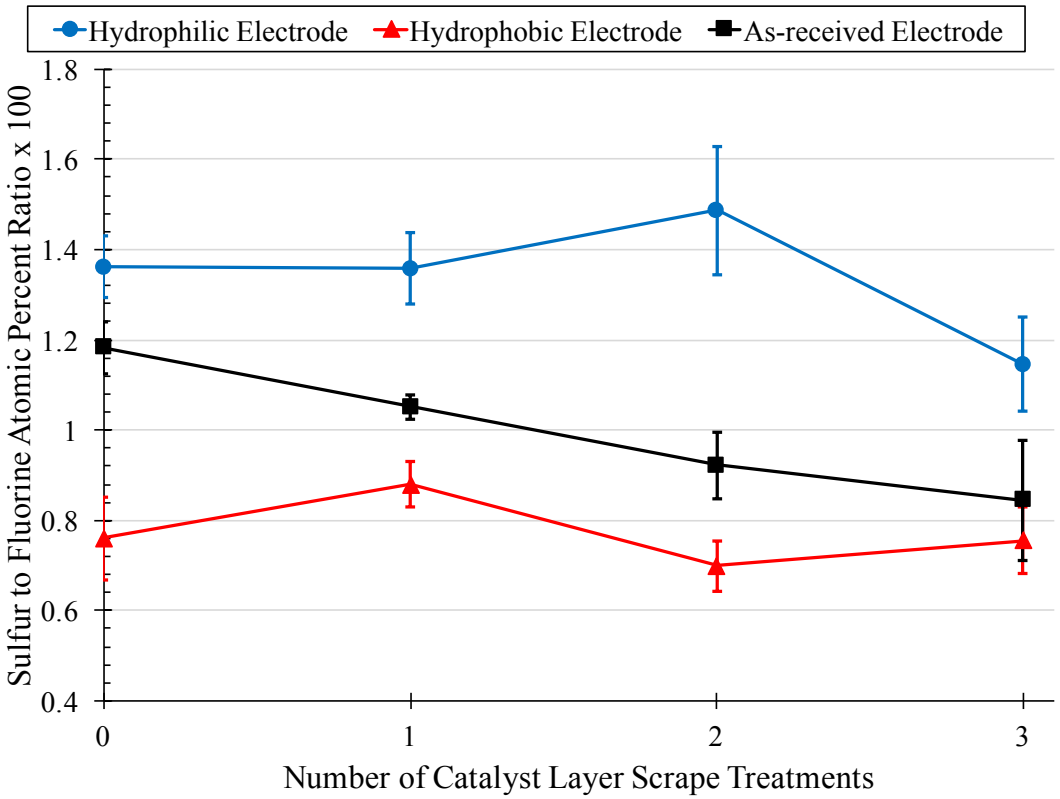

Figure 3.3. XPS characterization of catalyst layer.

Next, MEAs were constructed using the normal (i.e. conventional method), natural convection, and forced convection MEA procedures. The MEAs were tested at various temperatures, flow field types (cathode side only), and air humidification conditions. In study 1, various temperatures were used when testing the normal and natural convection MEAs. As

shown in Figure 3.4, increased temperature resulted in improved fuel cell performance. Comparing the 25°C base case to the 25°C with 50°C humidified hydrogen case, the polarization curve is shifted to the right, indicating the latter testing conditions enabled better hydration of the hydrogen electrode. For the 25°C with 50°C humidified hydrogen case, the water vapor in the incoming hydrogen stream condenses onto the surface of the hydrogen electrode due to the cooler temperature of the fuel cell. During discharge, protons produced by the oxidation of hydrogen at the hydrogen electrode drags 4-6 water molecules as they move from the anode to cathode.[21] The electro-osmotic drag process from the anode to cathode can lead to drying out of the hydrogen electrode. The condensation of water vapor at the hydrogen electrode due to heating the hydrogen humidification bottle to 25°C higher than the fuel cell temperature prevents the hydrogen electrode from drying out during discharge.[22-24] Figure 3.4 also shows the benefit of the natural convection MEA over the normal MEA fabrication technique. At 70°C, the peak power density increases by more than 83% from 288 mW/cm^2 for the normal MEA to 528 mW/cm^2 when implementing the natural convection MEA process.

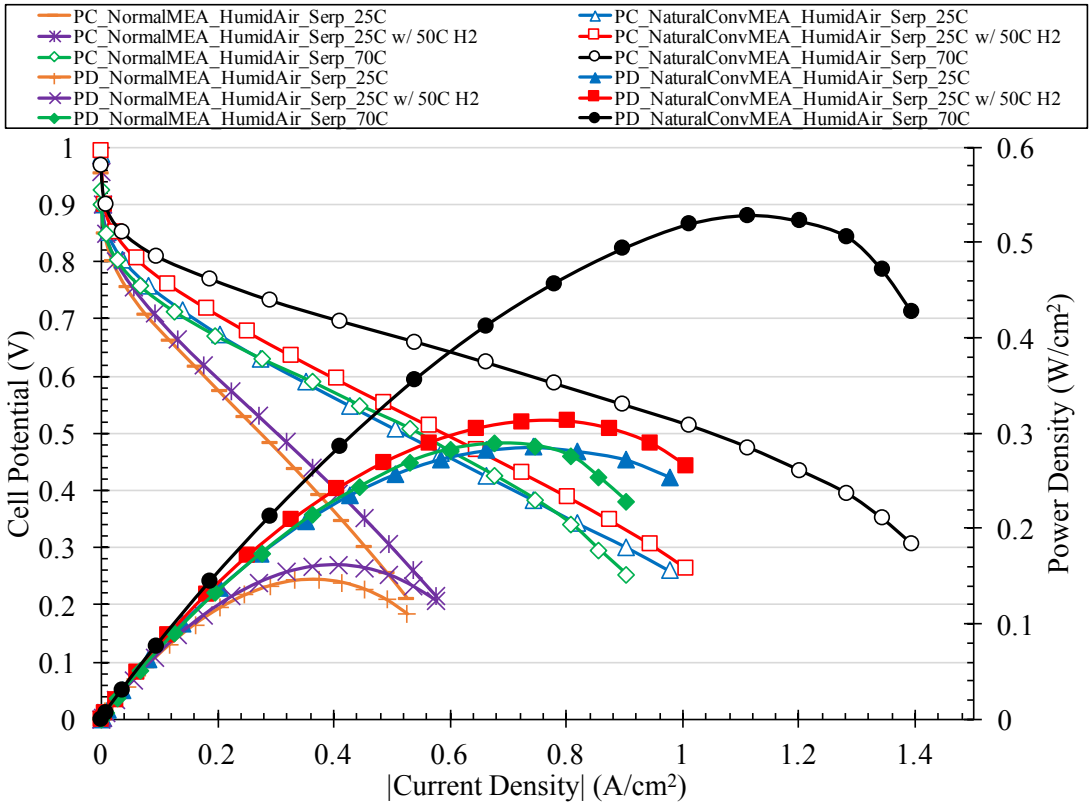

Figure 3.4. H_2-Air PEMFC discharge polarization and power density curves for normal MEA and natural convection MEA at various temperatures using humidified hydrogen, humidified air, and serpentine flow fields.

Figure 3.5 compares the polarization and power density curves when using either a serpentine or interdigitated flow field at the cathode. As expected, the interdigitated flow field results in improved mass transport during high current density due to increased penetration of oxygen into the electrode and improved removal of liquid water.[1, 22] In Figure 3.6, fuel cell temperature is increased from 25°C (shown in Figure 3.5) to 70°C to determine the effect of flow field type at the cathode during elevated temperatures. At elevated temperatures, the performance enhancement for the natural convection MEA when using an interdigitated vice serpentine flow field at the cathode is greater than at lower temperatures (25% versus 20% improvement). The observed benefit of using an interdigitated flow field on the cathode side is higher at elevated fuel cell temperatures than lower temperatures due to the interdigitated flow field's ability to

overcome the mass transport issues related to higher water production (during higher current density operation) in the cathode.

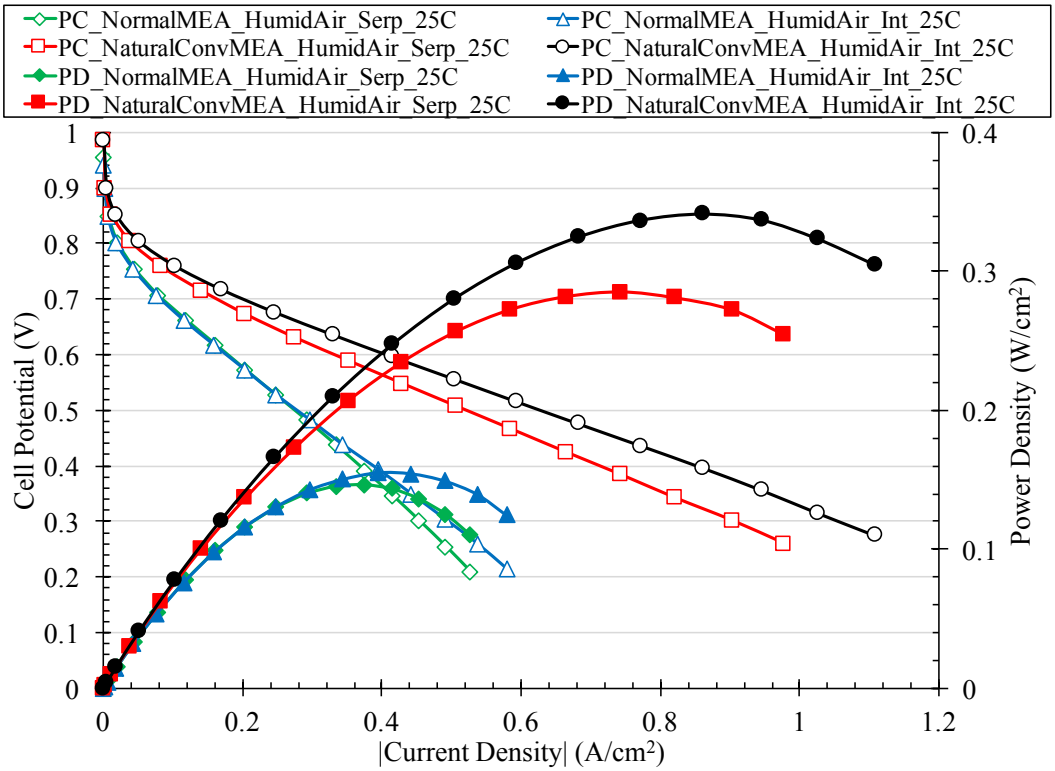

Figure 3.5. H_2-Air PEMFC discharge polarization and power density curves for normal MEA and natural convection MEA at 25°C using humidified hydrogen, humidified air, and serpentine & interdigitated flow fields.

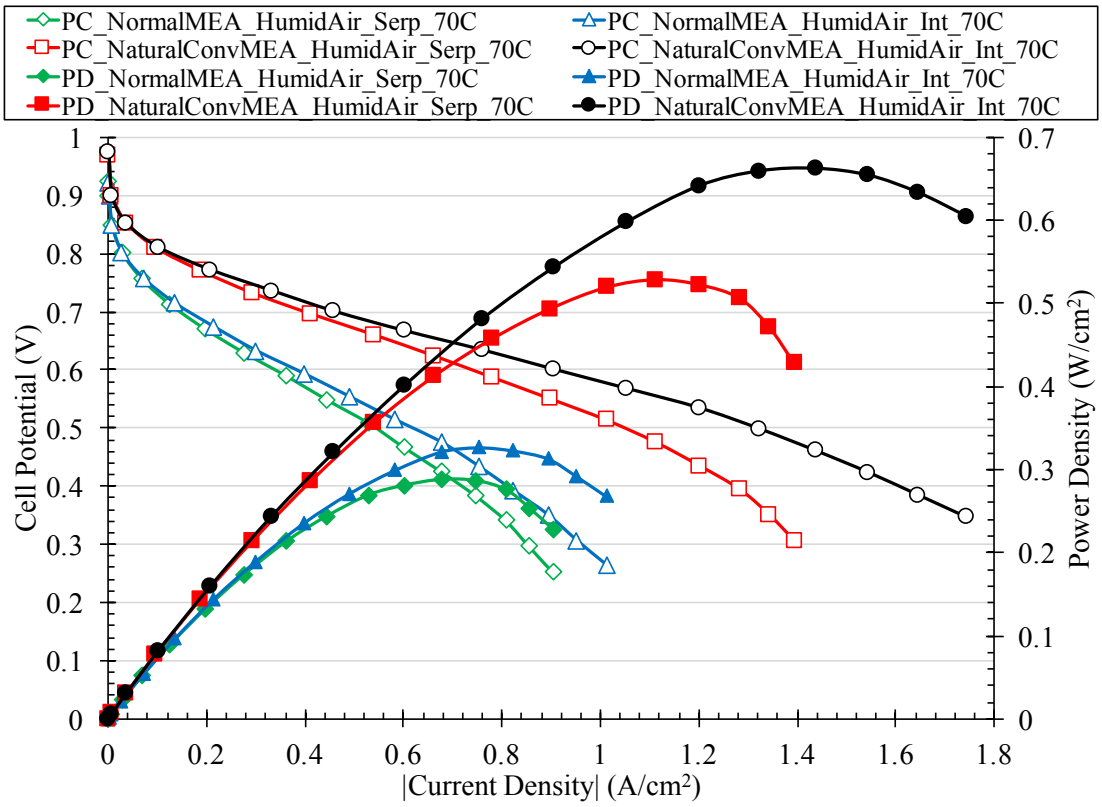

Figure 3.6. H_2-Air PEMFC discharge polarization and power density curves for normal MEA and natural convection MEA at 70°C using humidified hydrogen, humidified air, and serpentine & interdigitated flow fields.

Finally, the forced convection MEA method was compared to the normal and natural convection MEA methods. In Figure 3.7, each MEA was tested at 25°C using interdigitated flow fields at both electrodes and humidified air at the cathode. The order of performance (from high to low) for the various MEAs was: 1-min forced convection, natural convection, 2-min forced convection, 5-min forced convection, and normal MEA. As expected, the 5-min forced convection MEA underperformed the 1-min and 2-min forced convection MEAs. Our hypothesis stated that sufficient time is needed at saturated steam conditions (above Nafion's glass transition temperature) to allow the ionomer layer to relax and the sulfonate ionic groups to be able to reorient themselves. The natural convection MEA performed remarkably well compared to the forced convection MEAs. This is very encouraging since the natural convection MEA method is

simple and easy to apply to a large-scale manufacturing process. The 1 min forced convection MEA method leads to more than a 135% increase in peak power over the normal MEA at 25°C.

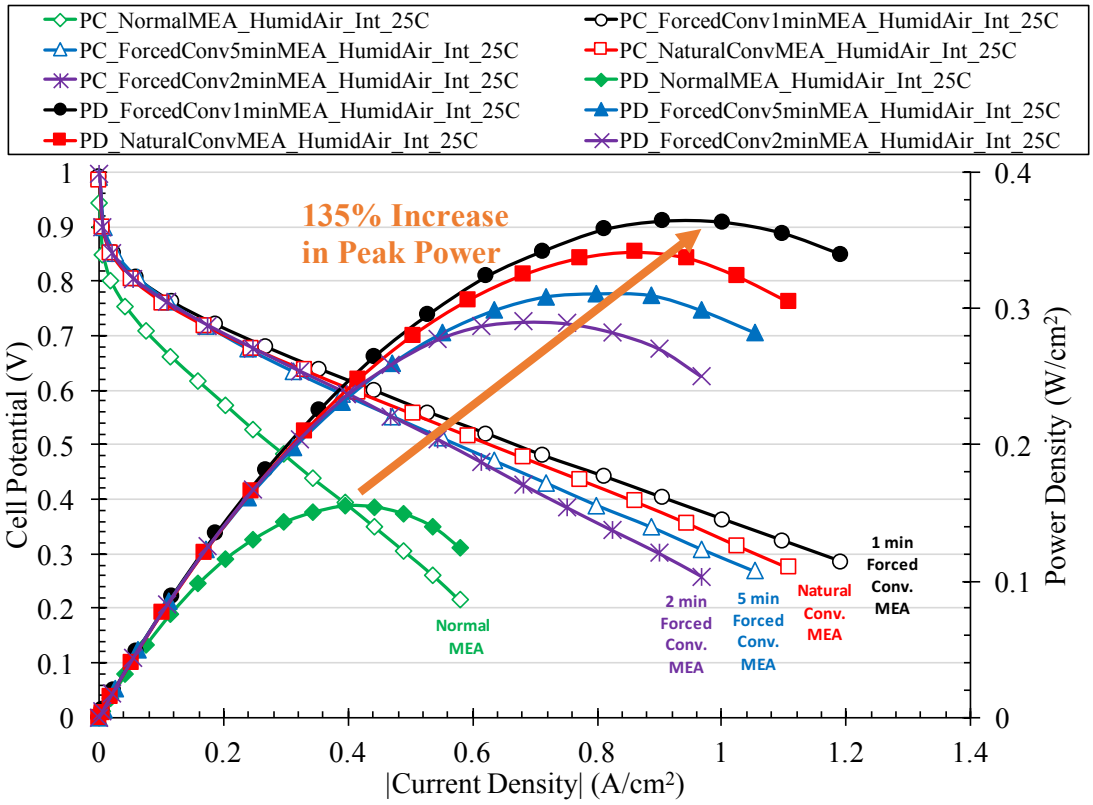

Figure 3.7. H_2-Air PEMFC discharge polarization and power density curves for normal MEA, natural convection MEA, and forced convection MEA at 25°C using humidified hydrogen, humidified air, and interdigitated flow fields.

In Figure 3.8, the forced convection MEA method was compared to the normal and natural convection MEA methods when operating the fuel cell at 70°C. The performance for each MEA method improves over the baseline 25°C case. The performance enhancement of the 1 min forced convection MEA leads to more than a 133% improvement in peak power over the normal MEA method. The order of performance for the various MEAs when operating at 70°C (i.e. Figure 3.8) aligns with the 25°C baseline case (i.e. Figure 3.7).

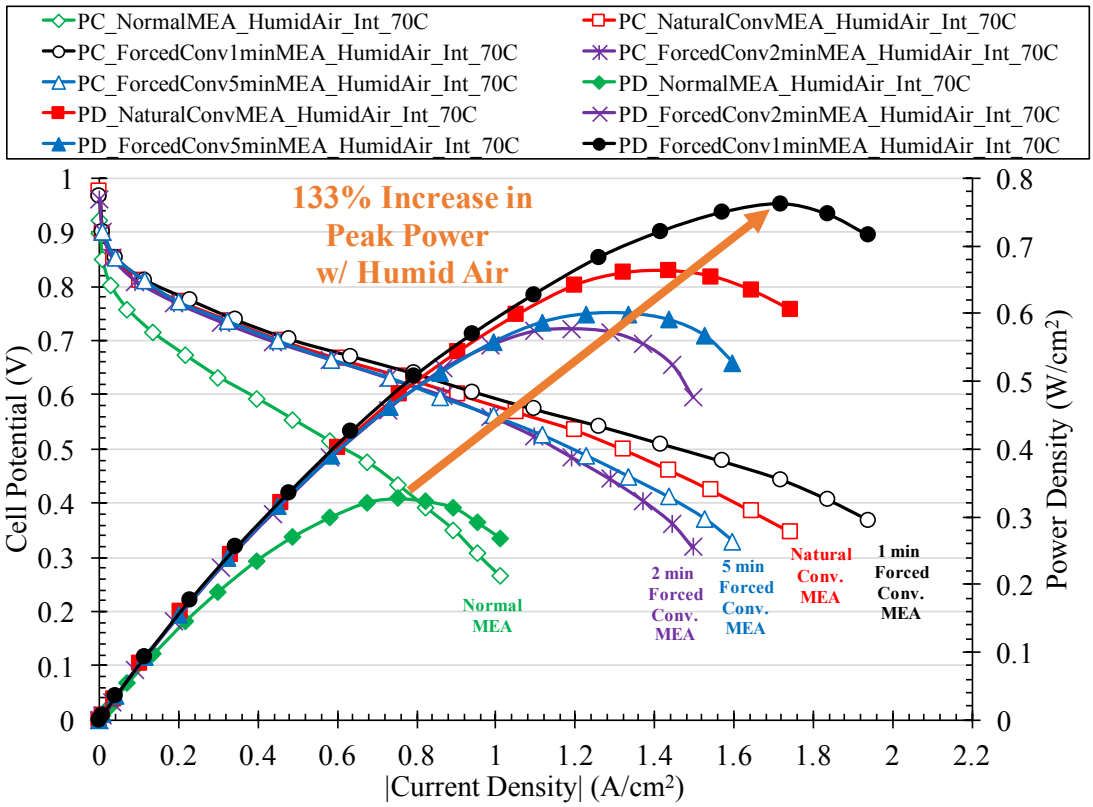

Figure 3.8. H_2-Air PEMFC discharge polarization and power density curves for normal MEA, natural convection MEA, and forced convection MEA at 70°C using humidified hydrogen, humidified air, and interdigitated flow fields.

Lastly, the various MEA fabrication methods were tested using dry air instead of humidified air. It is well known that flowing dry air to the cathode will lead to higher performance due to improved mass transport of oxygen.[21, 22] Dry air is better able to remove liquid water from the cathode, therefore reducing the impact of liquid water buildup and enabling better oxygen transport into the cathode to reach the catalyst reaction sites. As shown in Figure 3.9, the normal MEA is able to achieve a current density of more than 1 A/cm^2 at 0.5V, which is in alignment with previously published results using state-of-the-art fuel cells.[14, 22, 25-28] To our satisfaction, the 1 min forced convection MEA led to more than a 47% improvement in peak power density over the normal MEA when operating at 70°C with dry air. The 1 min forced convection MEA performed better than the natural convection MEA, which is in alignment with

the observed trend for the humidified air case (i.e. Figure 3.8).

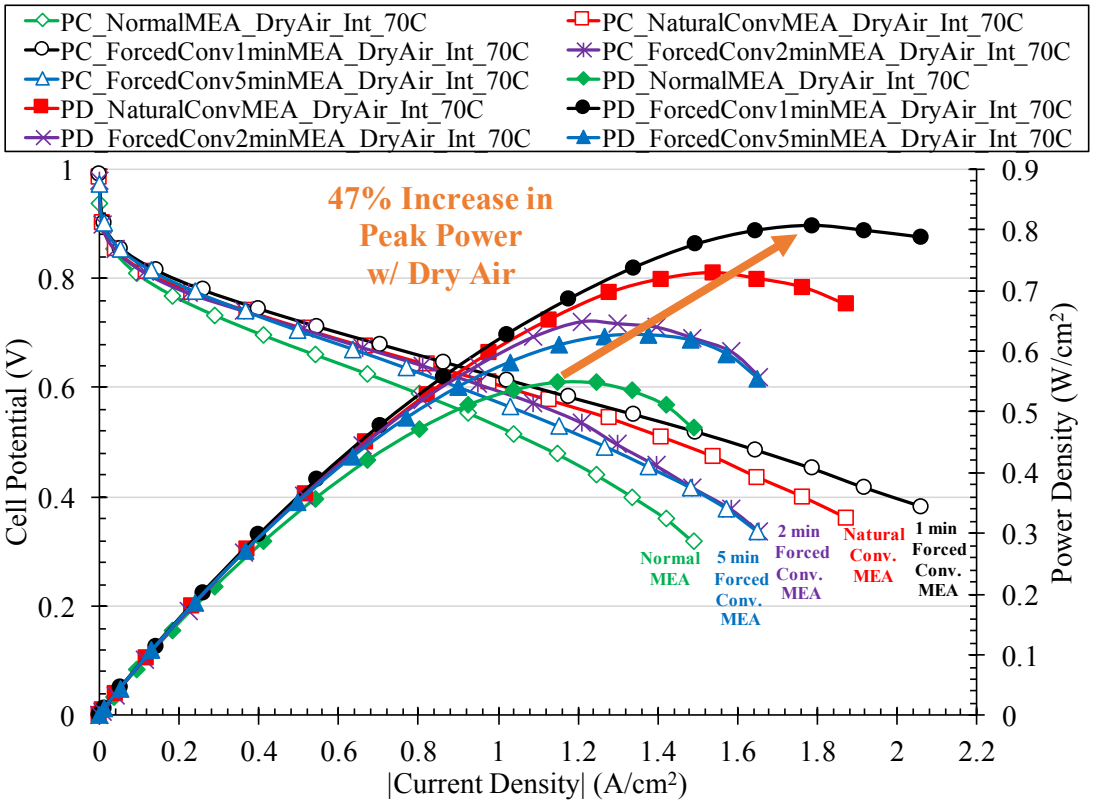

Figure 3.9. H_2-Air PEMFC discharge polarization and power density curves for normal MEA, natural convection MEA, and forced convection MEA at 70°C using humidified hydrogen, dry air, and interdigitated flow fields.

The results confirmed our hypothesis that a saturated steam environment is needed at the onset of MEA fabrication in order to allow the catalyst layer ionomer phase sufficient time to relax. As expected, this phenomenon resulted in suboptimal performance for the 5-min forced convection method. The 1-min forced convection case led to optimal two phase flow in the cathode catalyst layer during high current density operations as compared to the other methods.

3.5 Summary

In summary, a new heat treatment process was used to create a hydrophobic ionomer/gas interface in a fuel cell catalyst layer. After heat treating GDEs, XPS was used to characterize the

upper most surface of the catalyst layer. Additionally, a scraping technique was employed to reveal the catalyst layer's internal structure. XPS was used to characterize the ionomer-gas interface inside the gas pores of the catalyst layer after each successive removal of a portion of the catalyst layer.

The heat treatment method was then incorporated into the cathode catalyst layer by using both natural convection and forced convection during the MEA fabrication process. Various fuel cell parameters were studied, including operating temperature, flow field type, and air humidification state. Discharge performance curves for a H_2-Air PEMFC using the natural convection and 1 min forced convection MEAs showed remarkable performance compared to the conventionally-prepared MEA. We credit the superior fuel cell performance (47% increase in peak power density at 70°C) to improved mass transport effect, an increase in the effective proton conductivity in the cathode, or a combination of both phenomena.

We expect a hydrophobic ionomer-gas interface inside the gas pores of the catalyst layer will lead to improved mass transport of oxygen into and liquid water out of the cathode (proposed structure shown in Figure 3.10). Additionally, we anticipate that a hydrophilic ionomer-gas interface will lead to improved performance when flowing liquid electrolyte reactants (i.e. flow battery systems). Future studies will explore the notion of optimizing various flow batteries by using hydrophilic-treated GDEs.

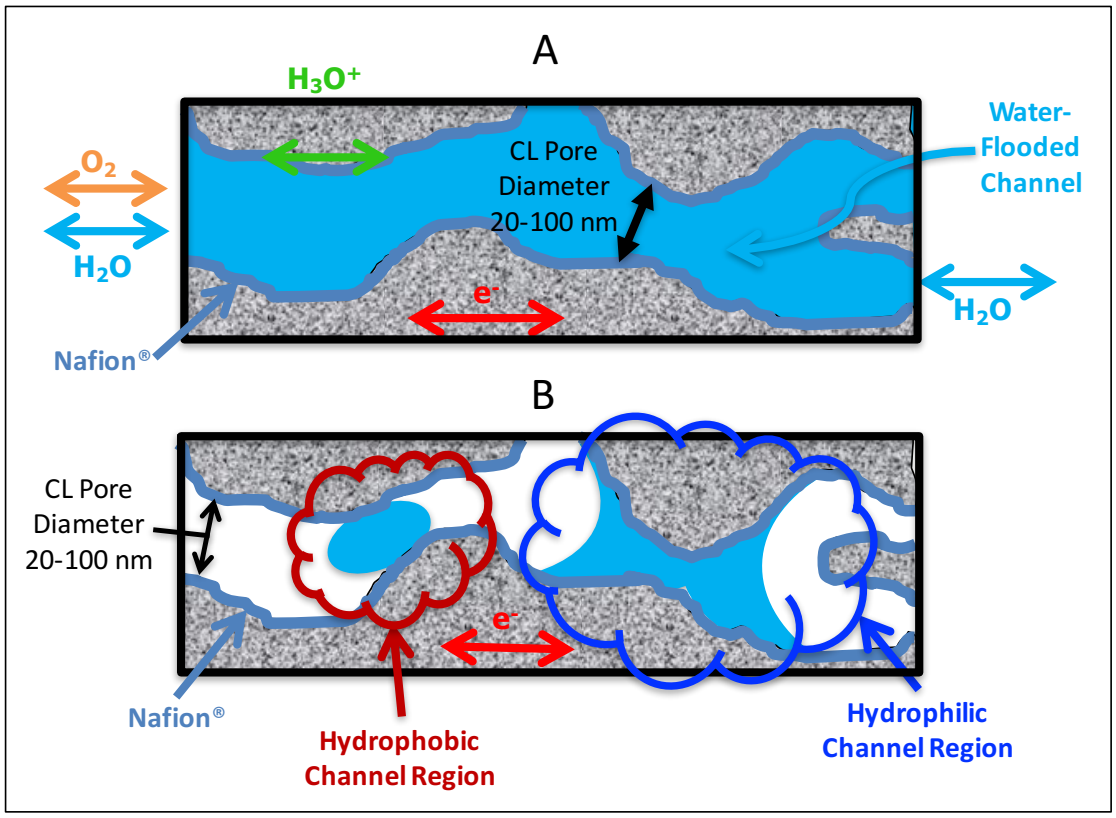

Figure 3.10. Cross-sectional side view of (A) water-flooded CL channel and (B) engineered CL ionomer surface.[16]

3.6 Acknowledgments

The authors wish to acknowledge the financial support from the University of Kansas (KU) Madison and Lila Self Fellowship. Supplies and imaging charges for this work were supported by the National Science Foundation through grant numbers EFRI-1038234 and CBET-1518755. The authors would like to thank Dr. Prem Thapa at the University of Kansas and Dr. Vijay Ramani, Dr. Huafang Li, and Yue Li at Washington University in St. Louis for their support and expertise in using the XPS. The authors would also like to thank Applied Porous Technologies, Inc. for providing the porous stainless steel disk used for MEA fabrication.

3.7 References for Chapter 3

1. T. V. Nguyen, *Journal of The Electrochemical Society*, **143**, L103 (1996).

2. R. Friedmann and T. V. Nguyen, *Journal of The Electrochemical Society*, **157**, B260 (2010).

3. M. Uchida, Y. Aoyama, N. Eda and A. Ohta, *Journal of The Electrochemical Society*, **142**, 4143 (1995).

4. J. Benziger, J. Nehlsen, D. Blackwell, T. Brennan and J. Itescu, *Journal of Membrane Science*, **261**, 98 (2005).

5. T. V. Nguyen, A. Ahosseini, X. Wang, V. Yarlagadda, A. Kwong, A. Z. Weber, P. Deevanhxay, S. Tsushima and S. Hirai, *Journal of The Electrochemical Society*, **162**, F1451 (2015).

6. T. V. Nguyen, M. V. Nguyen, G. Lin, N. Rao, X. Xie and D. M. Zhu, *Electrochemical and Solid-State Letters*, **9**, A88 (2006).

7. T. V. Nguyen, M. V. Nguyen, K. J. Nordheden and W. He, *Journal of The Electrochemical Society*, **154**, A1073 (2007).

8. V. Parry, G. Berthomé, J. Joud, O. Lemaire and A. A. Franco, *Journal of Power Sources*, **196**, 2530 (2011).

9. D. K. Paul, K. Karan, A. Docoslis, J. B. Giorgi and J. Pearce, *Macromolecules*, **46**, 3461 (2013).

10. R. P. Dowd, T. V. Nguyen, D. S. Moore, P. N. Pintauro and J. W. Park, *ECS Transactions*, **58**, 607 (2013).

11. N. Zamel, *Journal of Power Sources*, **309**, 141 (2016).

12. F. Zhang, S. G. Advani, A. K. Prasad, M. E. Boggs, S. P. Sullivan and T. P. Beebe, *Electrochimica Acta*, **54**, 4025 (2009).

13. E. Antolini, L. Giorgi, A. Pozio and E. Passalacqua, *Journal of Power Sources*, **77**, 136 (1999).

14. F. Mack, M. Klages, J. Scholta, L. Jörissen, T. Morawietz, R. Hiesgen, D. Kramer and R. Zeis, *Journal of Power Sources*, **255**, 431 (2014).

15. Z. Qi and A. Kaufman, *Journal of Power Sources*, **109**, 38 (2002).

16. R. P. Dowd, C. S. Day and T. V. Nguyen, *Journal of The Electrochemical Society*, **164**, F138 (2017).

17. A. Serizawa, Z. Feng and Z. Kawara, *Experimental Thermal and Fluid Science*, **26**, 703 (2002).

18. J. L. Sullivan, Z. Wronski, S. O. Saied and J. Sielanko, *Vacuum*, **46**, 1333 (1995).

19. P. Gazdzicki, I. Biswas and M. Schulze, *Surface and Interface Analysis*, **46**, 350 (2014).

20. G. Lin and T. V. Nguyen, *Journal of The Electrochemical Society*, **152**, A1942 (2005).

21. S. Srinivasan, E. A. Ticianelli, C. R. Derouin and A. Redondo, *Journal of Power Sources*, **22**, 359 (1988).

22. D. L. Wood, J. S. Yi and T. V. Nguyen, *Electrochimica Acta*, **43**, 3795 (1998).

23. R. Kuhn, P. Krüger, S. Kleinau, M. Dawson, J. Geyer, M. Roscher, I. Manke and C. Hartnig, *International Journal of Hydrogen Energy*, **37**, 7702 (2012).

24. W. Yan, C. Chen, S. Mei, C. Soong and F. Chen, *Journal of Power Sources*, **162**, 1157 (2006).

25. G. S. Avcioglu, B. Ficicilar, A. Bayrakceken and I. Eroglu, *International Journal of Hydrogen Energy*, **40**, 7720 (2015).

26. N. J. Cooper, T. Smith, A. D. Santamaria and J. W. Park, *International Journal of Hydrogen Energy*, **41**, 1213 (2016).

27. T. V. Nguyen and M. W. Knobbe, *Journal of Power Sources*, **114**, 70 (2003).

28. X. Wang and T. V. Nguyen, *Journal of Power Sources*, **197**, 50 (2012).

CHAPTER 4: A Study of the Alkaline-Based H_2-Br_2 and H_2-I_2 Reversible Fuel Cells

4.1 Abstract

The hydrogen-bromine (H_2-Br_2) and hydrogen-iodine (H_2-I_2) reversible fuel cell systems can be operated in the acid or alkaline modes. The alkaline versions were evaluated because of the advantages over the acidic systems such as higher cell potential, lower corrosivity, and lower catalyst cost for the hydrogen evolution and oxidation reactions. Fuel cells were assembled to validate the operational feasibility of the alkaline systems and to evaluate their performance. The results confirmed that the alkaline H_2-Br_2 and H_2-I_2 fuel cells have a higher cell voltage than their corresponding acidic systems while maintaining similarly fast electrode reaction kinetics. However, the performance of these alkaline fuel cells is currently limited by the low ionic conductivity of the K^+ form membranes, which is attributed to the slow diffusivity of the larger K^+ ion in these membranes, and providing equal access of gaseous and liquid reactants to the active sites for the hydrogen reaction. These limitations could be overcome by using thinner membranes, operating the fuel cell at higher concentrations and temperatures, and development of porous electrodes with better two-phase fluid distribution.

4.2 Introduction

The acidic hydrogen-bromine (H_2-Br_2) reversible fuel cell has been an attractive system for electrical energy storage because of its high round-trip conversion efficiency, high power density capability, and anticipated low costs. Since HBr solution serves as both the electrolyte and active materials for the fuel cell, no supporting electrolyte is needed. This aspect results in higher energy density; therefore, sparking great interest in this system for energy storage.[1-12] While all

previous studies have been with the acidic system, the H_2-Br_2 fuel cell system can also be operated in the alkaline mode. However, this mode had not been studied until recently.[13]

In an acidic H_2-Br_2 fuel cell, the charge and discharge electrode reactions are as follows:

$$\textit{Br}_2\ (+)\ \textit{Electrode:}\ 2HBr \underset{discharge}{\overset{charge}{\rightleftarrows}} Br_2 + 2H^+ + 2e^- \qquad \boldsymbol{E^o_{red} = +1.09\ V} \qquad \textbf{[1]}$$

$$\textit{H}_2\ (-)\ \textit{Electrode:}\ 2H^+ + 2e^- \underset{discharge}{\overset{charge}{\rightleftarrows}} H_2 \qquad \boldsymbol{E^o_{red} = +0.0\ V} \qquad \textbf{[2]}$$

All reported voltages are relative to the standard hydrogen electrode (SHE). During charge, the H^+ ions migrate from the Br_2 side across a proton conducting membrane (e.g., Nafion) to the H_2 side to maintain electroneutrality and charge balance. The process described above is reversed during discharge. The overall reaction is given below, with the standard cell potential of +1.09 V.

$$\textit{Overall Reaction:}\ 2HBr \underset{discharge}{\overset{charge}{\rightleftarrows}} Br_2 + H_2 \qquad \boldsymbol{E^o_{cell} = +1.09\ V} \qquad \textbf{[3]}$$

In an alkaline H_2-Br_2 fuel cell, the charge and discharge electrode reactions are as follows:

$$\textit{Br}_2\ (+)\ \textit{Electrode:}\ 2KBr \underset{discharge}{\overset{charge}{\rightleftarrows}} Br_2 + 2K^+ + 2e^- \qquad \boldsymbol{E^o_{red} = +1.09\ V} \qquad \textbf{[4]}$$

$$\textit{H}_2\ (-)\ \textit{Electrode:}\ 2H_2O + 2e^- \underset{discharge}{\overset{charge}{\rightleftarrows}} H_2 + 2OH^- \qquad \boldsymbol{E^o_{red} = -0.83\ V} \qquad \textbf{[5]}$$

During charge, the cations (e.g., K^+ when KOH and KBr are used) associated with the Br^- ions at the positive Br_2 electrode migrate across a cation (K^+) conducting membrane to the negative H_2

side, and vice versa during discharge, and combine with the OH^- ions to form KOH as shown in the overall reaction below. The processes described above are reversed during discharge. With these electrode reactions, the standard cell potential is +1.92 V.

$$\textit{Overall Reaction: } 2KBr + 2H_2O \underset{discharge}{\overset{charge}{\rightleftarrows}} Br_2 + H_2 + 2KOH \qquad \boldsymbol{E^o_{cell} = +1.92\ V} \qquad \textbf{[6]}$$

Note that in an acidic H_2-Br_2 system, the H^+ ion is the ionic carrier and in an alkaline H_2-Br_2 system, the K^+ ion (when KOH and KBr are used) is the ionic carrier. Based on the reactions shown above, the alkaline system offers a higher cell voltage, which is an advantage because of its potentially higher power output and higher energy density. The other advantages of this system include the fact that non-noble catalysts can be used for the hydrogen reactions and lower corrosiveness of KBr and KOH solutions relative to the HBr solution used in the acidic system.[14, 15] The primary challenge is anticipated to be the three-phase hydrogen electrode reaction involving a solid electronic conducting phase and a two-phase reactant system consisting of gaseous hydrogen and aqueous KOH.

Similar to the H_2-Br_2 system, the hydrogen-iodine (H_2-I_2) system can also be operated in the acidic and alkaline modes. The acidic version of the H_2-I_2 fuel cell was evaluated but not pursued by our group because of its low overall standard cell potential. While the iodine reactions have been found in many applications including dye sensitized solar cells,[16, 17] very few studies have been reported that use the iodine reaction in a flow battery or reversible fuel cell application.[18-20] Taking advantage of the higher overall reaction potential in alkaline solutions, we decided to evaluate the alkaline hydrogen-iodine fuel cell system because of the lower toxicity of iodine as compared to bromine.

Acidic Mode:

$$I_2\ (+)\ \text{Electrode:}\quad 2HI \underset{discharge}{\overset{charge}{\rightleftarrows}} I_2 + 2H^+ + 2e^- \qquad E^o_{red} = +0.54\ \text{V} \qquad [7]$$

$$H_2\ (-)\ \text{Electrode:}\quad 2H^+ + 2e^- \underset{discharge}{\overset{charge}{\rightleftarrows}} H_2 \qquad E^o_{red} = +0.0\ \text{V} \qquad [8]$$

$$\text{Overall Reaction:}\quad 2HI \underset{discharge}{\overset{charge}{\rightleftarrows}} I_2 + H_2 \qquad E^o_{cell} = +0.54\ \text{V} \qquad [9]$$

Alkaline Mode (with KOH/KI solutions)**:**

$$I_2\ (+)\ \text{Electrode:}\quad 2KI \underset{discharge}{\overset{charge}{\rightleftarrows}} I_2 + 2K^+ + 2e^- \qquad E^o_{red} = +0.54\ \text{V} \qquad [10]$$

$$H_2\ (-)\ \text{Electrode:}\quad 2H_2O + 2e^- \underset{discharge}{\overset{charge}{\rightleftarrows}} H_2 + 2OH^- \qquad E^o_{red} = -0.83\ \text{V} \qquad [11]$$

$$\text{Overall Reaction:}\quad 2KI + 2H_2O \underset{discharge}{\overset{charge}{\rightleftarrows}} I_2 + H_2 + 2KOH \qquad E^o_{cell} = +1.37\ \text{V} \qquad [12]$$

In this chapter, alkaline H_2-Br_2/H_2-I_2 fuel cells were assembled in multiple configurations, as shown in Figure 4.1, and tested to validate the concept and feasibility of the alkaline H_2-Br_2 and H_2-I_2 fuel cell systems. A schematic of the acid-based H_2-Br_2/H_2-I_2 fuel cell (Figure 4.1a) tested in our previous studies [5, 8, 10-12] was also included to illustrate the difference between the acid-based and alkaline-based (Figure 4.1b and Figure 4.1c) cell configurations, mainly the use of an additional electrolyte compartment for the KOH solution at the hydrogen electrode. Figure 4.1d shows the configuration used to evaluate the performance of the alkaline H_2-I_2 fuel cell with two-phase reactant feed to the hydrogen electrode. In this two-phase feed configuration, the KOH electrolyte compartment was eliminated and a single two-phase feed consisting of gaseous hydrogen and aqueous KOH solution was simultaneously injected into the

hydrogen electrode. This configuration looks very similar to the simpler acidic H_2-I_2 fuel cell configuration with the exception of the two-phase feed and K^+ membrane. The elimination of the KOH solution compartment and the use of two-phase feed injection were expected to greatly reduce the cell internal ohmic resistance and simplify the cell design.

As shown in Figure 4.1, a saturated calomel reference electrode (SCE) was used to separate the cell voltages into half-cell voltages. The half-cell voltages were used to validate that the high cell voltages obtained were from the more negative potential of the hydrogen reaction in an alkaline solution and to help identify the cell components impacting fuel cell performance the most. The reference electrode was connected to either the KOH electrolyte compartment using a KOH electrolyte bridge made of the same KOH solution or the iodine compartment using a KI salt bridge. For the cell configuration shown in Figure 4.1c, a platinum wire was also inserted into the KOH compartment to separate the full cell impedance into half-cell impedances during electrochemical impedance spectroscopy (EIS) measurements.

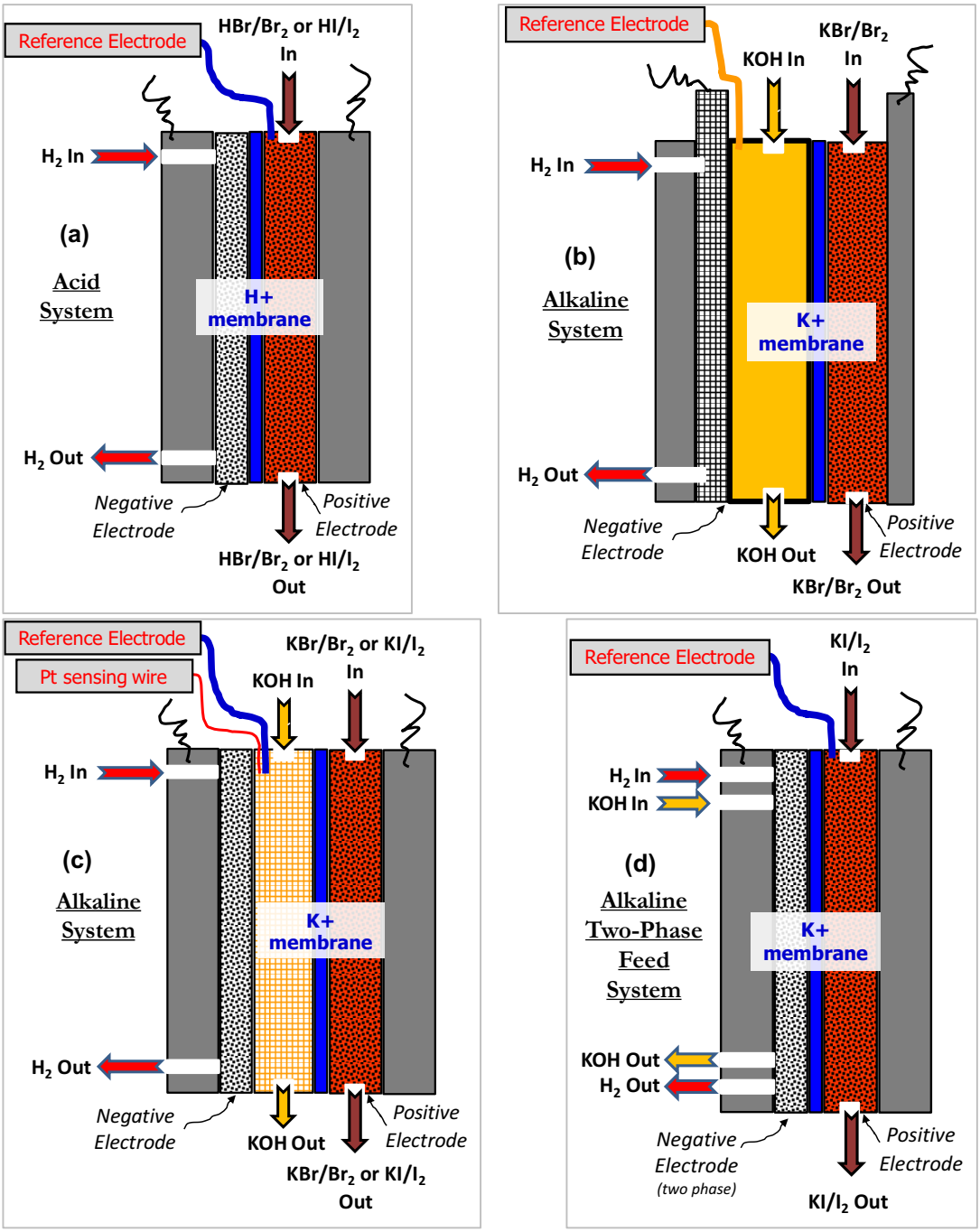

Figure 4.1. Cell configurations for the (a) acid-based H_2-Br_2 and H_2-I_2 reversible fuel cell systems, (b) alkaline-based H_2-Br_2 reversible fuel cell (Study 1), (c) single-phase feed for the alkaline-based H_2-Br_2 and H_2-I_2 reversible fuel cells (Study 2 and Study 3), and (d) two-phase feed for the alkaline-based H_2-I_2 reversible fuel cell (Study 4)

4.3 Experimental

The K^+ conducting membranes used for the alkaline H_2-Br_2 fuel cells were prepared by boiling H^+ conducting Nafion membranes in KOH solutions (1 M-5 M) for 1-4 h to convert them to K^+ form. After the membranes were boiled in KOH solutions, they were cooled to room temperature, rinsed with de-ionized water and used with no further treatment. A significant increase in the K^+ conductivity was observed between membranes treated in 1M and 3M KOH solutions. However, no significant changes in the K^+ conductivity were observed between membranes treated in 3 M and 5 M KOH solutions. The results supported the hypothesis that since the ion (H^+ or SO_3^-) concentration in Nafion 1100 equivalent weight membranes is about 1.8 M, the membranes need to be boiled in KOH solutions with molarities equal to or higher than 1.8M in order to replace the H^+ ions in these membranes with K^+ ions. Higher K^+ concentration provides a higher driving force to overcome the higher affinity of the SO^{3-} groups for the H^+ ions. Nafion membranes treated in 3M KOH solution were used for all studies presented in this work.

Four different fuel cell studies were conducted, all at room temperature (~22°C). Table 4.1 summarizes the experimental conditions for each study. In the first study, discharge and charge performances were collected to validate the concept and feasibility of the alkaline H_2-Br_2 system. The cell configuration for the first study is shown in Figure 4.1b. A nickel screen coated with a layer of Pt/C/PTFE containing 1.2 mg Pt/cm^2 geometric area was used as the hydrogen electrode and a solid carbon plate was used as the bromine electrode, both with active geometric area of approximately 4 cm^2. The PTFE phase was added to the hydrogen electrode to create a hydrophobic porous structure for hydrogen gas transport. Even though our ultimate goal is to test this system with a non-noble catalyst (e.g., nickel or nickel alloys [14, 15]) for the hydrogen

reaction, platinum on carbon support was used as the catalyst in the hydrogen electrodes for these studies. Electrical current was collected from the edges of the electrodes. A potassium ion (K^+) conducting Nafion 117 (~178 μm thick) membrane was used to facilitate potassium ion transport between the two electrodes and to keep the hydroxide, bromine and bromide anions from crossing from one side to the other. 1M KBr/0.5M Br_2 solution was recirculated through the bromine electrode and 1M KOH solution was recirculated through the hydrogen electrode. Positive and negative electrolyte volumes were 500 mL and 300 mL, respectively, for all studies. The KOH solution was fed to the KOH reservoir on one side of the hydrogen electrode while hydrogen gas at ambient pressure was fed to the opposite side from a PTFE gas distributor plate, both at 10 mL/min, as shown in Figure 4.1b. A SCE was inserted into the KOH chamber and used as a reference electrode. The reference electrode enables us to separate the overall cell voltage into individual electrode voltages during open circuit, as well as during discharge and charge. The discharge and charge polarization curves were obtained by applying constant potential in staircase mode from open circuit voltage (OCV) to +/- 300 mV in increments of 50 mV. The cell was held at each potential for at least 2 minutes in order for the cell to reach steady state. All electrode voltages reported in this chapter have been converted to SHE basis.

Table 4.1. Experimental Conditions.

Study #	1	2	3	4
System	Alkaline H_2-Br_2	Alkaline H_2-Br_2	Alkaline H_2-I_2	Alkaline H_2-I_2
Cell Configuration	Figure 4.1b	Figure 4.1c	Figure 4.1c	Figure 4.1d
Negative Electrode	Nickel screen coated with Pt/C/PTFE (1.2 mg Pt/cm^2)	SGL 35BC GDL coated with Pt/C/PTFE layer (0.8 mg Pt/cm^2)	SGL 35BC GDL coated with Pt/C/PTFE layer (0.8 mg Pt/cm^2)	10% wet-proof Toray 060 GDL (0.8 mg Pt/cm^2)
Positive Electrode	Solid carbon plate	2 layers of SGL 10AA	2 layers of SGL 10AA	Carbon nanotube GDL
Membrane	K^+-form of Nafion 117	K^+-form of Nafion 212 and K+ form of Nafion 115	K^+-form of Nafion 212	K^+-form of Nafion 212
Flow Fields	H_2 electrode - carbon interdigitated flow field; Br_2 electrode - carbon interdigitated flow field	H_2 electrode - carbon interdigitated flow field; Br_2 electrode - tantalum interdigitated flow field	H_2 electrode - carbon interdigitated flow field; Br_2 electrode - tantalum interdigitated flow field	H_2 electrode - carbon interdigitated flow field; Br_2 electrode - carbon interdigitated flow field
Electrolyte Compositions	1M KBr/0.5M Br_2 solution for the bromine electrode, 1M KOH solution and H_2 gas for the hydrogen electrode	1M KBr/0.3M Br_2 solution for the bromine electrode, 1M/3M KOH solution and H_2 gas for the hydrogen electrode	1M KBr/0.4M I_2 solution for the iodine electrode, 1M/2M/3M KOH solution and H_2 gas for the hydrogen electrode	1M KBr/0.4M I_2 solution for the iodine electrode, 3M KOH solution and H_2 gas for the hydrogen electrode
Additional Details	KOH Reservoir used in conjunction with a PTFE gas distributor plate at the H_2 electrode	1 mm glass-fiber mat served as an electrolyte reservoir for the KOH solution	1 mm glass-fiber mat served as an electrolyte reservoir for the KOH solution	2 phase reactant feed flow for H_2/KOH

In the second study, the cell was modified to improve the performance of the alkaline H_2-Br_2 system. The cell configuration for the second study is shown in Figure 4.1c. The hydrogen

electrode was made by applying a Pt/C/PTFE layer onto the micro-porous layer (MPL) side of a bilayer Sigracet GDL-35BC carbon gas diffusion medium. The catalyst loading was approximately 0.8 mg Pt/cm^2 geometric area, and the electrode geometric active surface area was about 2.25 cm^2 (1.5 cm x 1.5 cm). Two layers of Sigracet carbon gas diffusion layers (10AA) were used as the bromine electrode. Potassium ion (K^+)-form Nafion 212 (~51 μm thick) and 115 (~127 μm thick) membranes treated in 3M KOH were used in this study to evaluate the effect of membrane thickness on fuel cell performance. A layer of glass-fiber mat (purchased from 3M) with a thickness of approximately 1 mm was placed between the hydrogen electrode and the membrane to serve as an electrolyte reservoir for the KOH solution and to allow the cell components to be compressed to establish good electrical contact between the electrodes and the flow field/current collector plates. In order to study the effect of KOH concentration, KOH solutions at 1M and 3M were fed to the KOH reservoir side of the hydrogen electrode at flow rates between 0.6 and 0.95 mL/min with a peristaltic pump (Masterflex EW-77122-14) while neat hydrogen gas at about 121 kPa absolute was fed to the other side of the electrode at a rate of approximately 660 mL/min using a recirculation pump. At the bromine electrode, a solution of 1M KBr/0.3M Br_2 was fed at a flow rate of 1.5 mL/min with a peristaltic pump (Stenner EW-74206). This Br_2 flow rate is equivalent to 1.45 A/cm^2 or more than 12 times the maximum current densities obtained in this study. The high flow rate and excess electrolyte used in this study represent attempts to ensure that the bromine concentration over the entire electrode's outer surface was constant during the discharge and charge cycle. A carbon interdigitated flow field [21, 22] was used at the hydrogen electrode and a tantalum interdigitated flow field was used at the bromine electrode to reduce the mass transport resistance in the electrodes. Electrical current collection at the negative electrode was from the edge of a stainless steel plate placed in contact

with the carbon flow field block. Electrical current collection at the positive electrode was directly from the edge of the tantalum flow field plate. Similar to the first study, the discharge and charge curves were measured using constant potential in staircase mode from OCV to +/- 500 mV in increments of 50 mV and a step duration of 5 minutes (or long enough to obtain a steady state current). EIS (Gamry EIS 300) was conducted at 5 mV amplitude over a frequency range of 1 Hz to 100 kHz to measure the internal resistance of the entire fuel cell operated with different KOH solutions and membrane thicknesses.

In the third and fourth studies, two cell configurations were tested to evaluate the performance of an alkaline H_2-I_2 fuel cell. The first cell configuration, shown in Figure 4.1c, consisted of a single-phase reactant feed for the negative electrode. The second cell configuration, shown in Figure 4.1d, consisted of a two-phase reactant feed for the negative electrode. For the single-phase feed case (Study 3), we used the same cell components as the alkaline H_2-Br_2 fuel cell in the second study. To study the effect of KOH concentration on fuel cell performance, KOH solutions at 1M, 2M and 3M were fed to the KOH reservoir side of the hydrogen electrode at flow rates between 0.6 and 0.95 mL/min with a peristaltic pump while neat hydrogen gas at about 134 kPa absolute was fed to the other side of the electrode at a rate of approximately 660 mL/min using a recirculation pump. At the iodine electrode, a solution of 1M KBr/0.4M I_2 was fed at a flow rate of 1.5 mL/min with a peristaltic pump, corresponding to about 1.93 A/cm^2. This high flow rate and excess electrolyte represent attempts to ensure that the iodine concentration over the entire electrode's outer surface was constant during the discharge and charge cycle. Nafion 212 membrane in K^+-form was used in all H_2-I_2 runs.

For the two-phase feed case (Study 4), the KOH compartment was removed and different negative and positive electrode materials were used. 3M KOH solution was recirculated through

the negative electrode and the KOH flow rate was adjusted to obtain good performance. The best KOH flow rates were found to be 5.1 ml/min during discharge and 11.5 ml/min during charge. Higher KOH flow rate during charge was needed to purge the hydrogen gas generated in the negative electrode. An interdigitated flow field ensured that liquid KOH solution did not flood the negative porous electrode. To allow both gaseous hydrogen and aqueous KOH to reach the catalyst at the negative electrode, a single-layer 10% wet-proof Toray 060 gas diffusion layer was used as the catalyst layer support. In a previous study, we discovered that a highly hydrophobic MPL prevents liquid from passing through the MPL to reach the catalyst layer. The platinum catalyst loading in the negative electrode was 0.8 mg/cm^2 geometric area. To reduce transport and ohmic resistance while maintaining high active area in the positive electrode, a single layer of carbon nanotube (CNT) gas diffusion layer was used as the positive electrode. The CNT gas diffusion layer was synthesized in our lab for a prior acid-based H_2-Br_2 fuel cell study.[11, 12] The same H_2 and KI/I_2 flow rates used in the single-phase feed study were also used here. The main difference for this study is that both H_2 and KOH were injected directly to one side of the negative electrode, versus being injected into two separate compartments.

4.4 Results & Discussion

Study 1:

The objective of the first study was to validate the concept and feasibility of the alkaline H_2-Br_2 fuel cell system by showing that a higher cell and more negative hydrogen electrode potentials could be obtained, as well as demonstrate reversible discharge and charge performance. Figure 4.2a shows the cell and the individual half-cell voltages during one of the open circuit steps. Note the higher cell voltage and more negative voltage of the hydrogen electrode as a result of

operating the hydrogen reactions in an alkaline solution. Figure 4.2b shows the charge and discharge performance of the alkaline H_2-Br_2 fuel cell for the first study. The linear discharge and charge curves in Figure 4.2b suggests that most of the voltage loss in the system is due to ohmic resistances in the cell and confirms that the hydrogen (on platinum) and bromine reactions (on carbon) in the alkaline system are still quite fast. Next, the fact that the discharge curve for the full cell and hydrogen electrode show some mass transport effect at current densities greater than 15 mA/cm^2 highlights that the mass transport effect was at the hydrogen electrode. This mass transport effect could be attributed to the limited hydrogen diffusion rate through the liquid KOH electrolyte layer formed on the hydrophilic active area of the platinum electrode. Finally, the low performance observed in the first study can be attributed to the high internal resistance of the cell (~2.2 ohms). The high internal cell resistance can be attributed to using a thick membrane (183-micron Nafion 117), large gaps for KOH and KBr/Br_2 solutions, and edge current collection, especially for the solid carbon electrode.

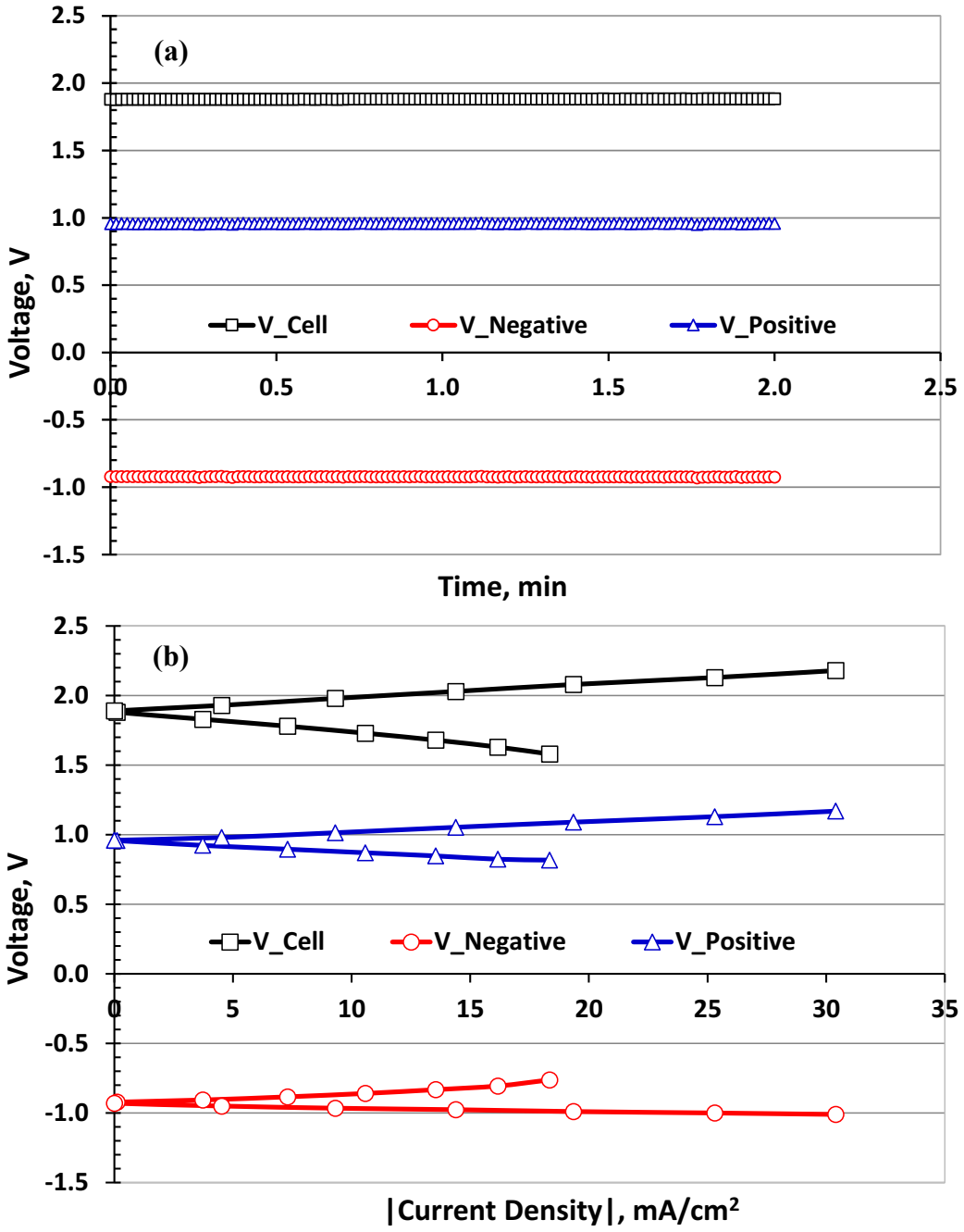

Figure 4.2. Study 1: Cell and individual electrode potentials of the alkaline H_2-Br_2 fuel cell during (a) open circuit and (b) charge and discharge.

Study 2:

After the concept and feasibility of the alkaline H_2-Br_2 fuel cell were validated in study 1, a second study was conducted to see if higher performance could be obtained by making some

modifications to the cell design. Modifications included using a porous hydrogen electrode with higher platinum catalyst surface area, thinner membranes, higher KOH concentration, and a porous bromine electrode with higher active surface area. For the hydrogen electrode, a high surface area porous electrode, similar to those used in H_2-O_2 proton exchange membrane fuel cells, was used. For the bromine electrode, two layers of porous carbon diffusion media instead of a solid carbon electrode were used to increase the active surface area. By using a porous electrode in which the positive electrolyte could be introduced into the electrode from the surface next to the flow field, the positive electrolyte compartment between the positive electrode and the membrane was eliminated. Carbon (for H_2) and tantalum (for Br_2) interdigitated flow field plates were used. Electrical current was collected in the direction normal to the surface of the electrodes as in a regular fuel cell. In this configuration, a porous glass-mat KOH reservoir layer was needed between the hydrogen electrode and the membrane to allow the cell to be compressed so that good electrical contact could be obtained between the electrodes and the current collector flow plates. Finally, thinner and less resistive membranes, 51-micron thick Nafion 212 and 127-micron thick Nafion 115, and higher (3M) KOH concentration were used to evaluate their effects on the fuel cell internal resistance and performance.

For study 2, Figure 4.3a shows the discharge and charge performance of the improved alkaline H_2-Br_2 fuel cell. The performance of the fuel cell in the first study was also included for comparison. Higher KOH concentration leads to more negative hydrogen electrode potential as described by the Nernst equation, thus higher cell OCV. To better illustrate the changes in the slope of the curves on the graph, the results in Figure 4.3a are replotted in Figure 4.3b where the vertical axis is changed to the cell voltage minus the OCV (i.e. essentially the overpotential of

the fuel cell). In this format, we can clearly see the effect of membrane thickness and KOH concentration on the slope of the polarization curves.

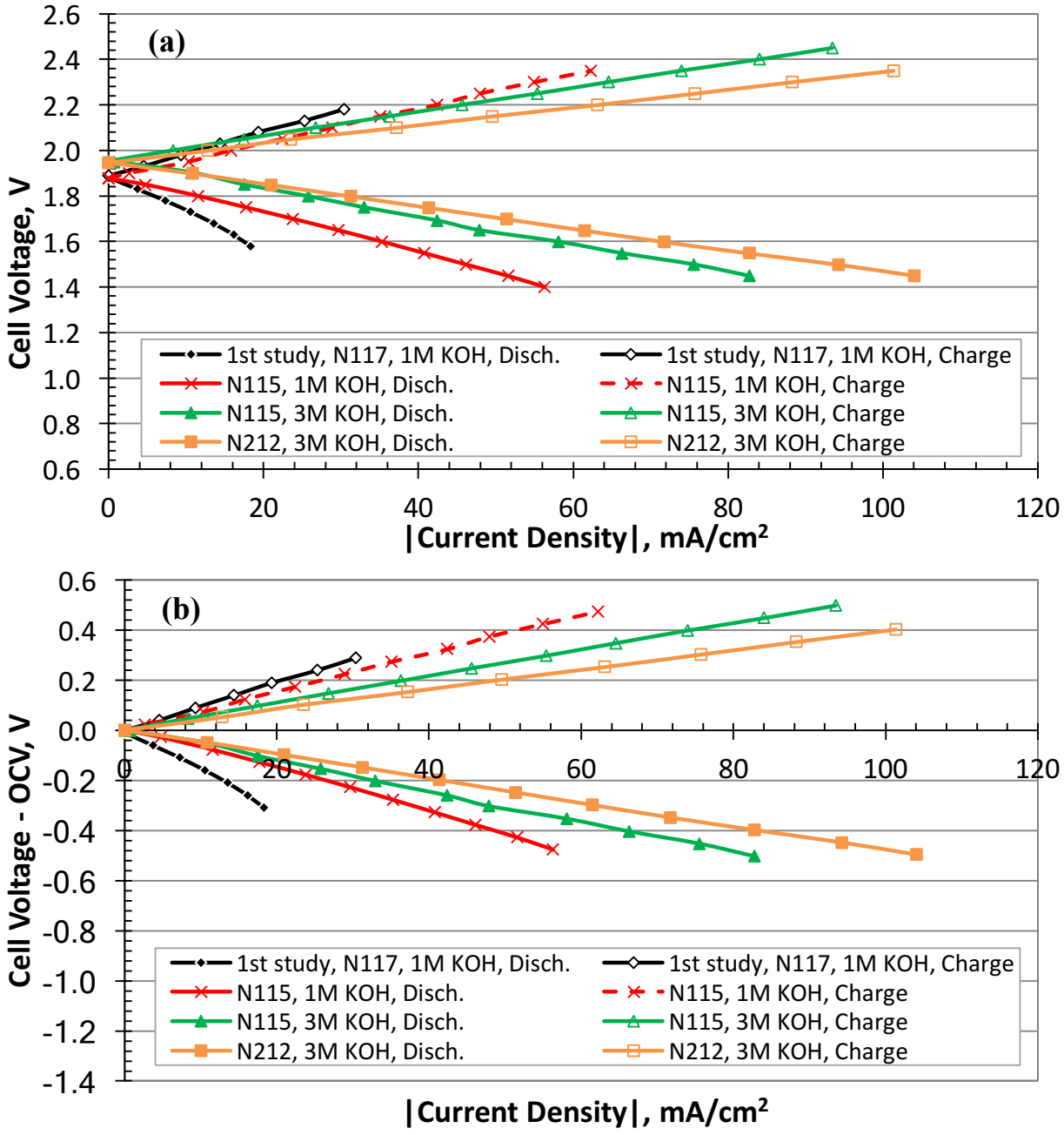

Figure 4.3. Studies 1 and 2: Effect of membrane thickness and KOH concentration on the performance of the alkaline H_2-Br_2 fuel cells, cell overpotential (cell voltage-OCV) was used in (b) to correct for different OCVs .

The results in Figure 4.3a and Figure 4.3b show that significant performance improvement was obtained in the second study when new electrode designs, interdigitated flow fields, thinner membranes and higher KOH concentrations were used. Both thinner membranes

and higher KOH concentrations led to lower slopes in the discharge and charge polarization curves and consequently higher fuel cell performance. The slopes of these curves represent all the resistances in the fuel cell such as electronic, ohmic, kinetics and transport resistances; so changes in the slope can be attributed with changes in the KOH concentration and membrane. Losses due to the electrical components such as the hydrogen and bromine electrodes, flow field plates, current collectors and electrical contact resistance are typically small, around 100 milliohms (or 44.4 milliohm cm^{-2}); while losses due to the ionic components such as the cation conducting membrane and electrolytes (KOH and KBr/Br_2) in the hydrogen and bromine half-cells are much higher. Note that high KOH concentration provides high ionic conductivity and high OH^- concentration, which is especially important during discharge. During discharge, the consumption of OH^- ions and generation of water by the hydrogen oxidation reaction can lead to a rapid decrease in the KOH concentration. This explains the smaller voltage losses obtained for charge than compared to discharge. During charge, water is consumed and KOH is generated making the electrolyte in the hydrogen electrode more conductive. For the alkaline-based H_2-Br_2 and H_2-I_2 reversible fuel cells, it is worth noting here that when KOH is produced at the negative electrode (increasing the ionic conductivity) during charge, KBr/KI is consumed at the positive electrode (decreasing the ionic conductivity). The opposite phenomenon occurs during discharge (ionic conductivity decreasing at the negative electrode and increasing at the positive electrode). Due to the combined effect of KOH production and H_2O consumption at the negative electrode, we expect the change in ionic conductivity at the negative electrode to have a larger impact on fuel cell performance than the change in the positive electrode's ionic conductivity. The best performance was obtained with 3M KOH solution and the 51-micron Nafion 212 membrane. The fuel cells with 3M KOH also benefit from a high open circuit voltage resulting from a more

negative hydrogen electrode potential. Note also that the discharge and charge curves remain linear while the cell current densities were much higher in this study. For the second study, the fuel cell performance is still dominated by the ohmic resistance in the cell. The previously observed mass transport effect in the hydrogen electrode at low current density in the first study has been resolved by the improved hydrogen electrode design.

In the second study, the fuel cell internal resistances were measured at the three conditions using EIS in order to determine the contribution of the ohmic resistance of the cell to the electrochemical performance. The overall cell internal resistance was measured by using the hydrogen electrode as the reference electrode. As shown in Figure 4.4, the intersection of the left-hand edge of each curve with the horizontal zero imaginary impedance occurs at high frequency and represents the pure ohmic resistance of the fuel cell. The intersection of the right-hand edge of each curve, before the 45-degree angle tail, occurs at lower frequency and represents the combined ohmic and charge transfer resistance in the fuel cell. The ohmic resistance (left-hand edge of the semicircle) was highest (~1.82 ohms) for the case with the thicker membrane (Nafion 115) and lower KOH concentration (1M). The lowest internal resistance (0.7 ohms) and best performance was obtained using the thinner membrane (Nafion 212) and higher KOH concentration (3M). The conductivity of the K^+-form membrane was measured, using a conductivity cell, to be about 0.006 S/cm (versus 0.070 S/cm for the same membrane in H^+-form). Based on the thickness (~51 μm for Nafion 212) and active area (2.25 cm^2) of the membrane, the resistance attributable to the membrane is about 0.4 ohm (best case). The high membrane resistance and the additional resistance of the KOH compartment result in the high internal resistance for these cells, which is about 7 to 10 times higher than of an acid-based H_2-Br_2 fuel cell. To obtain better performance, the internal resistance of the alkaline

system needs to be reduced further. Finally, the low charge transfer resistance, the difference between the combined resistance and the pure ohmic resistance, confirms that the kinetics of the hydrogen and bromine electrode reactions in this alkaline H_2-Br_2 fuel cell are quite fast.

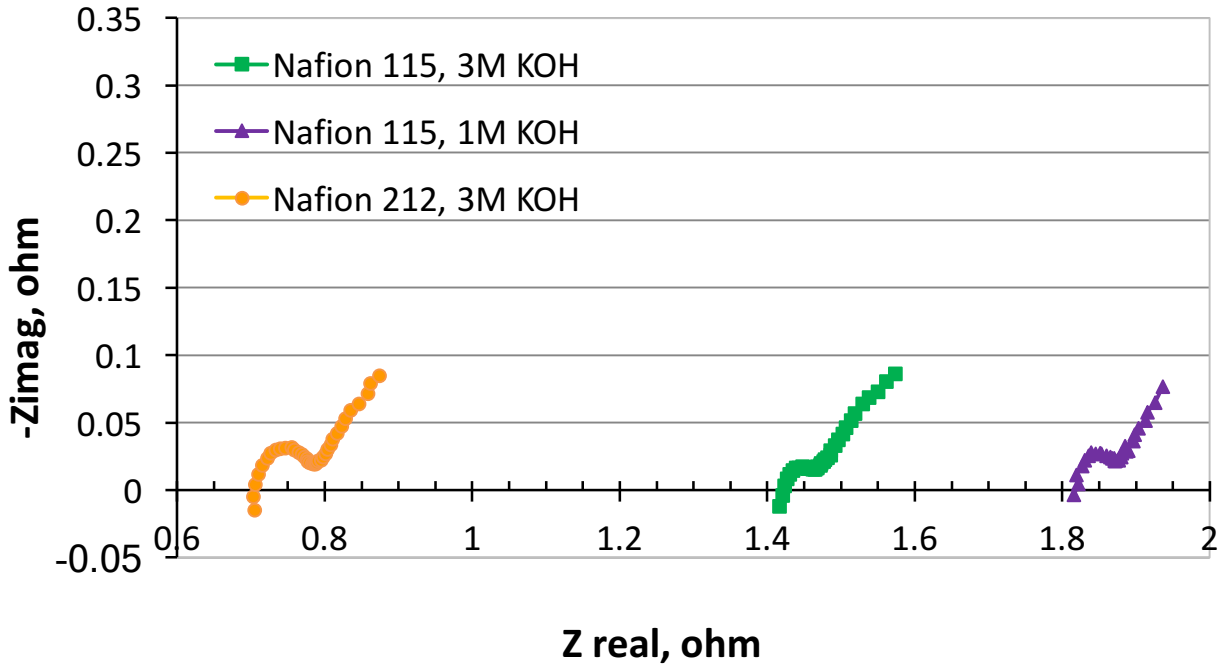

Figure 4.4. Study 2: Internal impedance of the alkaline H_2-Br_2 fuel cell with Nafion 115 & 212 membranes and different KOH concentrations.

In the second study, the internal resistances were used to remove the effect of the IR losses in the cell due to the different KOH concentrations and membrane thicknesses in order to evaluate the kinetic and transport effects. The IR-corrected cell voltages and overpotentials for these three runs are shown in Figure 4.5a and Figure 4.5b. The results in Figure 4.5b show that after the ohmic losses and the difference in the OCV due to KOH concentration are removed, then the performance of the 1M and 3M KOH concentration cases are quite similar. They showed similar voltage losses due to kinetics and concentration polarization at the two electrodes. At the lower 1M KOH concentration, there appears to be a more significant transport

effect during discharge and charge at current densities above 20 mA/cm^2. Finally, the power density for these runs are provided in Figure 4.6.

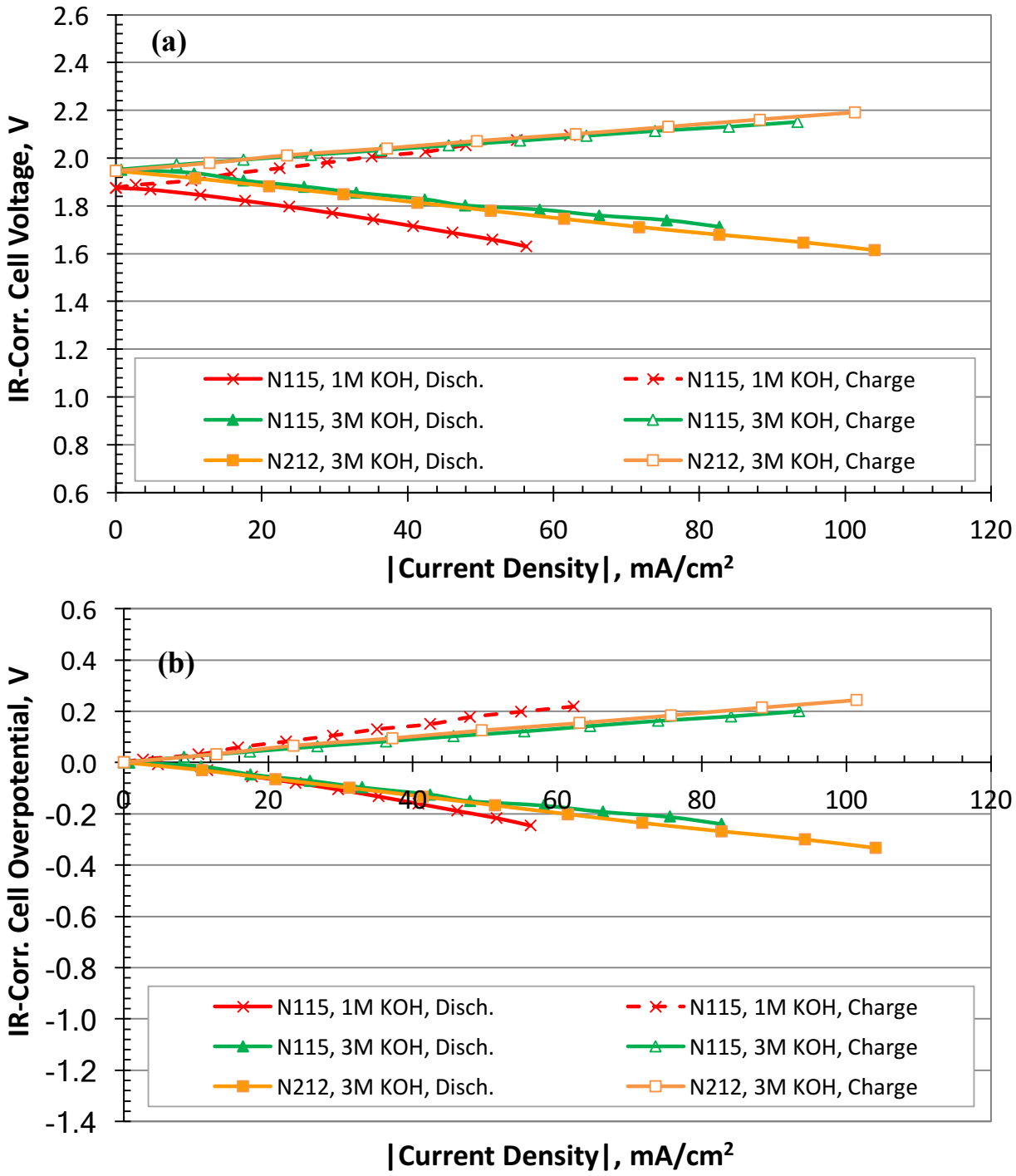

Figure 4.5. Study 2: IR corrected discharge and charge polarization curves of the alkaline H_2-Br_2 fuel cell, cell overpotential was used in (b) to correct for different OCVs.

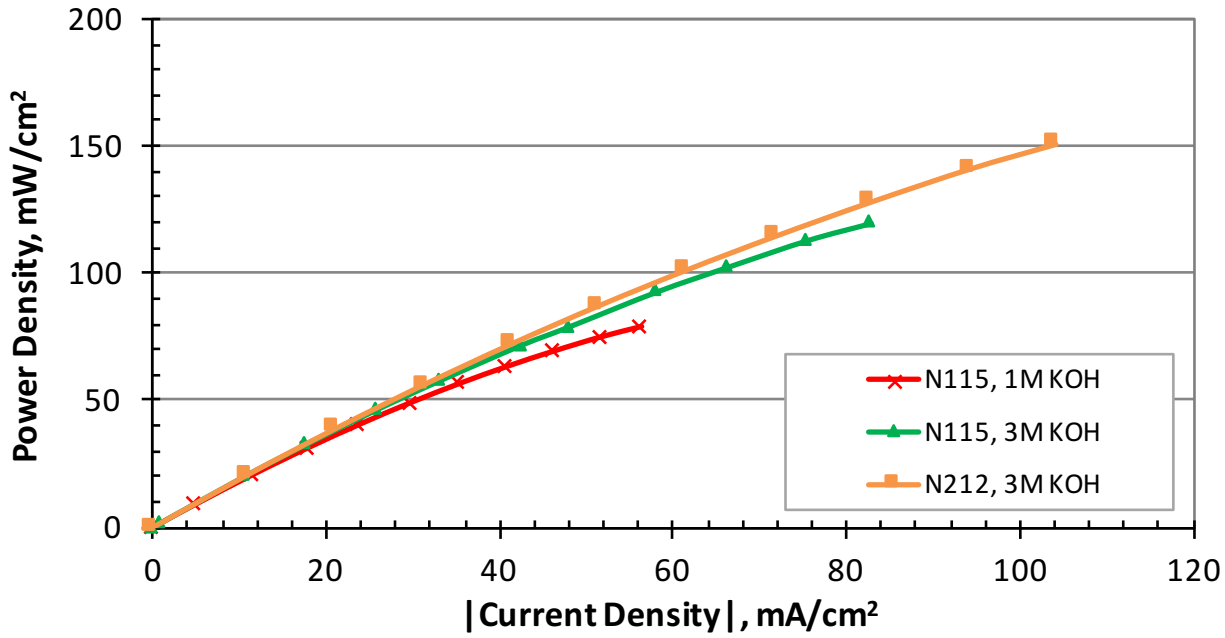

Figure 4.6. Study 2: Discharge power density of the alkaline H_2-Br_2 fuel cell tested with different KOH concentrations and membrane thicknesses.

Studies 3 and 4:

Studies 3 and 4 were completed to evaluate the performance of the alkaline H_2-I_2 fuel cell. As described earlier, two different cell configurations were used. The configuration shown in Figure 4.1c (for study 3) was used first to validate the concept and to evaluate the cell and individual electrode performances, as well as the effect of KOH concentration. The configuration shown in Figure 4.1d (for study 4) was used to evaluate the concept of two-phase (gaseous hydrogen and liquid KOH) reactant feed to the negative electrode.

For study 3, the full-cell and half-cell voltages at OCV are shown in Figure 4.7a. These results confirm the higher anticipated cell voltage and the more negative hydrogen reaction potential in an alkaline medium. Figure 4.7b shows the discharge and charge polarization curves for the same fuel cell at three different KOH concentrations (1M-3M). As observed in the H_2-Br_2 study, the OCV shifted higher and the discharge performance improved with increasing KOH

concentration. The charge performance did not vary much with increasing KOH concentration because during charge the hydrogen electrode reaction generates KOH and consumes H_2O, leading to higher conductivity and lower ohmic resistance in the electrode.

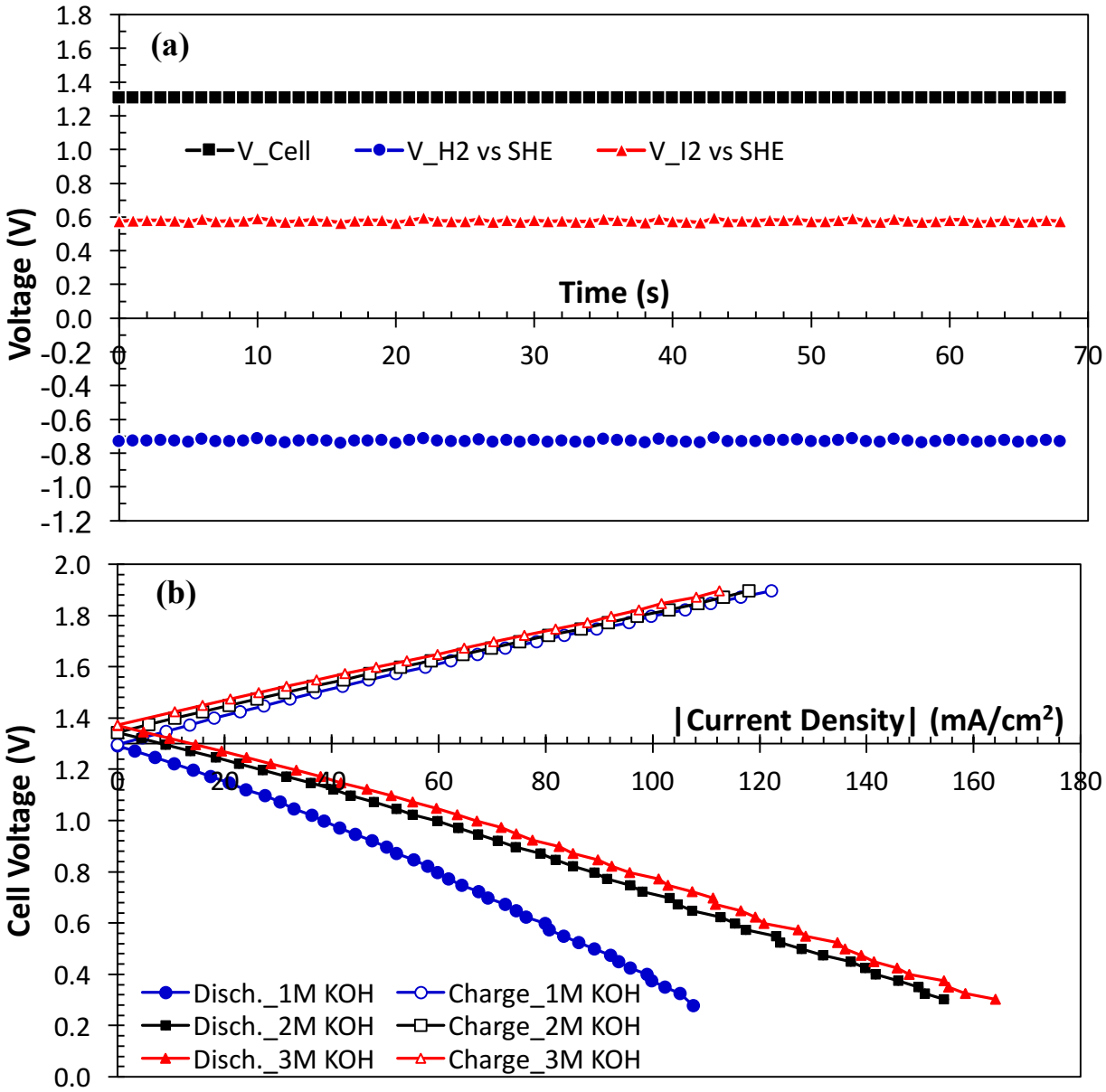

Figure 4.7. Study 3: Cell and individual electrode potentials of the alkaline H_2-I_2 fuel cell during (a) open circuit and (b) charge and discharge.

For study 3, we were able to measure the internal resistance of the full cell and two half-cells by inserting a platinum wire into the KOH compartment. For the 1M KOH case, the resistances were measured to be 2.2 ohms for the full cell, 0.65 ohms for the hydrogen half-cell, and 1.55 ohms for the iodine half-cell. The cell internal resistance is quite high, higher than that of the alkaline H_2-Br_2 cells, and could be attributed to the higher contact resistance between the

current collectors, flow field plates and gas diffusion electrodes due to using a low cell compression (< 788 kPa versus 1475 kPa). A low cell compression was used in order to avoid crushing the glass fiber mat in the KOH compartment. Note that with the location of the platinum sensing wire, the internal resistance of iodine half-cell includes the resistance of the K^+-form Nafion membrane and most of the KOH solution in the negative electrolyte compartment. Based on the conductivity, thickness (~51 μm), and active area (2.25 cm^2) of the K^+-form Nafion 212 membrane, the resistance attributable to the membrane is about 0.4 ohm. Based on the thickness of the KOH compartment (1 mm) and the conductivity of 1M KOH (~0.2 S/cm), the contribution of the KOH compartment to the cell resistance is about 0.2 ohms or more. The high remaining resistances of the two half-cells were attributed, as mentioned earlier, to the high contact resistance between the components in the cell. This problem could be minimized by eliminating the KOH compartment in order to allow higher cell compression.

In order to remove the effect of ohmic losses in the cell so that the effect of kinetics and mass transport on cell performance could be evaluated, the cell voltages were corrected for IR-loss using the cell impedance measured at open circuit. The resulting polarization curves are shown in Figure 4.8a and Figure 4.8b. Figure 4.8a shows the IR-corrected cell voltage versus the absolute of the current density while Figure 4.8b shows the cell overpotential (difference between the cell IR-corrected voltage and cell OCV). Plotting the cell overpotential allows us to remove the effect of the KOH concentration on the OCV. From these results it is quite clear that the discharge performance of the H_2-I_2 fuel cell with 1M KOH at the flow rate used in the study shows significant mass transport effect, starting at current density as low as 20 mA/cm^2. This mass transport effect at low current density can be attributed to the rapid decrease in the OH^- concentration during discharge as a result of both OH^- consumption and the dilution effect from

H_2O generation on the hydrogen reaction. As shown in Figure 4.8b, the mass transport effect of OH^- depletion on the fuel cell discharge performance is reduced, but not eliminated, when higher KOH concentrations are used. It is worth pointing out here that since IR correction was done using the cell internal resistance at open circuit, some IR loss component still exists in the polarization curves at high current densities when the concentrations of active species continue to change. On the other hand, close observation of the charge curves reveals that the slope of the polarization curves decreases slightly as the current density increases. This is attributed to the production of OH^- and consumption of H_2O leading to higher KOH electrolyte conductivity in the hydrogen electrode and hence lower IR losses in the cell.

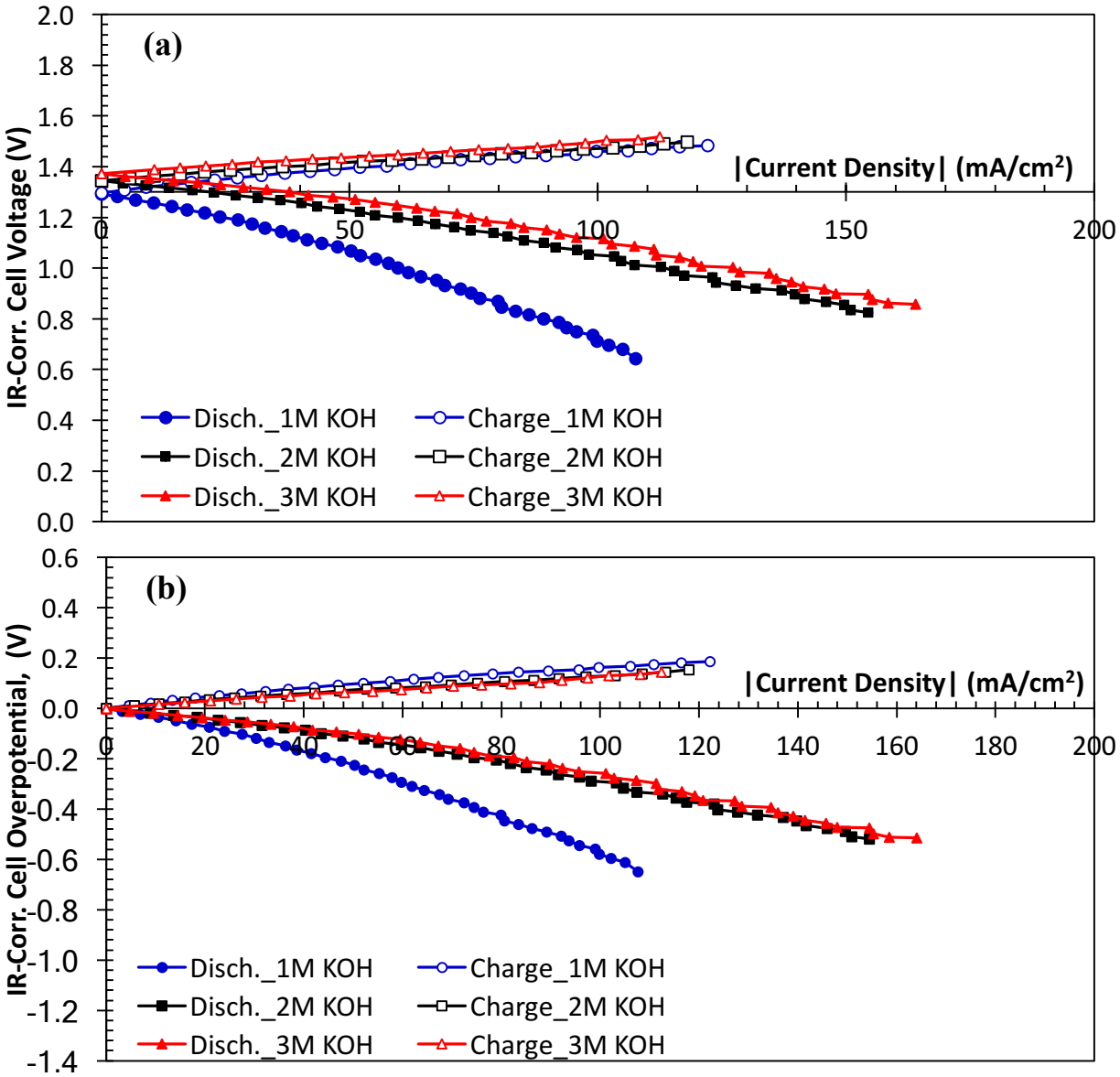

Figure 4.8. Study 3: IR corrected cell voltage (a) and cell overpotential (b) of the alkaline H_2-I_2 fuel cell showing better performance with increasing KOH concentration.

With the reference electrode and platinum sensing wires in the KOH compartment, the fuel cell performance can be separated into half-cell performances. The results can be used to identify the limiting electrode and limiting process at each electrode. Figure 4.9 shows the fuel cell discharge and charge polarization curves before and after IR correction for the 3M KOH

case. The discharge and charge curves for the hydrogen and iodine half-cells before and after IR correction are also provided in Figure 4.9. For IR correction, the half-cell resistances are measured using the Pt sensing wire in the KOH compartment as the reference electrode, whereas the full cell resistance is measured using the hydrogen electrode as the reference electrode. These results show that the iodine electrode performed much better than the hydrogen electrode. The iodine electrode exhibits very little activation and transport losses. The hydrogen electrode, whose reactions are known to be 2-3 orders of magnitude slower in alkaline media than acid media, [23] shows much higher activation loss during both charge and discharge, as well as significant transport polarization during discharge. A double dotted line extrapolated from the linear region of the discharge curve at low current density, representing the hydrogen polarization curve without transport resistance, is inserted to show the voltage loss that can be attributed to transport loss at the negative hydrogen electrode. This transport loss is associated with the difficulty of creating a three-phase (gas-liquid-solid) reactive surface and transporting gaseous hydrogen reactant simultaneously with liquid KOH to this surface. Finally, the power density curves for the three runs of study 3a are provided in Figure 4.10. The power densities of this alkaline fuel cell system are not as high as those of the H_2-Br_2 system because of its lower fuel cell voltage.

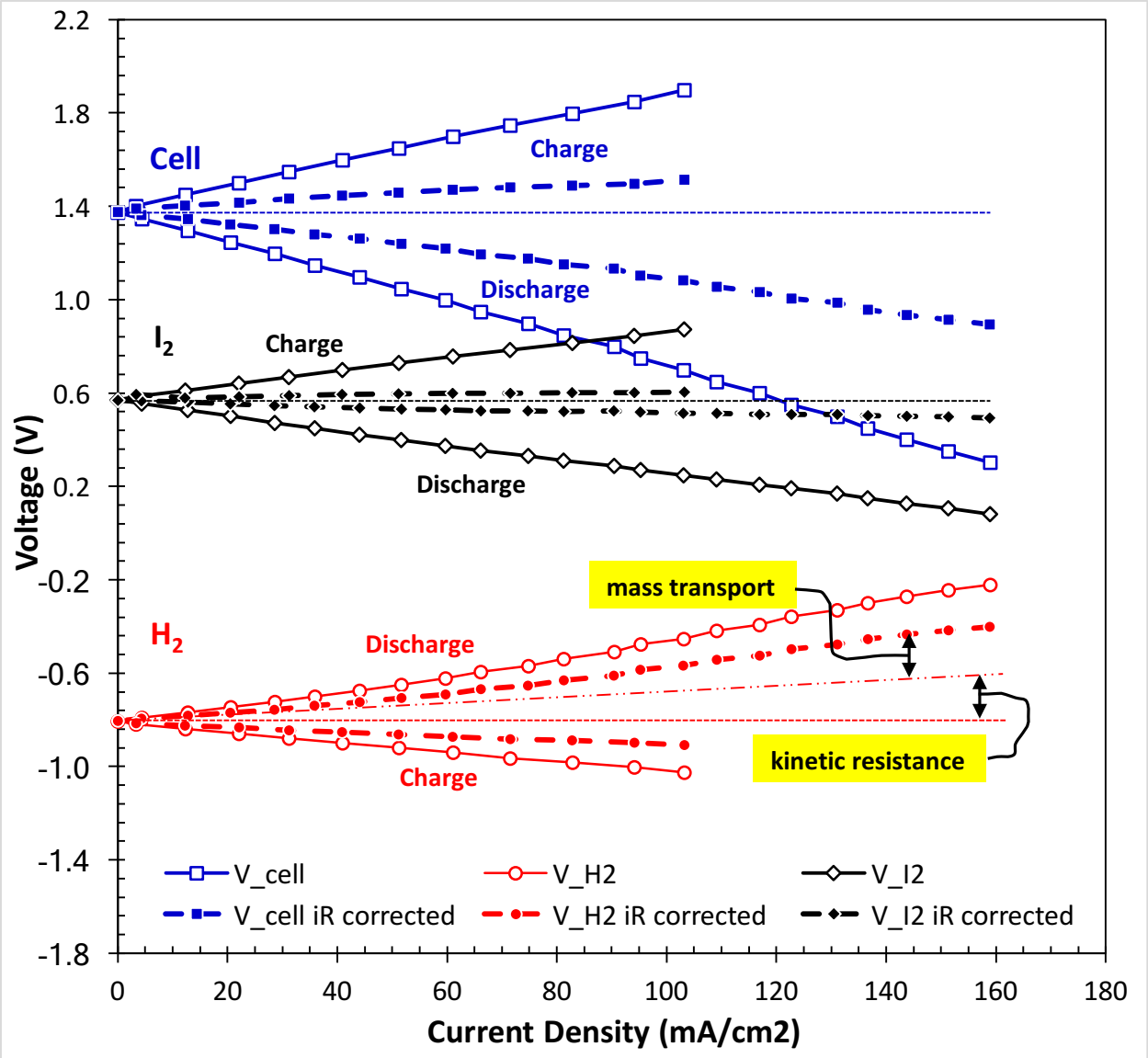

Figure 4.9. Study 3: Polarization curves of the full cell, H_2 half-cell, and I_2 half-cell of the alkaline H_2-I_2 fuel cell with 3M KOH concentration before and after IR correction. Results show the fuel cell performance is dominated by the H_2 electrode.

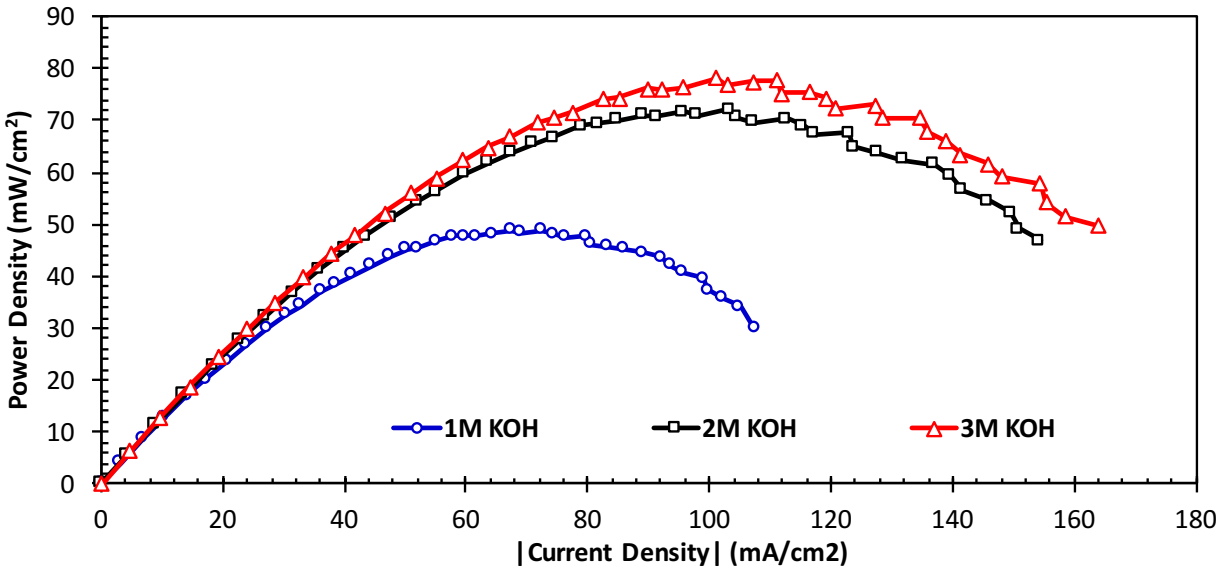

Figure 4.10. Study 3: Discharge power density of the alkaline H_2-I_2 fuel cell tested with different KOH concentrations.

Finally, the alkaline H_2-I_2 fuel cell system with two-phase reactant feed (study 4) at the negative electrode was evaluated. A 3M KOH solution was used for this study. By using two-phase feed, the KOH compartment was eliminated. This resulted in a reduction in the cell internal resistance from 2.2 ohms to 1.3 ohms, lower ohmic slope in the polarization curve during discharge and charge, and better performance as shown in Figure 4.11a and Figure 4.11b. The cell open circuit voltage was slightly shifted because of the higher hydrogen gas pressure needed to force liquid KOH out of the electrode. Peak power increased by 36% with this new two-phase feed configuration. The IR-corrected results in Figure 4.11b, with visual compensation for the vertical shift in the OCV, show reduced mass transport effect during discharge with this new feed approach. To confirm that the improved mass transport effect was at the negative hydrogen electrode, the cell IR-corrected voltage was decomposed into half-cell IR-corrected overpotentials using the reference electrode. The reference electrode was ionically connected to the positive electrode through a KI electrolyte bridge. Note that due to the location

of the reference electrode, the IR voltage loss in the cell was applied to the hydrogen half-cell. From the results in Figure 4.12, it is clear that the overpotential at the iodine electrode was quite small and most of the kinetic and mass transport losses in the fuel cell were attributed to the hydrogen electrode. As before, two dash lines extrapolated from the linear region at low current density were inserted to help separate the voltage loss due to mass transport from that of kinetics. During discharge, mass transport effect started at low current density (~30 mA/cm^2) and is attributed to the rapid decrease in OH^- concentration. During charge, the mass transport effect started at a higher current density (~ 90 mA/cm^2) and is attributed to the increase in the hydrogen gas evolution rate. The increase in hydrogen gas production decreases the transport rate of aqueous KOH to the negative electrode's surface. Since water is consumed at the negative electrode during charge, the shortage of aqueous KOH solution leads to a sharp increase in the overpotential.

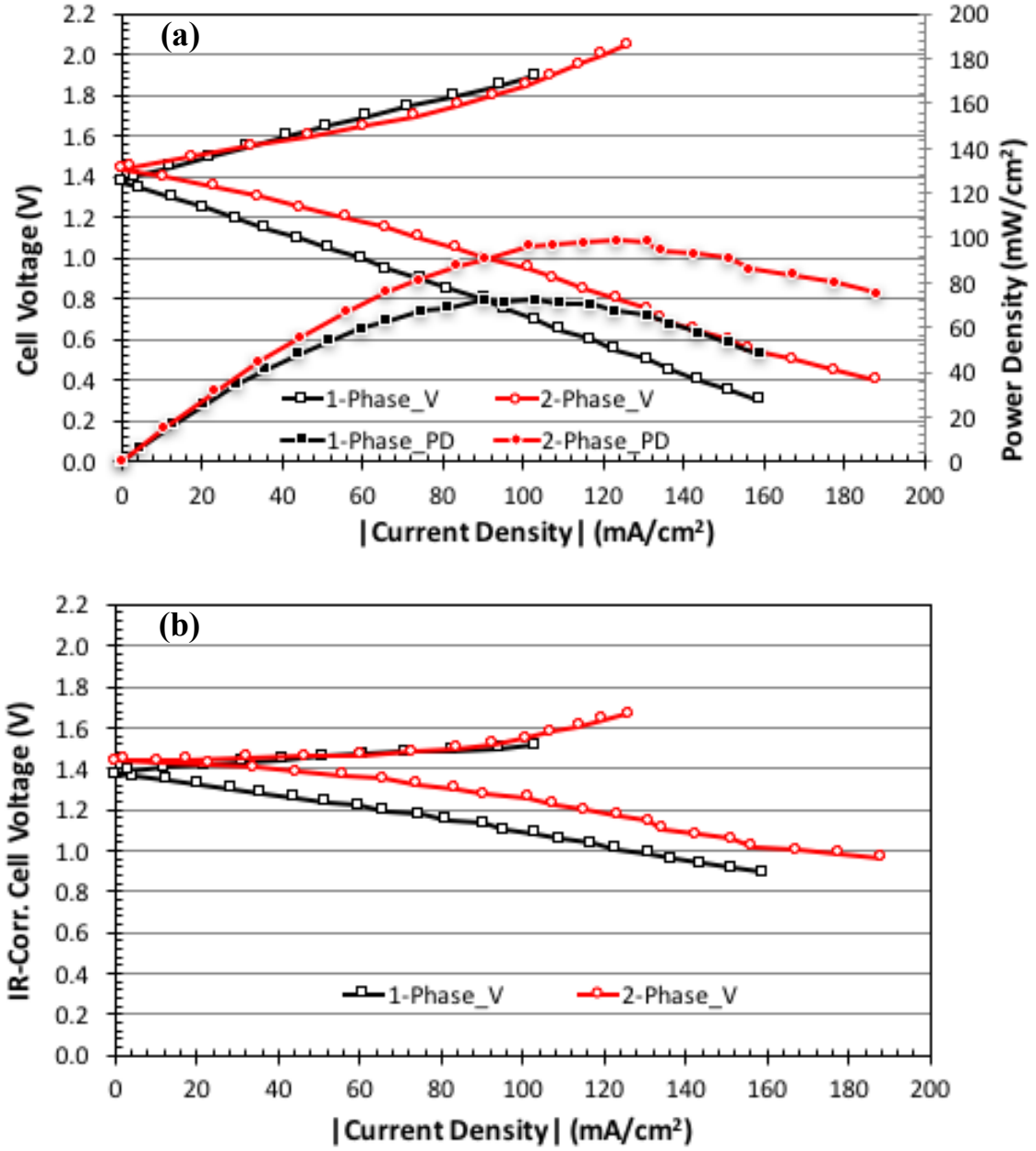

Figure 4.11. Study 4: Polarization and discharge power density curves of the alkaline H_2-I_2 fuel cell tested at 3M KOH with two-phase negative electrode in configuration 3d in comparison to single-phase electrode in configuration 3c, before (a) and after (b) IR correction.

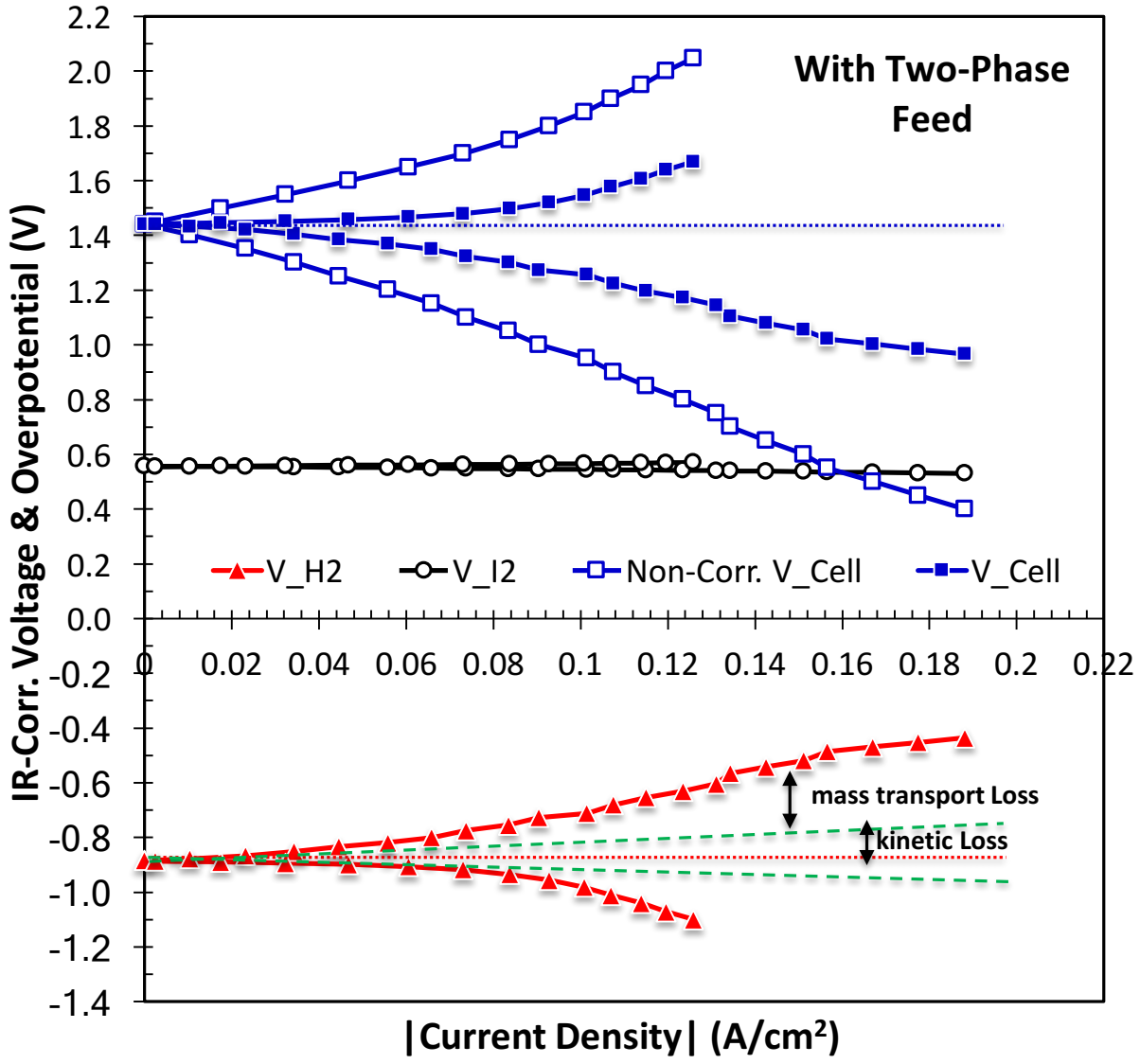

Figure 4.12. Study 4: IR-corrected polarization curves of the full cell, H_2 half-cell, and I_2 half-cell of the alkaline H_2-I_2 fuel cell with 3M KOH concentration and two-phase negative electrode feed. Results show the performance of this H_2-I_2 fuel cell is still dominated by the H_2 electrode.

4.5 Summary

The alkaline H_2-Br_2 and H_2-I_2 fuel cells are attractive because of their advantages over the acid systems such as higher cell voltage and lower cost catalysts for the hydrogen evolution and oxidation reactions. Fuel cells were assembled to validate the feasibility of these alkaline systems and to evaluate their performance under various configurations and conditions. Some of the

conditions evaluated were high KOH concentration and thinner cation exchange membranes. For the alkaline H_2-I_2 fuel cell, two configurations were used to evaluate the effectiveness of single-phase versus two-phase reactant feed for the hydrogen reaction at the negative electrode.

The results confirmed that the alkaline H_2-Br_2 and H_2-I_2 fuel cells have a higher cell voltage than the acid system, while maintaining fast electrode reaction kinetics like in the acid system. However, the performance of these alkaline systems is currently limited by high internal resistance of the existing electrode and cell design. A significant fraction of the internal resistance is caused by the low ionic conductivity of the K+ conducting membranes. The discharge and charge performances of these systems are controlled by the performance of the hydrogen negative electrode. A porous electrode that has more optimal three-phase distribution and can handle two-phase feed is expected to have a major impact on fuel cell performance. Future studies should include long-term durability testing of these alkaline fuel cell systems. During long-term operation, hydroxide crossover could cause an increase in the positive electrolyte pH over time and may impact long-term performance. Other areas for future studies should include non-precious alloy catalysts with high hydrogen oxidation and evolution (HER/HOR) activity, more conductive and perm-selective membranes, and evaluation of the effect of chemical products that could form from the crossover of OH^-, Br^- and Br_2.

4.6 Acknowledgments

This work was funded in part by the National Science Foundation through grant number EFRI-103234 and the Research Grants Council of Hong Kong through a General Research Fund (GRF HKU 700210P).

4.7 References for Chapter 4

1. V. Livshits, A. Ulus and E. Peled, *Electrochemistry Communications*, **8**, 1358 (2006).

2. K. T. Cho, P. Albertus, V. Battaglia, A. Kojic, V. Srinivasan and A. Z. Weber, *Energy Technology*, **1**, 596 (2013).

3. K. T. Cho, P. Ridgway, A. Z. Weber, S. Haussener, V. Battaglia and V. Srinivasan, *Journal of The Electrochemical Society*, **159**, A1806 (2012).

4. A. Ivanovskaya, N. Singh, R. F. Liu, H. Kreutzer, J. Baltrusaitis, T. V. Nguyen, H. Metiu and E. McFarland, *Langmuir : the ACS journal of surfaces and colloids*, **29**, 480 (2013).

5. H. Kreutzer, V. Yarlagadda and T. V. Nguyen, *Journal of The Electrochemical Society*, **159**, F331 (2012).

6. G. Lin, P. Chong, V. Yarlagadda, T. V. Nguyen, R. J. Wycisk, P. N. Pintauro, M. Bates, S. Mukerjee, M. C. Tucker and A. Z. Weber, *Journal of The Electrochemical Society*, **163**, A5049 (2016).

7. J. Masud, T. V. Nguyen, N. Singh, E. McFarland, M. Ikenberry, K. Hohn, C. Pan and B. Hwang, *Journal of The Electrochemical Society*, **162**, F455 (2015).

8. J. Park, R. Wycisk, P. Pintauro, V. Yarlagadda and T. V. Nguyen, *Materials*, **9**, 143 (2016).

9. M. C. Tucker, K. T. Cho, A. Z. Weber, G. Lin and T. Van Nguyen, *Journal of Applied Electrochemistry*, **45**, 11 (2014).

10. V. Yarlagadda, R. P. Dowd, J. W. Park, P. N. Pintauro and T. V. Nguyen, *Journal of The Electrochemical Society*, **162**, F919 (2015).

11. V. Yarlagadda, G. Lin, P. Chong and T. V. Nguyen, *Journal of The Electrochemical Society*, **163**, A5134 (2016).

12. V. Yarlagadda, G. Lin, P. Chong and T. V. Nguyen, *Journal of The Electrochemical Society*, **163**, A5126 (2016).

13. T. V. Nguyen, V. Yarlagadda, G. Lin, G. Weng, C. Li and K. Chan, *ECS Transactions*, **58**, 29 (2014).

14. S. Lu, J. Pan, A. Huang, L. Zhuang and J. Lu, *Proceedings of the National Academy of Sciences*, **105**, 20611 (2008).

15. W. Sheng, A. P. Bivens, M. Myint, Z. Zhuang, R. V. Forest, Q. Fang, J. G. Chen and Y. Yan, *Energy & Environmental Science*, **7**, 1719 (2014).

16. G. Boschloo and A. Hagfeldt, *Accounts of Chemical Research*, **42**, 1819 (2009).

17. A. Hauch and A. Georg, *Electrochimica Acta*, **46**, 3457 (2001).

18. B. Li, Z. Nie, V. Murugesan, E. Thomsen, D. Reed, J. Liu, W. Wang and V. Sprenkle, in *Electrochemical Society Spring 2015 Meeting*, Abstract No. 684, Chicago, Illinois (2015).

19. Q. Zhao, Y. Lu, Z. Zhu, Z. Tao and J. Chen, *Nano Letters*, **15**, 5982 (2015).

20. Y. Zhao, L. Wang and H. R. Byon, *Nature Communications*, **4**, 1896 (2013).

21. T. V. Nguyen, *Journal of The Electrochemical Society*, **143**, L103 (1996).

22. T. V. Nguyen and W. He, in *Handbook of Fuel Cells: Fundamentals, Technology, and Applications, (Volume 1) W. Vielstich, A. Lamm, and H. A. Gasteiger (editors)*, W. Vielstich, A. Lamm and H. Gasteiger Editors, p. 325, Wiley, New York, NY (2003).

23. W. Sheng, H. A. Gasteiger and Y. Shao-Horn, *Journal of The Electrochemical Society*, **157**, B1529 (2010).

CHAPTER 5: Performance Evaluation of a Hydrogen-Vanadium Reversible Fuel Cell

5.1 Abstract

Hydrogen-vanadium reversible fuel cells were tested using a Pt/C hydrogen electrode, carbon vanadium electrode and interdigitated flow fields at both electrodes. Vanadium electrolyte flow rate was varied to study its effect on mass transport performance. Two types of vanadium electrodes were explored, a single layer of high surface area carbon nanotube (CNT) electrode and three layers of nitric acid-treated carbon paper. Finally, four types of Nafion membranes were examined to determine the effect of membrane type and thickness on fuel cell charge and discharge performance. Higher performance was observed with higher vanadium flow rate, thinner membranes and a CNT vanadium electrode. Peak power density of greater than 540 mW/cm^2 was obtained using a NR212 membrane and CNT vanadium electrode.

5.2 Introduction

Hydrogen-vanadium fuel cells offer a feasible solution for storing electrical energy from the grid or directly from renewable energy sources such as wind and solar.[1] In a hydrogen-vanadium reversible fuel cell, the charge and discharge reactions are as follows:

Vanadium (+) Electrode: $2VO^{2+} + 2H_2O \underset{discharge}{\overset{charge}{\rightleftarrows}} 2VO_2^+ + 4H^+ + 2e^-$,

$$\boldsymbol{E^o_{red} = +0.99\ V} \qquad \textbf{[1]}$$

H_2 (−) Electrode: $2H^+ + 2e^- \underset{discharge}{\overset{charge}{\rightleftarrows}} H_2$,

$$\boldsymbol{E^o_{red} = +0.0\ V} \qquad \textbf{[2]}$$

Overall Reaction: $2VO^{2+} + 2H_2O \underset{discharge}{\overset{charge}{\rightleftarrows}} 2VO_2^+ + 2H^+ + H_2$,

$$E^o_{cell} = +0.99 \text{ V} \quad [3]$$

While charging, a hydrogen-vanadium fuel cell stores energy in the form of hydrogen and vanadium (V). During discharge, hydrogen is consumed at the negative electrode and vanadium (V) is reduced to vanadium (IV) at the positive electrode. Vanadium systems demonstrate no issues with membrane fouling or metal dendrite formation (e.g. iron and zinc electrode systems).[2, 3] Additionally, vanadium solutions have low volatility, low corrosivity, and do not produce toxic vapors. [4, 5] In particular, cells that utilize chlorine or bromine pose a significant safety concern due to their high vapor pressures and toxic properties.[6-8] Due to the relatively high cost of vanadium, the hydrogen-vanadium fuel cell is attractive over the all-vanadium system due to the 50% reduction in the amount of vanadium solution required. Since the cost of the vanadium electrolyte for the all-vanadium flow battery makes up roughly 40% of the total system cost, cutting the vanadium electrolyte requirement by half has a large impact on reducing the overall system cost.[1] Another benefit of a mixed gas/liquid electrolyte system (hydrogen gas at the negative electrode and liquid vanadium at the positive electrode) is the ease of separation if crossover occurs. Unfortunately, one of the major disadvantages of the hydrogen-vanadium system compared to the all-vanadium system is that a precious metal catalyst is required for HOR/HER at the hydrogen electrode.

Past research by Yufit et. al. has shown the feasibility of the hydrogen-vanadium fuel cell and the importance of vanadium electrode wettability on fuel cell performance.[9] The wettability of the vanadium electrode is important for two reasons. First, only wetted area or area with access to the electrolyte is active, and second, a more wetted porous electrode allows vanadium

electrolyte to more easily flow into and through the porous carbon electrode. The vanadium reaction is a one-phase (liquid) reaction involving solely aqueous ions and water. Yufit et al. achieved a peak performance of 114 mW/cm^2 using a vanadium flow rate of 200 mL/min and a catalytic active area of 25 cm^2. Additionally, studies by Menictas et. al. also revealed crossover of vanadium species during operation of the vanadium-oxygen fuel cell, sparking our interest in vanadium's effect on the hydrogen electrode catalyst.[10] Furthermore, Xie et. al. examined vanadium permeability through different proton exchange membranes, including XL100, NR211, NR212, N115, and N117. His group found that certain processing and pretreatment conditions could significantly reduce the permeability of vanadium, but the changes were largely absent after repeated fuel cell cycling.[11] Houser et. al. and other research groups have performed extensive optimization studies on the all-vanadium flow battery, but little work has been done thus far on the reversible hydrogen-vanadium fuel cell.[12, 13]

In this study, we examine the performance of a reversible hydrogen-vanadium fuel cell when using a Pt/C hydrogen electrode, a high surface area carbon electrode as the vanadium electrode, and interdigitated flow fields at both electrodes. First, we studied the effect of varying the vanadium electrolyte flow rate on fuel cell performance. Then, two different carbon electrodes were tested for the vanadium side to determine their effect on performance. In the first case, a carbon nanotube (CNT) vanadium electrode was tested. The high surface area CNT electrode was used in previous studies in a hydrogen-bromine fuel cell with remarkable performance.[14, 15] In the second case, 3 layers of nitric acid-treated SGL 10AA were used as the vanadium electrode. Finally, we explored the effect of membrane type (extruded versus solution-cast) and thickness on fuel cell performance.

5.3 Experimental

Three different studies were completed on the hydrogen-vanadium reversible fuel cell. In the first study, vanadium electrolyte flow rate was varied to determine the effect on mass transport performance at high current densities. For the second study, two types of vanadium electrodes were tested. In the third study, different proton exchange membrane types and thicknesses were explored. Table 5.1 lists the key parameters used for each study.

Table 5.1. Experimental Conditions.

Study #	**1**	**2**	**3**
Experimental Control	Vanadium electrolyte flow rate	Positive electrode type	Membrane type
Negative Electrode	SGL 35BC GDL coated with Pt/C/PTFE layer (0.48 mg Pt/cm^2)	SGL 35BC GDL coated with Pt/C/PTFE layer (0.48 mg Pt/cm^2)	SGL 35BC GDL coated with Pt/C/PTFE layer (0.48 mg Pt/cm^2)
Positive Electrode	3 layers of nitric acid-treated SGL10AA	Either 1 layer of CNT electrode or 3 layers of nitric acid-treated SGL10AA	3 layers of nitric acid-treated SGL10AA
Membrane	N115	N211	N115, N117, NR211, or NR 212
Flow Fields	Tantalum interdigitated flow fields	Tantalum interdigitated flow fields	Tantalum interdigitated flow fields
Electrolyte Composition	1M vanadium(V), 1M vanadium(IV) 3M sulfuric acid (H_2SO_4) at 50% state of charge (SOC)	1M vanadium(V), 1M vanadium(IV) 3M sulfuric acid (H_2SO_4) at 50% state of charge (SOC)	1M vanadium(V), 1M vanadium(IV) 3M sulfuric acid (H_2SO_4) at 50% state of charge (SOC)
Electrolyte Flow Rate	5 mL/min, 6 mL/min, or 12 mL/min	12 mL/min	12 mL/min
H_2 Pressure	0.136 MPa	0.136 MPa	0.136 MPa

Vanadium electrolyte solution (500 mL) was prepared of 1M vanadium(V) and 1M vanadium(IV) by dissolving the appropriate amount of vanadyl sulfate (Sigma Aldrich) in 3M

sulfuric acid (H_2SO_4) and then charging the fuel cell to 50% state of charge (SOC) to make vanadium(V). Excess electrolyte was used to ensure that the electrolyte concentration remained relatively constant during the polarization measurements. The membrane electrode assembly (MEA) was prepared by either one of two ways. In the first method, the MEA was prepared by hot pressing a proton exchange membrane onto a 3 cm by 3 cm Pt-coated GDL (0.45 mg/cm^2 Pt loading, 0.16 mg/cm^2 Nafion ionomer, SGL35BC from TVN Systems, Inc.). In the second method, the MEA was prepared by hot pressing a proton exchange membrane between a 3 cm by 3 cm Pt-coated GDL (0.45 mg/cm^2 Pt loading, 0.16 mg/cm^2 Nafion ionomer, SGL35BC from TVN Systems, Inc.) and a nitric acid-treated 3 cm by 3 cm GDL (SGL10AA from Ion Power, Inc.) that was coated with Nafion solution on one side to allow hot pressing. SGL35BC electrode thickness was ~320 μm. The catalyst layer (loading of 0.45 mg/cm^2 Pt, 0.16 mg/cm^2 Nafion ionomer) was sprayed directly onto the microporous layer side of SGL35BC. TVN Systems, Inc. reported that the Pt catalyst used for the catalyst layer is commercially available (Tanaka) with Pt particle diameter of 1-2 nm. Commercially available membranes were purchased from Ion Power Inc. (DE, USA). MEAs were made using NR211 (~25 um thick), NR212 (~51 um thick), N115 (~127 um thick), or N117 (~183 um thick). Hot pressing was completed at 135ºC and 0.552 MPa (80 psi) for 5 min. Assembly of the fuel cell was carried out at 1.103 MPa (160 psi) using expanded polytetrafluoroethylene (PTFE) gaskets and interdigitated tantalum flow fields with 9.0 cm^2 flow area. The interdigitated flow field dimensions were 1.5 mm channel width, 1 mm channel depth and 2.5 mm shoulder width.

The vanadium electrode consisted of either a single CNT electrode or 3 layers of nitric acid-treated SGL10AA. The CNT electrode was prepared by growing nanotubes onto SGL10AA carbon paper using chemical vapor deposition as outlined in reference 14. Nitric acid-treated

SGL10AA was made using a 3-step process in order to improve electrode wettability. First, SGL10AA carbon paper was submerged in water while evacuating the air above the water using a vacuum pump at 0.03 MPa for 5 min. Then, the carbon paper was soaked in 2M nitric acid for 24 h. Lastly, the carbon paper was thoroughly rinsed in deionized water and dried. 3 layers of SGL10AA were tested as the vanadium electrode because previous studies found that a single layer of SGL10AA did not have sufficient active area to provide high current density operation and when more than 3 layers were used the negative effect of increased transport distance from a thicker electrode became more dominant than the positive effect of having higher active surface area.[14, 15] In our previous studies with CNT electrodes in the hydrogen-bromine fuel cell we found that a single layer of CNT electrode on the bromine side yielded similar to or better performance than 3 layers of SGL10AA. The CNTs, which were grown onto the GDL carbon fibers, increase the active surface area available for the vanadium reaction while maintaining the same electrode thickness and transport distance of a single layer of SGL10AA electrode (~350 um). Increased electrode thickness (i.e. 3 layers of SGL10AA) leads to greater transport distance and fuel cell resistance, therefore making a single layer CNT electrode more attractive than using 3 layers of SGL10AA.

Fuel cell testing was completed using a hydrogen pressure of 0.136 MPa (5 psig) and vanadium electrolyte flow rate of 5, 6, or 12 mL/min (Equivalence of 1.55, 1.86, and 3.72 A/cm^2, respectively, for the vanadium (V) concentration used, 1.735M at an OCV of 1.09V). All testing was completed at room temperature (~23ºC). The start-up procedure included cycling the reversible fuel cells in charge (1.3 V) and discharge modes (0.6 V) every 10 min for over 12 h. Prior to collecting all discharge and charge polarization curves, the vanadium electrolyte was charged to ~90% SOC. Multiple polarization curves were collected to ensure adequate

membrane hydration and repeatable results.

Electrochemical impedance spectroscopy (EIS) was conducted on the hydrogen-vanadium fuel cell after operation in order to measure the total resistance of the fuel cell. EIS was also conducted on the fuel cell without the membrane in order to measure the electronic resistance of the fuel cell. Figure 5.1 shows the assembly layout for the reversible hydrogen-vanadium fuel cell.

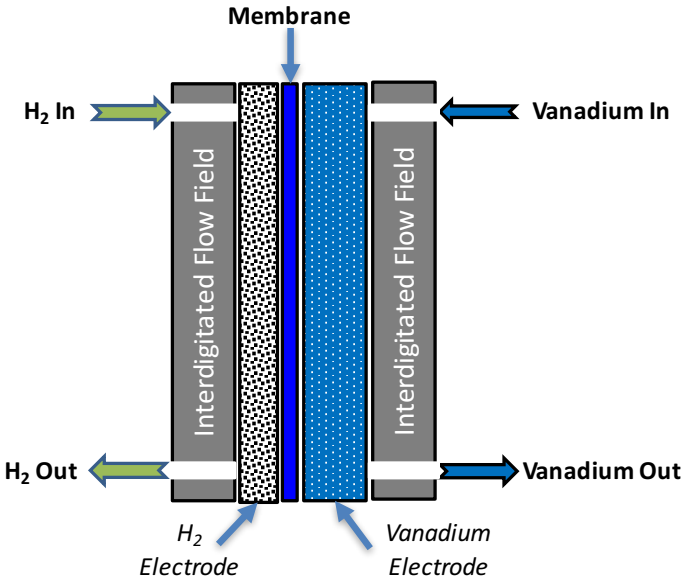

Figure 5.1. Hydrogen-vanadium reversible fuel cell

5.4 Results and Discussion

Due to charging the vanadium electrolyte solution to ~90% SOC prior to collecting polarization curves, the open circuit potential (OCV) for the hydrogen-vanadium reversible fuel cell was approximately 1.09 V (as predicted by the Nernst equation). All polarization curves have been normalized using the OCV (i.e. cell voltage minus OCV) in order to more easily compare all cases. Figure 5.2 shows the polarization and discharge power density curves for the hydrogen-vanadium fuel cell using various vanadium flow rates (Study 1). We observe better mass

transport performance at higher current densities as we increase the vanadium flow rate from 5 mL/min to 6 mL/min (1.55 and 1.86 A/cm^2, respectively, at the concentration used). During discharge at 5 mL/min, we start to observe a mass transport effect at around 100 mA/cm^2 and limiting current at 230 mA/cm^2. During discharge at 6 mL/min, we start to observe a mass transport effect at around 250 mA/cm^2 and limiting current above 350 mA/cm^2. This significant increase in performance after a 20% increase in flow stoichiometry is attributed to better transport of active materials to and removal of products from the porous electrodes because of deeper penetration of the electrolyte into the electrodes due to using interdigitated flow fields.[16-19] When increasing the vanadium flow rate to 12 mL/min (3.72 A/cm^2 equivalence), we observe a more subdued increase in performance at higher current densities. Since the performance at 6 mL/min and 12 mL/min are similar, a vanadium flow rate of 12 mL/min is used for all subsequent studies to eliminate the mass transport effect caused by low vanadium flow rate. We did not observe further mass transport improvement when increasing the vanadium flow rate above 12 mL/min. Previous hydrogen-vanadium studies completed by Yufit et. al. [9] with serpentine flow fields required vanadium flow rates above 150 mL/min (with 25 cm^2 active area and serpentine flow fields) in order to minimize mass transport limitations.

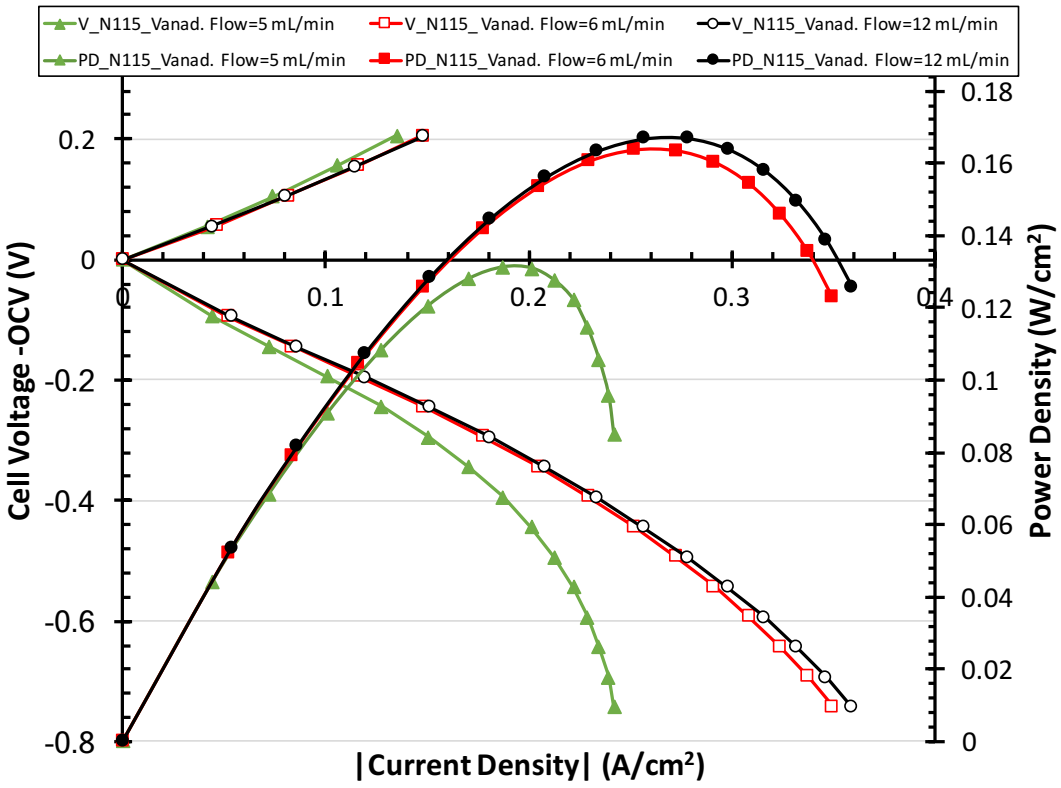

Figure 5.2. Study 1: Polarization and discharge power density curves of the reversible hydrogen-vanadium fuel cell at different vanadium electrolyte flow rates.

Figure 5.3 compares the fuel cell performance of a CNT vanadium electrode to the one made from 3 layers of nitric acid-treated SGL10AA (Study 2). We observe improved performance for the CNT electrode at higher current densities. The limiting currents for the CNT electrode and the 3 layer SGL10AA electrode were 0.7 A/cm^2 and 0.55 A/cm^2, respectively. The mass transport limitation observed in Figure 5.3 during charge for V_SGL10AA_NR212 arises due to the increased electrode thickness when using 3 layers of SGL10AA (~1050 µm) versus 1 layer of CNT electrode (~350 µm). From previous studies with the hydrogen-bromine system, a single layer of this CNT electrode was found to have active surface area equivalent to greater than 10 layers of conventional carbon electrode with an additional benefit of reduced thickness and therefore shorter transport distance from the flow channels. Therefore, the increased

performance can be attributed to the higher active surface area available to the CNT electrode. This leads to lower activation loss, faster transport, and lower ohmic resistance. The ohmic resistance of the electrolyte near the active area is reduced since the local current density per active site is lower when the total current is distributed over a larger area.

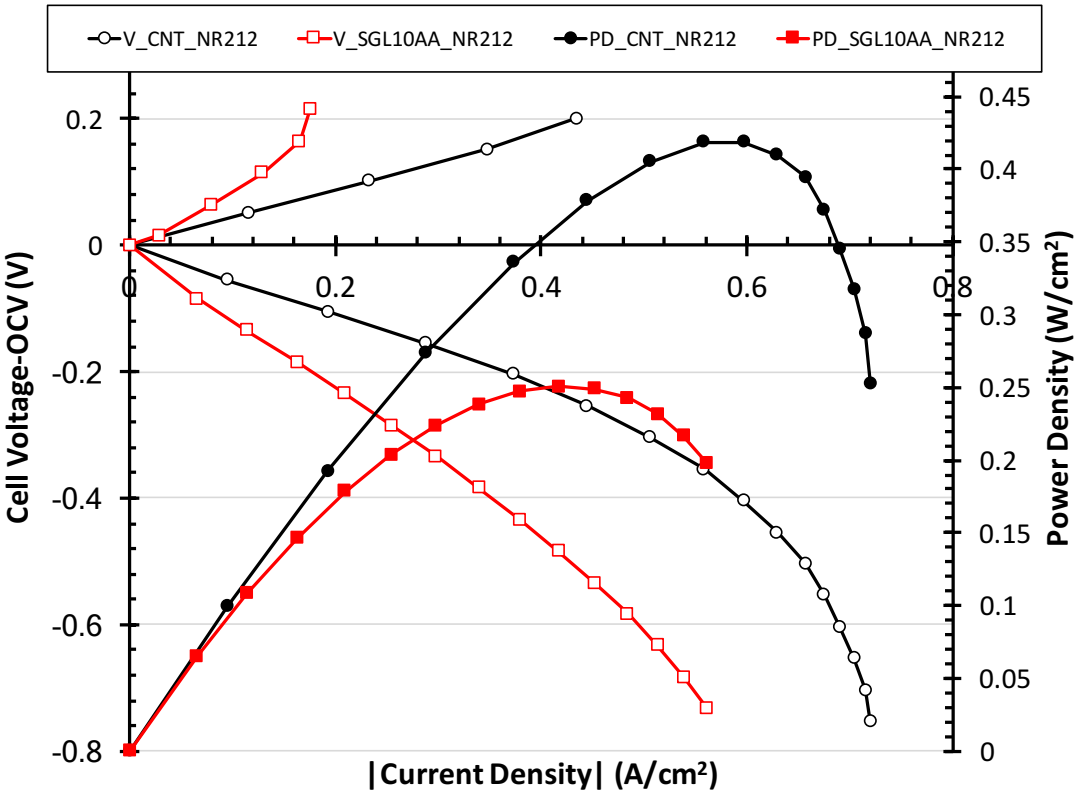

Figure 5.3. Study 2: Polarization and discharge power density curves of the reversible hydrogen-vanadium fuel cell comparing vanadium electrodes, CNT versus 3 layers of nitric acid-treated SGL10AA.

Figure 5.4 compares the fuel cell performance when using various types and thicknesses of Nafion membranes (Study 3). Identical positive (3 layers of SGL10AA) and negative (SGL35BC) electrodes, flow fields, hydrogen pressure, and electrolyte flow rate (12 mL/min) were used for each cell. We observe improved performance as membrane thickness decreased and a peak power density of more than 300 mW/cm^2 with NR211. Thinner membranes lead to

lower cell ohmic resistance or faster hydronium ions transport across the membrane during charge and discharge.

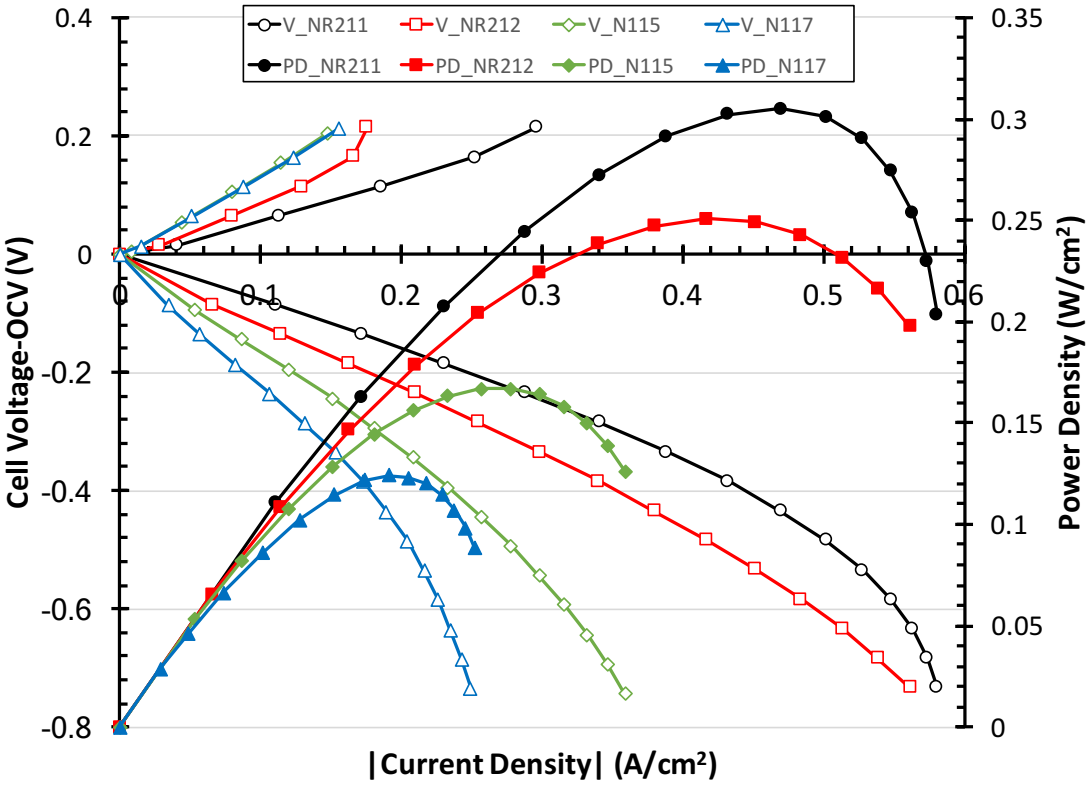

Figure 5.4. Study 3: Polarization and discharge power density curves of the reversible hydrogen-vanadium fuel cell for various proton exchange membrane types and thicknesses.

Figure 5.5 compares the discharge polarization curves before and after iR correction for various membrane types and thicknesses. The fuel cell resistance measured using EIS for NR211, NR212, N115, and N117 were 0.04, 0.068, 0.104, and 0.166 ohms, respectively. Full iR-corrected discharge polarization curves remove all ohmic losses in the fuel cell, including the ohmic resistance of the membrane. This allows us to directly compare the kinetic and mass transport effect for the various membrane types and thicknesses. First, with the ohmic resistance of the membranes removed, we observe similar kinetic performance in the low overpotential region for the two groups of membranes, the extruded N115/N117 membranes and the solution-

cast NR211/NR212 membranes. Next, we are able to identify the current density in which the mass transport effect starts to negatively impact the discharge polarization curves. For the extruded N115/N117 membranes, the mass transport effect starts at 0.18 A/cm^2. However, mass transport doesn't start to negatively impact the solution-cast NR211/NR212 membranes until greater than 0.5 A/cm^2. Overall, we observe increased performance when using solution-cast membranes, vice extruded, due to the improved mass transport effect. Solution-cast membranes (NR211 & NR212) are known to have a more hydrophilic surface (due to a higher concentration of sulfonate ion groups at the membrane's surface) than extruded membranes (N115 & N117).[20] The increased hydrophilicity of solution-cast membranes leads to increased ionic conduction near the membranes surface, therefore improving ionic and mass transport.

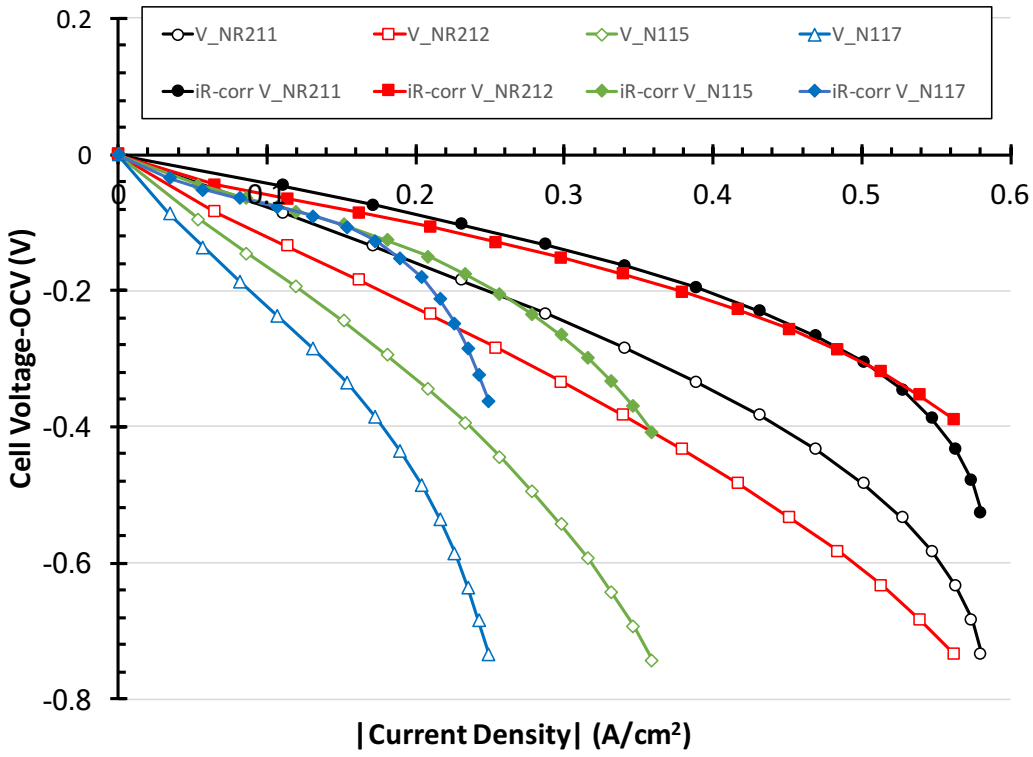

Figure 5.5. Study 3: Polarization curves before and after IR correction of the reversible hydrogen-vanadium fuel cell for various proton exchange membrane types and thicknesses.

Figure 5.6 graphs the polarization and power density curves for the reversible hydrogen-

vanadium fuel cell with a CNT vanadium electrode and NR212 membrane. Full iR-corrected and electronic iR-corrected polarization and power density curves are shown. Graphing the full and electronic iR-corrected curves allows us to visually analyze the current and power densities we expect to obtain if we overcame all ohmic losses in the fuel cell and compare these to the case of removing only the ohmic losses from electronic connections. When using improved current collectors in a commercial fuel cell, we expect very low ohmic losses attributed from electronic connections. Our fuel cells have not been designed for low electronic loss. The full iR-corrected curves provide us with the maximum achievable performance possible if all the ohmic losses due to the electrodes, electronic connections and membrane are overcome. After removing the iR loss, we can also see the kinetic loss effect and when mass transport loss begins. During discharge, we start to observe a mass transport effect at around 500 mA/cm^2 and limiting current at 700 mA/cm^2. However, during charge, we don't observe a mass transport effect within the overpotential or current density range evaluated. Based on the polarization curves in Figure 5.6, we observe very high kinetics on both charge and discharge, but mass transport losses take over during discharge as the overpotential is increased. Our studies show a 3-4 times increase in peak power density over the previous hydrogen-vanadium studies conducted by Yufit, et. al.[9] The performance enhancement is attributed to using interdigitated vice serpentine flow fields, thinner proton exchange membranes, and advanced CNT electrodes.

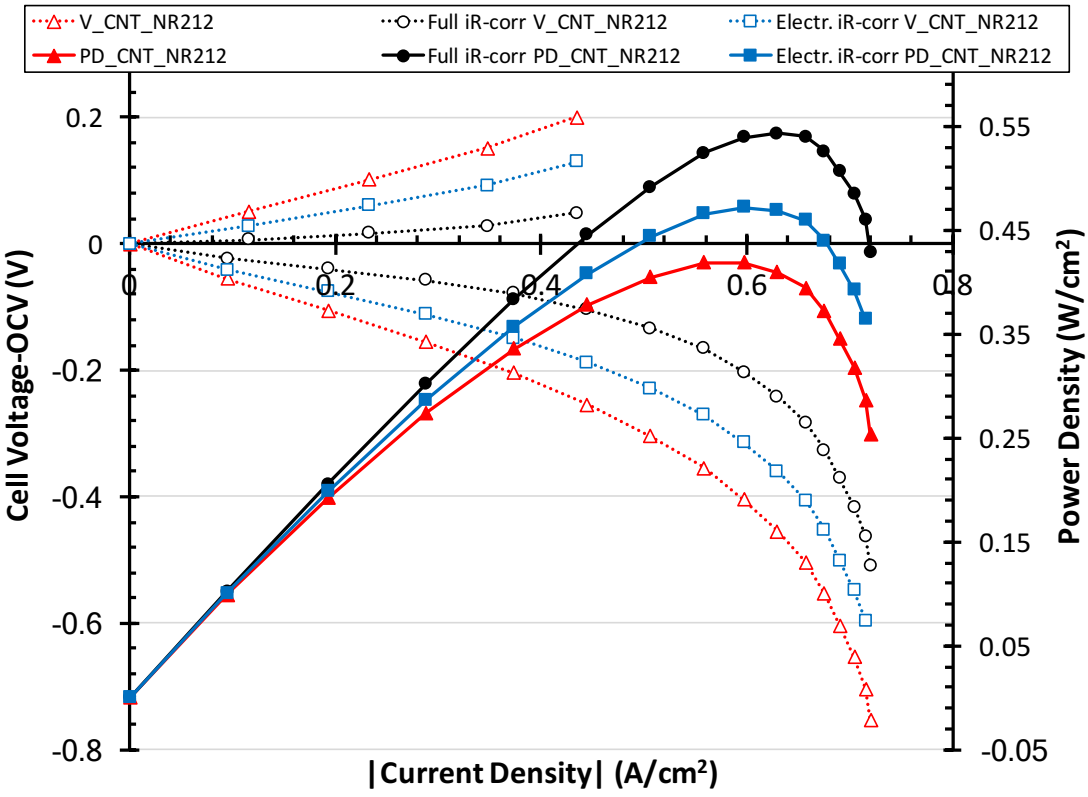

Figure 5.6. Polarization and discharge power density curves of the reversible hydrogen-vanadium fuel cell using a CNT vanadium electrode and NR212 membrane before and after IR correction.

5.5 Summary

We conducted a performance study on a reversible hydrogen-vanadium fuel cell using interdigitated flow fields at both electrodes. Two different types of vanadium electrodes (CNT and nitric acid-treated SGL10AA) were explored, as well as various types of proton exchange membranes. The hydrogen-vanadium fuel cell shows promising performance by achieving peak power greater than 540 mW/cm^2.

Further investigation is needed to determine whether electrospun nanofiber composite membranes made of perfluorosulfonic acid (PFSA) fibers and inert fibers to control membrane swelling will be suitable for the hydrogen-vanadium fuel cell. Electrospun nanofiber composite membranes offer the potential of lower vanadium crossover and lower membrane resistance.

Therefore, these membranes may lead to increased fuel cell performance and cycling efficiency.

5.6 Acknowledgments

The authors wish to acknowledge the financial support from the University of Kansas (KU) Madison and Lila Self Fellowship. Supplies for this work were supported by the National Science Foundation through grant no. EFRI-1038234. The authors would also like to thank Dr. Venkata Yarlagadda for providing the high surface area carbon nanotube electrodes, Yuanchao Li for his assistance in preparing the nitric acid-treated electrodes and Dr. Alan Pezeshki for the lengthy discussions related to the all-vanadium flow battery.

5.7 References for Chapter 5

1. M. Zhang, M. Moore, J. S. Watson, T. A. Zawodzinski and R. M. Counce, *Journal of The Electrochemical Society*, **159**, A1183 (2012).

2. M. Skyllas-Kazacos, M. H. Chakrabarti, S. A. Hajimolana, F. S. Mjalli and M. Saleem, *Journal of The Electrochemical Society*, **158**, R55 (2011).

3. A. Z. Weber, M. M. Mench, J. P. Meyers, P. N. Ross, J. T. Gostick and Q. Liu, *Journal of Applied Electrochemistry*, **41**, 1137 (2011).

4. P. Alotto, M. Guarnieri and F. Moro, *Renewable and Sustainable Energy Reviews*, **29**, 325 (2014).

5. C. Ponce de León, A. Frías-Ferrer, J. González-García, D. A. Szánto and F. C. Walsh, *Journal of Power Sources*, **160**, 716 (2006).

6. B. Huskinson, J. Rugolo, S. K. Mondal and M. J. Aziz, *Energy & Environmental Science*, **5**, 8690 (2012).

7. H. Kreutzer, V. Yarlagadda and T. V. Nguyen, *Journal of The Electrochemical Society*, **159**, F331 (2012).

8. V. Yarlagadda, R. P. Dowd, J. W. Park, P. N. Pintauro and T. V. Nguyen, *Journal of The Electrochemical Society*, **162**, F919 (2015).

9. V. Yufit, B. Hale, M. Matian, P. Mazur and N. P. Brandon, *Journal of the Electrochemical Society*, **160**, A856 (2013).

10. C. Menictas and M. Skyllas-Kazacos, *Journal of Applied Electrochemistry*, **41**, 1223 (2011).

11. W. Xie, R. M. Darling and M. L. Perry, *Journal of The Electrochemical Society*, **163**, A5084 (2015).

12. J. Houser, J. Clement, A. Pezeshki and M. M. Mench, *Journal of Power Sources*, **302**, 369 (2016).

13. A. M. Pezeshki, J. T. Clement, G. M. Veith, T. A. Zawodzinski and M. M. Mench, *Journal of Power Sources*, **294**, 333 (2015).

14. V. Yarlagadda, G. Lin, P. Chong and T. V. Nguyen, *Journal of The Electrochemical Society*, **163**, A5134 (2016).

15. V. Yarlagadda, G. Lin, P. Chong and T. V. Nguyen, *Journal of The Electrochemical Society*, **163**, A5126 (2016).

16. N. J. Cooper, T. Smith, A. D. Santamaria and J. W. Park, *International Journal of Hydrogen Energy*, **41**, 1213 (2016).

17. T. V. Nguyen, *Journal of The Electrochemical Society*, **143**, L103 (1996).

18. D. Wood, J. Yi and T. V. Nguyen, *Electrochimica Acta*, **43**, 3795 (1998).

19. W. Yan, C. Chen, S. Mei, C. Soong and F. Chen, *Journal of Power Sources*, **162**, 1157 (2006).

20. R. P. Dowd, C. S. Day and T. V. Nguyen, *Journal of The Electrochemical Society*, **164**, F138 (2017).

CHAPTER 6: Hydrogen-Vanadium Reversible Fuel Cell Crossover Study

6.1 Abstract

Vanadium crossover through the ion exchange membrane in vanadium-based redox flow battery systems results in self discharge and variations in electrolyte concentration. VO_2^+ crossover rate, or diffusion, through various Nafion membranes was measured directly with a hydrogen-vanadium reversible fuel cell. Measuring crossover of electrolyte species directly with a fuel cell as compared to an idealized dual-chamber system, allows for determining diffusivity under actual fuel cell testing conditions. This new in-situ technique for measuring VO_2^+ crossover with a fuel cell is shown to be reliable and easy to use. The crossover measurement method shows consistent results with VO_2^+ diffusivities of ~10^{-7} cm^2/s, as well as increased diffusion rates with thinner ion exchange membranes. This setup can also be used to measure the crossover of other vanadium ions, such as V(IV) or V(III) by using a V(IV)/V(III) or V(III)/V(II) redox, respectively, at the positive electrode. Electrospun blended nanofiber membranes were also fabricated and tested in the hydrogen-vanadium reversible fuel cell leading to lower crossover rates and high fuel cell performance, as compared to commercial Nafion films.

6.2 Introduction

As the use for intermittent energy sources, such as wind and solar, continue to increase globally, the need for efficient and cost effective energy storage solutions will grow. These energy storage solutions will enable the existing energy infrastructure to take full advantage of load levelling during peak and non-peak demand periods.[1-5] The hydrogen-vanadium reversible fuel cell is one

of the energy storage technologies being considered to meet future energy demands. The charge and discharge reactions for the hydrogen-vanadium reversible fuel cell are as follows:

Vanadium (+) Electrode: $2VO^{2+} + 2H_2O \underset{discharge}{\overset{charge}{\rightleftarrows}} 2VO_2^+ + 4H^+ + 2e^-$,

$$\boldsymbol{E^o_{red} = +0.99\ V} \quad \textbf{[1]}$$

H_2 (−) Electrode: $2H^+ + 2e^- \underset{discharge}{\overset{charge}{\rightleftarrows}} H_2$,

$$\boldsymbol{E^o_{red} = +0.0\ V} \quad \textbf{[2]}$$

Overall Reaction: $2VO^{2+} + 2H_2O \underset{discharge}{\overset{charge}{\rightleftarrows}} 2VO_2^+ + 2H^+ + H_2$,

$$\boldsymbol{E^o_{cell} = +0.99\ V} \quad \textbf{[3]}$$

During charge, vanadium (IV) is converted to vanadium (V) at the vanadium electrode, and hydrogen gas is produced at the hydrogen electrode. During discharge, the reactions are reversed to consume hydrogen gas at the hydrogen electrode and vanadium (V) at the vanadium electrode. A polymer electrolyte membrane separates the hydrogen/vanadium electrodes and provides an ionic medium for transporting hydronium ions.

One of the advantages of the hydrogen-vanadium fuel cell over the all-vanadium flow battery is the reduced volume of vanadium electrolyte. Due to the high cost of vanadium, reducing the quantity of vanadium electrolyte directly impacts the overall system cost.[6] Additionally, any crossover of electrolyte in the hydrogen-vanadium fuel cell is more easily separated due to the gas-liquid electrolyte pairing, as compared to flowing liquid electrolytes through both the positive and negative electrodes. Crossover in vanadium-based redox flow batteries leads to self-discharge and electrolyte composition variations over time. Yufit et. al. first demonstrated the feasibility of the hydrogen-vanadium reversible fuel cell by attaining a

peak discharge performance of 114 mW/cm^2.[7] Most recently, our group demonstrated improved fuel cell performance (540 mW/cm^2) by using a carbon nanotube (CNT) vanadium electrode, thinner membranes, and interdigitated flow fields.[8] The previous work on the hydrogen-vanadium reversible fuel cell sparked our group's interest in examining the effect of vanadium crossover through the polymer electrolyte membrane. Xie et. al. studied Nafion processing and pretreatment effects on vanadium transport through Nafion films.[9] His group measured the vanadium diffusivity of various membranes by using a dual-chamber, direct-permeation cell. The permeation test consisted of clamping a membrane between two chambers. Then, each chamber was filled with equal volumes of two solutions. Chamber one was filled with vanadyl sulfate and sulfuric acid, while chamber two was filled with magnesium sulfate and sulfuric acid. Finally, a UV-vis-NIR spectrometer was used to measure the increase of vanadyl sulfate concentration in chamber two over regular time intervals. Other studies have used a similar dual chamber technique to measure diffusion rates of various species through different types of membranes.[10-15] These past studies required the use of a stand-alone two chamber apparatus for calculating diffusion rates, instead of being able to determine the diffusion rate in-situ using a fully assembled fuel cell. Our group expects the membrane diffusion rate within a fuel cell to be different than the ideal two chamber setup. The crossover rate in an actual fuel cell is expected to be different due to the migrational (electric field) effect across the membrane, the reduction in the membrane area due to the solid phase of the electrodes, the compressive forces exerted on the membrane during fuel cell assembly, the effect of the membrane electrode assembly (MEA) hot pressing technique on membrane thickness and surface chemistry, and the fuel cell operating conditions (i.e. electrolyte flow and pressure on each side of the membrane). In this work, we explore a new technique for determining in-situ the membrane diffusion rates of VO_2^+ for a fully

assembled fuel cell. The technique was applied to MEAs made with different Nafion membranes. Additionally, MEAs were made with electrospun blended nanofiber (EBN) membranes. The EBN membranes were developed to reduce vanadium crossover rates while maintaining high fuel cell performance.

6.3 Experimental

While exploring the performance characteristics of the hydrogen-vanadium fuel cell, our group observed a self-discharging phenomenon. We first charged the vanadium electrolyte solution to convert vanadium (IV) to vanadium (V). During the charging operation, the color of the vanadium electrolyte changed from clear bright blue (denoting the presence of vanadium (IV)) to dark violet (denoting the presence of vanadium (V)). Next, the open circuit voltage (OCV) for the fuel cell was monitored for 24 hours while recirculating vanadium solution and hydrogen gas through the positive and negative electrodes, respectively. We found that the vanadium electrolyte solution reverted to the clear bright blue color, indicating that the vanadium (V) species had converted back to vanadium (IV). In order to study this observed self-discharge phenomena and confirm that the self-discharge reaction occurs at the hydrogen (negative) electrode, we recharged the vanadium electrolyte solution to make vanadium (V) and then transferred the charged vanadium electrolyte into two new storage bottles (labelled bottle A and B). Hydrogen was then purged through both bottles. A single piece (2 x 2 cm) of plain GDL (SGL35BC without catalyst) was placed in bottle A and a Pt-coated GDL (0.48 mg/cm^2 Pt loading, 0.16 mg/cm^2 Nafion ionomer, SGL35BC from TVN Systems, Inc.) was placed in bottle B. As shown in Figure 6.1, the vanadium electrolyte color in bottle B reverted back to clear bright blue within an hour, indicating that vanadium (V) converts to vanadium (IV) in the

presence of hydrogen gas and a Pt catalyst. No changes were observed with the control bottle (bottle A). These preliminary results indicate that the hydrogen-vanadium fuel cell can self-discharge if vanadium (V) crosses through the membrane to reach the hydrogen electrode. Additionally, the crossover of hydrogen gas to the vanadium electrode does not lead to self-discharge, which is expected since carbon is a very poor catalyst for hydrogen oxidation.

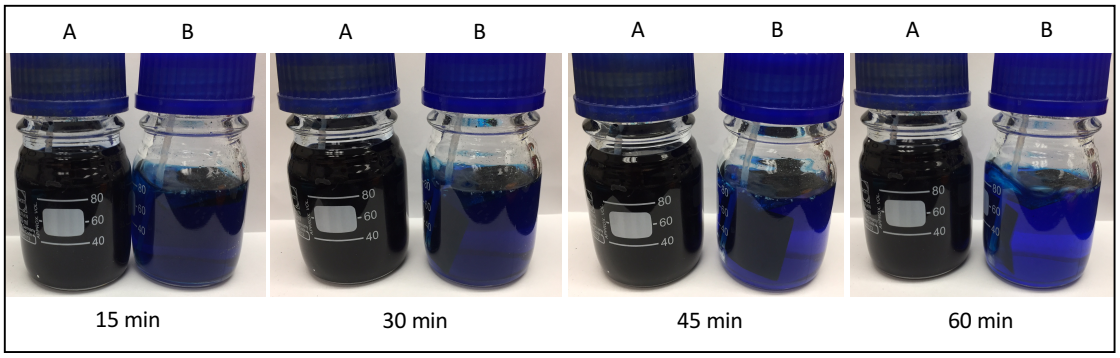

Figure 6.1. Vanadium solution self-discharge in the presence of hydrogen gas and Pt-coated GDL.

Our proposed mechanism of the self-discharge phenomena is provided in Figure 6.2. In the first step, vanadium (V) crosses through the membrane from the vanadium electrode to the hydrogen electrode. Next, vanadium (V) is reduced to vanadium (IV) at the platinum containing negative electrode, on both carbon and platinum surfaces, where the source of electrons comes from the oxidation of hydrogen to hydronium ions at the platinum catalyst of the negative electrode. This overall self-discharge reaction is identical to the overall discharge reaction given in Equation 3. The consumption of vanadium (V) sets up a concentration gradient across the membrane which leads to diffusion of additional vanadium (V) from the vanadium electrode to the hydrogen electrode. In turn, the production of vanadium (IV) at the hydrogen electrode sets up a concentration gradient across the membrane leading to the diffusion of vanadium (IV) from the hydrogen electrode to the vanadium electrode. First, this self-discharge will create a mixed

potential at the negative electrode and cause the cell open circuit voltage to decrease. If this self-discharge is allowed to occur continuously at open-circuit, it will lead to the depletion of vanadium (V) in the electrolyte that is circulated through the positive electrode and the reduction of hydrogen pressure at the negative electrode. This will lead to a drop in the cell open-circuit potential. Note that if the hydrogen pressure at the negative electrode is held constant, then the drop in the cell open-circuit potential is caused primarily by the depletion of vanadium (V) and production of vanadium (IV). This unsteady state (diffusion rate changes with concentration of vanadium (V)) and continuous drop in the cell open-circuit voltage can be used to determine the diffusion rate of vanadium (V) across the membrane.

Now, if a potentiostat is used to hold the fuel cell at a constant voltage, then a net steady-state, positive (charge) current will be supplied by the potentiostat to compensate for the self-discharge rate of vanadium (V) to vanadium (IV). In this mode, electrons flow from the potentiostat to the negative hydrogen electrode to feed the vanadium (V) reduction reaction so that no net hydrogen oxidation occurs and the hydrogen pressure remains constant. An equal number of electrons are withdrawn by the potentiostat from the vanadium electrode resulting in the oxidation of vanadium (IV) to vanadium (V). At steady-state, these two currents are equal to the transport rate of vanadium (V) across the membrane towards the negative hydrogen electrode. This phenomenon is well known to many secondary battery researchers and users.[16, 17] Consequently, this steady-state charging current can be used to measure the transport rate of vanadium (V) across the membrane to the negative electrode. While it is possible that this charging current could be controlled by the diffusion rate of vanadium (IV) across the membrane from the hydrogen electrode to the vanadium electrode, results in the literature have shown that the diffusion rate of vanadium (IV) is higher than that of vanadium (V) making it very

reasonable to assume that the steady-state charging current is controlled by the diffusion rate of vanadium (V).[18, 19]

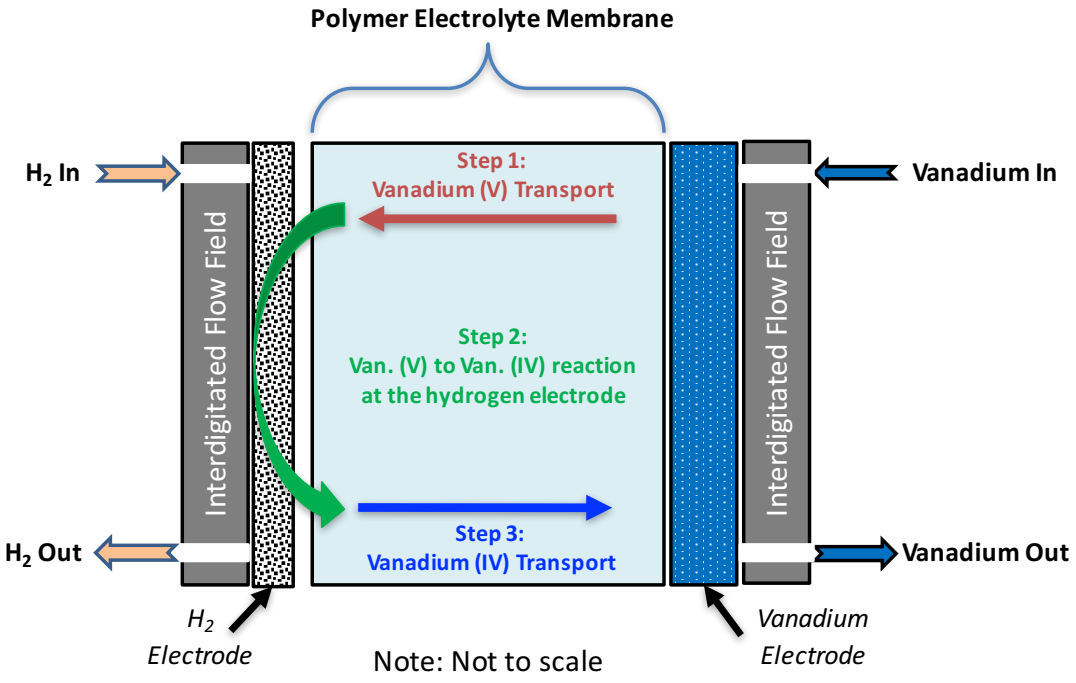

Figure 6.2. Proposed self-discharge reaction mechanism.

As described above, the observed self-discharge phenomena for the hydrogen-vanadium reversible fuel cell enables us to directly measure the crossover of vanadium (V) through the polymer electrolyte membrane. Two different crossover studies were completed on the hydrogen-vanadium reversible fuel cell. Both crossover studies investigated the effect of membrane type and thickness on the rate of vanadium crossover. In the first study (steady-state method), the fuel cell voltage was held constant at 1.05 V while measuring the current. The current was measured for more than 5 hours so that a steady-state charging current was reached. Once the current reached steady-state, we transitioned directly into the second study. For the second study (unsteady-state method), open circuit voltage (OCV) was monitored for greater than 5 hours in order measure the OCV drop over time.

Vanadium electrolyte solution (100 mL) was prepared by dissolving an appropriate amount of vanadyl sulfate (Sigma Aldrich) in 2.5M sulfuric acid (H_2SO_4) and then charging to 50% state of charge (SOC) in order to produce a 1M vanadium (V), 1M vanadium (IV), and 3M sulfuric acid electrolyte solution. The membrane electrode assembly (MEA) was prepared by hot pressing a polymer electrolyte membrane between a Pt-coated GDL (0.48 mg/cm^2 Pt loading, 0.16 mg/cm^2 Nafion ionomer, SGL35BC from TVN Systems, Inc.) and a nitric acid treated GDL (SGL10AA) at 135ºC and 0.552 MPa (80 psi) for 5 min. One side of the nitric acid treated GDL (side facing the membrane) was coated with a Nafion solution (Ion Power Inc.) and dried prior to MEA hot pressing in order to ensure proper adherence of the nitric acid treated GDL onto the membrane. MEAs were constructed using various Nafion membrane, including NR211 (~25 μm thick), NR212 (~51 μm thick), N115 (~127 μm thick), N117 (~183 μm thick) and two EBN membranes (~30 and 40 μm thick).

EBN membranes were made from Nafion/PVDF blended fiber mats, which were created by electrospinning the blend from a mixed solvent of N,N-dimethylacetamide (DMAc) and tetrahydrofuran (THF). Nafion (1100 EW) was dispersed into DMAc to make a 40 wt% solution. A 12.5 wt% solution of PVDF (Kynar HSV900) was prepared by dissolving the powder into a 7:3 (wt:wt) DMAc:THF mixed solvent. The proper amounts of the two solutions were mixed so that the final Nafion:PVDF (wt:wt) ratio in solution was 80:20. The total solids content in the electrospinning solution was 30 wt%. The Nafion/PVDF blended fibers were fabricated using a custom-built electrospinning apparatus with humidity control, where the relative humidity was maintained at 25% at a temperature of 22-24°C. The electrospinning solution was loaded into a syringe fitted with a 22-g needle. The needle tip-to-collector distance was 8 cm. While the solution was pumped at a constant flow rate of 0.25 mL/h, a 10 kV voltage was applied between

the needle and a rotating and oscillating grounded drum collector. A blended polymer fiber jet emitted from the needle deposited onto the drum forming a highly porous mat. After electrospinning, the fiber mat was dried at 60°C overnight to remove residual solvent and then pressed at 177°C for 5 minutes at 4000 psi. The resultant transparent, nonporous membrane was annealed for 90 min at 150°C under vacuum. Finally, the membrane was soaked in room-temperature 1.0 M H_2SO_4 for 16 h, followed by soaking in room-temperature water for 16 hr. Two EBN membranes were fabricated, with a dry thickness of 30 and 40 μm, and the same composition (80 wt% Nafion and 20 wt% PVDF).

The fuel cell was assembled at 1.103 MPa (160 psig) using expanded polytetrafluoroethylene (PTFE) gaskets and interdigitated tantalum flow fields (9 cm^2). When assembling the fuel cell, two additional layers of nitric acid treated GDL (for a total of 3 layers) was used as the vanadium electrode. The nitric acid treated GDL for the vanadium electrode was prepared using a 3-step process. First, the GDL was submerged in deionized water while using a vacuum pump at -0.03 MPa for 5 min to create a vacuum above the solution. This step ensured the pores of the carbon paper were filled with deionized water and fully wetted. Next, the GDL was soaked in 2M nitric acid for 24 h. Finally, the GDL was thoroughly rinsed in deionized water and dried at room temperature.

All fuel cell testing was completed at room temperature (~23ºC). Hydrogen was recirculated at a pressure of 0.136 MPa (5 psig) and vanadium electrolyte was recirculated with a peristaltic pump at 12 mL/min. A fuel cell startup procedure was carried out to ensure the membrane was properly hydrated prior to testing. The startup procedure consisted of cycling the fuel cell between discharge (0.6V) and charge modes (1.3V) every 10 min for more than 12 h.[8] Polarization curves were obtained for the EBN membranes in order to compare their

performance to our previously published results for NR211, NR212, N115 and N117.[8] Charge and discharge polarization curves were obtained using a constant voltage staircase mode with 50 mV increments every 2 min.

6.4 Results and Discussion

In the first study (steady-state method), current was monitored while holding the fuel cell voltage at 1.05V. Figure 6.3 graphs the steady-state current density for multiple membrane types when holding the cell voltage constant at 1.05V. Note that a different cell voltage could be used. Since each cell voltage corresponds to a different vanadium (V) and vanadium (IV) ratio (assuming the hydrogen gas pressure in the negative electrode is held constant), the diffusion rate of vanadium (V) can be measured at different concentrations to determine the concentration dependence of its diffusivity. As expected, the steady-state current density required to maintain the voltage at 1.05V was higher for thinner membranes. The increased crossover rate associated with thinner membranes requires a higher steady-state current density to maintain 1.05V. The steady-state current density dropped quickly as membrane thickness was increased from ~25um (NR211) to ~51 um (NR212). As membrane thickness was increased above ~127 um (N115) to ~183 um (N117), a less pronounced drop in steady-state current density was observed. The observed trend is in agreement with other research groups who reported increased crossover rates for thinner membranes through the use of a dual-chamber, direct-permeation cell.[9, 18]

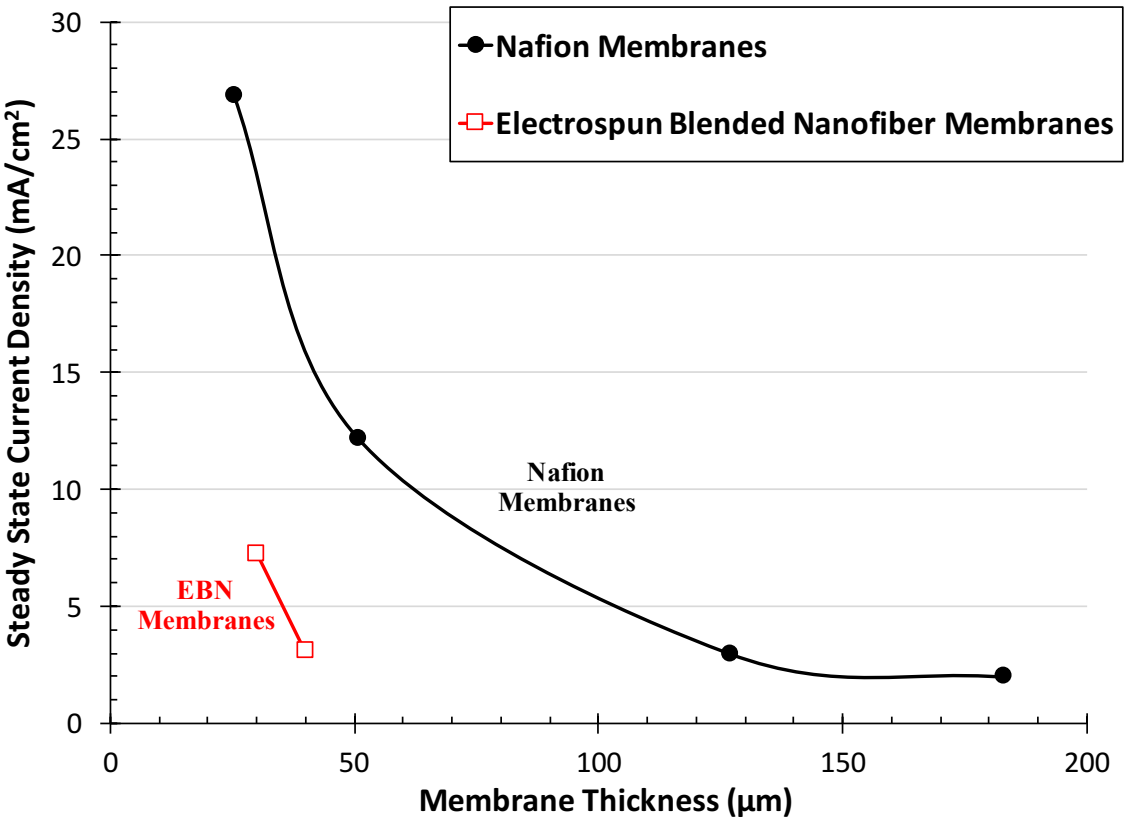

Figure 6.3. Steady-state crossover current density versus membrane thickness when holding the voltage at 1.05V.

In order to calculate the diffusivity of vanadium (V) through each membrane, the steady-state current was used to calculate the flux of vanadium (V) as follows:

$$Flux\ of\ VO_2^+ = \frac{Steady\text{-}state\ Current}{nFA}\ \ (moles/cm^2\text{-}s) \qquad \textbf{[4]}$$

where n is the moles of electrons per mole of vanadium (V) in accordance with Eq. [1], F is Faraday constant, and A is the active area of the fuel cell (9 cm^2). Diffusivity was then calculated using Eq. [5] below.[20]

$$Diffusivity = \frac{(Flux\ of\ VO_2^+)(Membrane\ Thickness)}{(VO_2^+\ Concentration\ @\ 1.05V)}\ \ (cm^2/s) \qquad \textbf{[5]}$$

Eq. [4] and Eq. [5] can be combined into a single diffusivity equation, which is shown below in Eq. [6].

$$Diffusivity = \frac{(Steady\text{-}state\ Current)(Membrane\ Thickness)}{(nFA)(VO_2^+\ Concentration\ @\ 1.05V)}\ \ (cm^2/s) \qquad \textbf{[6]}$$

Table 6.1 lists the steady-state crossover current density measured for each membrane and the calculated vanadium (V) diffusivity. The vanadium (V) diffusivity for the conventional Nafion membranes ranged from ~5.6 x 10^{-7} cm^2/s for the solution cast membranes (NR211 and NR212) to ~3.2 x 10^{-7} cm^2/s for the extruded membranes (N115 and N117). The vanadium (V) diffusivity for the EBN membranes ranged from 1.9 x 10^{-7} cm^2/s (30 μm thick) to 1.1 x 10^{-7} cm^2/s (40 μm thick). The vanadium diffusivities calculated for each membrane are in agreement (~10^{-7} cm^2/s) with other research groups who have studied vanadium crossover using a dual-chamber, direct-permeation cell.[9, 18, 21, 22] Due to the agreement in trend and similar order of magnitude for the calculated diffusivity, the steady-state crossover method appears to be suitable for measuring vanadium diffusivity in an actual fuel cell (i.e. in-situ method). Note that since this is concentrated solution of multiple ions, the flux of vanadium (V) across the membrane probably depends on the fluxes of water molecules and other counter ions such as vanadium (IV) and H^+.[23] However, for simplicity we will treat this multicomponent solution as a dilute solution where the transport of one ion is independent of the other ions. We also assume that the transport of vanadium (V) is the limiting process.

Table 6.1. Steady-state current density and calculated V^{5+} diffusivity when the holding voltage at 1.05V.

Membrane Type	Steady-State Crossover Current Density (mA/cm^2)	Calculated V^{5+} Diffusivity (cm^2/s)
NR211	27	5.9E-07
NR212	12	5.4E-07
N115	3.0	3.3E-07
N117	2.0	3.2E-07
EBN 30 μm	7.2	1.9E-07
EBN 40 μm	3.1	1.1E-07

The steady-state current density should be inversely proportional to the membrane thickness (i.e. diffusion distance).[18] The results in Figure 6.3 and Table 6.1 seem to support this for the two groups of conventional Nafion membranes (cast and extruded). Our group previously showed how the membrane fabrication method (cast versus extruded) will determine the membrane's surface structure (hydrophilic versus hydrophobic) and surface ionic activity.[24-27] This surface phenomenon seems to affect the diffusion of other ions (i.e. vanadium (V)) similarly to hydronium ions. In other words, the increased surface hydrophilicity of cast membranes as compared to extruded membranes seems to contribute to higher vanadium (V) diffusivity.

In the second diffusion study (unsteady-state method), the OCV drop was measured for more than 5 h. Figure 6.4 shows the change in OCV over time for the various membranes. The thinnest membrane (NR211) experienced a rapid OCV drop throughout the test. The drop rate increases sharply at approximately 4 h due to depletion of the vanadium (V) ion. The OCV drop for the other five membranes (NR212, N115, N117, EBN30, EBN40) is very gradual for more than 10 h. The difference in OCV drop between NR212, N115 and N117 could not be discerned in Figure 6.4 because the vanadium (V) diffusivities are small relative to the concentration of salt in the positive electrolyte reservoir. After narrowing the voltage axis to an appropriate range, Figure 6.5 reveals a trend in voltage drop as the membrane thickness increases. The thickest membrane (N117) exhibits the slowest voltage drop. The lower diffusivity expected when using a thicker membrane is in agreement with the trends shown in Figure 6.4 and Figure 6.5. The behavior shown in Figure 6.4 and Figure 6.5 is expected since lower diffusivity for a thicker membrane would lead to a lower conversion of vanadium (V) to vanadium (IV) at the hydrogen electrode.

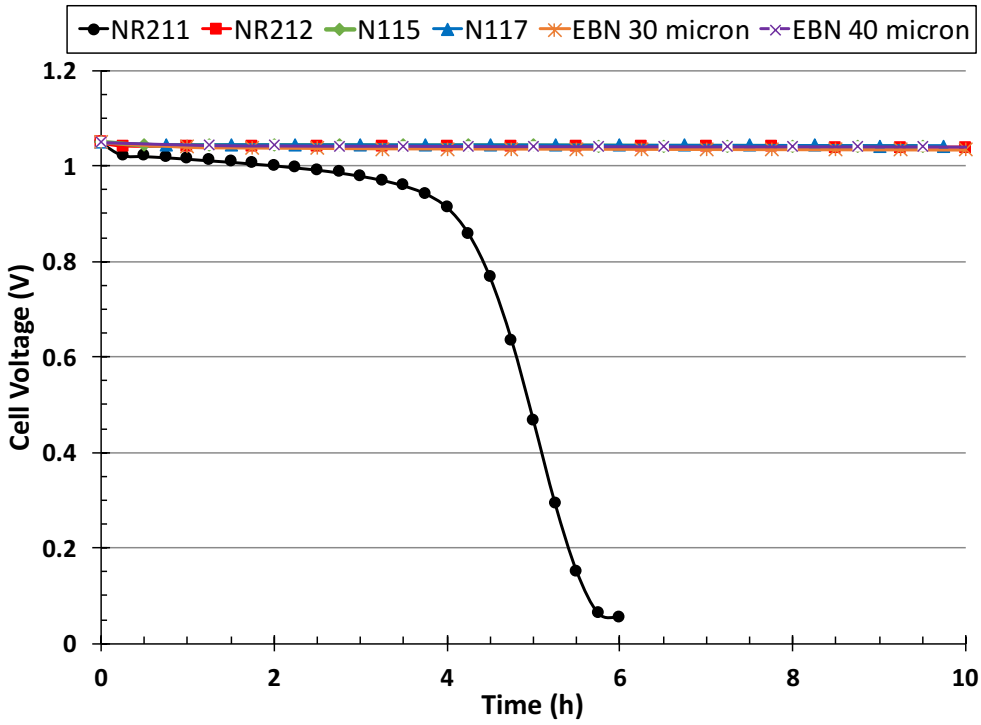

Figure 6.4. OCV drop over time for various membranes with 1.05V starting voltage.

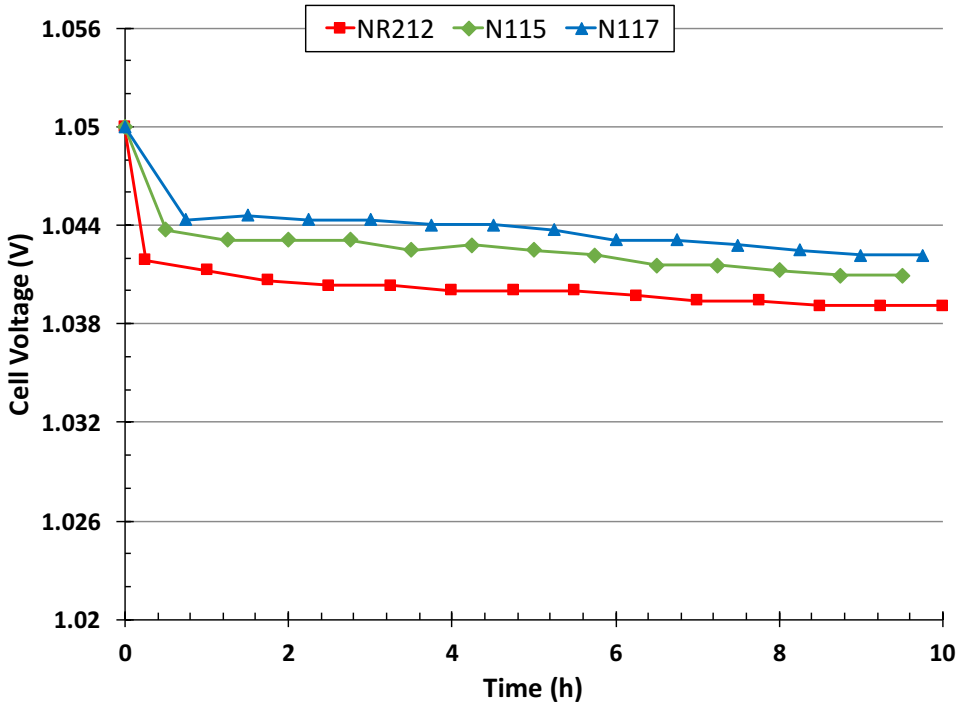

Figure 6.5. Magnified OCV drop over time for various membranes with 1.05V starting voltage.

As you may recall, immediately prior to the second study, the cell voltage was held at 1.05V until steady-state current was reached. This was done to ensure that all tests had the same starting point. The change in vanadium (V) concentration at the vanadium electrode is expected to drop over time as vanadium (V) is consumed at the hydrogen electrode due to crossover. Figure 6.6 graphs the voltage drop rate versus time for each conventional Nafion membrane type. As expected, the voltage drop rate is a maximum at the start of an experiment, and then plateaus after approximately 3 h has elapsed. As the vanadium (V) concentration difference across the membrane diminishes during an experiment (due to consumption of vanadium (V) at the hydrogen electrode), the voltage drop rate decreases.

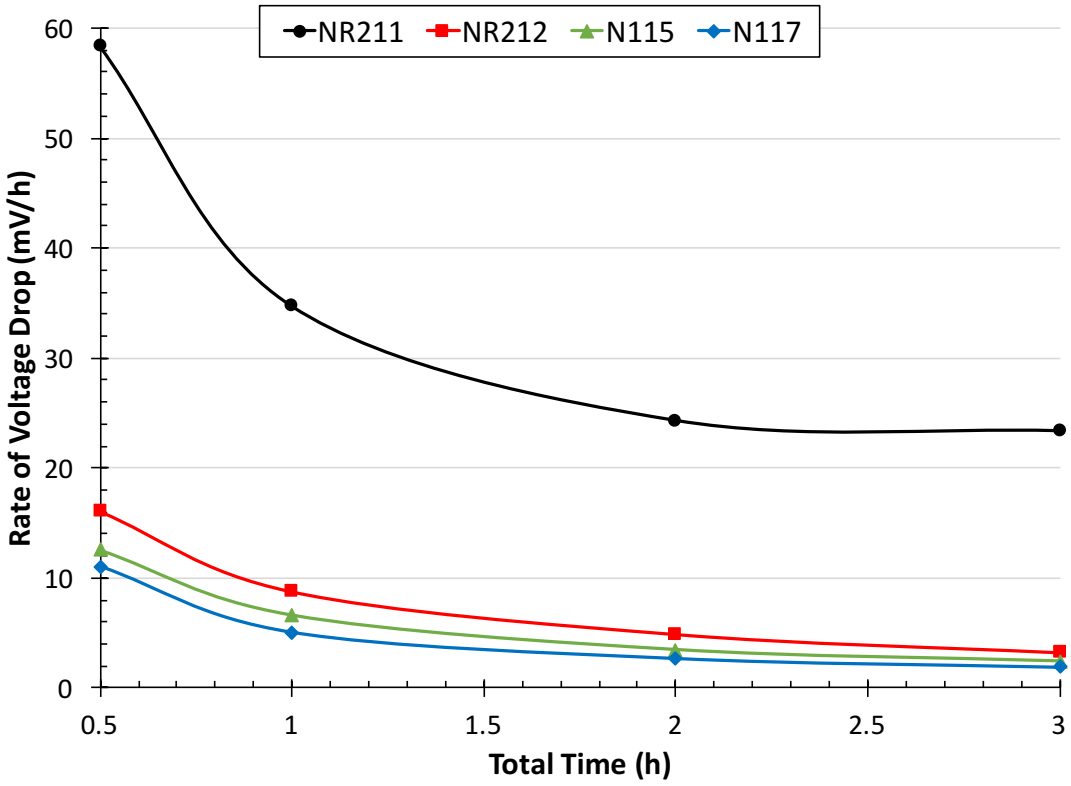

Figure 6.6. Rate of OCV drop over time for various membranes with 1.05V starting voltage.

In the present study, EBN membranes were tested in the hydrogen-vanadium reversible fuel cell. The resulting polarization and discharge power density curves were compared to

previously published data by our group with NR211, NR212 N115, and N117 films.[8] EBN membranes were designed in a way to reduce crossover while maintaining high fuel cell performance. The performance of the two EBN membranes (30 μm and 40 μm thick) are graphed in Figure 6.7 by overlaying the polarization and discharge performance curves with those using conventional Nafion membranes (NR211, NR212, N115, N117). The 30 μm thick EBN membrane had similar fuel cell performance as NR212 (~51 μm thick). However, as shown in Table 1, the crossover rate for the 30 μm thick EBN membrane was much lower than NR212, as indicated by a steady-state crossover current density of 7.2 mA/cm^2 versus 12.2 mA/cm^2 when holding the voltage at 1.05 V. Additionally, the 40 μm thick EBN membrane outperformed N115, while maintaining a similar crossover rate as N115 (3.1 mA/cm^2 versus 3 mA/cm^2). The lower crossover rate for the EBN membranes as compared to conventional Nafion membranes of similar thickness is a result of the inert polymer phase (i.e. PVDF) of the EBN membrane which physically restricts ionic channel swelling of the Nafion phase by electrolyte during cell operation.

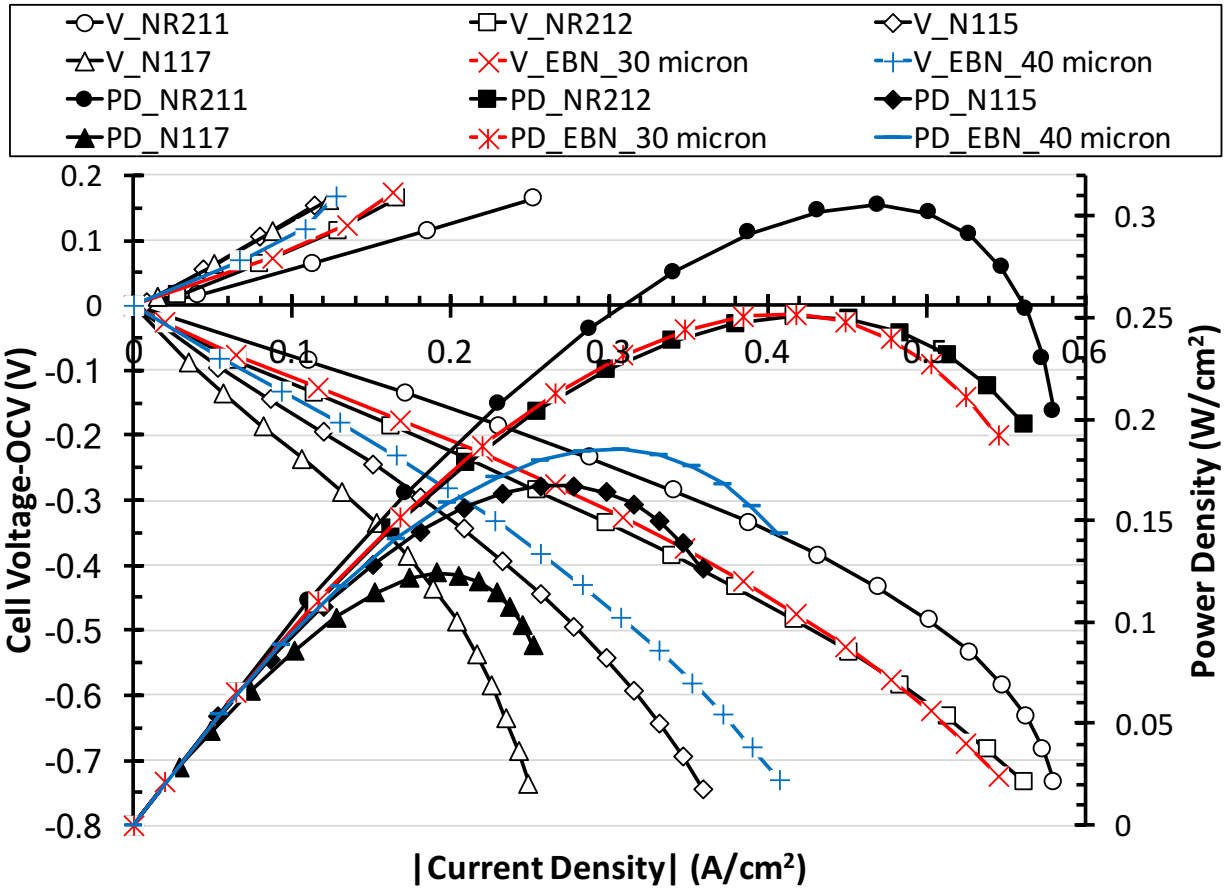

Figure 6.7. Polarization and discharge power density curves of the reversible hydrogen-vanadium fuel cell for EBN membranes relative to conventional Nafion membranes.

6.5 Summary

In summary, we measured the diffusivity of vanadium (V) ions directly with a hydrogen-vanadium reversible fuel cell using various membrane types (extruded, solution-cast, nanofiber-based) and thicknesses. For the first-time vanadium diffusivity has been measured directly with a fully assembled fuel cell. Two different methods (steady-state and unsteady-state) were explored for measuring the diffusivity. The steady-state method proved to be a more accurate method for measuring the vanadium (V) diffusivity. Additionally, EBN membranes, made from a hot-pressed mat of blended electrospun Nafion/PVDF nanofibers, performed very well in a hydrogen-vanadium reversible fuel cell with reduced crossover rates. EBN membrane

optimization will continue in an effort to lower crossover rates while increasing fuel cell performance.

Further investigations are needed to determine if the new crossover measurement technique can be applied to other fuel cell systems, such as the hydrogen-iodine fuel cell. For this new measurement technique to work, the electrolyte at the positive electrode must be able to react on the Pt catalyst at the hydrogen electrode when crossover occurs while not poisoning the Pt catalyst.

6.6 Acknowledgments

The authors wish to acknowledge the financial support from the University of Kansas (KU) Madison and Lila Self Fellowship. Supplies for this work were supported by the National Science Foundation through grant no. EFRI-1038234. The authors would also like to thank Yuanchao Li for his assistance in preparing the nitric acid-treated electrodes.

6.7 References for Chapter 6

1. P. Alotto, M. Guarnieri and F. Moro, *Renewable and Sustainable Energy Reviews*, **29**, 325 (2014).

2. T. V. Nguyen and R. F. Savinell, Flow Batteries, in *The Electrochemical Society Interface*, p. 54 (2010).

3. C. Ponce de León, A. Frías-Ferrer, J. González-García, D. A. Szánto and F. C. Walsh, *Journal of Power Sources*, **160**, 716 (2006).

4. M. Skyllas-Kazacos, M. H. Chakrabarti, S. A. Hajimolana, F. S. Mjalli and M. Saleem, *Journal of The Electrochemical Society*, **158**, R55 (2011).

5. A. Z. Weber, M. M. Mench, J. P. Meyers, P. N. Ross, J. T. Gostick and Q. Liu, *Journal of Applied Electrochemistry*, **41**, 1137 (2011).

6. M. Zhang, M. Moore, J. S. Watson, T. A. Zawodzinski and R. M. Counce, *Journal of The Electrochemical Society*, **159**, A1183 (2012).

7. V. Yufit, B. Hale, M. Matian, P. Mazur and N. P. Brandon, *Journal of the Electrochemical Society*, **160**, A856 (2013).

8. R. P. Dowd, V. S. Lakhanpal and T. V. Nguyen, *Journal of The Electrochemical Society*, **164**, F564 (2017).

9. W. Xie, R. M. Darling and M. L. Perry, *Journal of The Electrochemical Society*, **163**, A5084 (2015).

10. C. Jia, J. Liu and C. Yan, *Journal of Power Sources*, **203**, 190 (2012).

11. K. W. Knehr, E. Agar, C. R. Dennison, A. R. Kalidindi and E. C. Kumbur, *Journal of the Electrochemical Society*, **159**, A1446 (2012).

12. J. Pan, S. Wang, M. Xiao, M. Hickner and Y. Meng, *Journal of Membrane Science*, **443**, 19 (2013).

13. X. Teng, Y. Zhao, J. Xi, Z. Wu, X. Qiu and L. Chen, *Journal of Power Sources*, **189**, 1240 (2009).

14. W. Xie, J. Cook, H. B. Park, B. D. Freeman, C. H. Lee and J. E. McGrath, *Polymer*, **52**, 2032 (2011).

15. Y. Zhang, J. Li, L. Wang and S. Zhang, *Journal of Solid State Electrochemistry*, **18**, 3479 (2014).

16. H. Huang and T. V. Nguyen, *Journal of The Electrochemical Society*, **144**, 2420 (1997).

17. T. V. Nguyen and R. E. White, *Journal of The Electrochemical Society*, **140**, 2178 (1993).

18. R. M. Darling, A. Z. Weber, M. C. Tucker and M. L. Perry, *Journal of The Electrochemical Society*, **163**, A5014 (2016).

19. C. Sun, J. Chen, H. Zhang, X. Han and Q. Luo, *Journal of Power Sources*, **195**, 890 (2010).

20. E. L. Cussler, *Diffusion: Mass Transfer in Fluid Systems*, Cambridge University Press, Cambridge, UK (2009).

21. J. S. Lawton, A. Jones and T. Zawodzinski, *Journal of The Electrochemical Society*, **160**, A697 (2013).

22. X. Teng, C. Sun, J. Dai, H. Liu, J. Su and F. Li, *Electrochimica Acta*, **88**, 725 (2013).

23. J. Newman and K. E. Thomas-Alyea, in *Electrochemical Systems*, John Wiley & Sons, New Jersey (2004).

24. T. V. Nguyen, M. V. Nguyen, G. Lin, N. Rao, X. Xie and D. M. Zhu, *Electrochemical and Solid-State Letters*, **9**, A88 (2006).

25. T. V. Nguyen, M. V. Nguyen, K. J. Nordheden and W. He, *Journal of The Electrochemical Society*, **154**, A1073 (2007).

26. R. P. Dowd, C. S. Day and T. V. Nguyen, *Journal of The Electrochemical Society*, **164**, F138 (2017).

27. R. P. Dowd, T. V. Nguyen, D. S. Moore, P. N. Pintauro and J. W. Park, *ECS Transactions*, **58**, 607 (2013).

CHAPTER 7: Future Work and Recommendations

7.1 PEM Fuel Cell Catalyst Layer Development

This work revealed how the surface chemistry of a Nafion thin film ionomer in the fuel cell catalyst layer, as well as the surface of conventional Nafion membranes, could be tailored to be either hydrophobic or hydrophilic. In the future, the hydrophilic treated ionomer and membrane should be tested in various flow batteries to determine if the new surface structure will improve mass transport of liquid electrolyte, therefore lead to higher fuel cell performance. Since long-term fuel cell durability is important for the marketability of fuel cells for various applications, future studies should also focus on the durability of the engineered ionomer-gas interface inside the pores of the catalyst layer. Research in these areas are ongoing in our research group.

7.2 Alkaline-Based H_2-Br_2 and H_2-I_2 Reversible Fuel Cells Development

Currently, there is a technological need for large-scale energy storage in order to take full advantage of intermittent energy sources, reduce the negative environmental impact of conventional energy sources (petroleum-based), and enable energy independence for countries throughout the world. Additionally, as energy demand increases worldwide, distributed energy storage solutions will enable electric grid load leveling. In turn, effective use of electric grid load leveling will reduce or slow the need to expand or increase the capacity of distributed electric grid networks.

Reversible fuel cell and flow battery technology has the ability to meet multiple needs in the current energy market. The multitude of possible chemistries which could be used in reversible fuel cell and flow battery applications have yet to be explored. These untapped chemistries could accelerate energy storage solutions to the marketplace.

7.3 H_2-Vanadium Reversible Fuel Cell Development

Currently, the all-vanadium flow battery is one of the few commercially-available flow battery systems. The high cost of the all-vanadium system requires government subsidies (in places like Japan and the United States) to enable these energy storage systems to be marketable to potential customers. The hydrogen-vanadium reversible fuel cell requires half the volume of vanadium electrolyte required for the all-vanadium flow battery. The reduced vanadium electrolyte directly impacts the overall system cost. Unfortunately, the hydrogen electrode of the hydrogen-vanadium reversible fuel cell requires a catalyst. Multiple research groups are investigating cheaper and more abundant catalysts for the hydrogen oxidation and hydrogen evolution reactions. Exploration for new types of non-platinum group metal (non-PGM) catalysts is important to ensure low cost systems.

7.4 Contributions to these Areas

This work has benefited the research community and society through the following publications.

1. R.P. Dowd Jr., V. Yarlagadda, D. Konwar, G. Lin, G. Weng, C. Li, K. Chan and T.V. Nguyen, "A Study of Alkaline-Based H_2-Br_2 and H_2-I_2 Reversible Fuel Cells," *Journal of The Electrochemical Society*, **163**, F1471 (2016).
2. R.P. Dowd Jr., C.S. Day and T.V. Nguyen, "Engineering the Ionic Polymer Phase Surface Properties of a PEM Fuel Cell Catalyst Layer," *Journal of The Electrochemical Society*, **164**, F138 (2017).
3. R.P. Dowd Jr., V.S. Lakhanpal and T.V. Nguyen, "Performance Evaluation of a Hydrogen-Vanadium Reversible Fuel Cell," *Journal of The Electrochemical Society*, **164**, F564 (2017).

4. (Submitted) R.P. Dowd Jr., D. Powers, R. Wycisk, P.N. Pintauro and T.V. Nguyen, "Hydrogen-Vanadium Reversible Fuel Cell Crossover Study," *Journal of The Electrochemical Society*, (2017).
5. (Patent pending, expected submission June 2017) R.P. Dowd Jr., T.V. Nguyen, "Controlling the Ionic Polymer/Gas Interfacial Properties of a PEM Fuel Cell Catalyst Layer during Membrane Electrode Assembly Fabrication," *Journal of The Electrochemical Society*, (2017).
6. R.P. Dowd Jr., C.S. Day and T.V. Nguyen, "Engineering the Ionic Polymer Phase Surface Properties of a PEM Fuel Cell Catalyst Layer," *ECS Transactions*, **72**, 1 (2016).
7. R.P. Dowd Jr., T.V. Nguyen, D.S. Moore, P.N. Pintauro and J.W. Park, "Conductive AFM Study to Differentiate Between the Surface Ionic Conductivity of Nafion and Electrospun Membranes," *ECS Transactions*, **58**, 607 (2013).
8. R.P. Dowd Jr., A. Ying and T.V. Nguyen, "Preliminary Study of a Reversible Hydrogen-Vanadium Flow Battery," *ECS Transactions*, **72**, 11 (2016).

CHAPTER 8: Appendices

8.1 Appendix A: Experimental Data for Chapter 2

Table 8.1. Experimental data for Figure 2.9 (Hydrophobic Nafion 212).

Angle-resolved XPS	
XPS Take-off Angle (degrees)	**Sulfur to Carbon Atomic Percent Ratio**
	Hydrophobic Nafion 212
20	1.63
25	2.21
30	2.16
35	3.05
40	3.94
45	3.76
50	3.90
55	4.13
60	4.09
65	4.04
70	3.95

Table 8.2. Experimental data for Figure 2.9 (Hydrophilic Nafion 212).

Angle-resolved XPS	
XPS Take-off Angle (degrees)	**Sulfur to Carbon Atomic Percent Ratio**
	Hydrophilic Nafion 212
20	7.85
25	6.41
30	6.67
35	6.59
40	6.02
45	4.96
50	5.00
55	5.34
60	5.12
65	5.20
70	5.04

Table 8.3. Experimental data for Figure 2.9 (Boiled Hydrophobic Nafion 212).

Angle-resolved XPS	
XPS Take-off Angle (degrees)	**Sulfur to Carbon Atomic Percent Ratio**
	Boiled Hydrophobic Nafion 212
20	1.96
25	2.26
30	2.52
35	2.74
40	3.32
45	3.26
50	3.87
55	4.21
60	4.18
65	4.22
70	4.28

Table 8.4. Experimental data for Figure 2.9 (As-received Nafion 212).

Angle-resolved XPS	
XPS Take-off Angle (degrees)	**Sulfur to Carbon Atomic Percent Ratio**
	As-received Nafion 212
20	4.87
25	4.38
30	4.13
35	4.25
40	4.08
45	4.98
50	5.50
55	5.40
60	5.56
65	5.17
70	5.17

Table 8.5. Experimental data for Figure 2.9 (As-received Nafion 115).

Angle-resolved XPS	
XPS Take-off Angle (degrees)	**Sulfur to Carbon Atomic Percent Ratio**
	As-received Nafion 115
20	3.53
25	3.59
30	4.06
35	3.71
40	4.52
45	4.69
50	4.62
55	4.80
60	4.62
65	4.74
70	4.75

Table 8.6. Experimental data for Figure 2.10 (Conventional MEA).

H_2-Air PEMFC discharge polarization and power density curves		
Conventional MEA		
Voltage (V)	**Current Density (A/cm^2)**	**Power Density (W/cm^2)**
0.974	0.000	0.000
0.901	0.003	0.003
0.852	0.010	0.008
0.804	0.024	0.019
0.756	0.046	0.035
0.710	0.075	0.053
0.664	0.109	0.072
0.618	0.146	0.090
0.573	0.186	0.107
0.528	0.228	0.120
0.483	0.270	0.130
0.437	0.308	0.135
0.392	0.352	0.138
0.347	0.392	0.136
0.302	0.429	0.130
0.256	0.464	0.119
0.209	0.492	0.103
0.163	0.524	0.085

Table 8.7. Experimental data for Figure 2.10 (IR-corrected Conventional MEA).

H_2-Air PEMFC discharge polarization and power density curves		
IR-corrected Conventional MEA		
Voltage (V)	**Current Density (A/cm^2)**	**Power Density (W/cm^2)**
0.974	0.000	0.000
0.902	0.003	0.003
0.854	0.010	0.008
0.810	0.024	0.019
0.768	0.046	0.035
0.729	0.075	0.055
0.691	0.109	0.075
0.655	0.146	0.096
0.620	0.186	0.116
0.586	0.228	0.133
0.551	0.270	0.149
0.516	0.308	0.159
0.482	0.352	0.170
0.447	0.392	0.175
0.411	0.429	0.176
0.374	0.464	0.173
0.334	0.492	0.165
0.296	0.524	0.155

Table 8.8. Experimental data for Figure 2.10 (Disk MEA).

H_2-Air PEMFC discharge polarization and power density curves		
Disk MEA		
Voltage (V)	**Current Density (A/cm^2)**	**Power Density (W/cm^2)**
0.982	0.000	0.000
0.901	0.003	0.003
0.852	0.009	0.007
0.803	0.021	0.017
0.756	0.044	0.034
0.710	0.076	0.054
0.664	0.115	0.076
0.620	0.158	0.098
0.575	0.207	0.119
0.531	0.260	0.138
0.488	0.316	0.154
0.445	0.375	0.167
0.402	0.433	0.174
0.359	0.493	0.177
0.316	0.552	0.175
0.273	0.611	0.167
0.230	0.670	0.154
0.186	0.714	0.132

Table 8.9. Experimental data for Figure 2.10 (IR-corrected Disk MEA).

H_2-Air PEMFC discharge polarization and power density curves		
IR-corrected Disk MEA		
Voltage (V)	**Current Density (A/cm^2)**	**Power Density (W/cm^2)**
0.982	0.000	0.000
0.902	0.003	0.003
0.853	0.009	0.007
0.807	0.021	0.017
0.764	0.044	0.034
0.724	0.076	0.055
0.685	0.115	0.079
0.649	0.158	0.103
0.613	0.207	0.127
0.579	0.260	0.151
0.546	0.316	0.172
0.514	0.375	0.192
0.481	0.433	0.208
0.449	0.493	0.221
0.417	0.552	0.230
0.385	0.611	0.235
0.352	0.670	0.236
0.316	0.714	0.225

8.2 Appendix B: Experimental Data for Chapter 3

Table 8.10. Experimental data for Figure 3.3.

Sulfur to Fluorine Atomic Percent Ratio X 100						
	Hydrophilic Electrode		Hydrophobic Electrode		As-Received Electrode	
# Scrapes	Average	Std Dev	Average	Std Dev	Average	Std Dev
0	1.3618	0.0678	0.7611	0.0915	1.1840	0.0575
1	1.3585	0.0805	0.8798	0.0513	1.0510	0.0280
2	1.4866	0.1428	0.6990	0.0557	0.9226	0.0739
3	1.1454	0.1036	0.7559	0.0722	0.8458	0.1331

Table 8.11. Experimental data for Figure 3.4 (Normal MEA, 25ºC, Humid Air, Serpentine Flow Field).

H_2-Air discharge polarization and power density curves		
Normal MEA, 25ºC, Humid Air, Serpentine Flow Field		
Cell Potential (V)	**Current Density (A/cm^2)**	**Power Density (W/cm^2)**
0.210	0.526	0.110
0.255	0.491	0.125
0.301	0.453	0.136
0.346	0.415	0.144
0.392	0.374	0.147
0.437	0.333	0.146
0.482	0.291	0.140
0.527	0.247	0.130
0.572	0.204	0.116
0.617	0.161	0.099
0.662	0.118	0.078
0.707	0.077	0.054
0.754	0.044	0.033
0.801	0.020	0.016
0.849	0.007	0.006
0.899	0.002	0.002
0.955	0.000	0.000

Table 8.12. Experimental data for Figure 3.4 (Normal MEA, 25ºC w/ 50ºC H2, Humid Air, Serpentine Flow Field).

H_2-Air discharge polarization and power density curves		
Normal MEA, 25ºC w/ 50ºC H_2, Humid Air, Serpentine Flow Field		
Cell Potential (V)	**Current Density (A/cm^2)**	**Power Density (W/cm^2)**
0.215	0.576	0.124
0.260	0.536	0.139
0.305	0.495	0.151
0.350	0.453	0.159
0.396	0.409	0.162
0.440	0.364	0.160
0.485	0.318	0.154
0.530	0.271	0.144
0.574	0.224	0.128
0.619	0.177	0.109
0.664	0.132	0.088
0.709	0.091	0.065
0.755	0.055	0.041
0.802	0.026	0.021
0.849	0.008	0.007
0.899	0.002	0.002
0.957	0.000	0.000

Table 8.13. Experimental data for Figure 3.4 (Normal MEA, 70ºC, Humid Air, Serpentine Flow Field).

H_2-Air discharge polarization and power density curves		
Normal MEA, 70ºC, Humid Air, Serpentine Flow Field		
Cell Potential (V)	**Current Density (A/cm^2)**	**Power Density (W/cm^2)**
0.252	0.904	0.228
0.296	0.856	0.254
0.341	0.809	0.276
0.384	0.747	0.287
0.426	0.678	0.289
0.467	0.606	0.283
0.509	0.530	0.270
0.549	0.443	0.243
0.590	0.363	0.214
0.630	0.276	0.174
0.671	0.196	0.132
0.713	0.126	0.090
0.756	0.068	0.052
0.802	0.028	0.022
0.849	0.007	0.006
0.898	0.001	0.001
0.924	0.000	0.000

Table 8.14. Experimental data for Figure 3.4 (Natural Convection MEA, 25ºC, Humid Air, Serpentine Flow Field).

H_2-Air discharge polarization and power density curves		
Natural Convection MEA, 25ºC, Humid Air, Serpentine Flow Field		
Cell Potential (V)	**Current Density (A/cm^2)**	**Power Density (W/cm^2)**
0.260	0.977	0.254
0.302	0.902	0.272
0.343	0.820	0.281
0.384	0.743	0.285
0.425	0.663	0.282
0.466	0.585	0.273
0.507	0.507	0.257
0.548	0.428	0.235
0.589	0.351	0.207
0.631	0.274	0.173
0.673	0.204	0.137
0.715	0.140	0.100
0.759	0.082	0.062
0.804	0.038	0.030
0.851	0.012	0.010
0.899	0.002	0.002
0.987	0.000	0.000

Table 8.15. Experimental data for Figure 3.4 (Natural Convection MEA, 25ºC w/ 50ºC H2, Humid Air, Serpentine Flow Field).

H_2-Air discharge polarization and power density curves		
Natural Convection MEA, 25ºC w/ 50ºC H_2, Humid Air, Serpentine Flow Field		
Cell Potential (V)	**Current Density (A/cm^2)**	**Power Density (W/cm^2)**
0.263	1.007	0.265
0.306	0.945	0.289
0.348	0.875	0.305
0.390	0.802	0.312
0.431	0.724	0.312
0.472	0.646	0.305
0.513	0.565	0.290
0.554	0.485	0.269
0.595	0.406	0.241
0.636	0.328	0.209
0.677	0.253	0.171
0.719	0.181	0.130
0.762	0.116	0.088
0.806	0.061	0.049
0.851	0.024	0.021
0.899	0.006	0.006
0.993	0.000	0.000

Table 8.16. Experimental data for Figure 3.4 (Natural Convection MEA, 70ºC, Humid Air, Serpentine Flow Field).

H_2-Air discharge polarization and power density curves		
Natural Convection MEA, 70ºC, Humid Air, Serpentine Flow Field		
Cell Potential (V)	**Current Density (A/cm^2)**	**Power Density (W/cm^2)**
0.307	1.394	0.428
0.351	1.343	0.472
0.394	1.284	0.506
0.435	1.201	0.523
0.475	1.113	0.529
0.513	1.012	0.519
0.550	0.896	0.493
0.587	0.779	0.457
0.623	0.662	0.412
0.660	0.539	0.356
0.695	0.412	0.287
0.732	0.291	0.213
0.770	0.187	0.144
0.809	0.095	0.077
0.853	0.035	0.030
0.899	0.008	0.007
0.969	0.000	0.000

Table 8.17. Experimental data for Figure 3.5 (Normal MEA, 25ºC, Humid Air, Serpentine Flow Field).

H_2-Air discharge polarization and power density curves		
Normal MEA, 25ºC, Humid Air, Serpentine Flow Field		
Cell Potential (V)	**Current Density (A/cm^2)**	**Power Density (W/cm^2)**
0.210	0.526	0.110
0.255	0.491	0.125
0.301	0.453	0.136
0.346	0.415	0.144
0.392	0.374	0.147
0.437	0.333	0.146
0.482	0.291	0.140
0.527	0.247	0.130
0.572	0.204	0.116
0.617	0.161	0.099
0.662	0.118	0.078
0.707	0.077	0.054
0.754	0.044	0.033
0.801	0.020	0.016
0.849	0.007	0.006
0.899	0.002	0.002
0.955	0.000	0.000

Table 8.18. Experimental data for Figure 3.5 (Normal MEA, 25ºC, Humid Air, Interdigitated Flow Field).

H_2-Air discharge polarization and power density curves		
Normal MEA, 25ºC, Humid Air, Interdigitated Flow Field		
Cell Potential (V)	**Current Density (A/cm^2)**	**Power Density (W/cm^2)**
0.215	0.579	0.125
0.260	0.537	0.140
0.305	0.490	0.149
0.349	0.442	0.154
0.394	0.394	0.155
0.438	0.343	0.150
0.483	0.296	0.143
0.527	0.248	0.131
0.572	0.204	0.116
0.617	0.159	0.098
0.662	0.115	0.076
0.707	0.075	0.053
0.754	0.042	0.032
0.801	0.018	0.014
0.849	0.005	0.005
0.899	0.001	0.001
0.942	0.000	0.000

Table 8.19. Experimental data for Figure 3.5 (Natural Convection MEA, 25ºC, Humid Air, Serpentine Flow Field).

H_2-Air discharge polarization and power density curves		
Natural Convection MEA, 25ºC, Humid Air, Serpentine Flow Field		
Cell Potential (V)	**Current Density (A/cm^2)**	**Power Density (W/cm^2)**
0.260	0.977	0.254
0.302	0.902	0.272
0.343	0.820	0.281
0.384	0.743	0.285
0.425	0.663	0.282
0.466	0.585	0.273
0.507	0.507	0.257
0.548	0.428	0.235
0.589	0.351	0.207
0.631	0.274	0.173
0.673	0.204	0.137
0.715	0.140	0.100
0.759	0.082	0.062
0.804	0.038	0.030
0.851	0.012	0.010
0.899	0.002	0.002
0.987	0.000	0.000

Table 8.20. Experimental data for Figure 3.5 (Natural Convection MEA, 25ºC, Humid Air, Interdigitated Flow Field).

H_2-Air discharge polarization and power density curves		
Natural Convection MEA, 25ºC, Humid Air, Interdigitated Flow Field		
Cell Potential (V)	**Current Density (A/cm^2)**	**Power Density (W/cm^2)**
0.275	1.108	0.305
0.315	1.025	0.323
0.356	0.945	0.337
0.397	0.860	0.341
0.437	0.771	0.337
0.476	0.682	0.325
0.516	0.593	0.306
0.556	0.504	0.280
0.596	0.416	0.248
0.636	0.329	0.209
0.677	0.245	0.166
0.718	0.169	0.121
0.760	0.102	0.078
0.804	0.051	0.041
0.851	0.018	0.016
0.899	0.004	0.004
0.985	0.000	0.000

Table 8.21. Experimental data for Figure 3.6 (Normal MEA, 70ºC, Humid Air, Serpentine Flow Field).

H_2-Air discharge polarization and power density curves		
Normal MEA, 70ºC, Humid Air, Serpentine Flow Field		
Cell Potential (V)	**Current Density (A/cm^2)**	**Power Density (W/cm^2)**
0.252	0.904	0.228
0.296	0.856	0.254
0.341	0.809	0.276
0.384	0.747	0.287
0.426	0.678	0.289
0.467	0.606	0.283
0.509	0.530	0.270
0.549	0.443	0.243
0.590	0.363	0.214
0.630	0.276	0.174
0.671	0.196	0.132
0.713	0.126	0.090
0.756	0.068	0.052
0.802	0.028	0.022
0.849	0.007	0.006
0.898	0.001	0.001
0.924	0.000	0.000

Table 8.22. Experimental data for Figure 3.6 (Normal MEA, 70ºC, Humid Air, Interdigitated Flow Field).

H_2-Air discharge polarization and power density curves		
Normal MEA, 70ºC, Humid Air, Interdigitated Flow Field		
Cell Potential (V)	**Current Density (A/cm^2)**	**Power Density (W/cm^2)**
0.265	1.012	0.268
0.307	0.951	0.292
0.350	0.894	0.313
0.392	0.823	0.323
0.434	0.752	0.327
0.475	0.676	0.322
0.515	0.581	0.299
0.554	0.489	0.271
0.594	0.396	0.235
0.633	0.300	0.190
0.673	0.215	0.145
0.714	0.135	0.097
0.757	0.071	0.054
0.802	0.027	0.022
0.849	0.007	0.006
0.899	0.001	0.001
0.922	0.000	0.000

Table 8.23. Experimental data for Figure 3.6 (Natural Convection MEA, 70ºC, Humid Air, Serpentine Flow Field).

H_2-Air discharge polarization and power density curves		
Natural Convection MEA, 70ºC, Humid Air, Serpentine Flow Field		
Cell Potential (V)	**Current Density (A/cm^2)**	**Power Density (W/cm^2)**
0.307	1.394	0.428
0.351	1.343	0.472
0.394	1.284	0.506
0.435	1.201	0.523
0.475	1.113	0.529
0.513	1.012	0.519
0.550	0.896	0.493
0.587	0.779	0.457
0.623	0.662	0.412
0.660	0.539	0.356
0.695	0.412	0.287
0.732	0.291	0.213
0.770	0.187	0.144
0.809	0.095	0.077
0.853	0.035	0.030
0.899	0.008	0.007
0.969	0.000	0.000

Table 8.24. Experimental data for Figure 3.6 (Natural Convection MEA, 70ºC, Humid Air, Interdigitated Flow Field).

H_2-Air discharge polarization and power density curves		
Natural Convection MEA, 70ºC, Humid Air, Interdigitated Flow Field		
Cell Potential (V)	**Current Density (A/cm^2)**	**Power Density (W/cm^2)**
0.347	1.745	0.605
0.385	1.645	0.634
0.424	1.544	0.654
0.461	1.436	0.663
0.499	1.323	0.660
0.535	1.200	0.642
0.568	1.053	0.598
0.601	0.904	0.543
0.634	0.758	0.481
0.667	0.603	0.402
0.701	0.458	0.321
0.736	0.331	0.243
0.772	0.206	0.159
0.810	0.102	0.082
0.852	0.035	0.030
0.899	0.007	0.006
0.975	0.000	0.000

Table 8.25. Experimental data for Figure 3.7 (Normal MEA, 25ºC, Humid Air, Interdigitated Flow Field).

H_2-Air discharge polarization and power density curves		
Normal MEA, 25ºC, Humid Air, Interdigitated Flow Field		
Cell Potential (V)	**Current Density (A/cm^2)**	**Power Density (W/cm^2)**
0.215	0.579	0.125
0.260	0.537	0.140
0.305	0.490	0.149
0.349	0.442	0.154
0.394	0.394	0.155
0.438	0.343	0.150
0.483	0.296	0.143
0.527	0.248	0.131
0.572	0.204	0.116
0.617	0.159	0.098
0.662	0.115	0.076
0.707	0.075	0.053
0.754	0.042	0.032
0.801	0.018	0.014
0.849	0.005	0.005
0.899	0.001	0.001
0.942	0.000	0.000

Table 8.26. Experimental data for Figure 3.7 (Natural Convection MEA, 25ºC, Humid Air, Interdigitated Flow Field).

H_2-Air discharge polarization and power density curves		
Natural Convection MEA, 25ºC, Humid Air, Interdigitated Flow Field		
Cell Potential (V)	**Current Density (A/cm^2)**	**Power Density (W/cm^2)**
0.275	1.108	0.305
0.315	1.025	0.323
0.356	0.945	0.337
0.397	0.860	0.341
0.437	0.771	0.337
0.476	0.682	0.325
0.516	0.593	0.306
0.556	0.504	0.280
0.596	0.416	0.248
0.636	0.329	0.209
0.677	0.245	0.166
0.718	0.169	0.121
0.760	0.102	0.078
0.804	0.051	0.041
0.851	0.018	0.016
0.899	0.004	0.004
0.985	0.000	0.000

Table 8.27. Experimental data for Figure 3.7 (Forced Convection 1 min MEA, 25ºC, Humid Air, Interdigitated Flow Field).

H_2-Air discharge polarization and power density curves		
Forced Convection 1 min MEA, 25ºC, Humid Air, Interdigitated Flow Field		
Cell Potential (V)	**Current Density (A/cm^2)**	**Power Density (W/cm^2)**
0.285	1.192	0.339
0.324	1.097	0.355
0.363	1.001	0.363
0.402	0.906	0.364
0.441	0.811	0.358
0.480	0.712	0.342
0.520	0.623	0.323
0.559	0.529	0.296
0.599	0.442	0.265
0.639	0.352	0.225
0.679	0.267	0.181
0.720	0.187	0.135
0.762	0.116	0.089
0.806	0.060	0.048
0.852	0.023	0.020
0.899	0.006	0.005
0.990	0.000	0.000

Table 8.28. Experimental data for Figure 3.7 (Forced Convection 2 min MEA, 25ºC, Humid Air, Interdigitated Flow Field).

H_2-Air discharge polarization and power density curves		
Forced Convection 2 min MEA, 25ºC, Humid Air, Interdigitated Flow Field		
Cell Potential (V)	**Current Density (A/cm^2)**	**Power Density (W/cm^2)**
0.259	0.967	0.250
0.301	0.899	0.271
0.343	0.824	0.283
0.384	0.752	0.289
0.426	0.681	0.290
0.468	0.613	0.287
0.510	0.543	0.277
0.552	0.469	0.259
0.594	0.399	0.237
0.635	0.322	0.204
0.677	0.247	0.168
0.719	0.175	0.126
0.761	0.109	0.083
0.805	0.055	0.044
0.851	0.020	0.017
0.899	0.005	0.005
0.996	0.000	0.000

Table 8.29. Experimental data for Figure 3.7 (Forced Convection 5 min MEA, 25ºC, Humid Air, Interdigitated Flow Field).

H_2-Air discharge polarization and power density curves		
Forced Convection 5 min MEA, 25ºC, Humid Air, Interdigitated Flow Field		
Cell Potential (V)	**Current Density (A/cm^2)**	**Power Density (W/cm^2)**
0.268	1.053	0.283
0.309	0.968	0.299
0.350	0.886	0.310
0.390	0.799	0.311
0.430	0.718	0.309
0.471	0.635	0.299
0.512	0.552	0.283
0.552	0.471	0.260
0.593	0.390	0.232
0.634	0.312	0.198
0.676	0.238	0.161
0.718	0.172	0.124
0.761	0.112	0.085
0.806	0.061	0.049
0.851	0.026	0.022
0.899	0.007	0.006
0.990	0.000	0.000

Table 8.30. Experimental data for Figure 3.8 (Normal MEA, 70ºC, Humid Air, Interdigitated Flow Field).

H_2-Air discharge polarization and power density curves		
Normal MEA, 70ºC, Humid Air, Interdigitated Flow Field		
Cell Potential (V)	**Current Density (A/cm^2)**	**Power Density (W/cm^2)**
0.265	1.012	0.268
0.307	0.951	0.292
0.350	0.894	0.313
0.392	0.823	0.323
0.434	0.752	0.327
0.475	0.676	0.322
0.515	0.581	0.299
0.554	0.489	0.271
0.594	0.396	0.235
0.633	0.300	0.190
0.673	0.215	0.145
0.714	0.135	0.097
0.757	0.071	0.054
0.802	0.027	0.022
0.849	0.007	0.006
0.899	0.001	0.001
0.922	0.000	0.000

Table 8.31. Experimental data for Figure 3.8 (Natural Convection MEA, 70ºC, Humid Air, Interdigitated Flow Field).

H_2-Air discharge polarization and power density curves		
Natural Convection MEA, 70ºC, Humid Air, Interdigitated Flow Field		
Cell Potential (V)	**Current Density (A/cm^2)**	**Power Density (W/cm^2)**
0.347	1.745	0.605
0.385	1.645	0.634
0.424	1.544	0.654
0.461	1.436	0.663
0.499	1.323	0.660
0.535	1.200	0.642
0.568	1.053	0.598
0.601	0.904	0.543
0.634	0.758	0.481
0.667	0.603	0.402
0.701	0.458	0.321
0.736	0.331	0.243
0.772	0.206	0.159
0.810	0.102	0.082
0.852	0.035	0.030
0.899	0.007	0.006
0.975	0.000	0.000

Table 8.32. Experimental data for Figure 3.8 (Forced Convection 1 min MEA, 70ºC, Humid Air, Interdigitated Flow Field).

H_2-Air discharge polarization and power density curves		
Forced Convection 1 min MEA, 70ºC, Humid Air, Interdigitated Flow Field		
Cell Potential (V)	**Current Density (A/cm^2)**	**Power Density (W/cm^2)**
0.369	1.939	0.716
0.407	1.836	0.747
0.444	1.717	0.762
0.477	1.571	0.749
0.510	1.415	0.721
0.542	1.260	0.683
0.573	1.096	0.628
0.606	0.941	0.570
0.639	0.795	0.508
0.671	0.636	0.426
0.703	0.478	0.336
0.738	0.345	0.255
0.775	0.228	0.177
0.812	0.115	0.093
0.853	0.041	0.035
0.900	0.008	0.008
0.966	0.000	0.000

Table 8.33. Experimental data for Figure 3.8 (Forced Convection 2 min MEA, 70ºC, Humid Air, Interdigitated Flow Field).

H_2-Air discharge polarization and power density curves		
Forced Convection 2 min MEA, 70ºC, Humid Air, Interdigitated Flow Field		
Cell Potential (V)	**Current Density (A/cm^2)**	**Power Density (W/cm^2)**
0.319	1.497	0.477
0.363	1.445	0.525
0.405	1.372	0.555
0.445	1.288	0.573
0.484	1.192	0.577
0.523	1.096	0.574
0.561	0.986	0.553
0.597	0.868	0.518
0.631	0.726	0.458
0.665	0.582	0.386
0.698	0.436	0.304
0.733	0.307	0.225
0.770	0.189	0.145
0.809	0.091	0.074
0.852	0.032	0.027
0.899	0.007	0.006
0.961	0.000	0.000

Table 8.34. Experimental data for Figure 3.8 (Forced Convection 5 min MEA, 70ºC, Humid Air, Interdigitated Flow Field).

H_2-Air discharge polarization and power density curves		
Forced Convection 5 min MEA, 70ºC, Humid Air, Interdigitated Flow Field		
Cell Potential (V)	**Current Density (A/cm^2)**	**Power Density (W/cm^2)**
0.330	1.597	0.527
0.372	1.525	0.567
0.412	1.434	0.590
0.450	1.332	0.600
0.488	1.227	0.599
0.526	1.116	0.587
0.561	0.992	0.557
0.596	0.858	0.512
0.632	0.731	0.462
0.665	0.585	0.389
0.700	0.450	0.315
0.736	0.325	0.239
0.771	0.200	0.154
0.812	0.114	0.092
0.853	0.040	0.034
0.900	0.010	0.009
0.973	0.000	0.000

Table 8.35. Experimental data for Figure 3.9 (Normal MEA, 70ºC, Dry Air, Interdigitated Flow Field).

H_2-Air discharge polarization and power density curves		
Normal MEA, 70ºC, Dry Air, Interdigitated Flow Field		
Cell Potential (V)	**Current Density (A/cm^2)**	**Power Density (W/cm^2)**
0.318	1.490	0.474
0.360	1.421	0.512
0.400	1.336	0.535
0.440	1.246	0.548
0.479	1.147	0.549
0.517	1.039	0.537
0.553	0.925	0.512
0.589	0.801	0.472
0.625	0.674	0.421
0.660	0.542	0.358
0.695	0.413	0.287
0.732	0.291	0.213
0.769	0.182	0.140
0.809	0.094	0.076
0.853	0.036	0.031
0.900	0.009	0.008
0.938	0.000	0.000

Table 8.36. Experimental data for Figure 3.9 (Natural Convection MEA, 70ºC, Dry Air, Interdigitated Flow Field).

H_2-Air discharge polarization and power density curves		
Natural Convection MEA, 70ºC, Dry Air, Interdigitated Flow Field		
Cell Potential (V)	**Current Density (A/cm^2)**	**Power Density (W/cm^2)**
0.361	1.873	0.676
0.399	1.765	0.704
0.437	1.656	0.723
0.473	1.539	0.729
0.509	1.411	0.719
0.544	1.278	0.695
0.577	1.128	0.651
0.610	0.978	0.596
0.642	0.822	0.528
0.674	0.667	0.450
0.707	0.516	0.365
0.741	0.370	0.274
0.775	0.233	0.180
0.812	0.118	0.096
0.854	0.041	0.035
0.900	0.009	0.008
0.984	0.000	0.000

Table 8.37. Experimental data for Figure 3.9 (Forced Convection 1 min MEA, 70ºC, Dry Air, Interdigitated Flow Field).

H_2-Air discharge polarization and power density curves		
Forced Convection 1 min MEA, 70ºC, Dry Air, Interdigitated Flow Field		
Cell Potential (V)	**Current Density (A/cm^2)**	**Power Density (W/cm^2)**
0.382	2.056	0.785
0.416	1.919	0.799
0.452	1.787	0.807
0.485	1.645	0.799
0.519	1.497	0.776
0.551	1.338	0.737
0.582	1.178	0.686
0.614	1.020	0.627
0.646	0.862	0.557
0.679	0.704	0.478
0.711	0.548	0.389
0.744	0.399	0.297
0.778	0.260	0.202
0.815	0.141	0.115
0.855	0.055	0.047
0.900	0.013	0.011
0.991	0.000	0.000

Table 8.38. Experimental data for Figure 3.9 (Forced Convection 2 min MEA, 70ºC, Dry Air, Interdigitated Flow Field).

H_2-Air discharge polarization and power density curves		
Forced Convection 2 min MEA, 70ºC, Dry Air, Interdigitated Flow Field		
Cell Potential (V)	**Current Density (A/cm^2)**	**Power Density (W/cm^2)**
0.337	1.655	0.558
0.378	1.583	0.599
0.418	1.488	0.621
0.457	1.397	0.639
0.496	1.299	0.645
0.536	1.209	0.648
0.572	1.089	0.623
0.607	0.951	0.577
0.641	0.812	0.520
0.674	0.661	0.445
0.707	0.513	0.363
0.740	0.364	0.270
0.774	0.222	0.172
0.812	0.113	0.092
0.853	0.040	0.034
0.900	0.009	0.008
0.977	0.000	0.000

Table 8.39. Experimental data for Figure 3.9 (Forced Convection 5 min MEA, 70ºC, Dry Air, Interdigitated Flow Field).

H_2-Air discharge polarization and power density curves		
Forced Convection 5 min MEA, 70ºC, Dry Air, Interdigitated Flow Field		
Cell Potential (V)	**Current Density (A/cm^2)**	**Power Density (W/cm^2)**
0.336	1.650	0.555
0.377	1.574	0.594
0.417	1.481	0.618
0.455	1.377	0.626
0.493	1.268	0.625
0.530	1.151	0.610
0.566	1.029	0.582
0.601	0.901	0.542
0.636	0.770	0.490
0.671	0.636	0.427
0.705	0.498	0.351
0.740	0.365	0.271
0.776	0.240	0.187
0.814	0.132	0.108
0.855	0.052	0.044
0.900	0.012	0.011
0.972	0.000	0.000

8.3 Appendix C: Experimental Data for Chapter 4

Table 8.40. Experimental data for Figure 4.2a.

Time (min)	V_Cell (V)	V_Negative (V)	V_Positive (V)
0.0000	1.8788	-0.9227	0.9561
0.0167	1.8779	-0.9227	0.9553
0.0333	1.8793	-0.9224	0.9569
0.0500	1.8788	-0.9214	0.9574
0.0667	1.8789	-0.9230	0.9559
0.0833	1.8794	-0.9230	0.9564
0.1000	1.8788	-0.9233	0.9554
0.1167	1.8793	-0.9217	0.9575
0.1333	1.8788	-0.9224	0.9564
0.1500	1.8794	-0.9233	0.9561
0.1667	1.8791	-0.9224	0.9568
0.1833	1.8795	-0.9240	0.9555
0.2000	1.8793	-0.9217	0.9575
0.2167	1.8789	-0.9220	0.9569
0.2333	1.8793	-0.9233	0.9559
0.2500	1.8796	-0.9217	0.9579
0.2667	1.8794	-0.9282	0.9513
0.2833	1.8794	-0.9237	0.9558
0.3000	1.8801	-0.9220	0.9581
0.3167	1.8791	-0.9227	0.9564
0.3333	1.8794	-0.9207	0.9587
0.3500	1.8799	-0.9237	0.9562
0.3667	1.8798	-0.9275	0.9523
0.3833	1.8797	-0.9214	0.9583
0.4000	1.8799	-0.9214	0.9586
0.4167	1.8803	-0.9224	0.9579
0.4333	1.8801	-0.9240	0.9561
0.4500	1.8800	-0.9233	0.9567
0.4667	1.8804	-0.9227	0.9577
0.4833	1.8801	-0.9233	0.9568
0.5000	1.8804	-0.9220	0.9584
0.5167	1.8801	-0.9240	0.9561

0.5333	1.8799	-0.9227	0.9573
0.5500	1.8798	-0.9243	0.9555
0.5667	1.8801	-0.9233	0.9567
0.5833	1.8810	-0.9243	0.9567
0.6000	1.8805	-0.9217	0.9588
0.6167	1.8802	-0.9240	0.9562
0.6333	1.8799	-0.9224	0.9576
0.6500	1.8808	-0.9224	0.9584
0.6667	1.8802	-0.9237	0.9565
0.6833	1.8804	-0.9230	0.9574
0.7000	1.8804	-0.9253	0.9552
0.7167	1.8810	-0.9230	0.9580
0.7333	1.8810	-0.9233	0.9577
0.7500	1.8809	-0.9224	0.9586
0.7667	1.8814	-0.9227	0.9587
0.7833	1.8810	-0.9237	0.9574
0.8000	1.8809	-0.9240	0.9570
0.8167	1.8808	-0.9233	0.9574
0.8333	1.8808	-0.9237	0.9572
0.8500	1.8809	-0.9217	0.9592
0.8667	1.8810	-0.9237	0.9574
0.8833	1.8809	-0.9230	0.9579
0.9000	1.8820	-0.9243	0.9577
0.9167	1.8810	-0.9214	0.9596
0.9333	1.8808	-0.9227	0.9581
0.9500	1.8814	-0.9240	0.9574
0.9667	1.8819	-0.9240	0.9579
0.9833	1.8818	-0.9250	0.9568
1.0000	1.8815	-0.9240	0.9575
1.0167	1.8812	-0.9227	0.9585
1.0333	1.8813	-0.9243	0.9570
1.0500	1.8817	-0.9246	0.9571
1.0667	1.8819	-0.9233	0.9586
1.0833	1.8813	-0.9233	0.9580
1.1000	1.8821	-0.9230	0.9591
1.1167	1.8818	-0.9201	0.9617
1.1333	1.8818	-0.9243	0.9575
1.1500	1.8818	-0.9233	0.9584
1.1667	1.8820	-0.9266	0.9554

1.1833	1.8818	-0.9246	0.9572
1.2000	1.8820	-0.9230	0.9590
1.2167	1.8820	-0.9266	0.9554
1.2333	1.8820	-0.9246	0.9574
1.2500	1.8818	-0.9214	0.9604
1.2667	1.8825	-0.9240	0.9585
1.2833	1.8823	-0.9243	0.9580
1.3000	1.8819	-0.9243	0.9576
1.3167	1.8823	-0.9230	0.9593
1.3333	1.8823	-0.9240	0.9583
1.3500	1.8823	-0.9230	0.9593
1.3667	1.8824	-0.9253	0.9572
1.3833	1.8818	-0.9250	0.9569
1.4000	1.8823	-0.9217	0.9606
1.4167	1.8819	-0.9243	0.9576
1.4333	1.8824	-0.9240	0.9584
1.4500	1.8821	-0.9256	0.9565
1.4667	1.8819	-0.9240	0.9580
1.4833	1.8830	-0.9250	0.9581
1.5000	1.8824	-0.9250	0.9574
1.5167	1.8824	-0.9246	0.9578
1.5333	1.8824	-0.9237	0.9588
1.5500	1.8826	-0.9246	0.9580
1.5667	1.8824	-0.9269	0.9555
1.5833	1.8828	-0.9246	0.9581
1.6000	1.8825	-0.9256	0.9569
1.6167	1.8826	-0.9250	0.9577
1.6333	1.8819	-0.9233	0.9586
1.6500	1.8827	-0.9237	0.9590
1.6667	1.8824	-0.9253	0.9572
1.6833	1.8826	-0.9243	0.9583
1.7000	1.8822	-0.9237	0.9585
1.7167	1.8828	-0.9243	0.9585
1.7333	1.8827	-0.9243	0.9584
1.7500	1.8824	-0.9246	0.9578
1.7667	1.8824	-0.9331	0.9493
1.7833	1.8828	-0.9266	0.9562
1.8000	1.8827	-0.9256	0.9571
1.8167	1.8838	-0.9246	0.9592

1.8333	1.8829	-0.9250	0.9579
1.8500	1.8834	-0.9253	0.9581
1.8667	1.8828	-0.9259	0.9569
1.8833	1.8831	-0.9230	0.9601
1.9000	1.8829	-0.9285	0.9544
1.9167	1.8838	-0.9259	0.9579
1.9333	1.8833	-0.9272	0.9560
1.9500	1.8834	-0.9243	0.9591
1.9667	1.8831	-0.9256	0.9575
1.9833	1.8832	-0.9233	0.9599
2.0000	1.8835	-0.9259	0.9576

Table 8.41. Experimental data for Figure 4.2b.

V_Cell (V)	V_Positive (V)	V_Negative (V)	|Current Density| (mA/cm^2)
1.580	0.818	-0.762	18.341
1.630	0.824	-0.806	16.160
1.680	0.847	-0.833	13.548
1.730	0.870	-0.860	10.573
1.780	0.896	-0.884	7.300
1.830	0.923	-0.907	3.726
1.880	0.958	-0.922	0.118
1.890	0.960	-0.930	0.000
1.930	0.980	-0.950	4.524
1.980	1.014	-0.966	9.315
2.030	1.053	-0.977	14.388
2.080	1.090	-0.990	19.350
2.130	1.130	-1.000	25.305
2.180	1.169	-1.011	30.399

Table 8.42. Experimental data for Figure 4.3a (1st Study, N117, 1M KOH).

1st Study, N117, 1M KOH	
Cell Voltage (V)	**|Current Density| (mA/cm^2)**
1.580	18.341
1.630	16.160
1.680	13.548
1.730	10.573
1.780	7.300
1.830	3.726
1.880	0.118
1.890	0.000
1.930	4.524
1.980	9.315
2.030	14.388
2.080	19.350
2.130	25.305
2.180	30.399

Table 8.43. Experimental data for Figure 4.3a (N115, 1M KOH).

N115, 1M KOH	
Cell Voltage (V)	**|Current Density| (mA/cm^2)**
1.400	56.278
1.449	51.583
1.499	46.119
1.549	40.745
1.599	35.281
1.649	29.670
1.699	23.793
1.749	17.739
1.799	11.567
1.849	4.745
1.876	0.000
1.899	2.667
1.950	10.345
2.000	15.809
2.050	22.424
2.100	28.921
2.150	35.063
2.200	42.417
2.250	47.939
2.300	54.938
2.350	62.233

Table 8.44. Experimental data for Figure 4.3a (N115, 3M KOH).

N115, 3M KOH	
Cell Voltage (V)	**|Current Density| (mA/cm^2)**
1.449	82.739
1.499	75.533
1.548	66.290
1.599	58.109
1.649	47.891
1.692	42.384
1.749	32.978
1.798	25.772
1.849	17.503
1.902	10.711
1.949	0.729
1.952	0.000
1.999	8.337
2.050	17.462
2.100	26.765
2.150	36.304
2.200	45.636
2.250	55.381
2.300	64.536
2.350	73.957
2.400	84.027
2.450	93.448

Table 8.45. Experimental data for Figure 4.3a (N212, 3M KOH).

N212, 3M KOH	
Cell Voltage (V)	**|Current Density| (mA/cm^2)**
1.450	104.061
1.498	94.286
1.548	82.739
1.598	71.723
1.649	61.446
1.699	51.376
1.749	41.335
1.799	31.235
1.849	20.958
1.899	10.829
1.947	0.000
1.999	12.796
2.049	23.487
2.100	37.160
2.150	49.534
2.200	63.089
2.250	75.729
2.300	88.280
2.350	101.362

Table 8.46. Experimental data for Figure 4.3b (1st Study, N117, 1M KOH).

1st Study, N117, 1M KOH	
Cell Overpotential (V)	**|Current Density| (mA/cm^2)**
-0.310	18.341
-0.260	16.160
-0.210	13.548
-0.160	10.573
-0.110	7.300
-0.060	3.726
-0.010	0.118
0.000	0.000
0.040	4.524
0.090	9.315
0.140	14.388
0.190	19.350
0.240	25.305
0.290	30.399

Table 8.47. Experimental data for Figure 4.3b (N115, 1M KOH).

N115, 1M KOH	
Cell Overpotential (V)	**|Current Density| (mA/cm^2)**
-0.476	56.278
-0.428	51.583
-0.378	46.119
-0.328	40.745
-0.277	35.281
-0.227	29.670
-0.177	23.793
-0.127	17.739
-0.077	11.567
-0.027	4.745
0.000	0.000
0.023	2.667
0.073	10.345
0.123	15.809
0.174	22.424
0.224	28.921
0.274	35.063
0.324	42.417
0.374	47.939
0.424	54.938
0.474	62.233

Table 8.48. Experimental data for Figure 4.3b (N115, 3M KOH).

N115, 3M KOH	
Cell Overpotential (V)	**|Current Density| (mA/cm^2)**
-0.503	82.739
-0.453	75.533
-0.404	66.290
-0.353	58.109
-0.303	47.891
-0.260	42.384
-0.203	32.978
-0.154	25.772
-0.103	17.503
-0.050	10.711
-0.003	0.729
0.000	0.000
0.047	8.337
0.098	17.462
0.148	26.765
0.198	36.304
0.248	45.636
0.298	55.381
0.348	64.536
0.398	73.957
0.448	84.027
0.498	93.448

Table 8.49. Experimental data for Figure 4.3b (N212, 3M KOH).

N212, 3M KOH	
Cell Overpotential (V)	**|Current Density| (mA/cm^2)**
-0.497	104.061
-0.448	94.286
-0.398	82.739
-0.348	71.723
-0.298	61.446
-0.248	51.376
-0.198	41.335
-0.148	31.235
-0.098	20.958
-0.048	10.829
0.000	0.000
0.053	12.796
0.102	23.487
0.153	37.160
0.203	49.534
0.253	63.089
0.303	75.729
0.353	88.280
0.403	101.362

Table 8.50. Experimental data for Figure 4.4 (Nafion 212, 3M KOH).

Nafion 212, 3M KOH	
Zreal (ohm)	**-Zimag (ohm)**
0.7048	-0.0150
0.7034	-0.0051
0.7061	0.0038
0.7100	0.0115
0.7158	0.0181
0.7224	0.0235
0.7271	0.0271
0.7335	0.0298
0.7400	0.0306
0.7469	0.0313
0.7557	0.0314
0.7587	0.0297
0.7650	0.0278
0.7689	0.0263
0.7730	0.0246
0.7763	0.0228
0.7773	0.0213
0.7798	0.0202
0.7830	0.0196
0.7850	0.0194
0.7871	0.0192
0.7878	0.0195
0.7894	0.0203
0.7912	0.0213
0.7951	0.0221
0.7978	0.0243
0.8011	0.0268
0.8044	0.0300
0.8082	0.0334
0.8112	0.0376
0.8167	0.0421
0.8231	0.0470
0.8285	0.0527
0.8354	0.0590

0.8463	0.0639
0.8586	0.0716
0.8622	0.0790
0.8742	0.0846
0.8905	0.0900
0.8998	0.0999
0.9152	0.1033
0.9266	0.1158
0.9413	0.1253
0.9643	0.1373
0.9714	0.1552
1.0066	0.1631
1.0188	0.1921
1.0232	0.1994
1.0547	0.2267
1.0972	0.2543
1.1296	0.2635
1.2717	0.2924
1.2850	0.2772
1.3006	0.3161
1.3718	0.3010
1.4511	0.3188
1.4463	0.3142
1.5603	0.2600

Table 8.51. Experimental data for Figure 4.4 (Nafion 115, 1M KOH).

Nafion 115, 1M KOH	
Zreal (ohm)	**-Zimag (ohm)**
1.8250	-0.0252
1.8199	-0.0140
1.8157	-0.0036
1.8218	0.0046
1.8192	0.0113
1.8268	0.0180
1.8302	0.0220
1.8357	0.0252
1.8451	0.0268
1.8389	0.0279
1.8512	0.0272
1.8528	0.0267
1.8597	0.0255
1.8650	0.0245
1.8703	0.0233
1.8680	0.0233
1.8714	0.0215
1.8721	0.0218
1.8712	0.0222
1.8768	0.0220
1.8758	0.0227
1.8800	0.0246
1.8805	0.0274
1.8866	0.0287
1.8893	0.0290
1.8847	0.0324
1.8967	0.0364
1.8983	0.0411
1.9034	0.0459
1.9128	0.0515
1.9156	0.0575
1.9255	0.0645
1.9361	0.0766
1.9409	0.0819

1.9547	0.0890
1.9683	0.0981
1.9849	0.1069
1.9959	0.1160
2.0114	0.1260
2.0374	0.1352
2.0424	0.1460
2.0697	0.1567
2.0905	0.1701
2.1140	0.1825
2.1480	0.1958
2.1716	0.2174
2.2069	0.2199
2.2359	0.2486
2.2830	0.2516
2.3245	0.2665
2.3710	0.2667
2.4106	0.2838
2.4658	0.2821
2.4730	0.2817
2.5558	0.2777
2.5950	0.2717
2.6252	0.2592
2.6777	0.2566

Table 8.52. Experimental data for Figure 4.4 (Nafion 115, 3M KOH).

Nafion 115, 3M KOH	
Zreal (ohm)	**-Zimag (ohm)**
1.4180	-0.0339
1.4176	-0.0229
1.4162	-0.0123
1.4209	-0.0039
1.4233	0.0031
1.4267	0.0083
1.4305	0.0116
1.4345	0.0146
1.4388	0.0165
1.4426	0.0166
1.4481	0.0171
1.4500	0.0169
1.4528	0.0163
1.4551	0.0157
1.4602	0.0158
1.4617	0.0156
1.4641	0.0156
1.4656	0.0156
1.4675	0.0163
1.4681	0.0173
1.4721	0.0181
1.4729	0.0195
1.4764	0.0211
1.4785	0.0227
1.4812	0.0238
1.4858	0.0260
1.4861	0.0290
1.4917	0.0329
1.4968	0.0371
1.5021	0.0414
1.5068	0.0464
1.5138	0.0512
1.5185	0.0569
1.5291	0.0636

1.5383	0.0686
1.5505	0.0730
1.5618	0.0802
1.5734	0.0860
1.5873	0.0891
1.5980	0.0975
1.6102	0.1062
1.6253	0.1141
1.6378	0.1246
1.6556	0.1368
1.6784	0.1437
1.6926	0.1673
1.7139	0.1729
1.7540	0.2037
1.7834	0.2167
1.8219	0.2301
1.8658	0.2267
1.9236	0.2823
1.9732	0.2793
1.9831	0.2533
2.0341	0.2591
2.1064	0.2452
2.1418	0.2335
2.1577	0.2043

Table 8.53. Experimental data for Figure 4.5a (Nafion 115, 1M KOH).

N115, 1M KOH	
IR-Corr. Cell Voltage (V)	**|Current Density| (mA/cm^2)**
1.631	56.278
1.660	51.583
1.688	46.119
1.716	40.745
1.743	35.281
1.770	29.670
1.797	23.793
1.822	17.739
1.846	11.567
1.869	4.745
1.876	0.000
1.889	2.667
1.907	10.345
1.935	15.809
1.958	22.424
1.982	28.921
2.006	35.063
2.026	42.417
2.054	47.939
2.075	54.938
2.096	62.233

Table 8.54. Experimental data for Figure 4.5a (Nafion 115, 3M KOH).

N115, 3M KOH	
IR-Corr. Cell Voltage (V)	**|Current Density| (mA/cm^2)**
1.713	82.739
1.740	75.533
1.760	66.290
1.784	58.109
1.802	47.891
1.827	42.384
1.855	32.978
1.881	25.772
1.905	17.503
1.937	10.711
1.952	0.729
1.952	0.000
1.973	8.337
1.994	17.462
2.014	26.765
2.034	36.304
2.054	45.636
2.073	55.381
2.094	64.536
2.114	73.957
2.132	84.027
2.152	93.448

Table 8.55. Experimental data for Figure 4.5a (Nafion 212, 3M KOH).

N212, 3M KOH	
IR-Corr. Cell Voltage (V)	**|Current Density| (mA/cm^2)**
1.614	104.061
1.647	94.286
1.679	82.739
1.711	71.723
1.745	61.446
1.780	51.376
1.814	41.335
1.848	31.235
1.882	20.958
1.916	10.829
1.947	0.000
1.979	12.796
2.012	23.487
2.041	37.160
2.072	49.534
2.100	63.089
2.130	75.729
2.161	88.280
2.190	101.362

Table 8.56. Experimental data for Figure 4.5b (Nafion 115, 1M KOH).

N115, 1M KOH	
IR-Corr. Cell Overpotential (V)	**|Current Density| (mA/cm^2)**
-0.246	56.278
-0.217	51.583
-0.189	46.119
-0.161	40.745
-0.133	35.281
-0.106	29.670
-0.080	23.793
-0.054	17.739
-0.030	11.567
-0.008	4.745
0.000	0.000
0.012	2.667
0.031	10.345
0.059	15.809
0.082	22.424
0.105	28.921
0.130	35.063
0.150	42.417
0.178	47.939
0.199	54.938
0.219	62.233

Table 8.57. Experimental data for Figure 4.5b (Nafion 115, 3M KOH).

N115, 3M KOH	
IR-Corr. Cell Overpotential (V)	**|Current Density| (mA/cm^2)**
-0.239	82.739
-0.212	75.533
-0.192	66.290
-0.168	58.109
-0.150	47.891
-0.125	42.384
-0.097	32.978
-0.071	25.772
-0.047	17.503
-0.015	10.711
0.000	0.729
0.000	0.000
0.021	8.337
0.042	17.462
0.062	26.765
0.082	36.304
0.102	45.636
0.121	55.381
0.142	64.536
0.162	73.957
0.180	84.027
0.200	93.448

Table 8.58. Experimental data for Figure 4.5b (Nafion 212, 3M KOH).

N212, 3M KOH	
IR-Corr. Cell Overpotential (V)	**|Current Density| (mA/cm^2)**
-0.333	104.061
-0.300	94.286
-0.268	82.739
-0.235	71.723
-0.202	61.446
-0.167	51.376
-0.133	41.335
-0.099	31.235
-0.065	20.958
-0.031	10.829
0.000	0.000
0.032	12.796
0.065	23.487
0.094	37.160
0.125	49.534
0.154	63.089
0.184	75.729
0.214	88.280
0.244	101.362

Table 8.59. Experimental data for Figure 4.6 (Nafion 115, 1M KOH).

N115, 1M KOH	
Power Density (mW/cm^2)	**|Current Density| (mA/cm^2)**
78.801	56.278
74.722	51.583
69.122	46.119
63.105	40.745
56.413	35.281
48.924	29.670
40.429	23.793
31.031	17.739
20.811	11.567
8.775	4.745
0.000	0.000

Table 8.60. Experimental data for Figure 4.6 (Nafion 115, 3M KOH).

N115, 3M KOH	
Power Density (mW/cm^2)	**|Current Density| (mA/cm^2)**
119.859	82.739
113.224	75.533
102.624	66.290
92.900	58.109
78.970	47.891
71.706	42.384
57.693	32.978
46.343	25.772
32.372	17.503
20.375	10.711
1.421	0.729
0.000	0.000

Table 8.61. Experimental data for Figure 4.6 (Nafion 212, 3M KOH).

N212, 3M KOH	
Power Density (mW/cm^2)	**|Current Density| (mA/cm^2)**
150.900	104.061
141.282	94.286
128.110	82.739
114.648	71.723
101.295	61.446
87.271	51.376
72.284	41.335
56.185	31.235
38.750	20.958
20.564	10.829
0.000	0.000

Table 8.62. Experimental data for Figure 4.7a.

Time (s)	V_Cell (V)	V_H2 vs SHE (V)	V_I2 vs SHE (V)
0	1.307	-0.733	0.575
1	1.307	-0.729	0.579
2	1.308	-0.727	0.581
3	1.308	-0.726	0.582
4	1.308	-0.728	0.579
5	1.307	-0.736	0.571
6	1.308	-0.717	0.590
7	1.307	-0.732	0.575
8	1.307	-0.731	0.576
9	1.307	-0.729	0.579
10	1.307	-0.714	0.593
11	1.307	-0.727	0.581
12	1.307	-0.737	0.570
13	1.307	-0.729	0.578
14	1.307	-0.724	0.584
15	1.307	-0.729	0.578
16	1.307	-0.742	0.565
17	1.307	-0.728	0.579
18	1.307	-0.727	0.581
19	1.307	-0.726	0.581
20	1.307	-0.741	0.566
21	1.307	-0.726	0.581
22	1.307	-0.713	0.594
23	1.307	-0.729	0.578
24	1.307	-0.731	0.577
25	1.307	-0.732	0.575
26	1.307	-0.720	0.587
27	1.307	-0.736	0.571
28	1.307	-0.724	0.583
29	1.307	-0.736	0.572
30	1.307	-0.725	0.582
31	1.307	-0.734	0.574
32	1.307	-0.729	0.578
33	1.307	-0.734	0.573
34	1.307	-0.735	0.573

35	1.307	-0.719	0.588
36	1.307	-0.724	0.584
37	1.307	-0.729	0.579
38	1.307	-0.738	0.569
39	1.307	-0.718	0.590
40	1.307	-0.731	0.576
41	1.307	-0.734	0.574
42	1.307	-0.739	0.568
43	1.307	-0.712	0.595
44	1.307	-0.732	0.576
45	1.307	-0.730	0.577
46	1.307	-0.732	0.575
47	1.307	-0.724	0.584
48	1.307	-0.726	0.582
49	1.307	-0.722	0.585
50	1.307	-0.731	0.576
51	1.307	-0.731	0.576
52	1.307	-0.725	0.583
53	1.307	-0.713	0.594
54	1.307	-0.733	0.574
55	1.307	-0.736	0.571
56	1.307	-0.717	0.591
57	1.307	-0.730	0.578
58	1.307	-0.737	0.571
59	1.307	-0.731	0.576
60	1.307	-0.725	0.583
61	1.307	-0.724	0.584
62	1.307	-0.736	0.571
63	1.307	-0.732	0.575
64	1.307	-0.724	0.583
65	1.307	-0.734	0.573
66	1.307	-0.732	0.576
67	1.307	-0.726	0.581
68	1.307	-0.733	0.574

Table 8.63. Experimental data for Figure 4.7b (1M KOH).

1M KOH	
Cell Voltage (V)	**|Current Density| (mA/cm^2)**
0.278	107.639
0.325	105.083
0.350	102.252
0.374	99.854
0.399	98.989
0.424	95.765
0.449	93.681
0.474	92.148
0.499	89.120
0.524	86.172
0.549	83.419
0.573	80.628
0.598	79.959
0.623	76.303
0.648	74.455
0.673	72.410
0.698	69.226
0.723	67.496
0.748	64.350
0.773	61.873
0.798	59.790
0.822	57.902
0.847	55.307
0.872	52.152
0.897	50.314
0.922	47.601
0.947	44.416
0.972	41.468
0.997	38.597
1.021	36.278
1.046	32.936
1.071	30.380
1.096	27.510
1.121	23.932

1.146	20.865
1.171	17.327
1.196	14.181
1.221	10.564
1.246	6.947
1.271	3.212
1.292	0.000
1.324	4.652
1.349	9.055
1.373	13.459
1.399	18.059
1.424	22.856
1.448	27.377
1.473	32.253
1.498	36.931
1.523	42.082
1.548	46.957
1.573	52.029
1.597	57.494
1.622	62.252
1.647	67.245
1.672	72.396
1.697	78.254
1.722	83.444
1.747	89.538
1.772	95.632
1.797	99.721
1.822	106.051
1.846	110.848
1.871	116.431
1.896	122.171

Table 8.64. Experimental data for Figure 4.7b (2M KOH).

2M KOH	
Cell Voltage (V)	**|Current Density| (mA/cm^2)**
0.303	154.492
0.325	150.860
0.350	149.643
0.374	145.908
0.399	141.648
0.424	139.715
0.449	137.009
0.474	131.858
0.499	127.848
0.524	123.798
0.548	123.051
0.573	117.429
0.598	115.371
0.623	112.685
0.648	107.377
0.673	104.723
0.698	103.216
0.723	98.137
0.748	95.844
0.773	91.479
0.798	89.081
0.822	85.071
0.847	81.847
0.872	79.016
0.897	74.416
0.922	71.024
0.947	67.338
0.972	63.702
0.997	59.770
1.022	55.101
1.046	52.123
1.071	47.916
1.096	43.512
1.121	40.327

1.146	36.081
1.171	31.520
1.196	27.117
1.221	22.674
1.246	18.388
1.270	13.631
1.296	8.952
1.320	4.352
1.344	0.000
1.374	5.753
1.399	10.707
1.424	15.857
1.449	20.850
1.474	26.040
1.498	31.270
1.523	36.499
1.548	42.239
1.573	47.154
1.598	52.816
1.623	58.556
1.648	64.571
1.673	69.830
1.697	75.138
1.722	80.593
1.747	86.589
1.772	91.700
1.797	97.107
1.822	103.037
1.847	108.476
1.872	113.227
1.897	117.978

Table 8.65. Experimental data for Figure 4.7b (3M KOH).

3M KOH	
Cell Voltage (V)	**|Current Density| (mA/cm^2)**
0.304	164.027
0.325	158.499
0.350	155.311
0.375	154.427
0.400	147.972
0.424	145.646
0.449	141.373
0.474	139.014
0.499	135.947
0.524	134.571
0.549	128.595
0.574	127.219
0.599	120.777
0.623	119.205
0.649	116.485
0.673	111.767
0.698	111.276
0.723	107.344
0.748	102.842
0.773	101.151
0.798	95.726
0.823	92.344
0.847	89.749
0.872	85.110
0.898	82.476
0.922	77.561
0.947	74.465
0.972	71.663
0.997	67.191
1.022	63.505
1.047	59.554
1.072	55.150
1.097	51.100
1.121	46.618

1.146	41.743
1.171	37.968
1.196	33.368
1.221	28.650
1.246	24.050
1.271	19.411
1.296	14.535
1.321	9.660
1.345	4.784
1.371	0.106
1.372	0.000
1.424	10.667
1.449	15.867
1.474	21.077
1.499	26.335
1.524	31.545
1.548	37.206
1.574	42.514
1.598	48.304
1.623	54.005
1.648	59.755
1.673	64.817
1.698	70.322
1.723	76.023
1.747	81.910
1.772	87.769
1.797	92.290
1.822	97.441
1.847	101.687
1.872	108.096
1.897	112.421

Table 8.66. Experimental data for Figure 4.8a (1M KOH).

1M KOH	
IR-Corr. Cell Voltage (V)	**|Current Density| (mA/cm^2)**
0.678	107.639
0.715	105.083
0.730	102.252
0.746	99.854
0.767	98.989
0.780	95.765
0.797	93.681
0.817	92.148
0.830	89.120
0.844	86.172
0.859	83.419
0.873	80.628
0.895	79.959
0.907	76.303
0.925	74.455
0.943	72.410
0.955	69.226
0.974	67.496
0.987	64.350
1.003	61.873
1.020	59.790
1.038	57.902
1.053	55.307
1.066	52.152
1.084	50.314
1.099	47.601
1.112	44.416
1.126	41.468
1.140	38.597
1.156	36.278
1.169	32.936
1.184	30.380
1.198	27.510
1.210	23.932

1.224	20.865
1.235	17.327
1.248	14.181
1.260	10.564
1.272	6.947
1.282	3.212
1.292	0.000
1.307	4.652
1.315	9.055
1.323	13.459
1.332	18.059
1.339	22.856
1.346	27.377
1.353	32.253
1.361	36.931
1.366	42.082
1.373	46.957
1.379	52.029
1.384	57.494
1.391	62.252
1.397	67.245
1.403	72.396
1.406	78.254
1.412	83.444
1.414	89.538
1.416	95.632
1.426	99.721
1.427	106.051
1.434	110.848
1.439	116.431
1.442	122.171

Table 8.67. Experimental data for Figure 4.8a (2M KOH).

2M KOH	
IR-Corr. Cell Voltage (V)	**|Current Density| (mA/cm^2)**
0.877	154.492
0.886	150.860
0.906	149.643
0.917	145.908
0.926	141.648
0.943	139.715
0.958	137.009
0.964	131.858
0.974	127.848
0.984	123.798
1.006	123.051
1.010	117.429
1.027	115.371
1.042	112.685
1.047	107.377
1.062	104.723
1.082	103.216
1.088	98.137
1.104	95.844
1.113	91.479
1.129	89.081
1.139	85.071
1.152	81.847
1.166	79.016
1.174	74.416
1.186	71.024
1.197	67.338
1.209	63.702
1.219	59.770
1.226	55.101
1.240	52.123
1.250	47.916
1.258	43.512
1.271	40.327

1.280	36.081
1.288	31.520
1.297	27.117
1.305	22.674
1.314	18.388
1.321	13.631
1.329	8.952
1.337	4.352
1.344	0.000
1.354	5.753
1.363	10.707
1.370	15.857
1.378	20.850
1.386	26.040
1.393	31.270
1.400	36.499
1.405	42.239
1.414	47.154
1.420	52.816
1.425	58.556
1.430	64.571
1.437	69.830
1.443	75.138
1.450	80.593
1.454	86.589
1.462	91.700
1.469	97.107
1.474	103.037
1.480	108.476
1.489	113.227
1.498	117.978

Table 8.68. Experimental data for Figure 4.8a (3M KOH).

3M KOH	
IR-Corr. Cell Voltage (V)	**|Current Density| (mA/cm^2)**
0.913	164.027
0.914	158.499
0.927	155.311
0.949	154.427
0.950	147.972
0.966	145.646
0.975	141.373
0.991	139.014
1.005	135.947
1.025	134.571
1.027	128.595
1.047	127.219
1.048	120.777
1.067	119.205
1.082	116.485
1.089	111.767
1.112	111.276
1.122	107.344
1.130	102.842
1.149	101.151
1.154	95.726
1.166	92.344
1.181	89.749
1.189	85.110
1.204	82.476
1.211	77.561
1.224	74.465
1.239	71.663
1.247	67.191
1.258	63.505
1.268	59.554
1.277	55.150
1.287	51.100
1.295	46.618

1.301	41.743
1.312	37.968
1.320	33.368
1.328	28.650
1.335	24.050
1.343	19.411
1.350	14.535
1.357	9.660
1.363	4.784
1.371	0.106
1.372	0.000
1.384	10.667
1.390	15.867
1.395	21.077
1.401	26.335
1.407	31.545
1.410	37.206
1.416	42.514
1.418	48.304
1.422	54.005
1.426	59.755
1.432	64.817
1.436	70.322
1.440	76.023
1.443	81.910
1.446	87.769
1.454	92.290
1.460	97.441
1.469	101.687
1.470	108.096
1.479	112.421

Table 8.69. Experimental data for Figure 4.8b (1M KOH).

1M KOH	
IR-Corr. Cell Overpotential (V)	**|Current Density| (mA/cm^2)**
-0.614	107.639
-0.577	105.083
-0.562	102.252
-0.546	99.854
-0.525	98.989
-0.512	95.765
-0.495	93.681
-0.475	92.148
-0.461	89.120
-0.448	86.172
-0.433	83.419
-0.419	80.628
-0.397	79.959
-0.385	76.303
-0.367	74.455
-0.349	72.410
-0.337	69.226
-0.318	67.496
-0.305	64.350
-0.289	61.873
-0.272	59.790
-0.254	57.902
-0.239	55.307
-0.226	52.152
-0.208	50.314
-0.193	47.601
-0.180	44.416
-0.166	41.468
-0.152	38.597
-0.136	36.278
-0.123	32.936
-0.108	30.380
-0.094	27.510
-0.082	23.932

-0.068	20.865
-0.057	17.327
-0.044	14.181
-0.032	10.564
-0.020	6.947
-0.009	3.212
0.000	0.000
0.011	4.652
0.019	9.055
0.028	13.459
0.036	18.059
0.043	22.856
0.050	27.377
0.057	32.253
0.065	36.931
0.071	42.082
0.077	46.957
0.083	52.029
0.088	57.494
0.095	62.252
0.101	67.245
0.107	72.396
0.110	78.254
0.116	83.444
0.118	89.538
0.120	95.632
0.130	99.721
0.131	106.051
0.138	110.848
0.143	116.431
0.146	122.171

Table 8.70. Experimental data for Figure 4.8b (2M KOH).

2M KOH	
IR-Corr. Cell Overpotential (V)	**|Current Density| (mA/cm^2)**
-0.466	154.492
-0.458	150.860
-0.437	149.643
-0.427	145.908
-0.418	141.648
-0.400	139.715
-0.385	137.009
-0.380	131.858
-0.369	127.848
-0.359	123.798
-0.338	123.051
-0.334	117.429
-0.316	115.371
-0.301	112.685
-0.296	107.377
-0.281	104.723
-0.261	103.216
-0.256	98.137
-0.239	95.844
-0.231	91.479
-0.215	89.081
-0.205	85.071
-0.192	81.847
-0.178	79.016
-0.170	74.416
-0.158	71.024
-0.146	67.338
-0.135	63.702
-0.125	59.770
-0.117	55.101
-0.103	52.123
-0.094	47.916
-0.085	43.512
-0.072	40.327

-0.063	36.081
-0.056	31.520
-0.047	27.117
-0.039	22.674
-0.029	18.388
-0.023	13.631
-0.015	8.952
-0.007	4.352
0.000	0.000
0.011	5.753
0.019	10.707
0.026	15.857
0.035	20.850
0.042	26.040
0.049	31.270
0.056	36.499
0.062	42.239
0.070	47.154
0.076	52.816
0.081	58.556
0.086	64.571
0.093	69.830
0.100	75.138
0.106	80.593
0.111	86.589
0.119	91.700
0.125	97.107
0.130	103.037
0.137	108.476
0.146	113.227
0.154	117.978

Table 8.71. Experimental data for Figure 4.8b (3M KOH).

3M KOH	
IR-Corr. Cell Overpotential (V)	**|Current Density| (mA/cm^2)**
-0.459	164.027
-0.458	158.499
-0.445	155.311
-0.423	154.427
-0.423	147.972
-0.406	145.646
-0.397	141.373
-0.381	139.014
-0.368	135.947
-0.348	134.571
-0.346	128.595
-0.326	127.219
-0.324	120.777
-0.306	119.205
-0.291	116.485
-0.284	111.767
-0.260	111.276
-0.250	107.344
-0.242	102.842
-0.223	101.151
-0.218	95.726
-0.206	92.344
-0.191	89.749
-0.183	85.110
-0.168	82.476
-0.162	77.561
-0.148	74.465
-0.134	71.663
-0.126	67.191
-0.114	63.505
-0.104	59.554
-0.096	55.150
-0.086	51.100
-0.077	46.618

-0.071	41.743
-0.060	37.968
-0.052	33.368
-0.045	28.650
-0.037	24.050
-0.029	19.411
-0.023	14.535
-0.016	9.660
-0.009	4.784
-0.001	0.106
0.000	0.000
0.012	10.667
0.018	15.867
0.023	21.077
0.029	26.335
0.034	31.545
0.038	37.206
0.043	42.514
0.046	48.304
0.050	54.005
0.053	59.755
0.060	64.817
0.064	70.322
0.068	76.023
0.071	81.910
0.074	87.769
0.082	92.290
0.088	97.441
0.097	101.687
0.098	108.096
0.107	112.421

Table 8.72. Experimental data for Figure 4.9.

|Current Density| (mA/cm^2)	**V_Cell (V)**	**V_H2 (V)**	**V_I2 (V)**	**IR-Corr. V_Cell (V)**	**IR-Corr. V_H2 (V)**	**IR-Corr. V_I2 (V)**
158.915	0.304	-0.222	0.082	0.895	-0.402	0.493
151.347	0.350	-0.245	0.106	0.913	-0.416	0.497
143.745	0.400	-0.272	0.128	0.934	-0.435	0.500
136.668	0.450	-0.300	0.150	0.958	-0.454	0.504
131.065	0.500	-0.329	0.170	0.987	-0.478	0.509
122.743	0.549	-0.358	0.191	1.006	-0.497	0.509
116.911	0.599	-0.393	0.206	1.034	-0.525	0.509
109.113	0.649	-0.418	0.231	1.055	-0.542	0.513
103.052	0.699	-0.452	0.247	1.082	-0.569	0.513
95.215	0.748	-0.477	0.271	1.102	-0.585	0.518
90.418	0.798	-0.509	0.289	1.134	-0.611	0.523
81.257	0.848	-0.538	0.310	1.150	-0.630	0.520
74.769	0.898	-0.568	0.330	1.176	-0.653	0.523
66.120	0.948	-0.594	0.353	1.193	-0.669	0.524
59.711	0.997	-0.623	0.374	1.219	-0.691	0.529
51.661	1.047	-0.649	0.398	1.239	-0.707	0.532
44.043	1.097	-0.675	0.422	1.261	-0.725	0.536
35.835	1.147	-0.699	0.448	1.280	-0.739	0.541
28.545	1.197	-0.724	0.472	1.303	-0.756	0.546
20.551	1.246	-0.746	0.501	1.323	-0.769	0.554
12.753	1.297	-0.769	0.528	1.344	-0.783	0.561
4.365	1.346	-0.790	0.555	1.362	-0.795	0.567
0.000	1.375	-0.805	0.570	1.375	-0.805	0.570
3.335	1.402	-0.817	0.584	1.389	-0.814	0.593
12.279	1.449	-0.838	0.611	1.403	-0.824	0.579
22.109	1.499	-0.858	0.641	1.417	-0.833	0.583
31.217	1.549	-0.880	0.669	1.433	-0.844	0.588
40.915	1.598	-0.900	0.699	1.446	-0.853	0.593
51.203	1.648	-0.920	0.728	1.458	-0.862	0.595
61.066	1.698	-0.941	0.757	1.471	-0.872	0.599
71.485	1.748	-0.964	0.783	1.482	-0.884	0.598
82.821	1.798	-0.982	0.815	1.490	-0.889	0.601
94.099	1.847	-1.003	0.844	1.497	-0.897	0.600
103.234	1.897	-1.025	0.872	1.513	-0.908	0.605

Table 8.73. Experimental data for Figure 4.10 (1M KOH).

1M KOH	
Power Density (mW/cm^2)	**|Current Density| (mA/cm^2)**
29.919	107.639
34.120	105.083
35.763	102.252
37.395	99.854
39.521	98.989
40.632	95.765
42.067	93.681
43.686	92.148
44.484	89.120
45.144	86.172
45.767	83.419
46.230	80.628
47.826	79.959
47.550	76.303
48.264	74.455
48.752	72.410
48.321	69.226
48.784	67.496
48.123	64.350
47.801	61.873
47.689	59.790
47.617	57.902
46.851	55.307
45.485	52.152
45.142	50.314
43.886	47.601
42.049	44.416
40.296	41.468
38.474	38.597
37.049	36.278
34.461	32.936
32.548	30.380
30.154	27.510
26.824	23.932

23.916	20.865
20.289	17.327
16.957	14.181
12.896	10.564
8.654	6.947
4.081	3.212
0.000	0.000

Table 8.74. Experimental data for Figure 4.10 (2M KOH).

2M KOH	
Power Density (mW/cm^2)	**|Current Density| (mA/cm^2)**
46.812	154.492
48.984	150.860
52.338	149.643
54.597	145.908
56.552	141.648
59.238	139.715
61.481	137.009
62.473	131.858
63.775	127.848
64.856	123.798
67.472	123.051
67.331	117.429
69.042	115.371
70.257	112.685
69.605	107.377
70.476	104.723
72.079	103.216
70.931	98.137
71.674	95.844
70.674	91.479
71.053	89.081
69.959	85.071
69.358	81.847
68.915	79.016
66.767	74.416
65.482	71.024
63.750	67.338
61.902	63.702
59.579	59.770
56.289	55.101
54.536	52.123
51.335	47.916
47.707	43.512
45.213	40.327

41.356	36.081
36.899	31.520
32.423	27.117
27.679	22.674
22.908	18.388
17.314	13.631
11.598	8.952
5.746	4.352
0.000	0.000

Table 8.75. Experimental data for Figure 4.10 (3M KOH).

3M KOH	
Power Density (mW/cm^2)	**|Current Density| (mA/cm^2)**
49.802	164.027
51.513	158.499
54.320	155.311
57.879	154.427
59.122	147.972
61.796	145.646
63.525	141.373
65.905	139.014
67.857	135.947
70.541	134.571
70.552	128.595
72.984	127.219
72.314	120.777
74.322	119.205
75.545	116.485
75.216	111.767
77.707	111.276
77.618	107.344
76.908	102.842
78.177	101.151
76.382	95.726
75.969	92.344
76.055	89.749
74.256	85.110
74.024	82.476
71.532	77.561
70.542	74.465
69.661	71.663
66.977	67.191
64.893	63.505
62.347	59.554
59.102	55.150
56.042	51.100
52.280	46.618

47.846	41.743
44.471	37.968
39.908	33.368
34.983	28.650
29.961	24.050
24.668	19.411
18.832	14.535
12.757	9.660
6.437	4.784
0.145	0.106

Table 8.76. Experimental data for Figure 4.11 (1-Phase).

1-Phase			
Cell Voltage (V)	**IR-Corr. Cell Voltage (V)**	**|Current Density| (mA/cm^2)**	**Power Density (mW/cm^2)**
0.304	0.895	158.915	48.270
0.350	0.913	151.347	53.009
0.400	0.934	143.745	57.495
0.450	0.958	136.668	61.471
0.500	0.987	131.065	65.473
0.549	1.006	122.743	67.421
0.599	1.034	116.911	70.041
0.649	1.055	109.113	70.800
0.699	1.082	103.052	72.002
0.748	1.102	95.215	71.263
0.798	1.134	90.418	72.181
0.848	1.150	81.257	68.908
0.898	1.176	74.769	67.130
0.948	1.193	66.120	62.657
0.997	1.219	59.711	59.553
1.047	1.239	51.661	54.098
1.097	1.261	44.043	48.314
1.147	1.280	35.835	41.095
1.197	1.303	28.545	34.155
1.246	1.323	20.551	25.613
1.297	1.344	12.753	16.534
1.346	1.362	4.365	5.875
1.375	1.375	0.000	0.000
1.402	1.389	3.335	
1.449	1.403	12.279	
1.499	1.417	22.109	
1.549	1.433	31.217	
1.598	1.446	40.915	
1.648	1.458	51.203	
1.698	1.471	61.066	
1.748	1.482	71.485	
1.798	1.490	82.821	
1.847	1.497	94.099	

1.897	1.513	103.234	

Table 8.77. Experimental data for Figure 4.11 (2-Phase).

2-Phase			
Cell Voltage (V)	**IR-Corr. Cell Voltage (V)**	**|Current Density| (mA/cm^2)**	**Power Density (mW/cm^2)**
0.400	0.966	188.197	75.261
0.450	0.984	177.442	79.855
0.500	1.003	167.032	83.539
0.550	1.021	156.573	86.124
0.600	1.055	151.159	90.751
0.650	1.080	142.619	92.751
0.701	1.105	134.342	94.119
0.750	1.145	131.090	98.382
0.801	1.173	123.564	98.929
0.851	1.197	114.979	97.821
0.901	1.224	107.554	96.865
0.951	1.256	101.458	96.462
1.001	1.273	90.404	90.483
1.051	1.302	83.443	87.689
1.101	1.323	73.824	81.280
1.151	1.349	65.851	75.803
1.201	1.369	55.789	67.011
1.251	1.385	44.525	55.713
1.301	1.405	34.273	44.606
1.351	1.421	23.241	31.410
1.402	1.433	10.437	14.628
1.440	1.440	0.000	0.000
1.449	1.441	2.494	
1.499	1.446	17.534	
1.549	1.452	32.342	
1.599	1.458	46.834	
1.649	1.467	60.545	
1.699	1.479	73.075	
1.750	1.498	83.727	
1.800	1.520	92.861	
1.850	1.546	100.835	
1.900	1.578	107.015	
1.950	1.607	113.934	

2.000	1.640	119.609	
2.048	1.669	125.895	

Table 8.78. Experimental data for Figure 4.12.

2-Phase				
Cell Voltage (V)	**IR-Corr. V_Cell (V)**	**IR-Corr. V_H2 (V)**	**IR-Corr. V_I2 (V)**	**|Current Density| (mA/cm^2)**
0.400	0.966	-0.436	0.530	0.188
0.450	0.984	-0.452	0.532	0.177
0.500	1.003	-0.469	0.534	0.167
0.550	1.021	-0.486	0.535	0.157
0.600	1.055	-0.518	0.537	0.151
0.650	1.080	-0.542	0.538	0.143
0.701	1.105	-0.565	0.540	0.134
0.750	1.145	-0.604	0.541	0.131
0.801	1.173	-0.631	0.542	0.124
0.851	1.197	-0.654	0.543	0.115
0.901	1.224	-0.681	0.544	0.108
0.951	1.256	-0.711	0.545	0.101
1.001	1.273	-0.727	0.546	0.090
1.051	1.302	-0.755	0.548	0.083
1.101	1.323	-0.775	0.549	0.074
1.151	1.349	-0.800	0.550	0.066
1.201	1.369	-0.818	0.551	0.056
1.251	1.385	-0.833	0.552	0.045
1.301	1.405	-0.851	0.554	0.034
1.351	1.421	-0.867	0.555	0.023
1.402	1.433	-0.877	0.556	0.010
1.440	1.440	-0.884	0.557	0.000
1.449	1.441	-0.887	0.555	0.002
1.499	1.446	-0.890	0.557	0.018
1.549	1.452	-0.894	0.559	0.032
1.599	1.458	-0.899	0.560	0.047
1.649	1.467	-0.906	0.561	0.061
1.699	1.479	-0.917	0.562	0.073
1.750	1.498	-0.935	0.563	0.084
1.800	1.520	-0.956	0.564	0.093
1.850	1.546	-0.981	0.565	0.101
1.900	1.578	-1.012	0.567	0.107
1.950	1.607	-1.040	0.568	0.114

2.000	1.640	-1.072	0.569	0.120
2.048	1.669	-1.100	0.570	0.126

8.4 Appendix D: Experimental Data for Chapter 5

Table 8.79. Experimental data for Figure 5.2 (Vanadium Flow Rate = 5 mL/min).

H_2-Vanadium discharge polarization and power density curves		
Vanadium Flow Rate = 5 mL/min		
Cell Voltage - OCV (V)	**Current Density (A/cm^2)**	**Power Density (W/cm^2)**
0.205	0.135	
0.155	0.105	
0.105	0.074	
0.055	0.042	
0.000	0.000	0.000
-0.095	0.044	0.044
-0.144	0.072	0.068
-0.194	0.101	0.091
-0.244	0.127	0.108
-0.294	0.151	0.121
-0.344	0.170	0.128
-0.394	0.187	0.131
-0.444	0.201	0.131
-0.494	0.212	0.128
-0.544	0.222	0.122
-0.594	0.229	0.115
-0.644	0.235	0.106
-0.693	0.239	0.096
-0.743	0.242	0.085

Table 8.80. Experimental data for Figure 5.2 (Vanadium Flow Rate = 6 mL/min).

H_2-Vanadium discharge polarization and power density curves		
Vanadium Flow Rate = 6 mL/min		
Cell Voltage - OCV (V)	**Current Density (A/cm2)**	**Power Density (W/cm2)**
0.206	0.148	
0.156	0.116	
0.106	0.081	
0.056	0.046	
0.000	0.000	0.000
-0.094	0.052	0.052
-0.144	0.083	0.079
-0.194	0.116	0.105
-0.243	0.148	0.126
-0.293	0.177	0.142
-0.343	0.204	0.153
-0.393	0.229	0.161
-0.443	0.252	0.164
-0.493	0.272	0.164
-0.543	0.291	0.160
-0.593	0.308	0.155
-0.643	0.324	0.146
-0.692	0.338	0.135
-0.742	0.350	0.123

Table 8.81. Experimental data for Figure 5.2 (Vanadium Flow Rate = 12 mL/min).

H_2-Vanadium discharge polarization and power density curves		
Vanadium Flow Rate = 12 mL/min		
Cell Voltage - OCV (V)	**Current Density (A/cm2)**	**Power Density (W/cm2)**
0.205	0.148	
0.155	0.115	
0.105	0.080	
0.055	0.044	
0.000	0.000	0.000
-0.095	0.054	0.054
-0.145	0.086	0.082
-0.195	0.120	0.108
-0.245	0.151	0.129
-0.295	0.181	0.145
-0.345	0.208	0.156
-0.394	0.233	0.163
-0.444	0.257	0.167
-0.494	0.278	0.167
-0.544	0.298	0.164
-0.594	0.316	0.158
-0.644	0.332	0.150
-0.693	0.346	0.139
-0.743	0.359	0.126

Table 8.82. Experimental data for Figure 5.3 (CNT, NR212).

H_2-Vanadium discharge polarization and power density curves		
CNT, NR212		
Cell Voltage - OCV (V)	**Current Density (A/cm^2)**	**Power Density (W/cm^2)**
0.201	0.435	
0.151	0.348	
0.101	0.233	
0.051	0.116	
0.000	0.000	0.000
-0.055	0.095	0.100
-0.105	0.193	0.193
-0.155	0.289	0.274
-0.205	0.374	0.336
-0.255	0.445	0.378
-0.304	0.506	0.405
-0.354	0.558	0.419
-0.404	0.597	0.419
-0.454	0.630	0.410
-0.504	0.657	0.395
-0.554	0.675	0.372
-0.604	0.690	0.346
-0.654	0.705	0.318
-0.704	0.716	0.287
-0.754	0.720	0.253

Table 8.83. Experimental data for Figure 5.3 (SGL10AA, NR212).

H_2-Vanadium discharge polarization and power density curves		
SGL10AA, NR212		
Cell Voltage - OCV (V)	**Current Density (A/cm2)**	**Power Density (W/cm2)**
0.214	0.176	
0.164	0.166	
0.115	0.129	
0.065	0.080	
0.015	0.028	
0.000	0.000	0.000
-0.085	0.065	0.065
-0.135	0.114	0.108
-0.185	0.163	0.146
-0.235	0.210	0.178
-0.285	0.255	0.204
-0.334	0.298	0.224
-0.384	0.340	0.238
-0.434	0.380	0.247
-0.484	0.417	0.251
-0.534	0.452	0.249
-0.584	0.484	0.243
-0.634	0.513	0.232
-0.684	0.539	0.216
-0.734	0.562	0.198

Table 8.84. Experimental data for Figure 5.4 (NR211).

H_2-Vanadium discharge polarization and power density curves		
NR211		
Cell Voltage - OCV (V)	**Current Density (A/cm^2)**	**Power Density (W/cm^2)**
0.214	0.296	
0.164	0.252	
0.114	0.186	
0.065	0.113	
0.015	0.040	
0.000	0.000	0.000
-0.085	0.111	0.110
-0.135	0.172	0.163
-0.185	0.231	0.208
-0.235	0.288	0.244
-0.284	0.340	0.272
-0.334	0.389	0.291
-0.384	0.432	0.302
-0.434	0.470	0.305
-0.484	0.502	0.301
-0.534	0.528	0.290
-0.584	0.548	0.274
-0.634	0.563	0.254
-0.684	0.574	0.230
-0.734	0.580	0.203

Table 8.85. Experimental data for Figure 5.4 (NR212).

H_2-Vanadium discharge polarization and power density curves		
NR212		
Cell Voltage - OCV (V)	**Current Density (A/cm2)**	**Power Density (W/cm2)**
0.214	0.176	
0.164	0.166	
0.115	0.129	
0.065	0.080	
0.015	0.028	
0.000	0.000	0.000
-0.085	0.065	0.065
-0.135	0.114	0.108
-0.185	0.163	0.146
-0.235	0.210	0.178
-0.285	0.255	0.204
-0.334	0.298	0.224
-0.384	0.340	0.238
-0.434	0.380	0.247
-0.484	0.417	0.251
-0.534	0.452	0.249
-0.584	0.484	0.243
-0.634	0.513	0.232
-0.684	0.539	0.216
-0.734	0.562	0.198

Table 8.86. Experimental data for Figure 5.4 (N115).

H_2-Vanadium discharge polarization and power density curves		
N115		
Cell Voltage - OCV (V)	**Current Density (A/cm^2)**	**Power Density (W/cm^2)**
0.205	0.148	
0.155	0.115	
0.105	0.080	
0.055	0.044	
0.005	0.009	
0.000	0.000	0.000
-0.095	0.054	0.054
-0.145	0.086	0.082
-0.195	0.120	0.108
-0.245	0.151	0.129
-0.295	0.181	0.145
-0.345	0.208	0.156
-0.394	0.233	0.163
-0.444	0.257	0.167
-0.494	0.278	0.167
-0.544	0.298	0.164
-0.594	0.316	0.158
-0.644	0.332	0.150
-0.693	0.346	0.139
-0.743	0.359	0.126

Table 8.87. Experimental data for Figure 5.4 (N117).

H_2-Vanadium discharge polarization and power density curves		
N117		
Cell Voltage - OCV (V)	**Current Density (A/cm2)**	**Power Density (W/cm2)**
0.213	0.156	
0.163	0.124	
0.113	0.088	
0.063	0.051	
0.013	0.015	
0.000	0.000	0.000
-0.087	0.035	0.034
-0.137	0.057	0.054
-0.186	0.081	0.073
-0.236	0.107	0.091
-0.286	0.131	0.105
-0.336	0.154	0.115
-0.386	0.173	0.121
-0.436	0.190	0.123
-0.486	0.204	0.122
-0.536	0.216	0.119
-0.586	0.226	0.113
-0.636	0.235	0.106
-0.685	0.243	0.097
-0.735	0.249	0.087

Table 8.88. Experimental data for Figure 5.5 (NR211).

H_2-Vanadium discharge polarization curves		
NR211		
Cell Voltage - OCV (V)	**Current Density (A/cm^2)**	**IR-Corr Overpotential (V)**
0.000	0.000	0.000
-0.085	0.111	-0.046
-0.135	0.172	-0.074
-0.185	0.231	-0.103
-0.235	0.288	-0.132
-0.284	0.340	-0.163
-0.334	0.389	-0.196
-0.384	0.432	-0.230
-0.434	0.470	-0.267
-0.484	0.502	-0.305
-0.534	0.528	-0.346
-0.584	0.548	-0.388
-0.634	0.563	-0.433
-0.684	0.574	-0.479
-0.734	0.580	-0.527

Table 8.89. Experimental data for Figure 5.5 (NR212).

H_2-Vanadium discharge polarization curves		
NR212		
Cell Voltage - OCV (V)	**Current Density (A/cm2)**	**IR-Corr Overpotential (V)**
0.000	0.000	0.000
-0.085	0.065	-0.045
-0.135	0.114	-0.065
-0.185	0.163	-0.086
-0.235	0.210	-0.107
-0.285	0.255	-0.129
-0.334	0.298	-0.152
-0.384	0.340	-0.176
-0.434	0.380	-0.202
-0.484	0.417	-0.229
-0.534	0.452	-0.257
-0.584	0.484	-0.288
-0.634	0.513	-0.320
-0.684	0.539	-0.354
-0.734	0.562	-0.390

Table 8.90. Experimental data for Figure 5.5 (N115).

H_2-Vanadium discharge polarization curves		
N115		
Cell Voltage - OCV (V)	**Current Density (A/cm^2)**	**IR-Corr Overpotential (V)**
0.000	0.000	0.000
-0.095	0.054	-0.045
-0.145	0.086	-0.065
-0.195	0.120	-0.083
-0.245	0.151	-0.104
-0.295	0.181	-0.126
-0.345	0.208	-0.150
-0.394	0.233	-0.176
-0.444	0.257	-0.205
-0.494	0.278	-0.234
-0.544	0.298	-0.266
-0.594	0.316	-0.299
-0.644	0.332	-0.334
-0.693	0.346	-0.370
-0.743	0.359	-0.408

Table 8.91. Experimental data for Figure 5.5 (N117).

H_2-Vanadium discharge polarization curves		
N117		
Cell Voltage - OCV (V)	**Current Density (A/cm2)**	**IR-Corr Overpotential (V)**
0.000	0.000	0.000
-0.087	0.035	-0.035
-0.137	0.057	-0.051
-0.186	0.081	-0.065
-0.236	0.107	-0.077
-0.286	0.131	-0.090
-0.336	0.154	-0.106
-0.386	0.173	-0.127
-0.436	0.190	-0.153
-0.486	0.204	-0.181
-0.536	0.216	-0.213
-0.586	0.226	-0.248
-0.636	0.235	-0.284
-0.685	0.243	-0.323
-0.735	0.249	-0.363

Table 8.92. Experimental data for Figure 5.6 (CNT, NR212).

H_2-Vanadium discharge polarization and power density curves		
CNT, NR212		
Cell Voltage - OCV (V)	**Current Density (A/cm^2)**	**Power Density (W/cm2)**
0.201	0.435	
0.151	0.348	
0.101	0.233	
0.051	0.116	
0.000	0.000	0.000
-0.055	0.095	0.100
-0.105	0.193	0.193
-0.155	0.289	0.274
-0.205	0.374	0.336
-0.255	0.445	0.378
-0.304	0.506	0.405
-0.354	0.558	0.419
-0.404	0.597	0.419
-0.454	0.630	0.410
-0.504	0.657	0.395
-0.554	0.675	0.372
-0.604	0.690	0.346
-0.654	0.705	0.318
-0.704	0.716	0.287
-0.754	0.720	0.253

Table 8.93. Experimental data for Figure 5.6 (Full IR-Corr, CNT, NR212).

H_2-Vanadium discharge polarization and power density curves		
Full IR-Corr, CNT, NR212		
Cell Voltage - OCV (V)	**Current Density (A/cm2)**	**Power Density (W/cm2)**
0.048	0.435	
0.028	0.348	
0.016	0.233	
0.006	0.116	
0.000	0.000	0.000
-0.023	0.095	0.103
-0.040	0.193	0.205
-0.058	0.289	0.302
-0.079	0.374	0.383
-0.104	0.445	0.445
-0.134	0.506	0.492
-0.166	0.558	0.524
-0.203	0.597	0.539
-0.242	0.630	0.544
-0.282	0.657	0.540
-0.326	0.675	0.526
-0.371	0.690	0.507
-0.416	0.705	0.485
-0.462	0.716	0.460
-0.511	0.720	0.428

Table 8.94. Experimental data for Figure 5.6 (Electr. IR-Corr, CNT, NR212).

H_2-Vanadium discharge polarization and power density curves		
Electr. IR-Corr, CNT, NR212		
Cell Voltage - OCV (V)	**Current Density (A/cm^2)**	**Power Density (W/cm2)**
0.130	0.435	
0.093	0.348	
0.060	0.233	
0.028	0.116	
0.000	0.000	0.000
-0.041	0.095	0.101
-0.076	0.193	0.198
-0.112	0.289	0.287
-0.149	0.374	0.357
-0.188	0.445	0.408
-0.229	0.506	0.444
-0.271	0.558	0.466
-0.315	0.597	0.472
-0.360	0.630	0.469
-0.406	0.657	0.459
-0.453	0.675	0.440
-0.500	0.690	0.417
-0.548	0.705	0.392
-0.596	0.716	0.364

8.5 Appendix E: Experimental Data for Chapter 6

Table 8.95. Experimental data for Figure 6.3.

Membrane Type	Membrane Thickness (μm)	Steady-state Crossover Current Density (mA/cm^2)
NR211	25.4	26.9
NR212	50.8	12.2
N115	127	3.0
N117	183	2.0
EBN-30	30	7.2
EBN-40	40	3.1

Table 8.96. Experimental data for Figure 6.4 and Figure 6.5 (NR211, NR212, N115, N117).

OCV Drop for Various Membranes							
Time (h)	**NR211**	**Time (h)**	**NR212**	**Time (h)**	**N115**	**Time (h)**	**N117**
0.00	1.0500	0.00	1.0500	0.00	1.0500	0.00	1.0500
0.25	1.0232	0.25	1.0419	0.50	1.0437	0.75	1.0443
0.50	1.0208	1.00	1.0413	1.25	1.0431	1.50	1.0446
0.75	1.0183	1.75	1.0406	2.00	1.0431	2.25	1.0443
1.00	1.0153	2.50	1.0403	2.75	1.0431	3.00	1.0443
1.25	1.0119	3.25	1.0403	3.50	1.0425	3.75	1.0440
1.50	1.0089	4.00	1.0400	4.25	1.0428	4.50	1.0440
1.75	1.0052	4.75	1.0400	5.00	1.0425	5.25	1.0437
2.00	1.0015	5.50	1.0400	5.75	1.0422	6.00	1.0431
2.25	0.9969	6.25	1.0397	6.50	1.0416	6.75	1.0431
2.50	0.9924	7.00	1.0394	7.25	1.0416	7.50	1.0428
2.75	0.9866	7.75	1.0394	8.00	1.0413	8.25	1.0425
3.00	0.9795	8.50	1.0391	8.75	1.0409	9.00	1.0422
3.25	0.9710	9.25	1.0391	9.50	1.0409	9.75	1.0422
3.50	0.9594	10.00	1.0391				
3.75	0.9429						
4.00	0.9145						
4.25	0.8591						
4.50	0.7672						
4.75	0.6346						
5.00	0.4674						
5.25	0.2933						
5.50	0.1509						
5.75	0.0632						
6.00	0.0547						

Table 8.97. Experimental data for Figure 6.4 (EBN-30 and EBN-40).

OCV Drop for Various Membranes			
Time (h)	**EBN-30**	**Time (h)**	**EBN-40**
0.00	1.0500	0.00	1.0500
1.00	1.0394	1.25	1.0437
1.75	1.0379	2.00	1.0428
2.50	1.0370	2.75	1.0422
3.25	1.0361	3.50	1.0422
4.00	1.0358	4.25	1.0416
4.75	1.0354	5.00	1.0413
5.50	1.0351	5.75	1.0413
6.25	1.0348	6.50	1.0409
7.00	1.0345	7.25	1.0409
7.75	1.0342	8.00	1.0409
8.50	1.0339	8.75	1.0409
9.25	1.0336	9.50	1.0406
10.00	1.0333	10.25	1.0403

Table 8.98. Experimental data for Figure 6.6.

Rate of OCV Drop for Various Membranes				
Time (h)	**NR211**	**NR212**	**N115**	**N117**
0.50	58.33	16.09	12.60	11.00
1.00	34.70	8.77	6.62	5.05
2.00	24.33	4.88	3.45	2.68
3.00	23.39	3.21	2.40	1.89

Table 8.99. Experimental data for Figure 6.7 (NR211).

H_2-Vanadium discharge polarization and power density curves		
NR211		
Cell Voltage - OCV (V)	**Current Density (A/cm^2)**	**Power Density (W/cm^2)**
0.114	0.186	
0.065	0.113	
0.015	0.040	
0.000	0.000	0.000
-0.085	0.111	0.110
-0.135	0.172	0.163
-0.185	0.231	0.208
-0.235	0.288	0.244
-0.284	0.340	0.272
-0.334	0.389	0.291
-0.384	0.432	0.302
-0.434	0.470	0.305
-0.484	0.502	0.301
-0.534	0.528	0.290
-0.584	0.548	0.274
-0.634	0.563	0.254
-0.684	0.574	0.230
-0.734	0.580	0.203

Table 8.100. Experimental data for Figure 6.7 (NR212).

H_2-Vanadium discharge polarization and power density curves		
NR212		
Cell Voltage - OCV (V)	**Current Density (A/cm2)**	**Power Density (W/cm2)**
0.115	0.129	
0.065	0.080	
0.015	0.028	
0.000	0.000	0.000
-0.085	0.065	0.065
-0.135	0.114	0.108
-0.185	0.163	0.146
-0.235	0.210	0.178
-0.285	0.255	0.204
-0.334	0.298	0.224
-0.384	0.340	0.238
-0.434	0.380	0.247
-0.484	0.417	0.251
-0.534	0.452	0.249
-0.584	0.484	0.243
-0.634	0.513	0.232
-0.684	0.539	0.216
-0.734	0.562	0.198

Table 8.101. Experimental data for Figure 6.7 (N115).

H_2-Vanadium discharge polarization and power density curves		
N115		
Cell Voltage - OCV (V)	**Current Density (A/cm^2)**	**Power Density (W/cm^2)**
0.105	0.080	
0.055	0.044	
0.005	0.009	
0.000	0.000	0.000
-0.095	0.054	0.054
-0.145	0.086	0.082
-0.195	0.120	0.108
-0.245	0.151	0.129
-0.295	0.181	0.145
-0.345	0.208	0.156
-0.394	0.233	0.163
-0.444	0.257	0.167
-0.494	0.278	0.167
-0.544	0.298	0.164
-0.594	0.316	0.158
-0.644	0.332	0.150
-0.693	0.346	0.139
-0.743	0.359	0.126

Table 8.102. Experimental data for Figure 6.7 (N117).

H_2-Vanadium discharge polarization and power density curves		
N117		
Cell Voltage - OCV (V)	**Current Density (A/cm2)**	**Power Density (W/cm2)**
0.113	0.088	
0.063	0.051	
0.013	0.015	
0.000	0.000	0.000
-0.087	0.035	0.034
-0.137	0.057	0.054
-0.186	0.081	0.073
-0.236	0.107	0.091
-0.286	0.131	0.105
-0.336	0.154	0.115
-0.386	0.173	0.121
-0.436	0.190	0.123
-0.486	0.204	0.122
-0.536	0.216	0.119
-0.586	0.226	0.113
-0.636	0.235	0.106
-0.685	0.243	0.097
-0.735	0.249	0.087

Table 8.103. Experimental data for Figure 6.7 (EBN-30).

H_2-Vanadium discharge polarization and power density curves		
EBN (30 micron)		
Cell Voltage - OCV (V)	**Current Density (A/cm2)**	**Power Density (W/cm2)**
0.168	0.128	
0.118	0.108	
0.068	0.067	
0.000	0.000	0.000
-0.082	0.055	0.055
-0.132	0.093	0.089
-0.182	0.131	0.118
-0.232	0.166	0.141
-0.282	0.198	0.158
-0.332	0.228	0.171
-0.381	0.256	0.180
-0.431	0.283	0.184
-0.481	0.308	0.185
-0.531	0.331	0.182
-0.581	0.353	0.177
-0.631	0.372	0.168
-0.681	0.390	0.157
-0.731	0.407	0.143

Table 8.104. Experimental data for Figure 6.7 (EBN-40).

H_2-Vanadium discharge polarization and power density curves		
EBN (40 micron)		
Cell Voltage - OCV (V)	**Current Density (A/cm2)**	**Power Density (W/cm2)**
0.173	0.164	
0.123	0.135	
0.073	0.088	
0.000	0.000	0.000
-0.027	0.020	0.021
-0.077	0.065	0.065
-0.127	0.116	0.111
-0.176	0.168	0.151
-0.226	0.220	0.187
-0.276	0.266	0.213
-0.326	0.308	0.231
-0.376	0.348	0.244
-0.426	0.385	0.250
-0.475	0.419	0.252
-0.525	0.450	0.248
-0.575	0.478	0.239
-0.625	0.503	0.227
-0.675	0.525	0.211
-0.725	0.545	0.192